



HAL
open science

THERMOPHYSICAL PROCESSES AND REACTIVE TRANSPORT MECHANISMS INDUCED BY CO₂ INJECTION IN DEEP SALINE AQUIFERS

Ange Ndjaka

► **To cite this version:**

Ange Ndjaka. THERMOPHYSICAL PROCESSES AND REACTIVE TRANSPORT MECHANISMS INDUCED BY CO₂ INJECTION IN DEEP SALINE AQUIFERS. Fluid mechanics [physics.class-ph]. Université de Pau et des Pays de l'Adour, 2022. English. NNT : 2022PAUU3003 . tel-03663450

HAL Id: tel-03663450

<https://theses.hal.science/tel-03663450v1>

Submitted on 10 May 2022

HAL is a multi-disciplinary open access archive for the deposit and dissemination of scientific research documents, whether they are published or not. The documents may come from teaching and research institutions in France or abroad, or from public or private research centers.

L'archive ouverte pluridisciplinaire **HAL**, est destinée au dépôt et à la diffusion de documents scientifiques de niveau recherche, publiés ou non, émanant des établissements d'enseignement et de recherche français ou étrangers, des laboratoires publics ou privés.

THÈSE

UNIVERSITE DE PAU ET DES PAYS DE L'ADOUR

École doctorale des Sciences Exactes et leurs Applications

Laboratoire des Fluides Complexes et leurs Réservoirs

Présentée et soutenue le 16 février 2022

par **Ange Tatiana NDJAKA**

pour obtenir le grade de docteur
de l'Université de Pau et des Pays de l'Adour
Spécialité: Mécanique des fluides

THERMOPHYSICAL PROCESSES AND REACTIVE TRANSPORT MECHANISMS INDUCED BY CO₂ INJECTION IN DEEP SALINE AQUIFERS

MEMBRES DU JURY

PRÉSIDENT

- Mounir BOU-ALI Professeur / Université de Mondragon, Espagne

RAPPORTEURS

- Samuel MARRE Directeur de Recherche / CNRS - ICMCB Bordeaux, France
- Philippe GOUZE Directeur de Recherche / CNRS - Géosciences Montpellier, France

EXAMINATEURS

- Valentina SHEVTSOVA Directrice de Recherche / Fondation Ikerbasque, Espagne
- Fabrizio CROCCOLO Professeur / Université de Pau et des Pays de l'Adour, France
- Arnault LASSIN Ingénieur-Chercheur / BRGM, Orléans, France

INVITÉ

- Sylvain THIBEAU Docteur - Expert / TotalEnergies, France

DIRECTEURS

- Henri BATALLER Maître de conférences, HDR / Université de Pau et des Pays de l'Adour
- Mohamed AZAROUAL Ingénieur-Chercheur, HDR / BRGM / ISTO, Orléans, France

« Ce n'est que par le travail acharné et l'effort, par une énergie sombre et un courage résolu, que nous passons à de meilleures choses. » Theodore Roosevelt.

A ma feu grand-mère BITAMBO Charlotte épouse KOUM

A ma feu grand-mère NDOUMBE Angèle épouse NDJAKA MBELLA

Remerciements

Cette thèse fait partie de la chaire industrielle CO2ES (CO₂-Enhanced Storage) de l'Université de Pau et des Pays de l'Adour. Elle a été réalisée dans le cadre d'une collaboration entre le Laboratoire des Fluides Complexes et leurs Réservoirs (LFCR/UPPA-Anglet) et l'Unité Minéralogie, Géochimie et Modélisation des Milieux Géologiques de la Direction de l'eau, de l'Environnement, des Procédés & Analyses (DEPA/MG2) du BRGM. Tout au long de cette thèse, j'ai eu la chance d'être entourée par des personnes qui m'ont accompagnée et énormément soutenue tant sur le plan professionnel que personnel. Je tiens à leur dire MERCI à travers ces quelques lignes.

Je tiens particulièrement à remercier mes directeurs et encadrants de thèse qui ont cru en moi dès le départ, qui m'ont donnée l'opportunité d'intégrer leurs équipes de travail et qui m'ont accompagnée sans relâche pour mener à bien ce projet. MERCI à mon directeur de thèse Dr Henri BATALLER qui m'a toujours accompagnée et encouragée à travers ses conseils et discussions enrichissantes et qui a toujours tenu à ce que je sois dans de bonnes conditions de travail. Merci de m'avoir initiée aux techniques optiques. Je le remercie également pour sa gentillesse, sa patience et sa disponibilité permanente. MERCI à mon co-directeur de thèse Dr Mohamed AZAROUAL qui m'a toujours motivée pour que je redouble d'effort. Ses remarques pertinentes ont à chaque fois suscité de la curiosité en mon endroit et m'ont poussée à me remettre en question, afin de mieux développer mon esprit scientifique. MERCI à mon encadrant Pr Fabrizio CROCCOLO, qui m'a également initiée aux techniques optiques et pour son suivi permanent quant à l'évolution de mes travaux. Je le remercie pour sa gentillesse, sa disponibilité et sa réactivité. De par nos échanges enrichissants, il m'a toujours encouragée dans la valorisation de mes travaux. MERCI à mon encadrant Dr Arnault LASSIN, qui a fait de mon séjour à Orléans un moment très profitable et très enrichissant. La richesse de ses expériences m'a été d'un énorme apport quant à la contextualisation de mes travaux. Je tiens à le remercier pour sa gentillesse, sa disponibilité pour toujours répondre à mes questions, son écoute et sa réactivité.

J'exprime toute ma gratitude au Dr Samuel MARRE et au Dr Philippe GOUZE, qui m'ont fait l'honneur de rapporter cette thèse. Un grand Merci au Pr Mounir BOU-ALI qui a

accepté de présider cette thèse, et à mes examinateurs Dr Valentina SHEVTSOVA et Dr Sylvain THIBEAU, pour avoir accepté de participer à mon jury de thèse.

MERCI à Rizwan MINHAS pour son aide sur la partie expérimentale à travers son stage de Master, sa rigueur et sa gentillesse. Un très grand MERCI au Dr Loreto GARCIA FERNANDEZ, qui a été un pilier pour moi durant ma première année de thèse, tant sur le plan professionnel que personnel. MERCI au Dr Cedric GIRAUDET, pour m'avoir fait profiter de ses multiples connaissances et expériences, pour sa disponibilité et pour tous ses conseils. Je remercie tous les doctorants de la chaire COZES, Paul FRUTON, Dan BOUYOU BOUYOU et Mohammed CHRAGA qui, en partageant l'avancée de leurs travaux lors de nos meetings hebdomadaires, me motivaient indirectement à travailler, surtout lorsque j'étais confinée sur le site distant. MERCI à tous mes collègues doctorants pour tous les bons moments de convivialité que nous avons partagés. MERCI à Caroline HANIN ainsi qu'à toute la team du pavillon montauray.

Je voudrais remercier mes aînés, Dr Yannick ATEBA, Dr Josiane DJUIDJE et Dr Thierry SATOH, pour tous leurs conseils et encouragements. Un profond MERCI à tous mes amis, particulièrement Laura Fabiola TOKAM, Patricia Litz TCHIPAWU, Hilary MOGUE MENGOM, et Sara Olivia NDJIKE, pour leur encouragement, leur bienveillance et leur compréhension face à mes manquements durant ces trois dernières années. Je remercie de tout cœur Dr Alima NZIE et Darakhshan GARBA pour tous les supers moments passés ensemble, et qui ont fait de mon année à Orléans un moment inoubliable. MERCI à la team du Pays basque, Irène, Cyrus, Dan, Rostand, Adama, Victor, et Oscar pour tous les bons moments.

Enfin, je remercie toute ma famille. Un MERCI chaleureux à mon cher papa, Pr Jean Marie Bienvenu NDJAKA et ma chère maman Suzanne Félicité MATANGA KOUM, pour leur soutien incommensurable, pour leur présence perpétuelle malgré la distance, pour les conseils et pour les encouragements multiformes. Un énorme MERCI à ma marraine Dr Emire MAGA, qui est là pour moi depuis toujours, et pour ses encouragements. MERCI de tout cœur à mes frères Patrick Aimé NDJAKA, Joseph Aurélien NDJAKA MBELLA, Charmant BEHALAL NDJONMBOCK, Joël BEMA EYANGO, et mes sœurs Marie Ange Manuella NDJAKA BITAMBO, Danie Laure SOH NGAKE et Suzanne Larissa LOMBO MBELLA pour leur soutien indéfectible.

Dédicace spéciale à la team « tu finis quand ? » et « c'est quoi la suite ? ». Pour la fin, ça y est, c'est fini, et pour la suite, restez connectés.

!!!MERCİ A TOUS, MERCİ POUR TOUT !!!

Abstract

CO₂ storage in deep saline aquifers has been recognised as one of the most promising ways to mitigate atmospheric CO₂ emissions and thus respond to the challenges of climate change. However, the injection of CO₂ into the porous medium considerably disturbs its thermodynamic equilibrium. The near-well injection zone is particularly impacted with a strong geochemical reactivity associated with intense heat exchanges. This has a major impact on injectivity of the reservoir and the integrity of the storage. In addition to these effects, there is the added complexity of the presence of two immiscible phases: brine (wetting fluid) and CO₂ (non-wetting fluid). These effects lead to highly coupled Thermo-Hydro-Mechanical-Chemical (THMC) processes, whose interpretations have not yet been completed nor formally implemented into the numerical models.

This thesis work, combining experimental measurements and numerical modelling, focuses on the study of the coupling between the thermal gradients and the diffusive reactive transport processes taking place in the deep saline aquifers, particularly in the near-well injection zone. We studied the exchanges between a cold anhydrous CO₂ phase flowing in high permeability zones, and a hot salty aqueous phase trapped in the porosity of the rock. The strategy of the study starts with a simple approach in a free medium without CO₂ flow, in order to study the reactivity of saline solutions of different chemical compositions, and to evaluate the impact of a thermal gradient on this reaction network.

We have developed an experimental cell that allow to superimpose 2 to 3 layers of solution of different concentration and chemical composition. The analysis of the light scattered by the non-equilibrium fluctuations of concentration and temperature allows to obtain the diffusion coefficients of salts in water. Our results are in good agreement with literature values. Regarding the study of diffusive reactive transport, the analysis of the contrast of the images allowed us to highlight the fact that the precipitation of minerals, obtained by superimposing two aqueous layers of reactive, is accompanied by a convective instability that fades with time. Numerical modelling of the experimental results with PHREEQC using a heterogeneous multicomponent diffusion approach has allowed us to account for these convective instabilities. Different temperature gradients were applied to the reactive system, while keeping a mean temperature of 25 °C. The

experimental observations and numerical interpretations show that the temperature gradient has no significant influence on the behaviour of the system.

Subsequently, we numerically studied the desiccation process (evaporation of water) at the interface between a brine trapped in the rock porosity and the CO₂ flowing in a draining pore structure, simulating the conditions of the Dogger aquifer of the Paris basin. A model coupling the evaporation of water in the CO₂ stream and the heterogeneous multicomponent diffusion of salts predicts the appearance of a mineral assemblage at the evaporation front, mainly composed by halite and anhydrite. Modelling this phenomenon at the reservoir scale would require taking into account the evaporation rate as a function of the CO₂ injection rate and the change in porosity at the interface.

This thesis work has made it possible to highlight several physicochemical, thermophysical and diffusive transport phenomena at phase interfaces. This opens up new perspectives for improving numerical approaches and large-scale modelling, in particular of near-well injection of CO₂ and geological storage reservoirs, and supports future industrial developments and technologies for the ecological transition.

Résumé

Le stockage du CO₂ dans les aquifères salins profonds a été reconnu comme l'une des voies les plus prometteuses pour atténuer les émissions atmosphériques de CO₂ et répondre ainsi aux enjeux du changement climatique. Cependant, l'injection du CO₂ dans le milieu poreux perturbe considérablement son équilibre thermodynamique. La zone proche du puits d'injection est particulièrement impactée avec une forte réactivité géochimique associée à d'intenses échanges thermiques. Cela a un impact majeur sur l'injectivité du réservoir et l'intégrité du stockage. A ces effets s'ajoute une complexité supplémentaire liée à la présence de deux phases non miscibles : la saumure (fluide mouillant) et le CO₂ (fluide non-mouillant). Ces effets conduisent à des processus Thermo-Hydro-Mécaniques-Chimiques (THMC) fortement couplés, dont les interprétations ne sont pas encore abouties ni formellement implémentées dans les modèles numériques.

Ce travail de thèse, associant des mesures expérimentales et des modélisations numériques, porte sur l'étude du couplage entre les gradients thermiques et les processus diffusifs de transport réactif se déroulant dans les aquifères salins, notamment dans la zone proche du puits d'injection. Nous avons étudié les échanges entre une phase froide CO₂ anhydre qui s'écoule dans des zones de forte perméabilité, et une phase aqueuse salée chaude piégée dans la porosité de la roche. La stratégie de l'étude commence par une approche simple en milieu libre sans flux de CO₂ afin d'étudier la réactivité des solutions salines de différentes compositions chimiques et d'évaluer l'impact d'un gradient thermique sur ce réseau réactionnel.

Nous avons développé une cellule expérimentale permettant de superposer 2 à 3 couches de solution de concentration et composition chimique différentes. L'analyse de la lumière diffusée par les fluctuations de non-équilibre de la concentration et de la température permet de remonter aux coefficients de diffusion des sels dans l'eau. Nos résultats sont en bon accord avec les valeurs de la littérature. Pour ce qui est de l'étude du transport réactif diffusif, l'analyse du contraste des images a permis de mettre en évidence le fait que la précipitation de minéral, par mise en contact de deux couches aqueuses de sels réactifs, s'accompagne d'une instabilité convective qui s'estompe dans le temps. La modélisation numérique des résultats expérimentaux avec PHREEQC par une approche de diffusion multi-espèce hétérogène permet de rendre compte des instabilités convectives. Différents

gradients de température ont été appliqués au système réactif, tout en conservant une température moyenne de 25 °C. Les observations expérimentales et les interprétations numériques montrent que le gradient de température n'a pas d'influence significative sur le comportement du système.

Ensuite, nous avons étudié numériquement le processus de dessiccation (évaporation de l'eau) à l'interface entre une saumure piégée dans la porosité de la roche et du CO₂ circulant dans une structure porale drainante, simulant les conditions de l'aquifère du Dogger du bassin parisien. Un modèle couplant l'évaporation de l'eau dans le flux de CO₂ et la diffusion multi-espèces hétérogène des sels prévoit l'apparition d'un assemblage minéral au niveau du front d'évaporation, principalement composé d'halite et d'anhydrite. La modélisation de ce phénomène à l'échelle du réservoir nécessite la prise en compte de la vitesse d'évaporation en fonction du taux d'injection du CO₂ et de l'évolution de la porosité au niveau de l'interface.

Ce travail de thèse a permis de mettre en évidence plusieurs phénomènes physico-chimiques, thermo-physiques et de transport diffusif aux interfaces de phase. Ce qui ouvre de nouvelles perspectives d'amélioration des approches numériques et de modélisation à grande échelle notamment du proche puits d'injection du CO₂ et des réservoirs de stockage géologique et soutenir les futurs développements industriels et technologiques pour la transition écologique.

Contents

Remerciements	ii
Abstract.....	vi
Résumé.....	viii
Contents	x
List of Figures.....	xiv
List of Tables	xxii
General introduction.....	1
Chapter 1 : Bibliographic review of Supercritical CO₂ injection in deep saline aquifers	5
1.1 Contribution of carbon dioxide to the global warming.....	5
1.2 Carbon Capture and Storage technology for atmospheric CO₂ mitigation.....	7
1.2.1 CO ₂ capture	8
1.2.2 CO ₂ transport.....	10
1.2.3 CO ₂ storage.....	10
1.3 Geological formations for CO₂ storage.....	13
1.3.1 Criteria for geological sites selection.....	13
1.3.2 Geological reservoirs.....	14
1.4 Trapping mechanisms of CO₂ in deep saline aquifers	15
1.4.1 Structural trapping mechanism	16
1.4.2 Capillary trapping mechanism	16
1.4.3 Solubility trapping mechanism	17
1.4.4 Mineral trapping mechanism.....	17
1.5 Multiphase reactive transport and near-well behaviour.....	18
1.5.1 Physical and chemical behaviour	18
1.5.2 Thermal behaviour	19
1.5.3 Multiphase fluid flow behaviour.....	20

1.6	Summary of THC behavior in the near well injection zone	23
1.7	Phenomena at pore scale	26
1.7.1	Advection	29
1.7.2	Dispersion.....	30
1.7.3	Molecular diffusion	31
1.8	Conclusion and problem at stake.....	33
Chapter 2 : Multicomponent salts diffusion in water		39
2.1	Introduction	39
2.2	Brief background on transport phenomena.....	40
2.2.1	Phenomenological equation	40
2.2.2	Free diffusion or isothermal diffusion.....	41
2.2.3	Thermodiffusion or Soret effect.....	44
2.3	Optical methods to study the isothermal diffusion of salts in water	47
2.3.1	Electronic speckle pattern interferometry (ESPI)	48
2.3.2	Phase-shifting interferometry (PSI).....	49
2.3.3	Gouy interferometry.....	51
2.3.4	Rayleigh interferometry.....	53
2.4	Numerical modelling procedure.....	56
2.4.1	Thermodynamic properties of electrolytic solutions.....	57
2.4.1.1	Chemical potential.....	57
2.4.2.2	Thermodynamic models	57
2.4.2	PHREEQC description and working principle	65
2.4.3	Diffusive transport modelling in PHREEQC	66
2.5	Conclusion.....	70
Chapter 3 : Contribution to the study of the multicomponent salts diffusion in water		73
3.1	Introduction	73
3.2	Experimental procedure.....	73
3.2.1	Solutions preparation and characterisation	74
3.2.2	Free-diffusion cell.....	74
3.2.3	Shadowgraph setups	77

3.2.4	Dynamic near field imaging.....	78
3.2.5	Structure function analysis.....	80
3.2.6	Dynamics of the non-equilibrium fluctuations	81
3.2.7	Images contrast calculation.....	82
3.3	Free diffusion experiments.....	83
3.3.1	Calibration.....	83
3.3.2	Electrolyte diffusion coefficient measurements.....	88
3.3.3	Non-isothermal conditions	96
3.4	Superimposition of two aqueous layers of non-reactive salts	98
3.4.1	Experimental observations parallel to the gravity.....	98
3.4.2	Numerical modelling.....	100
3.5	Superimposition of two aqueous layers of reactive salts.....	107
3.5.1	Experimental observations parallel to the gravity	107
3.5.2	Numerical modelling.....	111
3.5.3	Experimental observations perpendicular to the gravity.....	116
3.5.4	Numerical modelling.....	119
3.6	Conclusion.....	125
Chapter 4 : Numerical modelling of the reactive transport process induced by the CO₂ storage in a deep saline aquifer		
129		
4.1	Conceptual scheme	129
4.2	Dogger Aquifer properties	133
4.2.1	Mineralogy of the basin.....	133
4.2.2	Composition of the water formation.....	134
4.3	Simulation conditions and some limitations of the PHREEQC and associated thermodynamic databases.....	135
4.4	Description of the simulation model	137
4.5	Modelling procedure with the PHREEQC program.....	139
4.6	Results and discussion.....	144
4.6.1	Evolution of the net volume of minerals	144
4.6.2	Evolution of the ionic strength and the molality of ionic species	145
4.6.3	Evolution of the amount of minerals.....	147

4.6.4	Evolution of the total net volume of each mineral.....	149
4.7	Conclusion.....	150
	General conclusion.....	153
	Bibliography.....	157
	Appendices.....	173
	Appendix A: Macroscopic properties of electrolytes.....	173
	Appendix B: Example of an input file in PHREEQC program.....	175
	Appendix C: Measurement of the densities of saline solution with the density meter (Anton Paar DMA 5000).....	177
	Appendix D: Spreading of Scientific Knowledge.....	179
	Appendix E: Publications.....	181

List of Figures

Figure 1.1: Evolution of the Earth surface temperature difference compared to the period from 1951 to 1980 (from NASA/GISS/GISTEMP v3): the solid black line is the global annual mean, the red one is the five-year lowess smooth and in blue are the uncertainty bars with 95% confidence limit [1].	5
Figure 1.2: Evolution of the average global temperature and atmospheric CO ₂ concentration since 1800 (Source: Leland McInnes at the English-language Wikipedia, CC BY SA 3.0 < http://creativecommons.org/licenses/by sa/3.0/ >, via Wikimedia Commons).	6
Figure 1.3: Schematic diagram of CCS technology showing different targets for CO ₂ geological storage.	8
Figure 1.4: Carbon capture technologies: a) Post-combustion, b) Pre-combustion and c) Oxyfuel combustion (©CO ₂ CRC).	9
Figure 1.5: Geosequestration of CO ₂ in saline aquifers associated with Trapping mechanisms [29].	16
Figure 1.6: Storage security over time depending on a combination of physical and geochemical trapping [33].	18
Figure 1.7: Coupled key processes involved by CO ₂ injection: interactions between them and qualitative influence on the well injectivity [51], [52].	19
Figure 1.8: Lenormand phase diagram for immiscible displacement during drainage [63], [64], [66].	22
Figure 1.9: Coupled processes during GCS [48].	23
Figure 1.10: Schematic zonation of processes occurring in the near-well region after sCO ₂ injection in a saline aquifer. The different radii (r_1 , r_2 , r_3 , r_4) depend on CO ₂ injection flow rate and reservoir properties [50], [78].	25
Figure 1.11: Pressure drop and CO ₂ saturation as functions of time during a typical drainage process inside a micromodel. $t_0 = 0$ is the starting point for the injection time [79].	27
Figure 1.12: Porosity and permeability values for different characteristics of pore-networks [80].	28
Figure 1.13: Images of liquid CO ₂ (white) distribution in the dual-permeability pore network at different capillary number. The flow direction is from left to right [82].	29
Figure 1.14: Illustration of diffusion due to the concentration difference a) in free medium and b) in the pore space [88].	32
Figure 1.15: Conceptual diagram of thesis work. b) Image taken from [100].	35
Figure 1.16: a) Geological Lab on Chip used to monitor carbonate precipitation. b) Typical sizes of the channel cross-section of the microreactor. c) Schematic illustration of the Tjunction part (red insert in a)) showing the counter flow injection of the two	

solutions in the horizontal inlet channels and their mixing flow in the vertical main channel where the calcium carbonate precipitates in the interdiffusion zone [67], [101].	36
Figure 1.17: Injection setup. The solution injection device controls the injection flow of three syringes in the precision of ml/s. A close-up of the side view within the cell is shown in the inset [102]......	37
Figure 1.18: 1D conception configuration for the study of the salts multicomponent diffusion.	38
Figure 2.1: Sketch for the mixing of two solutions by free diffusion in laboratory conditions.....	42
Figure 2.2: Time evolution of the concentration profile plotted vs the normalized height z during a free-diffusion for different times. The horizontal and vertical axes are exchanged for convenience. The thickness of the cell is $h=1$ cm. Initially two horizontal layers of the binary mixture of NaCl-H ₂ O at the uniform concentrations $C_1 = 0.19$ w/w and $C_2 = 0.09$ w/w are separated by a horizontal interface at the mid-height $a= h/2$ (i.e. $z = 0.5$). The homogeneous concentration at the end of the diffusion process is $C=0.14$ w/w and the diffusion coefficient is $D = 1.55 \times 10^{-5}$ cm ² /s [113]......	44
Figure 2.3: General principle of a Soret cell experiment.....	45
Figure 2.4: Time evolution of the normalized concentration profile plotted as a function of the normalized height z during a thermodiffusion process. The horizontal and vertical axes are exchanged for convenience. Plot of Eq. 2.13 for $N = 10$, $D = 1.55 \times 10^{-5}$ cm ² /s [113]. The thickness of the sample is $h=1$ cm.	46
Figure 2.5: ESPI interferometer. BS: beam splitters; CL: collimating lenses; DC: diffusion cell; FG&C: frame grabber and computer; L: laser; M: mirrors; NDF: neutral density filter; OL: object lens; OS: opal screen; SF: spatial filters [128]......	49
Figure 2.6: a) Schematic sketch of the Phase-shifting interferometer b) Design of the test cell [130].	50
Figure 2.7: Diffusion coefficient of NaCl in water as a function of average concentration, at 25 °C. Standard deviations are also plotted for each measurement [102].	50
Figure 2.8: Plot of mass diffusion coefficient obtained at various concentrations of sodium chloride in water. The square symbols are the measurements carried out with full interferogram analysis while circle symbols are for single fringe analysis [131].	51
Figure 2.9: Principle of Gouy interferometry. A sketch of the light source (LS), the lenses (L), and the cell (C) is shown together with the derived interference pattern [134].	52
Figure 2.10: Principle of Rayleigh interferometry. A sketch of the light source (LS), the lenses (L), and the cell (C). [134].....	54
Figure 2.11: The diffusion coefficients of NaCl solutions at 25 °C as a function of the molar concentration C [113].	54
Figure 2.12: The diffusion coefficients of CaCl ₂ solutions at 25 °C as a function of the molar concentration C [113].	55

Figure 2.13: The diffusion coefficients of Na ₂ SO ₄ solutions at 25 °C as a function of the square root of the molar concentration C [138].	56
Figure 2.14: Column divided into cells showing a composition is taken at a half-cell distance.	66
Figure 2.15: Diffusion cell illuminated by a light beam parallel to the concentration gradient.	70
Figure 3.1: a) 3D-drawing of the stainless steel annulus with the Teflon ring in the inner part. b) 2D-drawing of the same, as observed from the top.	75
Figure 3.2: 3D drawing of the diffusion cell	76
Figure 3.3: Shadowgraph optical setup summarized in six distinct blocks: 1) optical components; 2) Camera; 3) free-diffusion cell; 4) specific filling procedure; 5) temperature controllers; 6) computer equipment.	78
Figure 3.4: Main steps in the evaluation of the SF of the NEFs in a free diffusion experiment of NaCl into water (mean concentration $C_{\text{mean}}=2.7 \text{ mol.L}^{-1}$ and concentration difference between the two superimposed solutions of $\Delta C=2 \text{ mol.L}^{-1}$).	80
Figure 3.5: Structure function for different wave numbers of the free-diffusion experiment carried out with the binary mixture of TEG/water at the mean concentration of $C = 0.5 \text{ w/w}$, difference of concentration $\Delta C = 0.2 \text{ w/w}$ between the bottom and top layer solutions, mean temperature of 25°C and 80 minutes after closing the valves.	84
Figure 3.6: Ratio between the static structure factor and the signal background as a function of the wave number for the free-diffusion experiments, carried out with the binary mixture of TEG/water at mean concentration of $C = 0.5 \text{ w/w}$, and for different differences of concentration between the bottom and the top layers, at 25 °C and 80 minutes after closing the valves.	84
Figure 3.7: Decay times of the c-NEFs as a function of the wave numbers and time after closing the inlet/outlet valves for the free-diffusion experiment carried out with the binary mixture of TEG/water at $C = 0.5 \text{ w/w}$, difference of concentration $\Delta C = 0.2 \text{ w/w}$ and $T = 25 \text{ °C}$. The continuous black line corresponds to the curve obtained fitting Eq. 3.3 to data points obtained 80 minutes after starting the free-diffusion experiment.	85
Figure 3.8: a) Mass diffusion coefficient D and b) cut-off wave number q_c as a function of the normalized time for different concentration differences for the free-diffusion experiments carried out with the binary mixture of TEG/water at $C = 0.5 \text{ w/w}$ and $T = 25 \text{ °C}$	86
Figure 3.9: a) Mass diffusion coefficient and b) cut-off wave number as a function of the normalized time for different temperatures for the free-diffusion experiments carried out with the binary mixture of TEG/water at $C = 0.5 \text{ w/w}$ and a difference of concentration $\Delta C = 0.2 \text{ w/w}$	87
Figure 3.10: Structure function for different wave numbers of the free-diffusion experiment carried out with the binary mixture of NaCl/water at the mean concentration of $C = 2.7 \text{ mol.L}^{-1}$, mean temperature of 25°C, 40 minutes after closing the	

valves, and different differences of concentration ΔC between the bottom and top layer solutions, that are indicated under the figures.....	89
Figure 3.11: Ratio between the static structure factor and the signal background as a function of the wave number for the free-diffusion experiments carried out:	90
Figure 3.12: Decay times of the c-NEFs as a function of the wave numbers and time after closing the inlet/outlet valves for the free-diffusion experiment carried out with the binary mixture of NaCl/water at $C = 2.7 \text{ mol.L}^{-1}$, difference of concentration $\Delta C = 2 \text{ mol.L}^{-1}$ and $T = 25 \text{ }^\circ\text{C}$. The continuous black line corresponds to the curve obtained fitting Eq. 3.3 to data points obtained 40 minutes after starting the free-diffusion experiment.....	91
Figure 3.13: a) Mass diffusion coefficient D of NaCl in water and b) cut-off wave number q_c as a function of the normalized time for different concentration differences for the free-diffusion experiments carried out with the binary mixture of NaCl/water at $C = 2.7 \text{ mol.L}^{-1}$ and $T = 25 \text{ }^\circ\text{C}$	92
Figure 3.14: Structure function for different wave numbers of the free-diffusion experiment carried out at mean temperature of 25°C with:	93
Figure 3.15: Structure function for different wave numbers of the free-diffusion experiment carried out with the binary mixture $\text{Na}_2\text{SO}_4/\text{water}$ at mean temperature of $25 \text{ }^\circ\text{C}$, difference of concentration $\Delta C = 0.7 \text{ mol.L}^{-1}$ and 50 minutes after closing the valves with: a) $C = 1 \text{ mol.L}^{-1}$; b) $C = 0.5 \text{ mol.L}^{-1}$	94
Figure 3.16: Structure function for wave number $q = 209.5 \text{ cm}^{-1}$ and for different moments after closing the valves, carried out with: a) the binary mixture $\text{CaCl}_2/\text{water}$ ($C = 0.46 \text{ mol.L}^{-1}$, $\Delta C = 0.8 \text{ mol.L}^{-1}$, $T = 25^\circ\text{C}$); c) the binary mixture $\text{Na}_2\text{SO}_4/\text{water}$ ($C = 0.5 \text{ mol.L}^{-1}$, $\Delta C = 0.7 \text{ mol.L}^{-1}$, $T = 25^\circ\text{C}$). The continuous red line corresponds to the curve obtained fitting Eq. 3.2 to data points. In b) and d) we report the corresponding residuals between data points and the theoretical model.	95
Figure 3.17: Mass diffusion coefficient D as a function of the normalized time for the free-diffusion experiments carried out, circles are for the binary mixture of $\text{CaCl}_2/\text{water}$ ($C = 0.46 \text{ mol.L}^{-1}$, $\Delta C = 0.8 \text{ mol.L}^{-1}$, $T = 25^\circ\text{C}$) and rectangles are for the binary mixture $\text{Na}_2\text{SO}_4/\text{water}$ ($C = 0.5 \text{ mol.L}^{-1}$, $\Delta C = 0.7 \text{ mol.L}^{-1}$, $T = 25^\circ\text{C}$).	96
Figure 3.18: a) Mass diffusion coefficient D and b) cut-off wave number q_c as a function of the normalized time for the free-diffusion experiments carried out with the binary mixture of NaCl/water ($C \approx 2.7 \text{ mol.L}^{-1}$, $\Delta C = 2 \text{ mol.L}^{-1}$, $T_{\text{mean}} = 25 \text{ }^\circ\text{C}$). Circles are for the experiment without a difference of temperature and triangles are with a vertical difference of temperature $\Delta T = +20 \text{ K}$ across the cell.	97
Figure 3.19: Density as a function of the salt concentration in water at $T = 20 \text{ }^\circ\text{C}$, diamonds are for NaCl, circles for CaCl_2 and rectangles for Na_2SO_4 . Open symbols are for literature data [192] and filled symbols are points measured in this work.....	97
Figure 3.20: Normalized image differences :	98
Figure 3.21: a) Normalized image differences and b) contrast of shadowgraph image sequence 40 minutes after closing the valves in a free-diffusion experiment with the binary mixture $\text{CaCl}_2/\text{water}$ ($C = 0.46 \text{ mol.L}^{-1}$, $\Delta C = 0.8 \text{ mol.L}^{-1}$, $T = 25^\circ\text{C}$).....	99

Figure 3.22: Contrast of shadowgraph image sequences Ct as a function of time and for different moments after closing the valves:.....	100
Figure 3.23: Mesh of the column for the numerical modelling of the superimposition of two aqueous layers of non-reactive salts. a) Superimposition of a layer of a $CaCl_2$ solution (0.46 mol.L^{-1}) with a layer of $NaCl$ solution (2.637 mol.L^{-1}). b) Superimposition of layer of $NaCl$ solution (2.637 mol.L^{-1}) with a layer of a Na_2SO_4 solution (1.484 mol.L^{-1}).....	101
Figure 3.24: Concentration profiles representing the initial conditions of simulation of the diffusion column at the homogenous temperature of $25 \text{ }^\circ\text{C}$ and 1 atm : a) when a layer of a $CaCl_2$ solution (0.46 mol.L^{-1}) is brought in contact with a $NaCl$ solution (2.637 mol.L^{-1}). b) when a layer of a $NaCl$ solution (2.637 mol.L^{-1}) is brought in contact with a Na_2SO_4 solution (1.484 mol.L^{-1}).....	101
Figure 3.25: Evolution of the molality of ions when a layer of a $CaCl_2$ solution (0.46 mol.L^{-1}) is brought in contact with a $NaCl$ solution (2.637 mol.L^{-1}) at the homogenous temperature of $25 \text{ }^\circ\text{C}$ in the case of a) Homogeneous multicomponent diffusion after 10 minutes of diffusion, b) Homogeneous multicomponent diffusion after 1 hour of diffusion, c) Heterogeneous multicomponent diffusion after 10 minutes of diffusion and d) Heterogeneous multicomponent diffusion after 1 hour of diffusion.....	103
Figure 3.26: Evolution of the ionic strength over the column as a function of time when a layer of a $CaCl_2$ solution (0.46 mol.L^{-1}) is brought in contact with a $NaCl$ solution (2.637 mol.L^{-1}) at the homogenous temperature of $25 \text{ }^\circ\text{C}$ in the case of a) Homogeneous multicomponent diffusion and b) Heterogeneous multicomponent diffusion.	104
Figure 3.27: Evolution of the density of the solution over the column as a function of time when a layer of a $CaCl_2$ solution (0.46 mol.L^{-1}) is brought in contact with a $NaCl$ solution (2.637 mol.L^{-1}) at the homogenous temperature of $25 \text{ }^\circ\text{C}$ in the case of a) Homogeneous multicomponent diffusion and b) Heterogeneous multicomponent diffusion.	104
Figure 3.28: Evolution of the molality of ions when a layer of a $NaCl$ solution (2.637 mol.L^{-1}) is brought in contact with a Na_2SO_4 solution (1.484 mol.L^{-1}) at the homogenous temperature of $25 \text{ }^\circ\text{C}$ in the case of a) Homogeneous multicomponent diffusion after 10 minutes of diffusion, b) Homogeneous multicomponent diffusion after 1 hour of diffusion, c) Heterogeneous multicomponent diffusion after 10 minutes of diffusion and d) Heterogeneous multicomponent diffusion after 1 hour of diffusion.....	105
Figure 3.29: Evolution of the ionic strength profile as a function of time when a layer of a $NaCl$ solution (2.637 mol.L^{-1}) is brought in contact with a Na_2SO_4 solution (1.484 mol.L^{-1}) at the homogenous temperature of $25 \text{ }^\circ\text{C}$ in the case of a) Homogeneous multicomponent diffusion and b) Heterogeneous multicomponent diffusion.	106
Figure 3.30: Evolution of the density of the solution over the column as a function of time when a layer of a $NaCl$ solution (2.637 mol.L^{-1}) is brought in contact with a Na_2SO_4 solution (1.484 mol.L^{-1}) at the homogenous temperature of $25 \text{ }^\circ\text{C}$ in the case of a) Homogeneous multicomponent diffusion and b) Heterogeneous multicomponent diffusion.	107
Figure 3.31: a) Contrast of shadowgraph image sequences Ct as a function of time and for different moments after closing the valves in the case of the superimposition of the	

three layers at homogenous temperature of 25°C; b) normalized image differences 50 minutes after closing the valves.	109
Figure 3.32: Full resolution shadowgraph images 1 hour to 2h20 after closing the valves in the case of the superimposition of the three layers at homogenous temperature of 25 °C.....	109
Figure 3.33: a) Contrast of shadowgraph image sequences Ct as a function of time and for different moments after closing the valves in the case of the superimposition of the three layers with a vertical difference of temperature ΔT across the cell.	110
Figure 3.34: Repetition of the superimposition of the three layers with a vertical difference of temperature $\Delta T = 20^\circ\text{C}$ across the cell (contrast of shadowgraph image sequences Ct as a function of time and for different moments after closing the valves).	111
Figure 3.35: Mesh of the numerical modelling of the superimposition of a layer of a CaCl_2 solution (0.46 mol.L^{-1}) with a layer of a Na_2SO_4 solution (1.484 mol.L^{-1}) separated by a layer of NaCl solution (2.637 mol.L^{-1}).	111
Figure 3.36: Evolution of the profile of the saturation index of gypsum as a function of time at 25 °C and isothermal case $\Delta T = 0^\circ\text{C}$ a) homogeneous multicomponent diffusion, c) heterogeneous multicomponent diffusion. Evolution of the total amount of precipitated Gypsum along the column as a function of time: b) homogeneous multicomponent diffusion, d) heterogeneous multicomponent diffusion.....	112
Figure 3.37: Saturation indices of gypsum and anhydrite in binary aqueous Na_2SO_4 , NaCl and CaCl_2 solutions at equilibrium with the most stable of the two phases over the temperature range 20 to 70 °C. The size of the boxes on the right side of the chart is indicative of the salinity of the aqueous solutions.	114
Figure 3.38: Evolution of the total amount of Gypsum precipitated along the column as a function of time in the case of heterogeneous multicomponent diffusion for different temperature gradients.	115
Figure 3.39: working principle of the transversal configuration of the shadowgraphic device.	116
Figure 3.40: 3D drawing of the diffusion cell for the transversal configuration of the shadowgraphic device.	117
Figure 3.41: Full resolution shadowgraph images after closing the valves in the case of the superimposition of the three layers at homogenous temperature of 25 °C.....	119
Figure 3.42: Initial concentration profile within the simulated column, at the homogenous temperature of 25 °C and 1 atm.	120
Figure 3.43: Evolution of the molality of ions when layers of binary aqueous CaCl_2 , NaCl and Na_2SO_4 solutions are superimposed at the homogenous temperature of 25 °C in the case of a) Homogeneous multicomponent diffusion after 10 minutes of diffusion, b) Homogeneous multicomponent diffusion after 1 hour of diffusion, c) Heterogeneous multicomponent diffusion after 10 minutes of diffusion and d) Heterogeneous multicomponent diffusion after 1 hour of diffusion	120

Figure 3.44: Evolution of the ionic strength profile as a function of time when layers of binary aqueous CaCl ₂ , NaCl and Na ₂ SO ₄ solution are superimposed at the homogenous temperature of 25 °C in the case of a) homogeneous multicomponent diffusion and b) heterogeneous multicomponent diffusion.	122
Figure 3.45: Evolution of the profile of the saturation index of gypsum as a function of time a) homogeneous multicomponent diffusion, c) heterogeneous multicomponent diffusion. Evolution of the total amount of pure Gypsum in the pure phase assemblage along the column as a function of time: b) homogeneous multicomponent diffusion, d) heterogeneous multicomponent diffusion.	123
Figure 3.46: Evolution of the total amount of pure Gypsum in the pure phase assemblage over the column as a function of time in the case of heterogeneous multicomponent diffusion for different temperature gradient.....	125
Figure 4.1: Evolution of the temperature profile of the Dogger aquifer as a function of distance for different times with Eq. 4.1 with a thermal diffusivity of $0.758 \times 10^{-6} \text{ m}^2 \cdot \text{s}^{-1}$	132
Figure 4.2: Mesh for the numerical modelling for evaporation, diffusion and precipitation of salt within the Dogger aquifer.....	135
Figure 4.3: Concentration profile of Na in the column for one cycle of evaporation whose modelling procedure is exemplified by a) the first step corresponding to the evaporation together with the physical transport of aqueous solution. b) the second step corresponding to the diffusion process.....	140
Figure 4.4: Concentration profiles of Na in the column during two successive cycles of simulation.....	140
Figure 4.5: Evolution of the concentration profiles of a) Na, b) Cl, c) Ca and d) SO ₄ ions over 20 hours. In legend is the time given in hour.....	141
Figure 4.6: Evolution of ionic strength <i>I</i> over 20 hours. In legend is the time given in hour.....	142
Figure 4.7: Evolution of the of ionic strength <i>I</i> over 100 hours in a 3 cm-long column. In legend, the time is in hour.....	142
Figure 4.8: Evolution of saturation indices of a) anhydrite, b) halite, c) calcite and d) chalcedony over 20 hours. In legend is the time given in hour.....	143
Figure 4.9: Log-linear evolution of the total net volume of minerals as a function of time for different depths in the column in. The black dashed-line represents the initial volume of pore solution. In the legend, the distance are in meter.	144
Figure 4.10: Evolution of ionic strength <i>I</i> over 400 hours. In legend is the time given in hour.....	146
Figure 4.11: Evolution of the concentration profiles of ionic species over 400 hours. From the top to bottom at the left side: Na, Ca, and CO ₃ . From top to bottom at the right side: Cl, SO ₄ and Mg. In legend is the time given in hour.	147

Figure 4.12: Evolution of the amount of minerals likely to precipitate over 400 hours: a) anhydrite, b) halite, c) calcite and d) chalcedony.	148
Figure 4.13: Evolution of volume of a) anhydrite b) halite c) calcite and d) chalcedony as a function of time. The black dashed-line represents the initial volume of pore solution	149
Figure 4.14: Log-linear evolution of volume of each mineral allowed to precipitate as a function of time for different distance: a) 1 mm b) 2 mm c) 3 mm and d) 4 mm. The black dashed-line represents the initial volume of pore solution.....	150
Figure B.1: Graphical interface of PHREEQC for the description of an input file.	175
Figure B.2: Input file for the numerical modelling of the the superimposition of a layer of a CaCl_2 solution ($0.475 \text{ mol.kg}^{-1}$) with a layer of NaCl solution ($2.792 \text{ mol.kg}^{-1}$).	176

List of Tables

Table 2.1: Gouy data for NaCl solutions at 25 °C. [134] (see text for details).....	52
Table 3.1: Mass diffusion coefficients D obtained by free-diffusion experiments carried out with the TEG/water binary mixture at mean concentration C in mass fraction of TEG and homogeneous temperature T	88
Table 3.2: Concentration of saline solutions in molality at $T = 25$ °C and $P = 1$ atm.....	100
Table 4.1: Dogger aquifer mineralogy, amount of each mineral per 1.0194 L of saline water and list of minerals not initially present in the reservoir (amount = 0 mole) but likely to precipitate.....	134
Table 4.2: Chemical composition of water from the Dogger aquifer in the region of Fontainebleau (concentration are in ppm [50]).	134

General introduction

Since the advent of the industrial age, humanity has faced the problem of climate change, resulting from a deterioration of the atmospheric layer. This modification can come from processes specific to the Earth or from its interaction with the outside, but mainly from industrial activities. Indeed, the ever-increasing energy demand over the last decades has caused the increase of the greenhouse gases concentration in the atmosphere, resulting in an increase of the average temperature of our planet, as recorded by global temperature monitoring. Carbon dioxide (CO₂) has been recognised as the main greenhouse gas responsible of global warming and reducing its concentration is one of the main tasks of humankind. A portfolio of solutions has been proposed to mitigate CO₂ emissions in the atmosphere. Among them, the technology of Carbon Capture and Storage (CCS) seems to be a promising pathway. It consists in capturing all the CO₂ from large power plants before it is released to the atmosphere, transport the captured CO₂ to the storage sites, and store it underground in geological reservoirs. Several geological reservoirs are the targets for CO₂ storage such as deep saline aquifers, depleted oil and/or gas fields, or unmineable coal seams. Deep saline aquifers are made of porous rocks saturated with highly saline water unusable for agriculture and unfit for consumption. In addition, they have a huge storage capacity that can raise to several gigatons of CO₂ stored per year, making them the most suitable reservoir for CO₂ storage. The captured carbon dioxide is injected at liquid or supercritical state within the porosity of the porous medium. Once injected, the supercritical CO₂ (sCO₂) will react with the components of the reservoir and will be trapped through a combination of physical mechanisms (structural and residual trapping) and of geochemical mechanisms (solubility and mineral trapping). These trapping mechanisms take place following a chronological order and ensure long-term storage. However, numerous studies have shown that the injection of sCO₂ considerably disturbs the equilibrium state of the medium, and the near-well injection area is identified to be particularly impacted by CO₂ injection, leading to highly coupled THMC (Thermal-Hydrodynamical-Mechanical-Chemical) processes, which are simulated on a macroscopic scale but actually take place at the pore scale. Thus, it is required to improve the understanding and the description of those coupled processes for a full assessment of CCS technology.

One of the key parameters for this assessment is the injectivity, whose control is important to maintain a high storage capacity and avoid strong mechanical response, such as fault reactivation or seismic, of the considered aquifer. The injection of $s\text{CO}_2$ in saline aquifers is known to trigger several phenomena in the near well zone, in particular a strong chemical reactivity and intense heat exchange, salt precipitation and mineral dissolution, which could influence the evolution of the porosity and permeability, and therefore injectivity of the reservoir and the safety of the storage. In fact, the acidification of the brine due to CO_2 dissolution disturbs the chemical equilibria of the medium, leading to the dissolution and re-precipitation of minerals like carbonates. Moreover, due to the presence of two distinct immiscible phases (CO_2 and brine) in the porous medium during drainage, the evaporation of the initial brine into the flow of $s\text{CO}_2$ may provide more space for CO_2 , but simultaneously, the solution in the porosity becomes highly saline leading to salt precipitation. The addition of those precipitates inside the porosity could create strong stresses on the rocks or completely clog the percolation paths of $s\text{CO}_2$, reducing the injectivity. Salt precipitation in deep saline aquifers has been experimented from the field and from the laboratory. It has been shown that salt precipitation is governed by a combination of physical processes, which depends mostly on salt transport processes on a macroscopic scale and chemical processes, which mostly occur at the pore scale. Although the development of microfluidic tools for drainage experiments in porous media have significantly improved our knowledge, all the mechanisms involved during evaporation and salt precipitation at the pore scale are not yet well understood and formally implemented into the numerical models. They require deeper understanding as they may present non-intuitive behaviour. Restricting our interest to diffusive effects, larger localized temperature gradients that appear during CO_2 injection can have a strong influence on the dissolution of CO_2 in water, mass transfer in rocks, and precipitation process in the reservoir. Moreover, the evaporation of brine in the CO_2 flow results in a large concentration gradient between the evaporation front and the rest of the reservoir leading to a local salt precipitation at the interface and a retrodiffusion mechanism of ionic species in the reservoir. This induces a segregation of the dissolved chemical species in the pore solutions. Moreover, the porous medium being extremely complex, taking multicomponent diffusion into account in the models can provide real information because the reaction path can be disturbed. A consequence would be for example a shift in the level/localisation of precipitation in the reservoir, knowing that the precise location

where the salt precipitates or how the salt precipitation spatially spreads in a given porous medium remains unclear despite it may affect the variability of the permeability.

This PhD project is funded by E2S-UPPA, Institut Carnot ISIFoR and BRGM and is related to the chair CO₂ES (CO₂ Enhanced Storage), a partnership among E2S-UPPA, TotalEnergies, BRGM and the CNES. The goal of the Chair project is to improve our understanding of the various trapping and transport processes involved in CO₂ geological storage, and especially those processes that contribute to storage efficiency and safety.

This manuscript is organised in 4 chapters. The first chapter presents a literature review on the technology of carbon capture and storage in geological reservoirs and the mechanisms of CO₂ sequestration in saline aquifers. This chapter also describes the multiphase reactive transport and the near well behaviour of the CO₂ at macroscopic and pore scales. The geological reservoir being a complex medium, we propose to study by an experimental approach, the reactivity of a multi-component electrolytic system in a free medium, i.e. without a porous medium. The second chapter presents a background on mass transport phenomena in binary systems and the various experimental methods used for the measurement of mass diffusion coefficients of salts in water. This chapter also presents a description of the behaviour of electrolytes and of fluid-rock interactions by simulation models, which revolve around the fundamentals of thermodynamics of solutions. Chapter 3 focuses on the experimental methodology developed during this thesis for the measurement of transport properties and the study of a multicomponent reactive system with and without thermal gradient. This chapter also presents the interpretation of the experimental results based on geochemical modelling. Finally, chapter 4 focuses on the reactive transport modelling, at a cm scale, of a saline solution representative of real reservoirs and deals with the study of the process of desiccation (due to evaporation of water) at the interface between an aqueous phase trapped in the porosity of the rock and the supercritical CO₂ flowing in a draining pore structure.

Chapter 1 : Bibliographic review of Supercritical CO₂ injection in deep saline aquifers

1.1 Contribution of carbon dioxide to the global warming

The greenhouse effect is a natural warming process of the Earth, which results from the absorption of a significant part of the thermal radiations released from the Earth’s surface by greenhouse gases (GHGs) present in the atmosphere. This effect is therefore an essential phenomenon that makes our planet suitable for life. However, an increase of GHGs concentration in the atmosphere promotes an increase of the global mean temperature, thus contributes to what is called global warming. Fig. 1.1 shows the land-ocean temperature index from 1880 to 2019 with base period from 1951 to 1980 and represents the global temperature monitoring. It reveals an augmentation of the average temperature of our planet. According to this figure, the warming over land and ocean in 2019 was about 0.95 °C above the 20th century average, and no drop is expected.

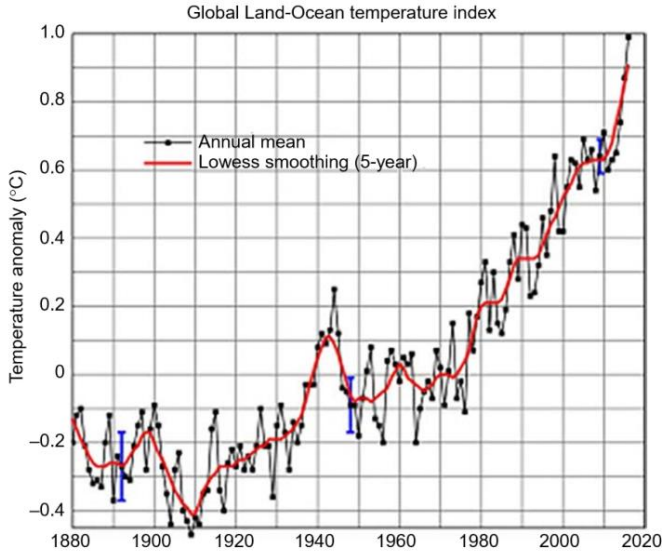


Figure 1.1: Evolution of the Earth surface temperature difference compared to the period from 1951 to 1980 (from NASA/GISS/GISTEMP v3): the solid black line is the global annual mean, the red one is the five-year lowess smooth and in blue are the uncertainty bars with 95% confidence limit [1].

It is now largely accepted that this increase of the average mean temperature since the beginning of the industrial revolution is directly related to the increase of the concentration of GHGs in the atmosphere, mostly due to industrial activities. According to

the census of the Intergovernmental Panel on Climate Change (IPCC), there are more than forty GHGs [2], but carbon dioxide (CO₂) remains by far the most abundant greenhouse gas in the atmosphere and the main responsible of global warming [3]. Most of the CO₂ emissions come from the world energy consumption (42%) [4]. In fact, in order to respond to the ever-increasing energy needs, the burning of fossil fuels like petroleum and coal has mainly led to a drastic increase of the atmospheric CO₂ concentration, crossing the threshold of 407 ppm in 2018 according to the World Meteorological Organization (WMO) [5].

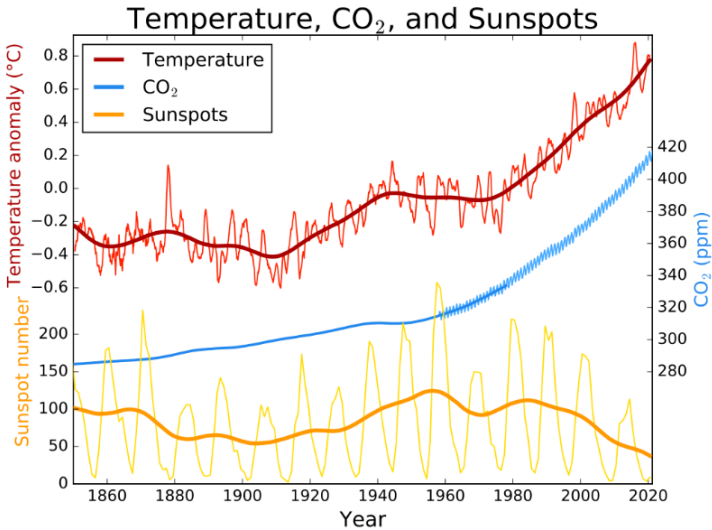


Figure 1.2: Evolution of the average global temperature and atmospheric CO₂ concentration since 1800 (Source: Leland McInnes at the English-language Wikipedia, CCBY SA 3.0 <<http://creativecommons.org/licenses/by-sa/3.0/>>, via Wikimedia Commons).

The scientific evidence that the overwhelming increase of CO₂ concentration in the atmosphere has mainly contributed to the increase of the global average temperature, thus leading to global warming [3] can be seen in Fig. 1.2. The consequences of the latter are numerous and significant: extreme weather events, augmentation of tornados and hurricanes, droughts, floods, melting of the poles and glaciers, rising sea levels, loss of biodiversity, etc. Global warming is thus one of the major concerns of humankind and many researchers are alerting for the need to take immediate measures in order to limit emissions of GHGs, and particularly CO₂.

1.2 Carbon Capture and Storage technology for atmospheric CO₂ mitigation

Though the lockdown due to Covid-19 pandemic in 2020 has caused a drop in CO₂ emissions because of the shutdown of many industries, the Covid-19 pandemic may not be a short-term solution to climate change [5], [6]. Faced with the emergency, a portfolio of solutions has been proposed to reduce greenhouse gas emissions in the future and to respond to the current challenges of global warming. As proposed by Caldeira *et al.*, [7] these possibilities are organized in different categories:

- Reduce our dependence on fossil fuels by using alternative energies: photovoltaic, wind power, hydraulic, biofuels, nuclear, geothermal, etc.
- Energy conservation and efficiency through the development of hybrid vehicles and energy-efficient buildings.
- CO₂ utilization, aiming to consume it as a reagent in various industrial processes.
- The capture of CO₂ from big power plants or natural gas processing plants and its oceanic and geological sequestration.
- Increase natural carbon sinks through better forest management and protection of agricultural land.
- CO₂ storage by mineral carbonation: chemical transformation of CO₂ into stable inorganic carbonate minerals using oxides of alkali or alkaline metals, naturally present in silicate rocks [8].

Among all these solutions, the technology of CO₂ Capture, transport and geological Storage (CCS) is recognised as a key and represents one of the most efficient and immediate mid-term solution to reduce CO₂ emissions and its global warming consequences. The CCS consists in capturing the CO₂ from large power plants before it is released to the atmosphere, transport the captured CO₂ to the storage sites, and store it underground in deep geological reservoirs (Fig. 1.3). According to the BLUE Map scenario of the International Energy Agency (IEA), this technology would now seem essential and is expected to contribute with at least 20% of the reduction of CO₂ release to the atmosphere by 2050 [9].

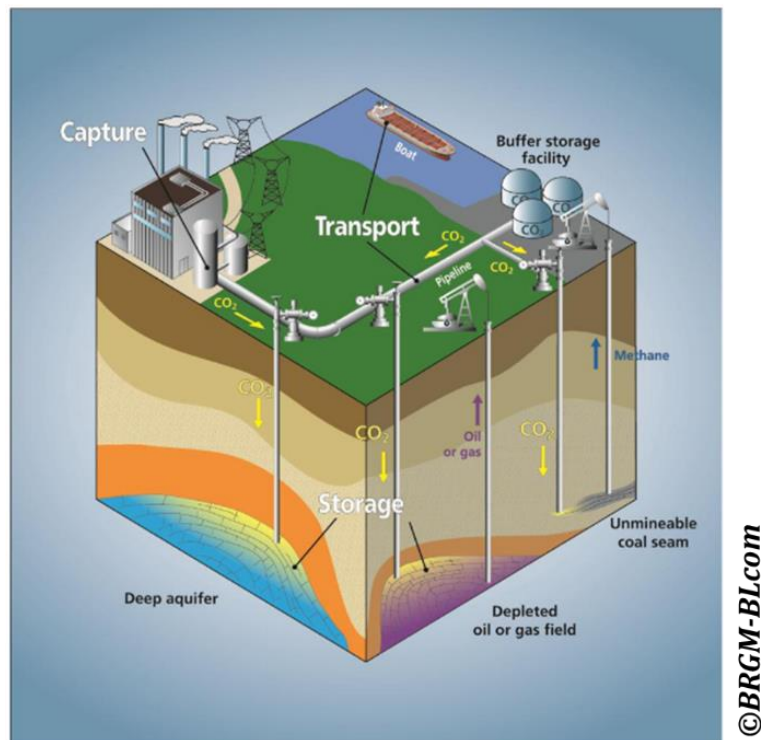


Figure 1.3: Schematic diagram of CCS technology showing different targets for CO₂ geological storage.

1.2.1 CO₂ capture

This first step consists in capturing waste CO₂ directly from large industrial sites such as power plants, natural gas production sites or cement factories, and is usually the most expensive step in the CCS process [10]. CO₂ capture can be performed through three main processes represented in Fig. 1.4:

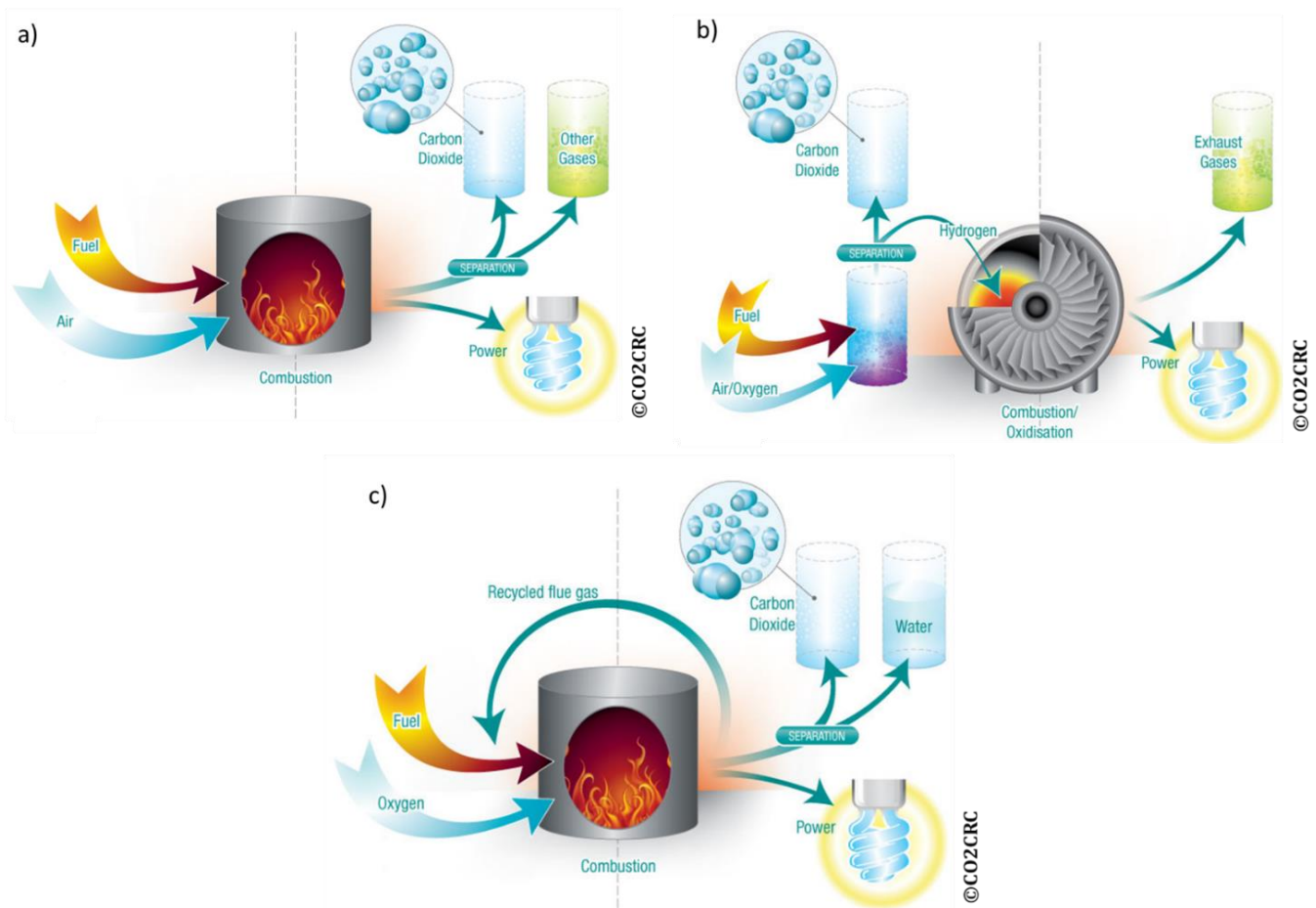


Figure 1.4: Carbon capture technologies: a) Post-combustion, b) Pre-combustion and c) Oxyfuel combustion (©CO2CRC).

- **Post-combustion carbon capture:** After the combustion of fuel and air, CO₂ is separated from the other exhaust gases which contain a mixture of nitrogen (N₂), water and some oxygenated compounds such as SO₂, NO₂ and O₂. The separation can be performed by different techniques such as absorption by physical or chemical solvents, adsorption on solids, membrane separation technique or even cryogenics. The most widely used is the chemical absorption with organic amines like monoethanolamine (MEA).
- **Pre-combustion carbon capture:** It consists in capturing CO₂ before combustion takes place. The principle is first to transform the fuel into syngas by gasification with oxygen or air. Then, the mixture of carbon monoxide and water coming from gasification is chemically transformed into a mixture of CO₂ and H₂. Finally the CO₂ is separated from H₂ using a solvent like methanol. At the end, the combustion of hydrogen produces energy.

- Oxyfuel combustion: unlike the post-combustion process, the combustion involves fuel and oxygen using recycled flue gas, leading to an exhaust gas that mainly contains CO₂ and water vapour. The separation of the exhaust gas becomes easy and allows producing a high purity CO₂ stream.

1.2.2 CO₂ transport

CO₂ transport is the second step in the CCS technology. The captured CO₂ from the punctual (spot) sources is compressed and safely transported, usually through pipelines, up to storage sites. Pipelines allow the transport of large quantities of liquefied CO₂ involved in CCS and have proven to be a safe method.

1.2.3 CO₂ storage

CO₂ sequestration is the last step of the CCS technology. Based on economic factors, accessibility of storage sites, and long-term storage objectives, CO₂ sequestration in geological formations appears to be a most promising solution. Several industrial pilots have already been implemented around the world to demonstrate the technical feasibility and reliability of CCS technology. They are summarized in a study report of the French National Institute for Industrial Environment and Risks (INERIS) [11]:

- Sleipner and Snøhvit: One of the first application was carried out in 1996 at the Sleipner offshore site in Norway (in the North Sea). The CO₂ injection rate was about 2700 t/day, with more than 16 Mt successfully stored by 2016 [12]. The CO₂ comes from the Sleipner natural gas field and is injected nearly 1000 meters deep into the Utsira Sand aquifer, a geological formation located under the ocean floor representing the largest local saline aquifer [13]. For the monitoring of CO₂ injected at the Sleipner site, a parallel project called SACS (Saline Aquifer CO₂ Storage) was set up in 1998 [14]. In 2008, a new Norwegian injection site has been operational at Snøhvit in the Barents Sea, also for offshore storage of CO₂ coming from natural gas processing. The CO₂ injection rate was about 2000 t/day, with approximately 1.1 Mt of CO₂ successfully stored by April 2011 [15].
- Weyburn in Canada: It was an international research program launched in 2000 and completed in September 2012. It studied CO₂ injection and geological storage in depleted

oil fields. This project aimed to develop and demonstrate technology solutions required for the design, implementation, monitoring and verification of CO₂ geological storage projects. 95% pure CO₂ coming from a gasification plant in the United States was injected at 1500 meters deep for EOR (Enhanced Oil Recovery) purposes. The injection rate was 3 Mt of CO₂ per year.

- The pilot of Lacq-Rousse: conducted by Total, this pilot was the first French CO₂ Capture Storage pilot and was operational from 2010 to 2013. The CO₂ was injected in this storage site made of a depleted natural gas reservoir located 4500 meters deep. Although the CO₂ injected was not a huge quantity (90 kt), this pilot was an actor of CCS at the international level, because it included all the steps of CCS.
- In Salah: Another operation was carried out in 2004 on the In Salah site in Algeria, which is a natural gas field. It is an onshore CCS project whose outcomes have been of great benefit to other CCS projects around the world as it has for example shown the need for detailed characterisation of the reservoir geology and geomechanics and the importance to perform regular risk assessment [16]. The CO₂ was injected at a rate of 3500 t/day in a Sandstone aquifer located at a depth of about 1900 meters, whose storage capacity would be 17 Mt.
- Ketzin: As part of the European project CO₂SINK (CO₂ Storage by Injection into a Natural saline aquifer at Ketzin, Germany) started in 2004, a pilot for CO₂ capture and storage has been developed. The main objectives of this project were to study the behaviour of CO₂ underground in real conditions and ultimately to provide operational results for numerical models. Approximately 67 kt of CO₂ (purity > 99.9%) were injected into the saline aquifer of the Ketzin site located at approximately 800 meters deep.

As highlighted by the IPCC, CCS is a proven and a crucial transition technology allowing us to achieve climate targets by reducing GHG emissions while meeting our energy needs. Much work is underway to develop and improve the technology. However, a full deployment of CCS on a large scale lies on three main issues, namely economic, social, and technical; the main obstacle being undoubtedly the economic aspect related to CO₂ capture which turns out to be the most expensive [17]. Restricting our interest to the

technical issue, the mechanisms related to CCS involve various scientific fields such as fluid mechanics, physics, chemistry, geochemistry, geosciences and microbiology. Therefore, a multidisciplinary great deal is always underway to develop and improve the technology. The main challenges for the deployment of CCS from a technical point of view imply:

- The determination of the storage capacities of reservoirs candidate for CO₂ storage: The estimation of storage capacity should include an important parameter: injectivity. Injectivity represents the amount of CO₂ that can actually be injected as a function of time into an injection well at given wellhead pressure. The injectivity depends primarily on the permeability of the reservoir. Indeed, a low permeability imposes a high injection overpressure. However, this injection pressure must take into account the physical limits of the reservoir rock as well as of the cover rock (caprock). This is to avoid a rapid pressure increase in the reservoir due to a reduced injectivity, which can lead to rock fracturing as was observed at the Snøhvit site. In fact, it was reported that the site was very close to a caprock fracturing after one or two years of injection. Therefore, injection was temporarily stopped and the injection pressure was lowered [18]. The injectivity also depends on the number of injection wells and their inclination (vertical or horizontal well).
- Technical control of risk assessment of CO₂ leakage, including long-term monitoring and its impact on the environment directly close to the reservoir (ecosystems, atmosphere...). Based on experience feedback from incidents that occurred on CO₂ storage sites and on other underground storage sites, INERIS has devoted several reports and publications to identify and analyse the risks associated to CCS [19], [20].
- Ensure the efficiency of the injection of CO₂ and the safety of the wells during the entire period of injection of the fluids. Moreover, ensure the integrity of the reservoir during and after the injection of CO₂
- A deep comprehension of non-isothermal processes that play a major role in all stages of CCS. For example, thermal stresses induced by temperature difference between the wellbore and the surrounding rock may lead to casing failure. Moreover, CO₂ injection inside the storage formation induces temperature changes leading to coupled processes with non-trivial interpretations. These coupled processes also play a relevant role in “Utilization” options that may provide an added value to the injected

CO₂, such as Enhanced Oil Recovery (EOR), Enhanced Coal Bed Methane (ECBM) and geothermal energy extraction combined with CO₂ storage. [21]

- Assessment of the distance between the storage site and the sources of CO₂ capture. The French agency for Ecological Transition (ADEME) suggests that access to the CO₂ sites storage is an important obstacle and that priority areas of research could be: i) new techniques for characterizing sites and their storage capacity; ii) techniques intended to ensure safety (including long-term monitoring, prevention of leaks, remediation) [11].

To achieve the levels of CCS deployment, it is essential that the challenges and enabling factors of deployment, as well as the vast opportunities offered by technology, are well understood and urgently taken into account.

1.3 Geological formations for CO₂ storage

1.3.1 Criteria for geological sites selection

Geological reservoir intended for the geological sequestration of CO₂ consists of porous rocks, i.e. a solid matrix and empty spaces called pores. These pores can be filled with miscible or immiscible fluids through which a solute moves. The interconnections between these pores form networks of pores constituting the flow pathways, which control / ensure the displacement of the solute within the formation. The pore networks thus define the capacity of the porous medium to be passed through by a fluid under the effect of gravity or any pressure: this is the permeability k . In addition to permeability, another essential characteristic of a porous medium is the porosity ϕ . In a general way, porosity is defined as the ratio of the pore volume V_P to the total volume of the sample V_T ($\phi = V_P / V_T$). To ensure safe storage, candidate geological reservoirs for CO₂ sequestration must comply with some requirements. The criteria for identifying a geological CO₂ storage site should be based on geoscience analysis that includes [22]–[24]:

- Sufficient storage capacity to store large amounts of CO₂.
- Sufficient injectivity: Geological storage sites must have sufficiently high porosity and permeability to facilitate injection and hold large amounts of CO₂.
- A CO₂ storage reservoir must be in a tectonically stable zone in order to avoid leakage of the stored CO₂ due to the formation or the activation of fractures.

- The presence of an impermeable caprock (most often it is a clayey rock characterized by a very low permeability), with a good seal that ensures efficient fluid confinement and prevents the leakage of CO₂.
- The storage site must be at a minimum depth of 800 m where the temperature and pressure conditions are favourable to maintain CO₂ in a supercritical state. According to the phase diagram of CO₂, it exists as a supercritical state at temperature higher than 31 °C and a pressure greater than 7.38 MPa [25]. At these conditions, CO₂ has the density of a liquid that increases depending on the temperature and pressure, but behaves like a gas, which optimizes the number of CO₂ molecules that can occupy the total available pore space (volume) in geological reservoir, thus ensuring the storage of a large quantity of CO₂. The ability to store CO₂ increases with depth. The storage sites located between 800 m and 2000 m depths have temperature ranges from 30 °C to 60 °C and pressure from 7.8 MPa to 19.6 MPa considering a geothermal gradient of 25 °C/km and a hydrostatic pressure [4], [26].

1.3.2 Geological reservoirs

Based on the criteria mentioned above, there are several types of geological units candidates for CO₂ storage as shown in Fig 1.3. They consist of:

- Depleted oil or gas field reservoirs: They are candidates because of their good seal and stability on the geological time scale and have good storage capacities of the order of several Gt. Without the injection of CO₂, these reservoirs are difficult to exploit because they are already depleted. Therefore, the injection of supercritical CO₂ (sCO₂) into these geological formations helps recovering more oil while allowing CO₂ storage. The sCO₂ injected acts as an acidifier and a powerful solvent, reducing the viscosity of the hydrocarbons and thus facilitating their recovery.
- Unmineable coal seam: They also have a good storage capacity of several Gt. In these formations, methane is present at approximately 95% [27], but CO₂ has a better affinity for coal compared to methane [28]. Thus, the CO₂ injected into these geological formations helps the ECBM (Enhanced Coal Bed Methane) purpose.
- Deep saline aquifers: Saline aquifers are located at very great depths generally between 800 and 3000 m deep, with thickness up to 200 m and spreading laterally over several km [29], [30]. They are made of porous and permeable reservoir rocks

saturated with highly saline brine in the spaces between the rock grains. The salinity is much higher than that of the sea [31]. As a result, the water of such aquifers is unusable for agriculture and unfit for consumption. The confinement of reservoir rock of the deep saline aquifers is ensured by an impermeable caprock. They are considered as having, by far, the largest potential CO₂ storage capacity, being estimated of the order between 1000 and 10⁴ Gt of CO₂ [31], [32]. Deep saline aquifers are also widely spread around the world, so that they can be close to CO₂ capture sites [27] and the need for CO₂ transport would be reduced.

The main factors that require major assessment to decide the feasibility of CO₂ storage in a candidate geological formation are the storage capacity, containment efficiency and injectivity. Of all the possible geological sites for the geological storage of CO₂, the deep saline aquifers are recognised as the most promising candidates. In the next paragraphs, we describe the trapping mechanisms of CO₂ in deep saline aquifers

1.4 Trapping mechanisms of CO₂ in deep saline aquifers

Geological sequestration of CO₂ into deep saline aquifers is a promising solution to mitigate CO₂ emissions in the atmosphere and thus responds to the challenges of climate change [33]. The injection of sCO₂ (preferably injected dry to avoid corrosion problems) into saline aquifer reservoirs considerably perturbs their (physical and chemical/thermodynamic) initial equilibrium state. In fact, the sCO₂ injected moves within the geological formation and reacts with the components of the porous medium, depending on pressure, temperature, mineralogical composition of the rock and the brine. Thereafter, CO₂ will be sequestered through a combination of physical trapping mechanisms (structural and residual/capillary trapping) and geochemical trapping mechanisms (solubility and mineral trapping) [34]. These four main mechanisms (shown in Fig. 1.5) play a prominent role in the effectiveness of CO₂ sequestration.

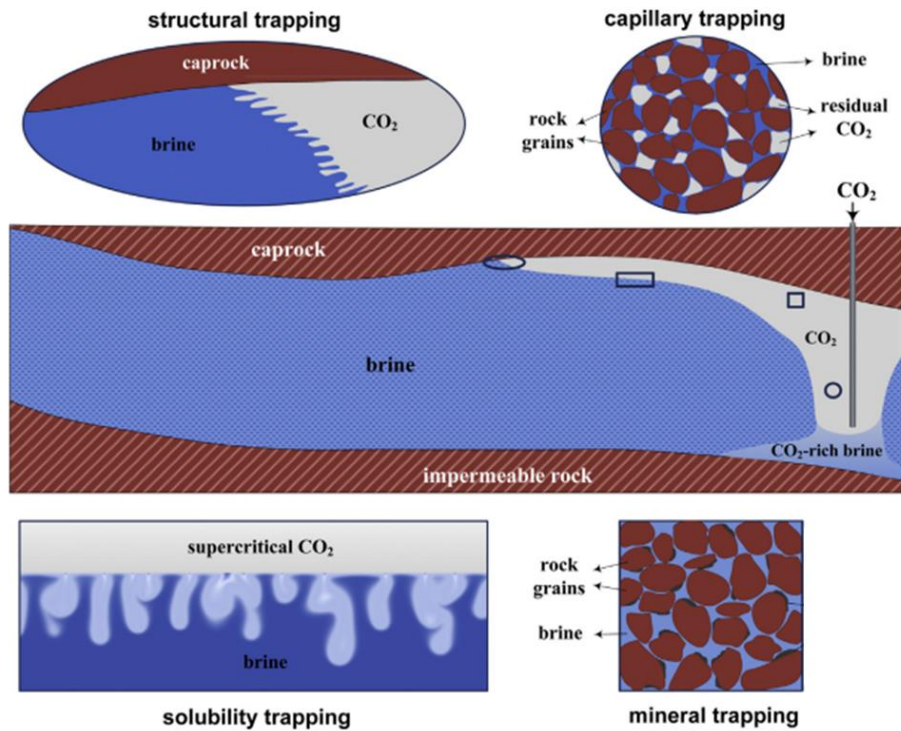


Figure 1.5: Geosequestration of CO₂ in saline aquifers associated with Trapping mechanisms [29].

1.4.1 Structural trapping mechanism

It occurs immediately after injection and is chronologically the first mechanism for CO₂ trapping. It plays the main role in retaining CO₂ in the geological formation. In fact, in an aquifer located between 800 m and 3000 m deep, the brine has a density and a viscosity that vary respectively in the range of 945-1230 kg.m⁻³ and 0.19-1.58 mPa·s, while those for sCO₂ vary respectively in the range of 266-766 kg.m⁻³ and 0.02-0.06 mPa·s. [31]. Due to this large density difference, the sCO₂ migrates toward the upper limit of the reservoir until it reaches an impermeable rock cover (caprock) that stop its ascent and forms a structural closure preventing CO₂ leakage towards shallower aquifers. Subsequently, the CO₂ propagates below the caprock around the injection point, as a gravitational flow in response to the injection pressure, its own buoyancy and the slope of the caprock even if the injection is stopped [29].

1.4.2 Capillary trapping mechanism

Also called residual trapping, this mechanism occurs almost immediately after the percolation of CO₂. During its ascent through the rock formation to the upper limits of the aquifer, sCO₂ displaces the interstitial fluid initially present in the formation. It is

subsequently trapped in the narrow pore spaces of the rock by capillary forces. CO₂ remains in its supercritical state, but is immobilized in the structure of the rock. This mechanism increases the security of the storage [35].

1.4.3 Solubility trapping mechanism

It is recognized as one of the most important and most effective mechanisms that ensure long-term CO₂ storage [36], [37]. The CO₂ droplets immobilized within the pores by the residual trapping as well as the CO₂ plume retained below the caprock by structural trapping, will dissolve in the brine. The solubility of CO₂ in the brine depends on many parameters such as pressure, temperature and salinity [38]–[43]. This dissolution will generate the formation of a diffuse layer (a plume of CO₂-rich brine), which is denser than the initial brine, inducing gravity-driven flows and convective fluid circulations. Consequently, the CO₂-rich brine will migrate downward the reservoir. The dissolution of CO₂ in water produces a weak acid, namely carbonic acid [36]. The main advantage of solubility trapping is that once the CO₂ dissolves, it no longer exists as a separate phase, thus eliminating the buoyancy forces that push it to rise to the surface [2].

1.4.4 Mineral trapping mechanism

It is the safest and most permanent form of CO₂ storage over the long term. It consists of mineralizing the dissolved CO₂ into stable solid carbonates.

The injected sCO₂ inside aquifers interacts with the various components of the porous medium and is sequestered through a combination of physical and geochemical trapping mechanisms mentioned above that ensure the effectiveness of Geological CO₂ Storage (GCS). Mineralogical trapping is relatively slow and can span hundreds or even thousands of years [44], [45], [46], and its dynamics strongly depends on the mineralogical compositions, on the structure of the rocks and on the temperature and pressure conditions existing in the aquifer, but also on the properties of the CO₂ injected.

Finally, Fig. 1.6 summarizes chronologically the different trapping mechanisms that take place on the geological scale during the CO₂ sequestration in deep saline aquifers. It should be noted that the relative magnitudes of these trapping mechanisms and their evolution with time will depend on the physical state and mineralogy of the reservoir, and the complex coupling of fluid-flow and fluid–rock interactions.[47]

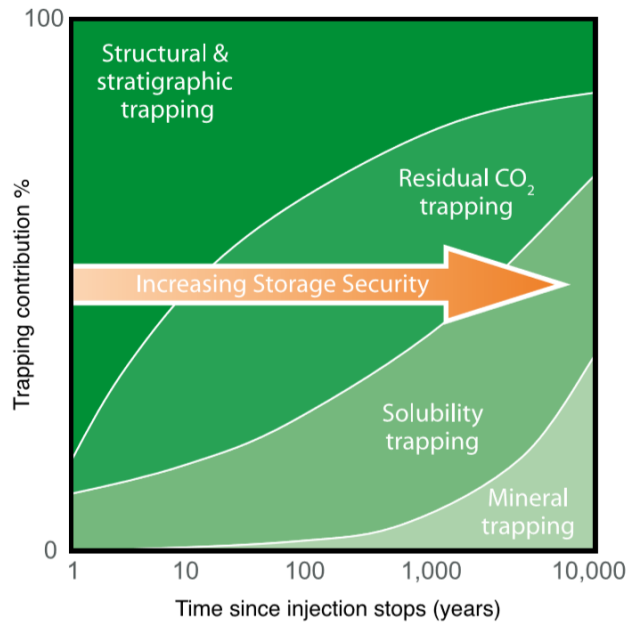


Figure 1.6: Storage security over time depending on a combination of physical and geochemical trapping [33].

1.5 Multiphase reactive transport and near-well behaviour

1.5.1 Physical and chemical behaviour

A massive injection of CO₂ into the subsurface considerably perturbs the equilibrium conditions (temperature, pressure, pH...) of the host reservoir, and the re-equilibration of the medium is nonlinear in space and time, with various processes taking place on very different timescales [48]. Recent numerical simulations indicate that the near-well injection zone is an underground hydrogeological system identified to be the most sensitive area and particularly disturbed by sCO₂ injection [49], [50]. In this zone, physical phenomena (e.g. variations in temperature, pressure and gas saturation) and geochemical reactions (e.g. pH variation of the initial brine, CO₂ dissolution, mineral dissolution/precipitation) occur massively and are combined to enhance or alter the initial porosity and permeability of the medium and thus the well injectivity. The injectivity parameter expresses the behaviour of the porous medium under imposed conditions such as the injection pressure, temperature, flow and their time evolution [51]. As can be seen on Fig. 1.7, injectivity depends on the evolution of the relationship between petrophysical properties of the medium (e.g. porosity and relative permeability), properties of the injected fluid and characteristics of the reservoir rock (hydrodynamic

properties, geochemical reactivity, transport...). Therefore, a control of all parameters directly linked to the injectivity is of great interest for the success of GCS.

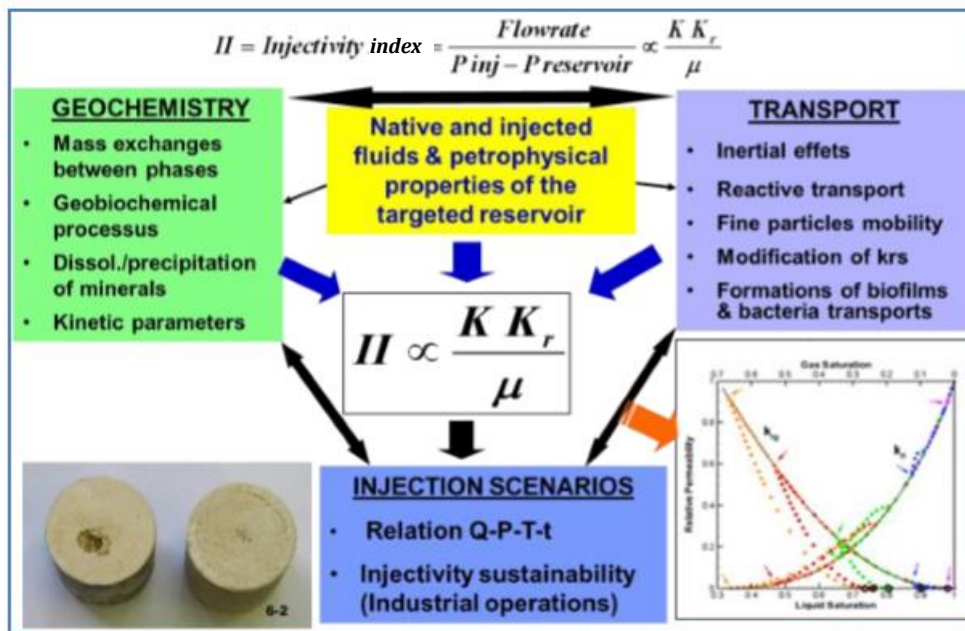


Figure 1.7: Coupled key processes involved by CO₂ injection: interactions between them and qualitative influence on the well injectivity [51], [52].

1.5.2 Thermal behaviour

In addition to the hydrodynamic disturbances and the high chemical reactivity present in near-well injection zone, another major perturbation during the injection of sCO₂ into saline aquifer is the introduction of a thermal gradient [53]. The naturally occurring geothermal gradient itself generates instabilities in the reservoir. In fact, the common geothermal gradients for saline aquifers is on average between 25 and 45 °C/km [22]. This natural vertical geothermal gradient causes density variations in the aquifer reservoir. The temperature difference as well as the concentration difference can cause instabilities of the CO₂-rich brine layer and initiate the so-called double-diffusive natural convection [29]. In addition to this geothermal gradient, larger localized temperature gradients that appear during CO₂ injection can have a strong influence on the dissolution of CO₂ in water, mass transfer in rocks, and precipitation process in the reservoir [54]. CO₂ injection also induces temperature changes that have various origins such as the advection of the CO₂ injected at a given temperature, the Joule Thomson effect, endothermic evaporation of water and exothermic dissolution of CO₂ [49], [55], [56].

These temperature gradients generated during the injection are due to the fact that CO₂ most likely reaches the target reservoir at colder temperature than that corresponding to the geothermal gradient [57]. Therefore, non-isothermal or thermal effects may significantly influence the CO₂ sequestration particularly in the near-well injection zone. In fact, temperature is a major parameter that affects CO₂ properties (density, viscosity, solubility in brine [58], [59]...), surface tension, wettability [60]. However, in the early studies, the impact of thermal effects on the overall behaviour of the system has been most often neglected in order to facilitate the understanding of the first order processes involved during CO₂ storage. As a result, most of the knowledge gained on the processes involved in CCS neglects the coupling with thermal effects. Nevertheless, the awareness that the comprehension of non-isothermal processes is crucial for a successful deployment of CCS projects has recently motivated an increasing interest to understand thermal effects.[21]

1.5.3 Multiphase fluid flow behaviour

In addition to these thermal effects, the presence of two distinct immiscible phases (sCO₂ and brine) brings additional complexity, as the flows are two-phase and the drainage process in the porous medium can be influenced by many factors. These factors include the viscosity and density of the fluids, the surface tension between them, the wetting properties, their respective flow rates, the topology of the pore network, and the considered length scales [61]. Drainage refers to a two-phase flow where the non-wetting fluid (CO₂) displaces the wetting fluid (brine). In the case of drainage, the wettability properties (which define the ability of a fluid to spread on mineral with respect to another fluid [62]), associated to the surface tension (γ) between the two fluids are the key factors which allow us to predict the mobility of fluids inside the porous medium and the capillary forces. Capillary pressure is the pressure difference between the non-wetting and the wetting fluid across a curved interface. The capillary forces prevent the non-wetting fluid from spontaneously entering in a pore throat of radius r as long as the pressure is smaller than a threshold capillary pressure P_c given by the Young–Laplace law [63]:

$$P_c = \frac{2\gamma \cos\theta}{r} \quad (1.1)$$

where γ is the interfacial tension, θ the contact angle. The presence of viscous forces can modify the capillary pressure and promote the entrance of invading fluid (CO₂) through smaller pore throats. That is why the multiphase fluids flow in porous media can be characterised by two dimensionless numbers namely the capillary number C_a and the viscosity ratio M [63], [64] given by:

$$C_a = \frac{\mu_{nw} u}{\gamma \cos \theta} \quad (1.2)$$

$$M = \frac{\mu_{nw}}{\mu_w} \quad (1.3)$$

where μ_{nw} and μ_w , are respectively the viscosities of the non-wetting and of the wetting fluids, and u is the mean velocity of the non-wetting fluid. The capillary number represents the ratio of viscous forces over capillary forces while the viscosity ratio is useful to determine whether a displacement is stable or not. In the case of drainage, Lenormand identified three main regimes for immiscible displacements of fluids during the transport of two-phase flow [63]–[65]. These three regimes are governed by the two dimensionless numbers mentioned above and correspond to the limits when the viscous or capillary forces involved during displacement are dominant or negligible. In each case, the displacement takes one of the basic forms: viscous fingering, capillary fingering, or stable displacement (Fig. 1.8).

- Viscous fingering appears for low M (injected non-wetting fluid less viscous than wetting fluid) and rather large C_a (fast non-wetting fluid, and/or weak capillary forces); the principal displacement is due to viscous forces. Capillary effect and pressure drop in the injected fluid are negligible. Due to viscosity, small pores are invaded (Fig. 1.8-a).
- Capillary fingering appears at low capillary number (slow injection rate and/or large capillary forces) and rather large viscosity ratio (injected non-wetting fluid generally more viscous than wetting fluid). The principal displacement is due to capillary forces and viscous forces are negligible in both fluids. Larger pores are invaded first (Fig. 1.8-b).

- Stable displacement takes place at large C_a and M values, meaning that the invading fluid presents a stable front. (Fig. 1.8-c) and all pores are invaded by the non-wetting fluid.

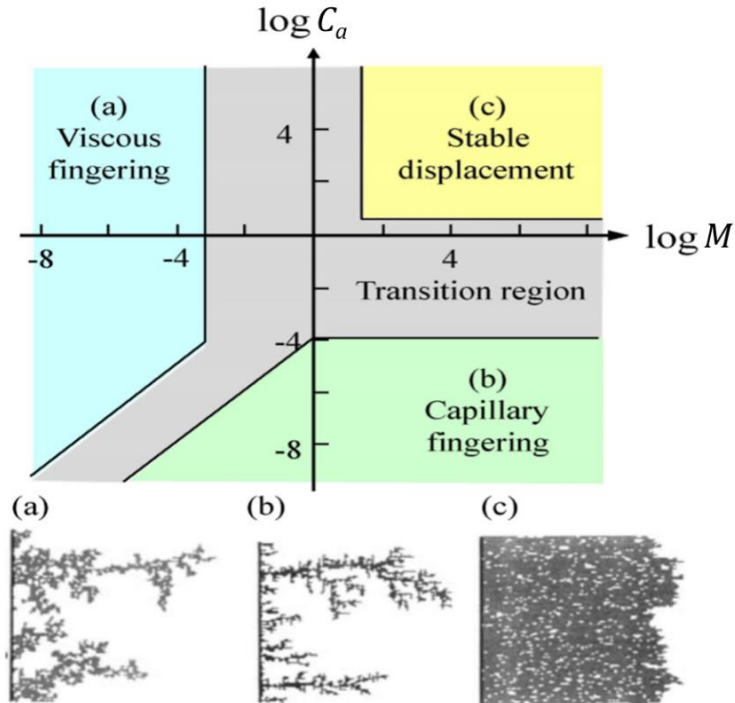


Figure 1.8: Lenormand phase diagram for immiscible displacement during drainage [63], [64], [66]

At the reservoir scale, the displacement of brine by supercritical CO₂ is characterised by a viscosity ratio of less than 1 ($\log M$ between -1.6 and -0.7) [67]. Depending on the velocity of the sCO₂, the principal mechanism of the displacement flow can be capillary-dominated or viscous-dominated flow. Another source of perturbation taking place in the subsurface may be due to microbial metabolisms. Microbial reactions can impact the integrity, capacity, and safety of CO₂ storage sites [48]. Research activities have been carried out about the effects of CO₂ injection on autochthonous microbial communities and how they can affect the storage integrity by enhancing or inhibiting mineral dissolution. [68]–[70].

All these effects and disturbances that are mentioned above lead to highly coupled thermo-hydro-mechanical-chemical-biological (THMCB) processes with non-intuitive consequences on the porous medium. A summary of all these coupled processes taking place during sCO₂ injection is given in Fig. 1.9.



Figure 1.9: Coupled processes during GCS [48].

The sCO₂ injected into aquifers induces interactions with itself, in situ brine and reservoir rock, leading to a variety of highly coupled processes. Therefore, it is required to take into account all these coupled processes, which occur at different spatial and temporal scales for a full assessment of CCS technology. This thesis focuses on the study of the THC coupling, which will be described in the next paragraphs.

1.6 Summary of THC behavior in the near well injection zone

Recent laboratory experiments and numerical modelling focused on the study of the behaviour of the near-well area during scCO₂ injection in saline aquifers. The results gave rise to a conceptual zonation scheme with radial geometry of processes occurring in the near-well region (Fig. 1.10) and demonstrated that chemical processes vary, with time, according to the distance from the injection well [52]. First, the massive and continuous injection of dry CO₂ acts as a piston and displaces away the brine initially present close to the well bore. A dessicated non-reactive zone is created around the injection well (zone

5). Only dehydration of some primary hydrated minerals (like gypsum or clay minerals) can occur there.

Then, immobile residual water entrapped in pores or distributed on grain surface as thin wetting film, is in contact with the constant flow of dry scCO₂ (with very low vapour pressure) initiating an evaporation regime (zone 4). As vaporization progresses, the relative permeability of the porous medium with respect to CO₂ increases allowing further evaporation. Consequently, the molar fraction of the water in the CO₂ stream increases with distance from the well because a significant portion of brine evaporates into the CO₂ stream, leading both to the extension of the drying front and the increase of the concentration of salt dissolved in the brine. When the salt concentration exceeds its solubility limit, precipitation occurs. Possibly, other secondary minerals can also precipitate from residual brines because of the salting-out effect. This can alter the injectivity of the reservoir because of the resulting reduction of the permeability and porosity of the porous medium [71]–[73]. In fact, to understand how salt precipitation affects the injectivity, a number of laboratory experiments have been performed in sandstone and carbonate rocks. As an example, Muller *et al.* [74] conducted a test on a dry Berea sandstone core sample with 100 mD permeability and around 20 % porosity, saturated with a 25 wt% NaCl solution. After the experiment, they reported 60% reduction in the absolute permeability allocated to salt precipitation, based on Scanning Electron Microscopy (SEM) micrographs. Using Magnetic Resonance Imaging (MRI), Wang *et al.* [75] carried out a similar test on the Berea sandstone core sample with 143 mD permeability and around 17 % porosity saturated with a 25 wt% NaCl solution. After the experiment, they reported 50 % reduction in the absolute permeability allocated to salt precipitation near the core inlet. On the micro scale, Kim *et al.* [76] have coupled a microfluidic technique with a porous medium by developing a lab-on-a-chip approach to study pore-scale salt precipitation dynamics during CO₂ sequestration in saline aquifers. They found a porosity reduction between 15–25 % and large bulk NaCl crystals that grow in the brine phase, away from the CO₂ interfaces. Most of the reactive water mass exchange is triggered and takes place in the drying out zone [51], [77].

Within zone 3, a two-phase flow zone where both brine and CO₂ are present as flowing phases within the system. A chemical equilibrium is established between the two phases, leading to pH variations. Because of aqueous phase-mineral interactions, dissolution of

carbonate minerals present in the reservoir [52] occurs in this zone and buffers water acidification. Dissolution of minerals constitutes the most important process but, depending on reservoir conditions (T, P), precipitation of secondary minerals are not excluded.

The zone 2 is a monophasic zone saturated with the brine initially present within the medium. In this zone, the CO₂ dissolved into the brine is mainly carbonic acid. As a result, the pH of the brine decreases and reaches 3.5-5.0, buffered by the alkalinity of native brines and the interactions with rock minerals.

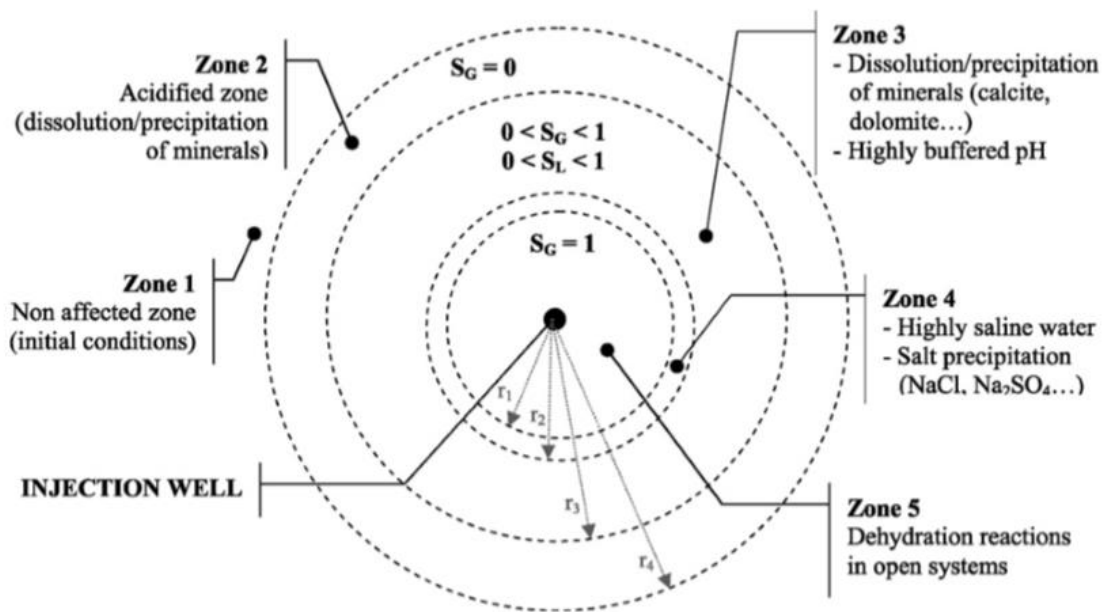


Figure 1.10: Schematic zonation of processes occurring in the near-well region after sCO₂ injection in a saline aquifer. The different radii (r_1, r_2, r_3, r_4) depend on CO₂ injection flow rate and reservoir properties [50], [78].

According to this zonation scheme, the region of interest for our study is located in the zone 4. In this zone, both two-phase flow reactive transport and salt precipitation occur, possibly leading to local heterogeneous porosity and permeability. However, simulations that made it possible to define the different zones described in Fig. 1.10 were performed with the numerical simulation program TOUGHREACT. The latter considers that the porous medium is homogeneous in each cell of the mesh and is based on a description of the flows according to Darcy's law. Consequently, the flow typology as described according to the Lenormand diagram (see Fig. 1.8) is not reproduced in detail. With TOUGHREACT, the two-phase flow is expressed at macroscopic scale with parameters

such as the relative permeability of one fluid with respect to another. Therefore, the notion of digitation at the pore scale is not included in the program.

1.7 Phenomena at pore scale

Understanding the mechanisms involved in CO₂ trapping at the pore scale remains very crucial because, at this scale, many sensitive processes such as chemical reactions, precipitation of minerals and the diffusion of ionic species in fluids can express in a meaningful way. From a numerical point of view, the typical length scale used to describe processes involved in the context of CO₂ storage is the reservoir scale, where it is often assumed that the porous medium has a homogeneous structure, with the consequence that the distribution of fluids and their movement inside the pore network remains conceptual. A complete simulation requires experimental data both for validation and insight into the full, complex interplay of phenomena occurring at the pore-scale [76]. The study of the trapping mechanisms involved during CO₂ injection at pore scale was possible thanks to microfluidic approaches by using Geological Labs on Chip micromodels. Actually, the micromodels are not truly representative of geological reservoir as a whole, but they are representative of the hydrodynamic mechanisms encountered in a real porous medium. They aim at investigating the flow paths of fluids in a small portion of the formation.

Morais *et al.* [79] identified three key flowing and storage mechanisms during drainage experiments at the pore scale, namely: (i) the invasion where the CO₂ phase invades the porous medium and displaces water to occupy the pore space; (ii) the percolation which corresponds to the breakthrough time (t_p) when the CO₂ reaches the outlet of the micromodel, leaving behind some water due to capillary forces; and (iii) the drying, which corresponds to a slower elimination process in which the dry injected CO₂ vaporizes the water remaining in the pore network [79]. All these steps are summarized in Fig. 1.11 below.

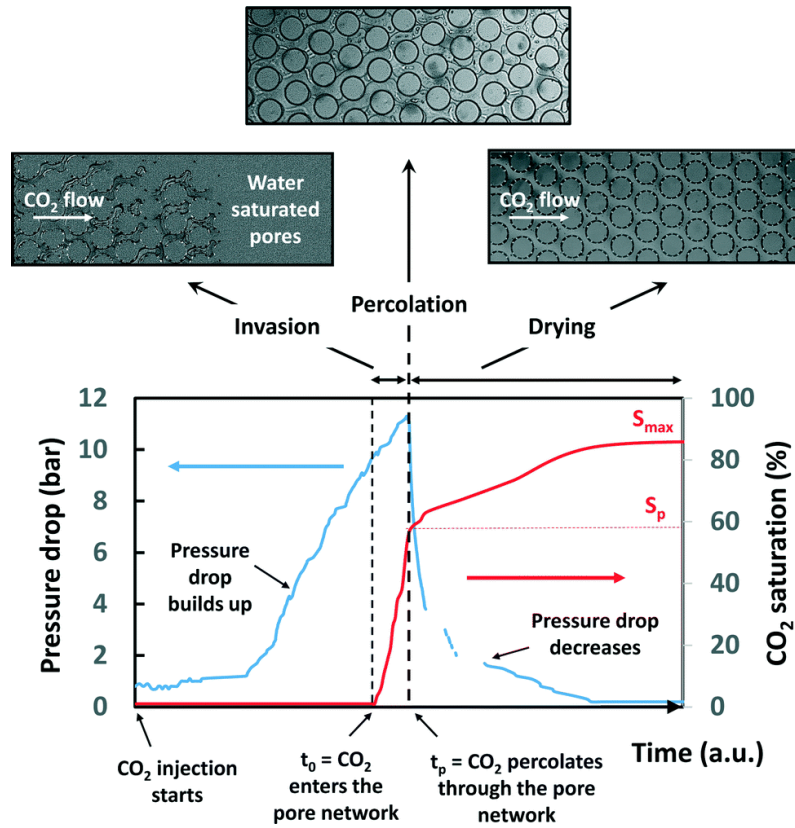


Figure 1.11: Pressure drop and CO₂ saturation as functions of time during a typical drainage process inside a micromodel. $t_0 = 0$ is the starting point for the injection time [79].

Restricting our interest to the transport and movement of fluids in porous media, hydrodynamic studies using microfluidic approaches have made it possible to determine the parameters that can influence the efficiency of storage, particularly pore network characteristics (permeability) and the injection flow rate. Permeability generally depends on the configuration of the pore network, the porosity and the depth of the channels of the porous microsystem. In fact, Joseph *et al.* [80] conducted experiments to calculate the effective porosity and permeability of on-chip porous media containing different pore-networks. As represented on Fig. 1.12, they found that as the number of pores and throats in on-chip porous media increases, the porosity increases.

Table 1
Quantification of on-chip porous media in terms of number of pores and throats.

Network type	Number of pores	Number of throats
Network 1	2000	6000
Network 2	3000	9000
Network 3	3000	9000
Network 4	6000	20 000

Table 2
Surface profile properties (width, average roughness and average depth) of fabricated chips.

Network	Width (mm)	Average roughness (μm)	Average depth (μm)
1	4.89	4.54	40.44
2	4.95	6.17	40.76
3	4.96	5.24	41.44
4	4.96	6.67	41.10

Table 3
Porosity and permeability values of different networks.

Network type	Design ϕ porosity	Porosity from ϕ optical images	Permeability \dot{C} (Darcy)	Permeability $\dot{C}(\times 10^{-12}\text{m}^2)$
Network 1	0.42	0.39 ± 0.04	2.66 ± 0.06	2.625 ± 0.059
Network 2	0.44	0.42 ± 0.04	5.50 ± 0.40	5.428 ± 0.395
Network 3	0.66	0.65 ± 0.05	10.88 ± 1.03	10.738 ± 1.025
Network 4	0.69	0.67 ± 0.03	15.93 ± 0.55	15.723 ± 0.543

Figure 1.12: Porosity and permeability values for different characteristics of pore-networks [80].

Zhao *et al.* [81] conducted a study for the visualisation of CO₂ flooding in immiscible and miscible displacements in a high-pressure condition using a 400 MHz Magnetic Resonance Imaging (MRI) system. For CO₂ miscible displacement, they observed a piston-like displacement and the phenomenon of the miscible regions and CO₂ front was obvious. For immiscible displacement, they observed a phenomenon of CO₂ fingering due to the difference in fluid viscosities and densities. Thus, the displacement process of CO₂ in porous media can be affected by the hydrodynamic forces such as capillary pressure endured during process, the physical and chemical properties of the fluids (viscosity, density, solubility) and of the porous matrix (pore size, permeability).

Zhang *et al.* [82], [83] evaluated the impacts of porous media heterogeneity and capillary forces on a liquid CO₂-water displacement in a pore network micromodel with two distinct permeability zones (dual permeability), at a pressure greater than the supercritical CO₂ phase-transition pressure of 7.3 MPa. Their results demonstrated a

preferential displacement of CO₂ through the high permeability zone. In their results, they also characterised the displacement mechanism of capillary and viscous fingering. The injection rates were expressed as the log of the capillary number ($\log Ca$). They found that at slow injection rates, the displacement of the non-wetting fluid occurs only through the high permeability zone with large entrapped zones of water, indicating capillary fingering. This is because the higher capillary force in the low permeability zone resists penetration by the non-wetting fluid. The mechanism shifts from capillary fingering to viscous fingering with the increase of the injection flow rate. The liquid CO₂ started invading the low permeability zone only when the capillary number reached a certain threshold value of $\log Ca = -3.36$ as can be seen in Fig. 1.13.

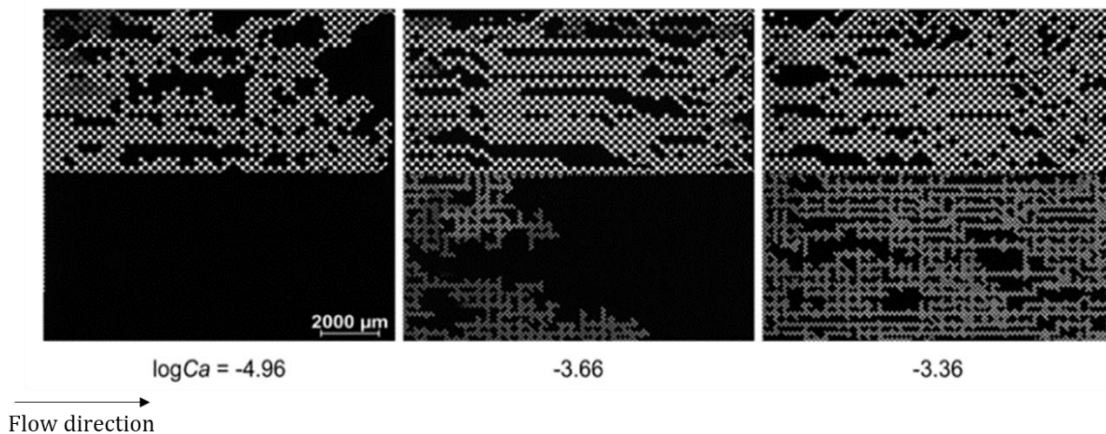


Figure 1.13: Images of liquid CO₂ (white) distribution in the dual-permeability pore network at different capillary number. The flow direction is from left to right [82].

The roughness of the channel walls is also a parameter that could influence the displacement of CO₂ in the porous media, because an important roughness of the channel walls can reduce the velocity of the flow. The mechanisms governing transport also depends on the flow of fluids in the porous medium. At pore scale, three main mechanisms govern the transport of elements in the porous medium: advection, dispersion and molecular diffusion.

1.7.1 Advection

Advection or convection is a process of moving elements in solution by displacement of fluid. This is one of the predominant mechanisms behind displacement flows of matter where solutes are transported at the same speed as the fluid within the medium without

varying their concentration. In a one-dimensional environment, the advection transport equation is given by:

$$\frac{\delta C}{\delta t} = -U_x \frac{\delta C}{\delta x} \quad (1.4)$$

C is the concentration of the migrant species and U_x the linear mean velocity of the fluid.

1.7.2 Dispersion

Dispersion takes place when the solute moves through a porous medium. According to Ozgur and Gümrah [84], the dispersion can be influenced by different parameters such as the flow velocity, the complex tortuosity of the pore network, the interactions of solutes with rocks, etc. In a saturated heterogeneous porous media like saline aquifers, the dispersion of a fluid can be described as a function of the dimensionless Peclet number, Pe [85], which characterizes the relative importance of dispersion compared to advection and is given by:

$$Pe = \frac{u \cdot L}{D_h} \quad (1.5)$$

where L (m) is a characteristic length of transport and u ($m \cdot s^{-1}$) is the Darcy velocity, that is the linear flow velocity averaged over the cross-section of the capillary. D_h ($m^2 \cdot s^{-1}$) is the hydrodynamic dispersion coefficient. In 1972, Bear [86] made a distinction between two types of dispersion: kinematic dispersion and hydrodynamic dispersion. The kinematic dispersion defines the variation of velocity of the fluid according to the transversal or longitudinal directions within the porous medium due to the microstructure of the medium. While the hydrodynamic dispersion is the sum of the molecular diffusion and the kinematic dispersion because in practical case, the effect due to molecular diffusion cannot be dissociated from that due to kinematic dispersion [87]. The spatio-temporal variation of the concentration due to the dispersion in porous medium is an unidirectional flow defined by:

$$\frac{\delta C}{\delta t} = D_h \cdot \frac{\delta^2 C}{\delta x^2} \quad (1.6)$$

where C is the concentration, t the time and x the position. The hydrodynamic dispersion coefficient D_h is defined as:

$$D_h = \alpha \cdot u + D_{eff} \quad (1.7)$$

where α is the dispersivity (m) and D_{eff} is the effective diffusion coefficient ($m^2 \cdot s^{-1}$). When $u \approx 0$, $D_h \approx D_{eff}$ and $u \cdot L \ll D_{eff}$. Thus $Pe \ll 1$. Hence, for low Peclet numbers ($Pe \ll 1$), the transport mechanism is governed by diffusion while for $Pe \gg 1$, advection dominates.

1.7.3 Molecular diffusion

Molecular diffusion is a physical phenomenon related to the random molecular motion due to the collision between particles. It refers to the microscopic process by which matter or heat is transported within a system without collective movement. Unlike kinematic dispersion, molecular diffusion can take place independently of convection (or advection). In geological reservoirs, molecular diffusion is generally a non-stationary/transient process whose duration is highly dependent on the pressure and temperature of the system. Its driving force is exclusively due to concentration gradients. Indeed, if the concentration is not homogeneous between distinct zones, and without external force fields, a flow of particles from the regions of higher concentrations to the regions of lower concentrations is established according to the Fick's first law. In porous media, the diffusion process due to the concentration difference is mitigated due the presence of the solid matrix (Fig. 1.14b). In fact, here the solute species travel longer paths than in a free fluid due to the complexity of the pore structure (Fig. 1.14a) [88].

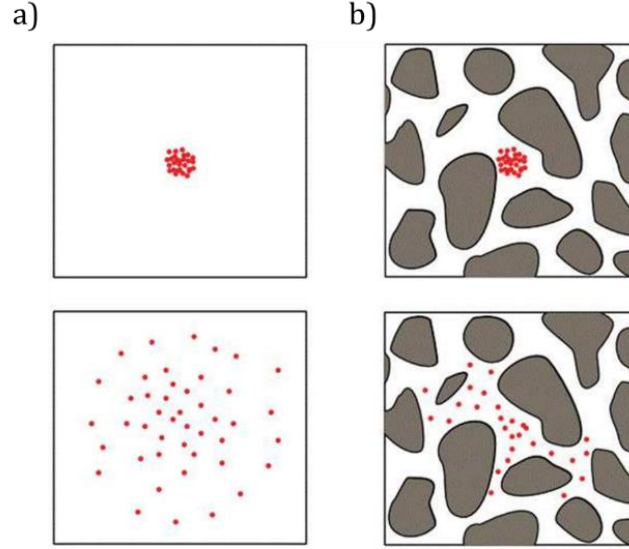


Figure 1.14: Illustration of diffusion due to the concentration difference a) in free medium and b) in the pore space [88].

To account for slower diffusion in porous media, an effective diffusion coefficient D_{eff} is defined and can be related to the molecular diffusion coefficient D by [89]:

$$D_{eff} = \emptyset \cdot D_p = \emptyset \cdot \frac{D}{\tau} \quad (1.8)$$

where \emptyset is the porosity, D_p the pore-water diffusion coefficient, and the tortuosity τ is a term used to describe the structural complexity of the medium. Geometrically, it can be approximated by the ratio between the real distance traveled by following a tortuous path, and the effective distance crossing this same medium in a straight line. D_{eff} depends on the pressure and the temperature according to Arrhenius law.

During the transport of fluids, all the transport mechanisms mentioned above may operate simultaneously or individually with a preferential predominance of a given mechanism. The process of transport of a solute in a porous medium can be governed by an overall transport equation defined as the contribution of all transport processes according to the equation:

$$\emptyset \cdot \frac{\delta C}{\delta t} = -U_x \frac{\delta C}{\delta x} + D_h \cdot \frac{\delta^2 C}{\delta x^2} \quad (1.9)$$

$\emptyset \cdot \frac{\delta C}{\delta t}$ is the global flow, $-U_x \frac{\delta C}{\delta x}$ the contribution of the advection mechanism and $D_h \cdot \frac{\delta^2 C}{\delta x^2}$ the contribution of diffusion/dispersion mechanisms. These two contributions are

additive, which means that one can take place independently of the other. Therefore, in the absence of advection within the fluid, the mass and heat transport are only due to diffusion, with $D_h = D_{eff}$. In this thesis we only focused on the diffusive transport mechanism.

1.8 Conclusion and problem at stake

Up to now, the main mechanisms involved in the injection of CO₂ into saline aquifers are known. Because these reservoirs are located in the deep underground, the existing work is mostly theoretical and considers some laboratory experiments and monitoring results from some pilot scale tests. It allowed highlighting the preponderant coupled processes involved with the reactive transport phenomena that occur in the near-well injection zone. According to Fig. 1.10, the region of interest for our study is the zone 4. In this zone, both two-phase flow reactive transport and salt precipitation occur, possibly leading to local heterogeneous porosity and permeability. However, in line with a more detailed description of the processes that are taking place at the pore scale, such a configuration may favour, in the context of CO₂ injection, localized temperature gradients larger than the natural geothermal gradient related to local heterogeneities like fluid distribution. This could generate diffusive transport phenomena that could induce segregation of chemical species in the medium, and, in turn, accelerate/delay salt precipitation in some place of the porous/fractured medium.

Precipitation adds solid matter in the reservoir with a potential consequence of clogging CO₂ percolation paths, which can reduce the injectivity. The precipitation process and the amount of salt formed depend on the salinity of the initial brine, the residual water entrapped in pores, the gas injection flow rate and the capillary forces within the system [90]. Salt precipitation in deep saline aquifers are governed by a combination of physical and chemical processes [77]. However, up to now, there is no consensus on the precise location where the salt precipitates or how the salt precipitation spatially spreads in a given porous medium [91]. However, some authors have claimed in their studies that salt precipitates locally near the inlet of the medium, which is often attributed to capillary-driven backflow of brine into the dried zone. [91], [92].

As for the thermal gradient, the mass transport of chemical species in response to a temperature gradient is called thermodiffusion or Soret effect. Under certain conditions,

it can lead to an efficient separation of chemical species [93], [94]. Since the discovery of the Ludwig-Soret or (Soret) effect in the 19th century [95], [96], the existence of thermal gradients in geological reservoirs or in hydrothermal solutions, and their impact on the selective distribution of the concentration of chemical species by the thermodiffusion phenomenon, have been a topic of active research [97], [98]. This effect is evidenced by the establishment of a concentration gradient due to the diffusive migration of chemical species into a medium induced by a temperature gradient. For example, authors like Dandurand *et al.* [99], have shown that in a porous medium filled with fluids containing dissolved ions, the Soret effect can give rise to supersaturations, even from dilute solutions, resulting in crystallization or mineral deposits. Taking into account the thermal gradients in the models arouses more and more interest, but a possible coupling with concentration gradients through Soret effect is not yet mentioned in the literature to the best of our knowledge. As part of this thesis, our interest is to deepen the thinking on the influence of thermal gradients on diffusive reactive transport in the storage conditions of CO₂ in saline aquifers, and to assess their importance.

Within the aquifer, the reactive transport zones can be located at different places where the flow regime for the displacement in a drainage configuration corresponds to viscous fingering of the CO₂-rich phase into the brine, according to the classification by Lenormand. The case of drainage mainly governed by capillary forces can also be considered when the pressure heterogeneities in each of the phases are negligible compared to the capillary pressure P_c . The largest pores where capillary pressure is the lowest are first invaded by the injected fluid. This therefore leads us to the conceptual diagram of the locks to focus on in this thesis (Fig. 1.15c). We are interested by the precipitation of salts associated with the diffusion process. In fact, we consider in the porous medium a preferential flow of CO₂ injected into the pores which have a high permeability and which are in contact with pores of lower permeability containing brine trapped in the pore space. With a continuous evaporation of brine in the CO₂ stream, the salt concentration will increase at the evaporation front. This will generate a concentration gradient in the weakly permeable porosity and will lead to a "retro diffusion" process. Over time, when the salt concentration reaches the solubility limit of the corresponding mineral, the mineral will precipitate at the evaporation front. It is also envisaged that the existence of large temperature gradients can have an impact on the chemical differentiation of the system.

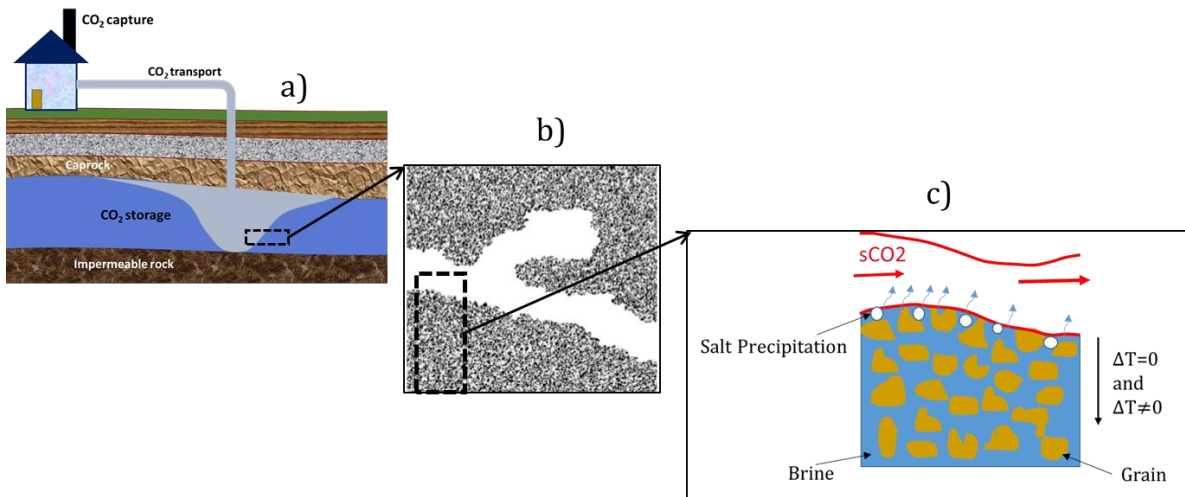
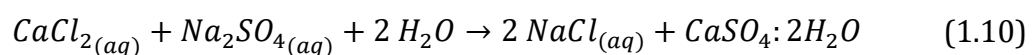


Figure 1.15: Conceptual diagram of thesis work. b) Image taken from [100].

The main objective of the thesis is to study the coupling between the thermal gradients and the reactive transport processes taking place in the deep saline aquifers. The PhD project is twofold: i) evaluate to which extent transport phenomena contribute to differentiating brines within a reservoir and thus affect salt precipitation phenomena, ii) understand the physico-chemical processes at the interface between brine and sCO₂ in systems stressed by large thermal gradients. Our conceptual diagram being quite complex (Fig. 1.15-c), the study is divided into several stages, in order to gradually increase the complexity of the system and tackle the coupled processes. To achieve our main objective, this study will be based on experimental and numerical approaches:

On the experimental level: we start from a simple approach in free medium without CO₂. Because the brine is a multicomponent system, the idea is to generate and study the reactivity between saline solutions of different ionic compositions in isothermal conditions and to study the impact of a thermal gradient on this reaction network. Depending on the composition of the water formation and the physical conditions (temperature and pressure), several minerals such as halite (NaCl), anhydrite (CaSO₄), gypsum (CaSO₄:2H₂O) and calcite (CaCO₃) can precipitate. Within the framework of this thesis, we propose to study the chemical reaction of precipitation of gypsum in isothermal and non-isothermal conditions. The reaction is given by the following equation:



To study this chemical reaction, one possibility would be to use microfluidic devices. The idea would be to use a micromodel with a "T" channel geometry, which would consist of two different fluid inlet channels that meet each other at a T-junction zone feeding a large mixing zone. As can be seen on Fig.1.16, this type of device has been used by Morais [67] and Beuvier *et al.* [101] to monitor the precipitation of carbonates and could well be adapted to monitor the precipitation of gypsum from the reaction of Ca^{2+} and SO_4^{2-} ions.

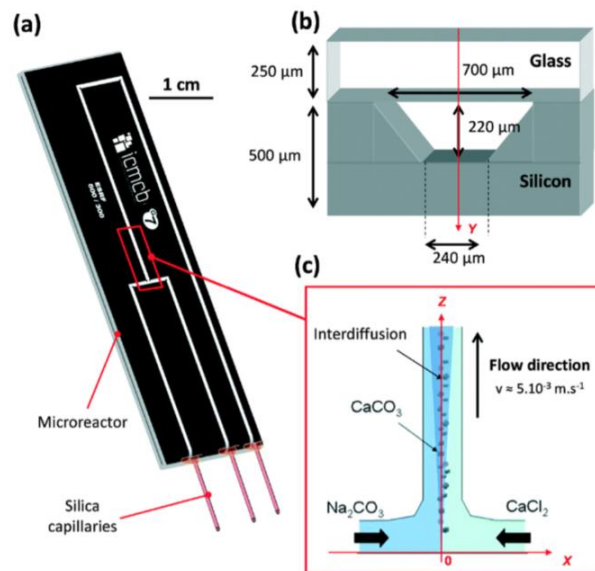


Figure 1.16: a) Geological Lab on Chip used to monitor carbonate precipitation. b) Typical sizes of the channel cross-section of the microreactor. c) Schematic illustration of the Tjunction part (red insert in a)) showing the counter flow injection of the two solutions in the horizontal inlet channels and their mixing flow in the vertical main channel where the calcium carbonate precipitates in the interdiffusion zone [67], [101].

To this system, we can add heating wires along the side walls of the central channel. Thus, by Differential Dynamic Microscopy (DDM), the impact of the thermal gradient on the precipitation reactions could be studied in a quantitative and qualitative way. Another possibility would be to use diffusion cells where it is possible to bring two distinct layers of solutions into contact so that they are stable in the gravity field. An example of a device based on this type of configuration was used by Torres *et al.* [102] and is represented below:

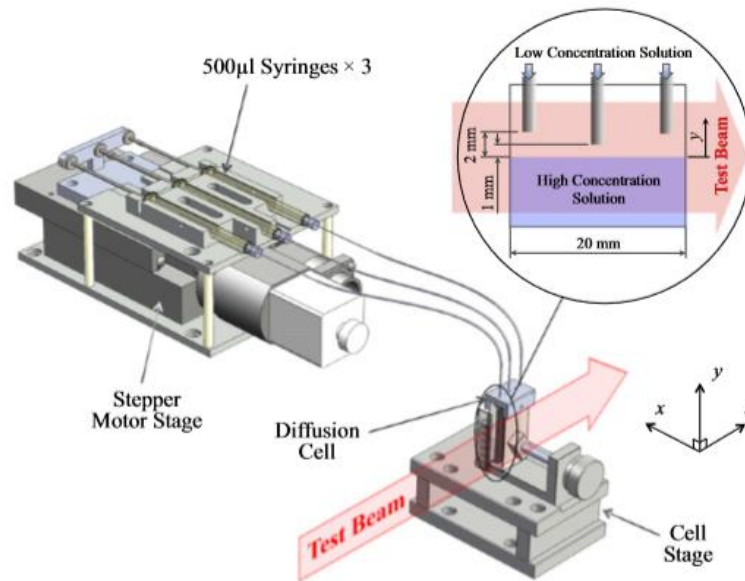


Figure 1.17: Injection setup. The solution injection device controls the injection flow of three syringes in the precision of ml/s. A close-up of the side view within the cell is shown in the inset [102].

This type of configuration allows the location of the precipitate to be visualised in the vertical plane, which is a major contribution to answering questions about the location of precipitates that form in geological reservoirs. Furthermore, this configuration offers the possibility of imposing thermal gradients parallel to the gravity field, which is representative of geological reservoirs. The use of diffusion cells in experimental devices is an expertise of the Laboratory of Complex Fluids and their Reservoir of the University of Pau and the Adour countries (LFCR UPPA-Anglet). Therefore, we propose to put into contact a solution of calcium chloride (CaCl_2) and a solution of sodium sulfate (Na_2SO_4) inside a diffusion cell. However, gypsum crystals form more or less rapidly and present a solubility limit, of about $0.0151 \text{ mol.kg}^{-1}$ at 25°C and atmospheric pressure [103], [104]. In order to delay the reaction and monitor the precipitation process over time, we add a solution of sodium chloride (NaCl) between the two previous saline solutions, which acts as a buffer solution. The 1D conceptual configuration of our system is represented as follow:

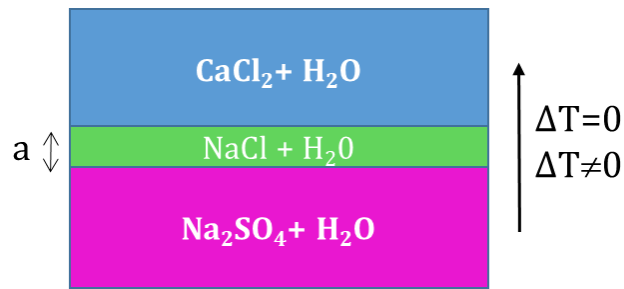


Figure 1.18: 1D conception configuration for the study of the salts multicomponent diffusion.

From Fig. 1.18 above, it can be noted that the gypsum precipitation time given by this configuration is purely dependent on the thickness a of the buffer solution. The thickness of the layer on the top and the bottom are defined by l_1 and l_2 respectively. Depending on the dimensions of the diffusion cell, this configuration can give rise to hydrodynamic instability. This experimental configuration will be studied with and without temperature gradient by using an optical technique that will be described later. It is important to mention that this type of well-stratified configuration can never be observed in geological reservoirs. Our main objective is to have a complex multicomponent system that exhibits salt concentration gradients and salt precipitation and to understand the impact of the thermal gradient on the reaction.

On the numerical level: The first aim is to reproduce and interpret the experimental results. Then, applying our results to saline solutions representative of real reservoirs and, finally, introducing a condition of constant composition of CO_2 gas phase in contact with the water formation.

Chapter 2 : Multicomponent salts diffusion in water

2.1 Introduction

In the previous chapter, we presented our multicomponent system, which consists of bringing three layers of saline solution of different chemical composition and concentration into contact with each other in order to monitor the gypsum formation process. However, in order to predict the behaviour of this multicomponent system, it is important to be able to predict accurately the behaviour of each individual saline solution at a given pressure and temperature condition and the behaviour of each pair of solutions. Regarding the behaviour of each aqueous saline solution, namely CaCl_2 , NaCl and Na_2SO_4 aqueous solutions, its diffusion in water is assumed to behave as a binary diffusion. The physical explanation lies in the electrostatic interactions between the cations and the anions forming the electrolyte. In fact, in a given electrolyte dissolved in an aqueous solution, the total charge of the anions is equal to the total charge of the cations. In addition, in order to respect the principle of electroneutrality, the ions involved in an electrolyte have the same net motion. In an electrolyte, the ion that tends to move more slowly has its diffusion accelerated while its associated ion that tends to move faster has its diffusion slowed down [105]. As for the behaviour of multicomponent mixtures, the diffusion of ions can be influenced by the composition of the solution, the activity coefficients, the pH, the ionic strength, the interaction between aqueous species, and charge numbers of solutes. To maintain local electroneutrality, solute-solute coulombic effects can considerably modify the diffusive flow of charge species [106]. The presence of ionic species leads to electrostatic interactions resulting in phenomena of attraction and/or repulsion, possibly including neutral polarizable aqueous species. Because of these interactions, the nature of the various dissolved minerals therefore confers particular properties to the brines, which are far from those of ideal solutions. This chapter presents a background on mass transport phenomena in binary systems and the various experimental methods used for the measurement of mass diffusion coefficients of salts in water. This chapter also presents a description of the behaviour of electrolytes and of fluid-rock interactions by simulation models, which revolve around the fundamentals of thermodynamics of solutions.

2.2 Brief background on transport phenomena

2.2.1 Phenomenological equation

Transport phenomena occurs in almost any multicomponent mixture present in nature and industry and its understanding is of great interest for many applications such as chemistry, nuclear energy, plasma physics, geochemistry, petroleum engineering, CO₂ storage, etc...[107]. In fact, the understanding of transport processes can be of help in studying the transient processes, thermal processes, diffusion in porous media, flow patterns in reacting systems, characterization of physiological and cellular processes. A suitable characterization of transport processes in complex mixtures requires a thorough understanding of simpler fluids like in binary mixtures.

In a convectionless not chemically reactive binary system, with non-uniform concentration and temperature, the heat and mass transfers are described by phenomenological equations:

$$\vec{q} = -\rho\Gamma\vec{\nabla}C - \lambda_T\vec{\nabla}T \quad (2.1)$$

$$\vec{j} = -\rho D\vec{\nabla}C - \rho C(1-C)D_T\vec{\nabla}T \quad (2.2)$$

where \vec{q} and \vec{j} are respectively the heat and mass flow, ρ is the fluid density, Γ is the Dufour coefficient, $\vec{\nabla}C$ and $\vec{\nabla}T$ are the concentration and temperature gradients respectively. λ_T is the thermal conductivity of the material, D and D_T are, respectively, the mass diffusion and the thermodiffusion coefficients, C is the mass fraction of the mixture, expressed as a percentage on a weight-per-weight basis (w/w). The first term on the right-hand side of Eq. 2.1 refers to a heat flux induced by a concentration gradient and is called the Dufour effect. Its contribution in liquid mixtures is very small compared to the Fourier contribution, represented by the second term on the right-hand side of Eq. 2.1.

The mass flow \vec{j} contains the contributions of the mass transfer flux governed by the concentration gradient and the temperature gradient. The first term on the right-hand side of Eq. 2.2 expresses the Fickian diffusion, as postulated in the Fick's first law of diffusion. It describes a mass flux from regions of high concentration to regions of low concentration due the inhomogeneity of the concentration in the system. The second term

on the right-hand side of Eq. 2.2 is the components separation induced by the thermodiffusion or Ludwig-Soret effect. It describes the molecular movement produced by the inhomogeneity of the temperature. At stationary state, the total mass flow vanishes ($\vec{j}=0$). Hence, Eq. 2.2 becomes:

$$\vec{\nabla}C = -C(1-C)S_T\vec{\nabla}T \quad (2.3)$$

where $S_T = D_T/D$ is the Soret coefficient. It can be positive or negative [108], [109], which indicates the direction of migration of the solutes (to the cold or to the hot region). Eq. 2.3 represents the magnitude of the concentration gradient directly coupled to the external temperature gradient. Since we have concentration gradients during free-diffusion and thermodiffusion processes, then there is a contribution of Fickian diffusion in both cases. However, in the case of free-diffusion ($\Delta T = 0$ K), only the contribution of the Fickian diffusion is present.

The rate of diffusive heat transfer compared to the Fickian diffusion is described by the Lewis number, Le . It is a dimensionless number defined as the ratio of thermal diffusivity to mass diffusivity given by:

$$Le = \frac{\kappa}{D} \quad (2.4)$$

where κ is the thermal diffusivity. In liquid mixtures, thermal diffusivity is much greater than mass diffusion ($Le \gg 1$), leading to the fact that the tendency to reach a homogeneous state is faster for temperature than for concentration [110]. A general description of isothermal diffusion and thermodiffusion experiments is provided in the following part.

2.2.2 Free diffusion or isothermal diffusion

In a constant gravitational field, a typical free-diffusion experiment consists in carefully layering two miscible fluids with the denser on the bottom and the lighter on the top, creating an initial step concentration gradient at uniform temperature ($\Delta T = 0$) as shown in Fig. 2.1. The figure more exactly represents two solutions containing the same components with an initial concentration gradient and mixing by diffusion. The two

solutions are initially separated by a sharp horizontal interface, which is stabilized by the gravitational field.

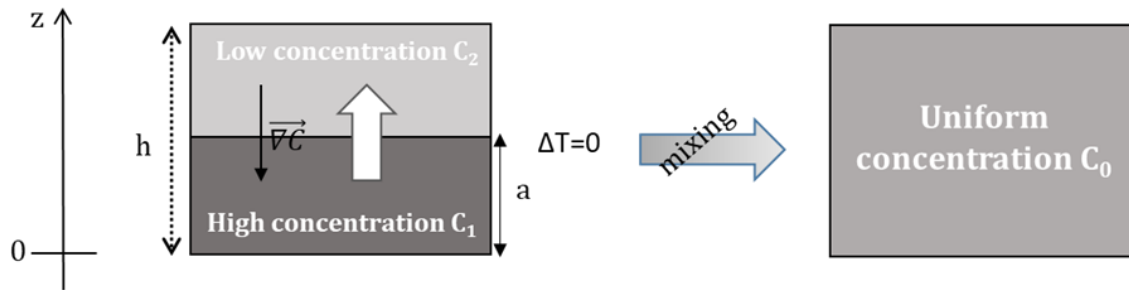


Figure 2.1: Sketch for the mixing of two solutions by free diffusion in laboratory conditions.

The typical initial condition is the step function concentration profile, which can thus be written for the concentration $C(z,t)$ of the denser component as [111]:

$$C(z, 0) = \begin{cases} C_1, & 0 < z < a \\ C_2, & a < z < h \end{cases} \quad (2.5)$$

where h is the height of the diffusion cell, corresponding to the total thickness of the two superimposed solution layers and z is the vertical position within the diffusion cell. C_1 and C_2 are the uniform initial concentrations of the denser solution and of the lower one respectively, with the condition $C_1 > C_2$. In the model, the two horizontal layers are separated by a horizontal interface supposed to be at mid-height of the cell $a=h/2$. Once the two fluids are left into contact, a diffusive Fickian flow starts to transport mass across the interface and as time goes by, the diffusive process evolves. The initial sharp concentration gradient is smoothed by diffusion and decreases with time. The time-dependent theory assumes that the macroscopic concentration evolves in time according to the usual diffusion equation given by Eq. 2.6. It describes the time evolution of the macroscopic concentration, once the dependence of the mass flux from hydrodynamic variables is prescribed [111]:

$$\frac{\partial C}{\partial t} + \frac{1}{\rho} \nabla \cdot \mathbf{j} = 0. \quad (2.6)$$

The evolution of the concentration profile during the free diffusion process, obtained by solving the diffusion equation with the initial condition of Eq. 2.5 and is given by [112]:

$$C(\tilde{z}, t) = \left(\frac{C_1 + C_2}{2}\right) + \frac{2}{\pi} \Delta C \sum_{j=1}^{\infty} \frac{1}{j} \sin\left(\frac{j\pi}{2}\right) \exp\left(-\frac{Dj^2\pi^2}{h^2}t\right) \cos(j\pi\tilde{z}) \quad (2.7)$$

where \tilde{z} is the normalized height ($\tilde{z}=z/h$) and $(C_1+C_2)/2$ is the homogeneous concentration at the end of the diffusion process. During a free-diffusion process, the concentration difference between the top and bottom in the cell is assumed to remain constant. This assumption is true in the case of unbounded diffusion, where two infinitely thick layers of fluid are allowed to diffuse one into each other. In practice the assumption is valid only during a given time interval after the beginning of the diffusion process, which depends on the vertical size of the vessel and on the diffusion coefficient. As soon as the concentration near the boundaries begins to change, the features of the macroscopic diffusion process cease to depend on the diffusion coefficient only, and they are influenced by the height of the vessel also [111]. The characteristic diffusive time τ_d in a free-diffusion process is given by [112]:

$$\tau_d = \frac{(h/2)^2}{(\pi D)} \quad (2.8)$$

A plot of the evolution of the concentration profile given by the Eq. 2.7 is illustrated in Fig. 2.2. It is the time evolution of the concentration profile plotted vs the normalized height \tilde{z} during a free-diffusion. The thickness of the sample is $h=1$ cm. As an example, initially two horizontal layers of the binary mixture of NaCl-H₂O at the uniform concentrations $C_1=19$ w/w and $C_2=0.09$ w/w are separated by a horizontal interface at the mid-height $a= h/2$. The homogeneous concentration at the end of the diffusion process is $C =0.14$ w/w and the diffusion coefficient taken from literature is $D = 1.55 \times 10^{-5}$ cm²/s [113].

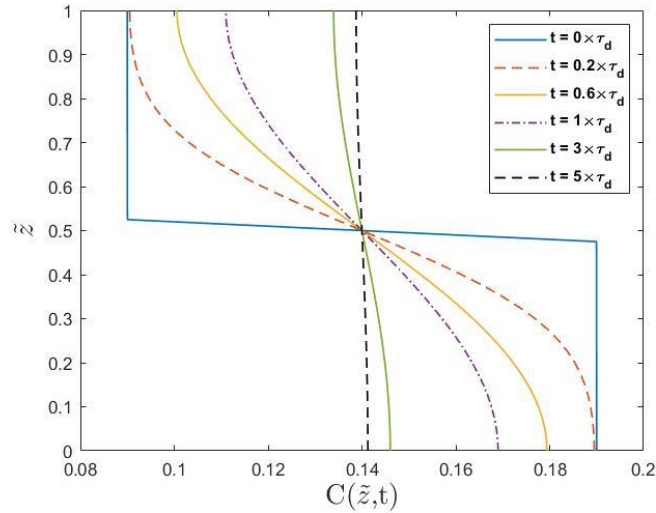


Figure 2.2: Time evolution of the concentration profile plotted vs the normalized height \tilde{z} during a free-diffusion for different times. The horizontal and vertical axes are exchanged for convenience. The thickness of the cell is $h=1$ cm. Initially two horizontal layers of the binary mixture of NaCl-H₂O at the uniform concentrations $C_1 = 0.19$ w/w and $C_2 = 0.09$ w/w are separated by a horizontal interface at the mid-height $a = h/2$ (i.e. $\tilde{z} = 0.5$). The homogeneous concentration at the end of the diffusion process is $C=0.14$ w/w and the diffusion coefficient is $D = 1.55 \times 10^{-5}$ cm²/s [113].

In the early stages of the diffusion process, the concentration at the boundaries does not change in time, as the diffusive remixing occurs only around the midheight. From Fig. 2.2 we can clearly see that the initial net concentration gradient in the diffusion cell is smoothed by diffusion and decreases with the time. In theory, the concentration gradient disappears completely at infinite times. In practice, the concentration gradient is considered to be 99% smoothed after a time t corresponding to 5 times the diffusion time ($t = 5 \times \tau_d$), when the latter is defined as in Eq. 2.8.

2.2.3 Thermodiffusion or Soret effect

Thermodiffusion, also called the Soret effect, describes the coupling between temperature gradients and the resulting mass fluxes. Unlike free diffusion, the mixture is initially at a uniform concentration in the case of thermodiffusion. When applying a positive thermal gradient (i.e heating from above and cooling from the bottom) to a convectionless system, there is a heat flow governed by the Fourier's law and a mass flow, which tends to gradually separate the molecules along the gradient by the Soret effect effect until a stationary state related to the appearance of a concentration gradient. This process is illustrated in Fig. 2.3 below.

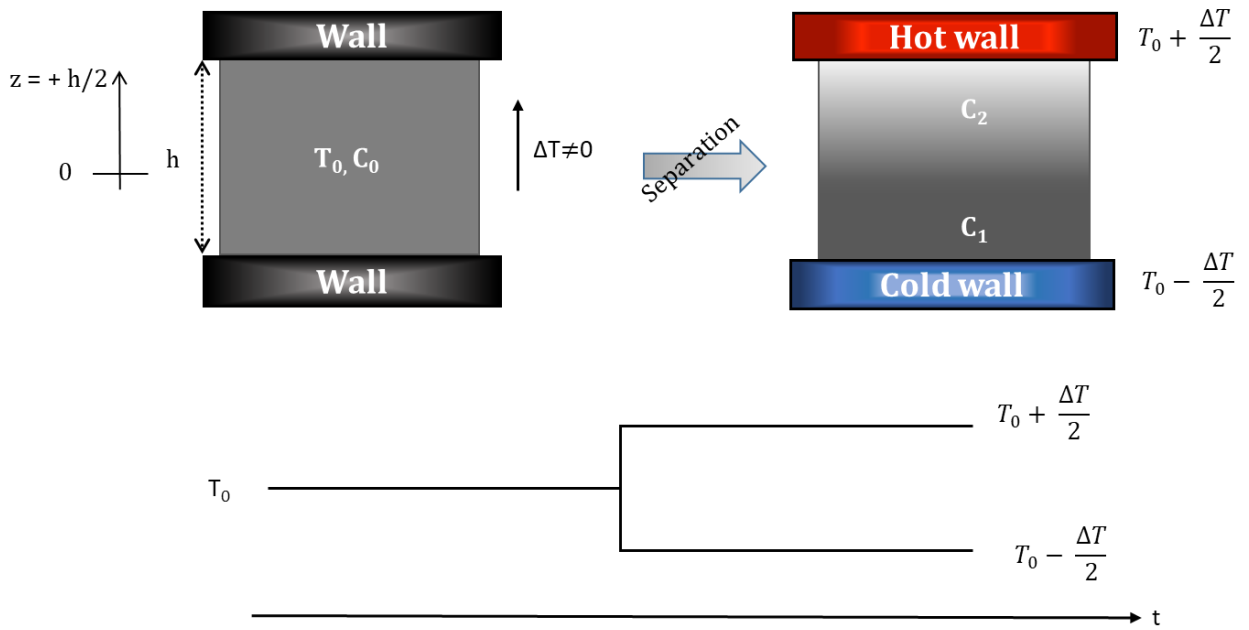


Figure 2.3: General principle of a Soret cell experiment

In Fig. 2.3, a solution contained in a diffusion cell is subjected to a linear temperature gradient, with the initial condition that the distance h in the cell varies from $-h/2$ to $h/2$. The system will respond with mass fluxes (Eq. 2.2) leading to a time-dependent concentration gradient along the direction of the temperature gradient inside the bulk. To determine the time-dependence of Eq. 2.2, the appropriate governing equation is the continuity equation defined by Eq. 2.6. By applying principles of mass and component conservation, and after transformation we obtain the dimensionless form of the diffusion equation: [114]

$$\frac{\partial \tilde{C}}{\partial \tilde{t}} = \frac{\partial^2 \tilde{C}}{\partial \tilde{z}^2} \quad (2.9)$$

where
$$\tilde{C} = \frac{C}{\Delta C_\infty} \quad (2.10)$$

$$\tilde{z} = \frac{z}{h} \quad (2.11)$$

$$\tilde{t} = \frac{tD}{h^2} \quad (2.12)$$

ΔC_∞ is the magnitude of the mass separation. The solution to Eq. 2.9 in the case of a parallelepipedic Soret cell is [114]:

$$\begin{aligned} \tilde{C} - \tilde{C}_0 = \tilde{z} + \frac{1}{2} \sum_{n=-N}^N (\tilde{z} - n) (-1)^n \left[\operatorname{erf} \left(\frac{2\tilde{z} - 2n - 1}{4\sqrt{\tilde{t}}} \right) \right] - \left[\operatorname{erf} \left(\frac{2\tilde{z} - 2n + 1}{4\sqrt{\tilde{t}}} \right) \right] \\ + \sum_{n=-N}^N (-1)^n \sqrt{\frac{\tilde{t}}{\pi}} \left[\exp \left(-\frac{(2\tilde{z} - 2n - 1)^2}{16\tilde{t}} \right) - \exp \left(-\frac{(2\tilde{z} - 2n + 1)^2}{16\tilde{t}} \right) \right] \end{aligned} \quad (2.13)$$

The time evolution of the concentration profile plotted vs the normalized height \tilde{z} during thermodiffusion for a binary mixture is represented in Fig. 2.4. The diffusion coefficient of a binary mixture of NaCl-H₂O at a homogeneous concentration of $C=0.14$ w/w is $D = 1.55 \times 10^{-5} \text{ cm}^2/\text{s}$ [113]. The thickness of the sample is $h=1$ cm and the number of terms in the summations in Eq. 2.13 is $N=10$. At steady state a linear concentration profile is formed inside the sample.

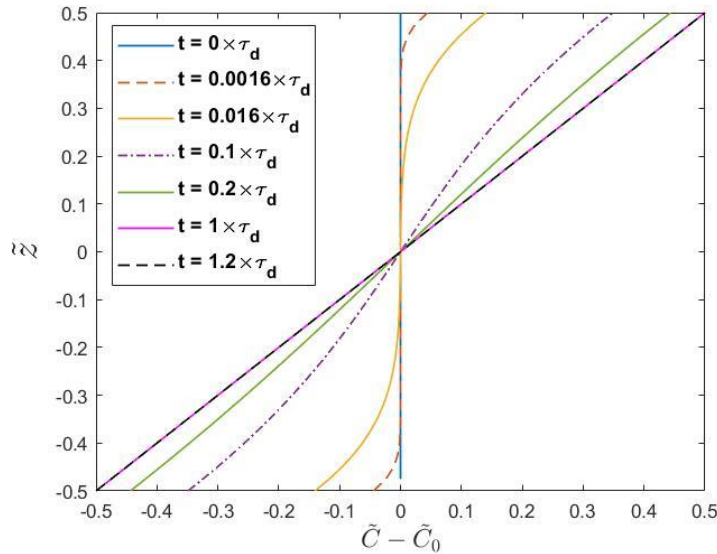


Figure 2.4: Time evolution of the normalized concentration profile plotted as a function of the normalized height \tilde{z} during a thermodiffusion process. The horizontal and vertical axes are exchanged for convenience. Plot of Eq. 2.13 for $N = 10$, $D = 1.55 \times 10^{-5} \text{ cm}^2/\text{s}$ [113]. The thickness of the sample is $h=1$ cm.

From Fig. 2.4 it can be seen that the separation of the sample over time induces a concentration gradient. At steady state, a linear concentration profile is formed inside the sample. In this case, the characteristic diffusive time is given by $\tau_d = \frac{h^2}{\pi D}$. A complete separation by Soret effect is obtained after a time t corresponding to 1 time the diffusion time ($t = 1 \times \tau_d$).

Caldwell and Eide [115] have measured the Soret coefficients and isothermal diffusivity of aqueous solutions of five principal salt constituents of seawater as a function of mean concentration, temperature and pressure, namely NaCl, CaCl₂ and Na₂SO₄ solutions. They reported a magnitude of the Soret coefficient in absolute value for those aqueous solutions in the order of $|S_T| \sim 10^{-3} \text{ }^\circ\text{C}^{-1}$. Hence, according to Eq. 2.3, for a binary mixture at a mean concentration of $C = 0.5 \text{ w/w}$ and for a temperature difference $\Delta T = 20 \text{ }^\circ\text{C}$ between the hot and the cold parts of the system, the separation by Soret effect between the top and the bottom of the diffusion cell is 0.005 w/w or 0.5% . The magnitude of Soret effect appears to be very small. At high pressures and temperatures, separations of the order of 4% can be achieved, which still remains small. Therefore, the Soret effect has very small impact on concentration gradients. Alone it cannot be expressed in a significant way to compete with other transport phenomena, especially in the context of geological storage of CO₂ in deep saline aquifers. However, there are configurations where the separation via Soret effect can be important. For example in a double diffusive step, i.e. in a vertical interface stabilised by a salt gradient [116], [117]. Consequently, in the present work, we will not consider the Soret effect. We will only focus on the measurement of the diffusion coefficient of salts in water.

2.3 Optical methods to study the isothermal diffusion of salts in water

The measurement of the mass diffusion coefficient of salts in water can be predicted theoretically or calculated from empirical correlations, which involve several properties such as activity coefficient, conductance, concentration, temperature, dielectric constant, viscosity of the solvent. [118]–[121]. In the literature, several experimental techniques have also been used for the measurement of the diffusion coefficient of the binaries NaCl-H₂O, CaCl₂-H₂O and Na₂SO₄-H₂O from dilute concentration to high concentration at $25 \text{ }^\circ\text{C}$ and atmospheric pressure. These experimental methods include the decaying pulse technique [122], the diaphragm cell method [123]–[125] and some optical techniques. The latter are generally recognized as powerful tools for investigating fluid flow phenomena in transparent media [126] and the most accurate methods to measure mass diffusion coefficients. They can provide both a qualitative and quantitative analysis. Among these optical techniques, the most widely used for the measurement of the mass diffusion coefficients of salts in water are interferometric techniques [127], owing to their

non-destructive nature and the possibility to visualise directly and instantaneously the evolution of the diffusion field as the free diffusion process takes place in the test cell. In order to avoid any convection phenomenon, the denser solution is injected in the bottom part of the diffusion cell in the presence of a gravitation field. They are based on the analysis of the variation of the refractive index in a transparent media: a test beam perpendicular to the concentration gradient passes through the diffusion cell. Interfering this beam with a reference beam results in time-dependent interferograms that are recorded and analysed in real time or after the experiment. The following part presents the conventional interferometric techniques commonly used.

2.3.1 Electronic speckle pattern interferometry (ESPI)

Riquelme *et al.* [128] used electronic speckle pattern interferometry (ESPI) shown in Fig. 2.5 for the measurement of the diffusion coefficient of a 1.75 mol.L^{-1} solution of NaCl diffusing into distilled water at a mean temperature of $23.5 \text{ }^\circ\text{C}$. It consists of a Mach-Zehnder type interferometer that is illuminated by a laser beam. The latter could first pass through a neutral density filter to avoid saturating a camera and is then divided by a beam splitter. One beam, the so-called test beam passes through the cell, while the other, called reference, propagates in the air. A second beam splitter then recombines them. The recombined beam passes through an opal screen before entering the camera in order to generate speckles. The diffusion cell consists of two sheets of glass. The cell is first half-filled with distilled water. After allowing the movements resulting from the injection to dissipate, the salt solution is slowly injected from below using a powered syringe. It follows an acquisition of images.

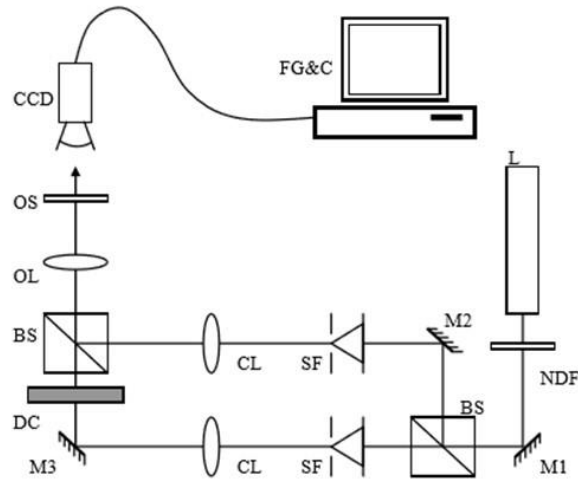


Figure 2.5: ESPI interferometer. BS: beam splitters; CL: collimating lenses; DC: diffusion cell; FG&C: frame grabber and computer; L: laser; M: mirrors; NDF: neutral density filter; OL: object lens; OS: opal screen; SF: spatial filters [128].

2.3.2 Phase-shifting interferometry (PSI)

A phase shifting interferometer (PSI) was developed in the 1970s by Bruning *et al.* [129]. PSI was used to measure the diffusion coefficients of salts in water as a function of the concentration of salts at room temperature and atmospheric pressure. The experimental system is illustrated in Fig. 2.6. In this technique, the optical system is a Mach-Zehnder interferometer where one plays on the polarization of the beams in order to produce an additional phase shift suitably calculated between the recorded images. This allows going back to the phase shift between the test beam and the reference beam. The diffusion cell is composed of a square quartz cell like those used in spectroscopy. In order to avoid mass transport due to convection, the density gradient and gravity must be in the same direction. Thus, the cell is first half-filled with the denser solution. The lighter solution is then injected through the top of the cell. The system is kept at constant temperature. The diffusion coefficient is then determined from measurements of transient concentration profiles obtained by analyzing the interferograms.

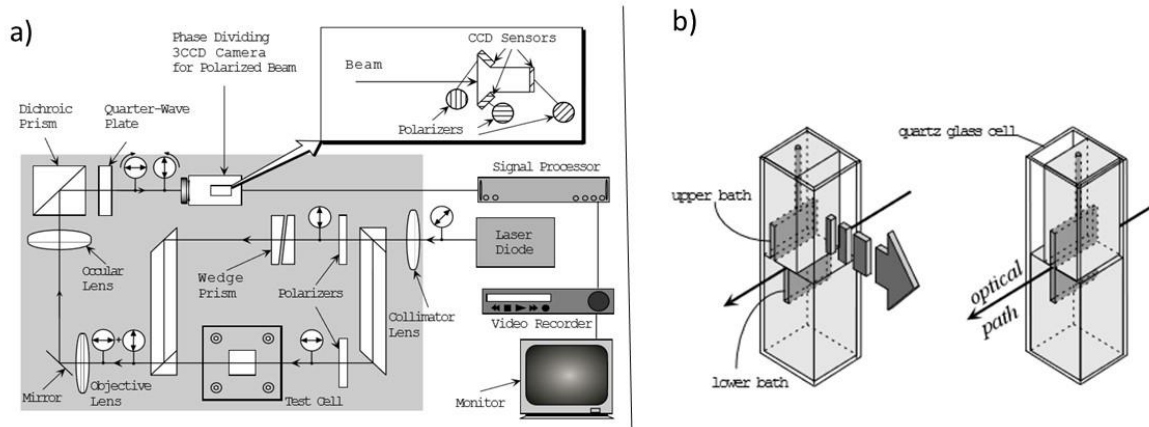


Figure 2.6: a) Schematic sketch of the Phase-shifting interferometer b) Design of the test cell [130].

Using this method, Torres *et al.* [102] measured the diffusion coefficient of NaCl in water at 25 °C in the concentration range between 0.5 mg.mL⁻¹ and 10 mg.mL⁻¹ of NaCl with a concentration difference set for all the runs at 2 mg.mL⁻¹, except for the average concentration of 0.5 mg.mL⁻¹ where the concentration difference in concentration was set to 1 mg.mL⁻¹. The measured values are illustrated below in Fig. 2.7.

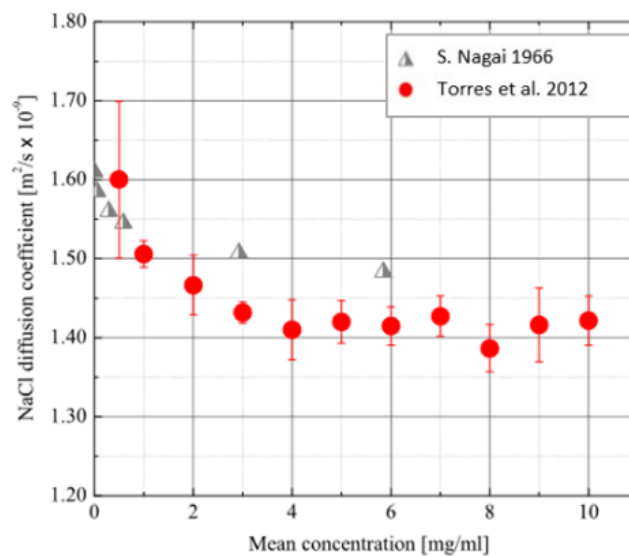


Figure 2.7: Diffusion coefficient of NaCl in water as a function of average concentration, at 25 °C. Standard deviations are also plotted for each measurement [102].

According to this figure, the diffusion coefficient of NaCl in water depends on the average concentration. We observe a decrease of D between 0.5 and 4 mg.mL⁻¹ and then, it remains relatively constant from 4 to 10 mg.mL⁻¹.

Another interferometric technique similar to the previous one, using the same optical system, was used by Nimdeo *et al.* [131] with some small differences in cell design and

analysis. Indeed, in this new configuration, the diffusion cell is rather octagonal and is made of two square optical windows. The volume cavity created is larger. Unlike the previous technique, here the cell is first completely filled with the lighter solution. Then the denser solution is injected from the bottom of the cell. The concentration front interferograms are recorded over time and are analyzed using two approaches for the determination of the mass diffusion coefficient. The first technique involves the entire analysis of the interferogram. It is the most detailed and is recommended for good quality interferences. While the second technique consists of the analysis of a single fringe of the image of the phase shift. The latter is preferable when one does not have a control on the position of the diffusion front in the diffusion cell. In their study, Nimdeo *et al.* [131] focused on the concentration range between 5 and 26 wt% NaCl.

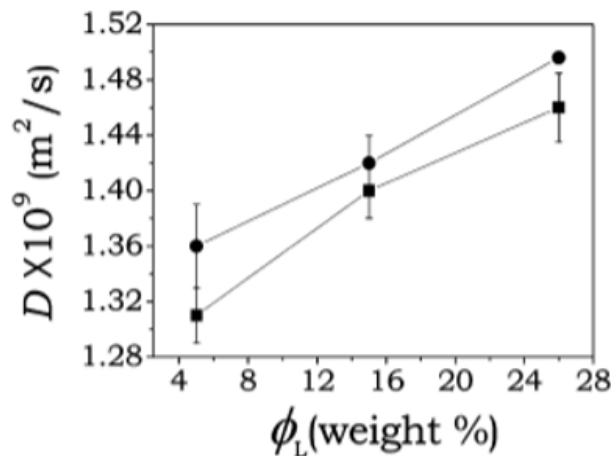


Figure 2.8: Plot of mass diffusion coefficient obtained at various concentrations of sodium chloride in water. The square symbols are the measurements carried out with full interferogram analysis while circle symbols are for single fringe analysis [131].

For both analysis methods, it is observed that the mass diffusion coefficient in this range of concentration increases with the average concentration.

2.3.3 Gouy interferometry

The diffusion coefficients of salts in aqueous solution at atmospheric pressure and ambient temperature have also been measured by the Gouy interferometry technique. The detailed description of the theory of this method is given by Longworth [132] and Kegeles et Gosting [133]. The principle of this technique is illustrated in Fig. 2.9. It is an optical system consisting of a monochromatic light source, which delivers a light beam collimated by a lens. The entire light beam passes through the diffusion cell in which two

solutions of different concentrations are brought into contact in the direction of gravity. Because the cell contains refractive index (refractive index profil as illustrated by the red line in Fig. 2.9), the light passing through the center of the diffusion cell is deflected while the light passing through the extremes/boundaries is undisturbed. The difference in the deflecting angle produce interferograms that are viewed and recorded. The diffusion coefficients are obtained by analysis of the interference fringes.

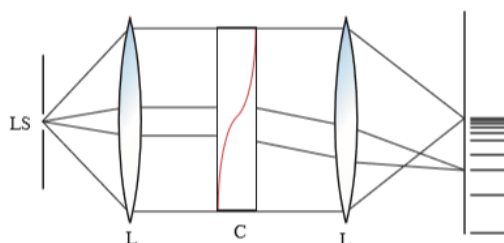


Figure 2.9: Principle of Gouy interferometry. A sketch of the light source (LS), the lenses (L), and the cell (C) is shown together with the derived interference pattern [134].

Gouy interferometry has been used by Hall *et al.* [135] for the measurement of the diffusion coefficient of CaCl_2 aqueous solution at 25 °C for concentrations from 0.0152 to 3.530 mol.L⁻¹. It has also been used by Vitagliano et Lyons [136] and Chang et Myerson [137] for the measurement of the diffusion coefficient of salts including NaCl in aqueous solution at 25 °C for concentrations up to 5.0 mol.L⁻¹. Because these two studies agree well, table 2.1 only summarizes the values taken from Vitagliano et Lyons [136].

Table 2.1: Gouy data for NaCl solutions at 25 °C. [136] (see text for details)

\bar{C} (mol.L ⁻¹)	ΔC (mol.L ⁻¹)	J_m	$10^5 \times \Delta n / \Delta C$ (L.mol ⁻¹)	$10^5 \times D$ (cm ² /sec)
0.02715	0.0656	42.44	1029	1.526
0.02757	0.0475	44.65	1024	1.512
0.08059	0.1039	48.39	1016	1.490
0.09644	0.1085	50.64	1019	1.483
0.1267	0.1345	62.54	1015	1.479
0.1419	0.1427	66.26	1013	1.481
0.2082	0.1508	69.43	1005	1.472
0.2082	0.1508	69.43	1005	1.474
0.2130	0.1529	70.39	1005	1.473
0.3000	0.200	91.36	9970	1.473
0.3416	0.1927	87.70	993.5	1.477
0.5004	0.2076	92.06	967.7	1.473
0.6987	0.2073	91.41	964.0	1.477

1.0000	0.2000	86.73	946.3	1.485
2.0028	0.2244	91.41	889.2	1.519
2.0305	0.3674	149.21	886.6	1.517
3.000	0.2400	94.17	856.4	1.565
4.000	0.200	74.60	814.1	1.594
4.5261	0.2604	96.58	809.5	1.592
5.000	0.300	108.63	790.3	1.590

In Table 2.1, \bar{C} is the average concentration in mol.L⁻¹, Δc the concentration difference across the boundary, J_m the total number of fringes in the Gouy pattern. $(\Delta n/\Delta c) = (J_m/\Delta c)(\lambda/a)$ Where a is the length along the optic axis of the diffusion cell and $\lambda = 5460.7 \text{ \AA}$. D is the diffusion coefficient at \bar{C} in cm².s⁻¹. D_{NaCl} in water were measured at 25 °C from dilute solutions to high concentrations. It can be seen that, from the concentration of 0.02715 mol.L⁻¹ up to 0.2 mol.L⁻¹, D decreases with increasing concentration. Between 0.2 mol.L⁻¹ and 0.5 mol.L⁻¹, the D remains almost constant. This trend is consistent with the work of Torres *et al.* [102]. Thereafter, D increases linearly with the concentration until it reaches a maximum around 4.0 mol.L⁻¹ as observed by Nimdeo *et al.* [131]. From this maximum, D begins to decrease again.

2.3.4 Rayleigh interferometry

The Rayleigh interferometer is a two-beam interferometer, which makes use of the interference patterns between the reference beam and the test beam to analyse the refractive index variations within a cell. The Rayleigh interferometry is a technique very similar to the Gouy interferometry and the principle is the same. Rayleigh interferometry differs from the Gouy one in the way that instead of passing the entire light beam through the diffusion cell, two sections of the collimated beam are isolated by a pair of apertures as illustrated in Fig. 2.10. One of these beams is the reference beam, which remains undisturbed and is used to provide a comparison wavefront while the other beam, the so-called the test beam passes through the diffusion cell to be tested. At the end, the two beams are combined together to make an interferogram. The latter contains information about the variations of refractive index within the cell.

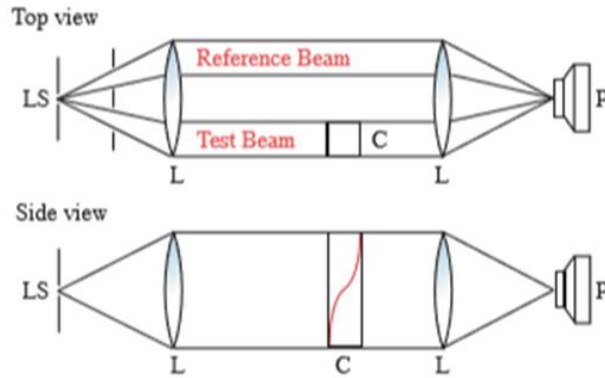


Figure 2.10: Principle of Rayleigh interferometry. A sketch of the light source (LS), the lenses (L), and the cell (C). [134].

Rard and Miller [113], [138] have measured the diffusion coefficient of several electrolytes at 25 °C including NaCl-H₂O, CaCl₂-H₂O and Na₂SO₄-H₂O from dilute solutions to near saturation by free diffusion Rayleigh interferometry. For each salt, they worked over a full concentration range and the reported diffusion coefficients are with an accuracy of 0.1 - 0.2%. The concentration range is from 0.018 to 5.32 mol.L⁻¹ for NaCl-H₂O (see Fig. 2.11), from 0.0064 to 5.57 mol.L⁻¹ for CaCl₂-H₂O (see Fig. 2.12), and from 0.005 to 1.53 mol.L⁻¹ for Na₂SO₄-H₂O (see Fig. 2.13).

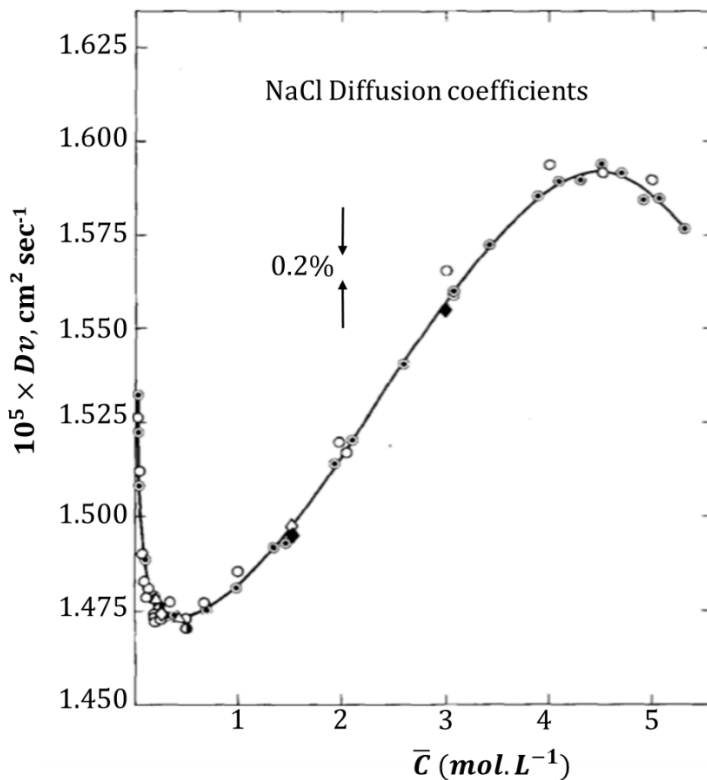


Figure 2.11: The diffusion coefficients of NaCl solutions at 25 °C as a function of the molar concentration \bar{C} [113].

Fig. 2.11 represents a combination of all the measurements of the diffusion coefficients of NaCl-H₂O carried out by Rard and Miller [113] at 25 °C. It can be seen that the dependence of the diffusion coefficient of NaCl-H₂O on its concentration exhibits a non-ideal behaviour. This behaviour was also observed for the diffusion of CaCl₂ in water as shown in Fig. 2.12.

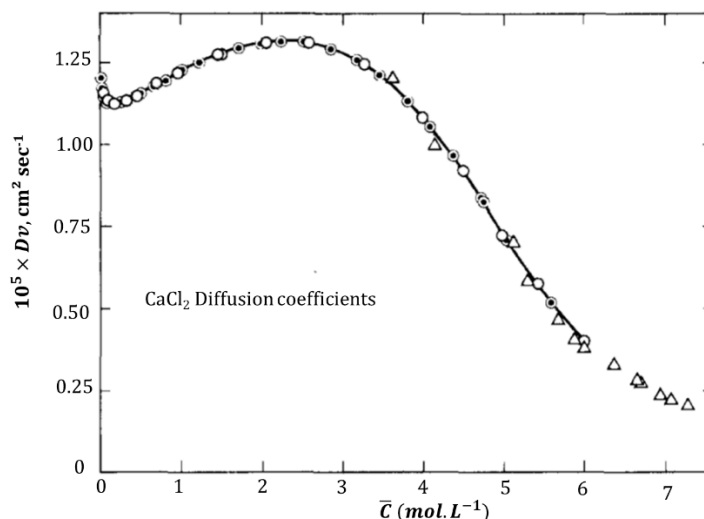


Figure 2.12: The diffusion coefficients of CaCl₂ solutions at 25 °C as a function of the molar concentration \bar{c} [113].

For these two electrolytes (NaCl and CaCl₂), one would expect to observe a regular decrease of the diffusion coefficient with increasing concentration. Indeed, as presented in the work of Gonçalves and Kestin [139], [140], both the density and the viscosity of NaCl [139] and CaCl₂ [140] solutions increase with concentration for a given temperature. A more concentrated solution being denser, it would therefore diffuse less quickly. However, their diffusion coefficient presents three distinct areas. For very dilute concentrations, the diffusion coefficient decreases with increasing concentration until it reaches a minimum. This behavior was predicted by the theory of Debye and Hückel [141] and confirmed by that of Fuoss and Onsager [142] for the domain of low electrolyte concentrations. In concentrated zones, there is a regular increase of the diffusion coefficient with increasing concentration up to a certain maximum. According to Vitagliano and Lyons [136], this maximum has been observed for all electrolytes of sufficient solubility so that the decrease in mobility, which accompanies increasing viscosity, may overwhelm the thermodynamic factor $(1 + c (d \ln \gamma / dc))$ which tends to increase the value of D at high electrolyte concentration [136]. Finally, as we get closer to saturation, D begins to decrease again with increasing concentration. This could result

from competition between the effect of activity coefficients, friction coefficients or hydrodynamic interactions.

While NaCl-H₂O and CaCl₂-H₂O and many other salts exhibit both a minimum and a maximum as a function of concentration, D of Na₂SO₄-H₂O decreases regularly with increasing concentration.

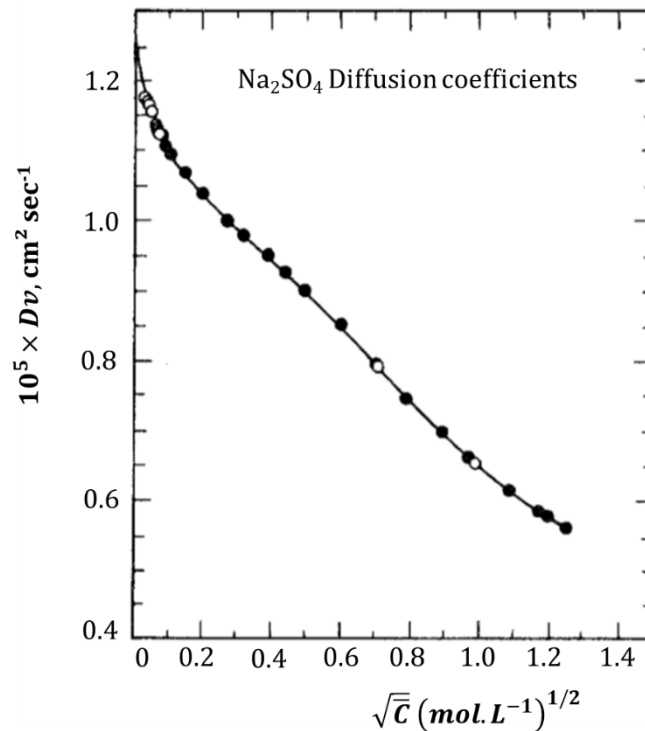


Figure 2.13: The diffusion coefficients of Na₂SO₄ solutions at 25 °C as a function of the square root of the molar concentration \bar{C} [138].

2.4 Numerical modelling procedure

The purpose of a model is to predict the evolution of physicochemical parameters of a system within the limits of validity of the model used, from measurable data. The results obtained from a model can be verified by experiments. Brines are very complex and contain highly saline solutions whose evaporation leads to the formation of mineral salts in the form of crystals (solids) from the dissolved ionic species they contain. The description of the behaviour of electrolytes and of fluid-rock interactions by simulation models revolve around the fundamentals of thermodynamics of solutions.

2.4.1 Thermodynamic properties of electrolytic solutions

2.4.1.1 Chemical potential

The chemical potential μ of a species in a phase is the energy that can be used (absorbed or released) during a transformation, for one mole of species and at a given state of the system, neglecting the thermal and mechanical energies. The chemical potential μ ($\text{J}\cdot\text{mol}^{-1}$) of a compound i in an aqueous solution is related to the activity of this element a_i by:

$$\mu_{aq,i(T,P,m_i)} = \mu_{aq,i(T,P)}^0 + RT \ln a_{i(T,P,m_i)} \quad (2.14)$$

where $\mu_{aq,i(T,P)}^0$ (in $\text{J}\cdot\text{mol}^{-1}$) is the chemical potential of the species i at the standard state at temperature T and pressure P . R is the ideal gas constant ($8.314 \text{ J}\cdot\text{K}^{-1}\cdot\text{mol}^{-1}$). The activity a_i of an aqueous species depends on the pressure, the temperature, and the solution composition and is related to the molality (see appendix A for a reminder of definitions) of the element i by:

$$a_{i,aq} = \gamma_{i,aq(P,T,m_{j \neq i,aq})} \frac{m_{i,aq}}{m_0} \quad (2.15)$$

where $\gamma_{i,aq}$ is the activity coefficient (dimensionless), $m_{i,aq}$ is the molality of the aqueous species i , $m_{j \neq i,aq}$ is the molality of each of the other aqueous species j and m_0 is a reference molality chosen to be equal to $1 \text{ mol}\cdot\text{kg}^{-1}$ [143]. The estimation of the activity of aqueous species requires the calculation of their activity coefficient taking into account the effect of salinity, temperature, and pressure. For ideal solutions, the activity coefficient $\gamma_{i,aq}$ is equal to 1. However, due to interactions between particles, even at low concentrations, electrolytic solutions do not behave like ideal solutions. The choice of the model for calculating the activity coefficient is important in order to properly describe the chemical behavior and properties of electrolytic solutions. Indeed, the chemical potential and the activity coefficient are directly involved in the calculation of many properties [144].

2.4.2.2 Thermodynamic models

The model used to calculate the activity coefficients for solutes mainly depends on the ionic strength I which describes the number of electrical charges in the solution and

represents the overall activity of ions in an aqueous solution. The ionic strength I is related to the molality of aqueous species by:

$$I = \frac{1}{2} \sum m_i z_i^2 \quad (2.16)$$

where z_i is the charge number of ion i . I is in mol.kg⁻¹.

❖ Debye-Hückel theory

Hence, for $I < 0.1$ mol.kg⁻¹, the activity coefficient can be calculated using the extended Debye-Hückel theory given by:

$$\log \gamma_i = -\frac{Az_i^2\sqrt{I}}{1 + B a_i \sqrt{I}} \quad (2.17)$$

where A and B are temperature dependent constants; at 25 °C $A = 0.5085$ and $B = 0.3285 \times 10^{10}/m$ [145], [146]. The empirical ion-size parameter a_i is a measure of the effective diameter of the hydrated ion. In 1925, Hückel improved the extended Debye-Hückel law given in Eq. 2.17, by adding an adjustable parameter H . For $0.1 < I < 0.2$ mol.kg⁻¹, the activity coefficient can be calculated using this improved equation of the extended Debye-Hückel equation given by:

$$\log \gamma_i = -\frac{Az_i^2\sqrt{I}}{1 + B a_i \sqrt{I}} + HI \quad (2.18)$$

where A and B represent the Debye-Hückel constants characteristic of the solvent and the temperature, H is a constant which corrects the deviation from Debye Hückel's law.

❖ Davies equation

The Davies equation is another relation often used to calculate activity coefficients and is applicable up to an ionic strength of about 0.5 mol.kg⁻¹ and is given by:

$$\log \gamma_i = -Az_i^2 \left(\frac{\sqrt{I}}{1 + \sqrt{I}} - 0.3 I \right) \quad (2.19)$$

The activity coefficients of low salinity solutions can be easily calculated by ion association approaches such as Debye-Hückel, extended Debye-Hückel or Davies. These approaches are implemented in most of the geochemical codes such as PHREEQC [147]. However, for higher salinities ($I > 0.7 \text{ mol.kg}^{-1}$) the calculated results diverge from observations, even in the case of NaCl solutions. In these cases, the use of a more specific interaction approach is necessary. Numerous models have been developed, and one of the most powerful able to describe aqueous systems up to very high salinities (above several moles per kg of water) is the Pitzer's model [148].

❖ Pitzer's model

The model of Pitzer for calculating the activity coefficient of solutes [148], [149] is one of the most widely used models for describing the chemical properties of electrolyte solutions at high concentrations. It represents a significant advance in physical chemistry that has facilitated the construction of accurate thermodynamic models [150]. It has been shown that the Pitzer approach could be expanded to accurately calculate ion activity products, and thus solubilities, in complex brines and to predict the behavior of natural fluids from subzero temperatures to very high temperatures, up to 573.15 K [151]. The governing equations and the underlying physics have been discussed in detail elsewhere [148], [149], [152]–[155]. They have been used, modified and extended in various ways depending on the chemical system or the range of salinity studied. The Pitzer's model is a semi-empirical model whose equations are based on the Debye-Huckel theory that describes the long-range interactions. Pitzer improved on the latter theory by developing a virial term to take specific short-range interactions into account, allowing the model to be used with much more concentrated solutions. Here we give only the general equations for calculating the logarithm of the activity coefficients for a cation M (γ_M), an anion X (γ_X), and a neutral species N (γ_N) in a complex aqueous mixture [156]:

$$\ln \gamma_M = \left\{ \begin{array}{l} z_M^2 F + \sum_a m_a (2B_{Ma} + ZC_{Ma}) + |z_M| \sum_c \sum_a m_c m_a C_{ca} \\ + \sum_c m_c (2\Phi_{Mc} + \sum_a m_a \psi_{Mca}) \\ + \sum_{a'} \sum_{a''} m_a m_{a'} \psi_{Maa'} \\ + 2 \sum_n m_n \lambda_{Mn} + 3 \sum_n m_n^2 \mu_{Mnn} \\ + 6 \sum_n \sum_{n'} m_n m_{n'} \mu_{Mnn'} \\ + 6 \sum_n \sum_a m_n m_a \zeta_{Mna} \\ + 6 \sum_n \sum_c m_n m_c \eta_{Mnc} \end{array} \right\} \quad (2.20)$$

$$\ln \gamma_X = \left\{ \begin{array}{l} z_X^2 F + \sum_c m_c (2B_{cX} + ZC_{cX}) + |z_X| \sum_c \sum_a m_c m_a C_{ca} \\ + \sum_a m_a (2\Phi_{Xa} + \sum_c m_c \psi_{cXa}) \\ + \sum_c \sum_{c'} m_c m_{c'} \psi_{cc'X} \\ + 2 \sum_n m_n \lambda_{Xn} + 3 \sum_n m_n^2 \mu_{Xnn} \\ + 6 \sum_n \sum_{n'} m_n m_{n'} \mu_{Xnn'} \\ + 6 \sum_n \sum_a m_n m_a \zeta_{ncX} \\ + 6 \sum_n \sum_c m_n m_c \eta_{Xna} \end{array} \right\} \quad (2.21)$$

$$\ln \gamma_N = \left\{ \begin{array}{l} 2 \sum_n m_n \lambda_{Nn} + 3 \sum_n m_n^2 \mu_{Nnn} \\ + 6 \sum_n m_n m_n \mu_{Nnn} \\ + 6 \sum_n \sum_{n'} m_n m_{n'} \mu_{Nnn'} \\ + 2 \sum_c m_c \lambda_{Nc} + 2 \sum_a m_a \lambda_{Na} + \sum_c \sum_a m_c m_a \zeta_{Nca} \\ + \sum_c \sum_{c'} m_c m_{c'} \eta_{Ncc'} \\ + \sum_a \sum_{a'} m_a m_{a'} \eta_{Naa'} \\ + 6 \sum_n \sum_c m_n m_c \mu_{Nnc} + 6 \sum_n \sum_a m_n m_a \mu_{Nna} \end{array} \right\} \quad (2.22)$$

where m_i is the molality of the species i ($i = a, c, n$). The subscripts a, c and n refer to anions, cations and neutral species, respectively. The summations are over the total number of cations or anions present in the complex aqueous mixture. The double summation denotes the sum over all distinguishable pairs of dissimilar anions, cations or neutral species. B and Φ are measurable combinations of the second virial coefficients. C and ψ are measurable combinations of the third virial coefficients. B and C are parameterized from single electrolyte data, while Φ and ψ are parameterized from mixed (ternary) system data. The function F in Eq. 2.20 and Eq. 2.21 is the sum of the Debye-Hückel term given by [157]:

$$F = \frac{f'(I)}{2} + \sum_{c=1}^{N_c} \sum_{a=1}^{N_a} m_c m_a B'_c \quad (2.23)$$

$$\text{with} \quad f'(I) = \left(\frac{\partial f}{\partial I} \right)_{\rho, T} = -2A^\varphi \left[\frac{\sqrt{I}}{1 + b\sqrt{I}} + \frac{2}{b} \ln(1 + b\sqrt{I}) \right] \quad (2.24)$$

where A^φ is the Debye-Hückel limiting law slope for osmotic coefficients. It is a function of the temperature, density and dielectric constant of water. b is a universal empirical constant equal to $1.2 \text{ kg}^{0.5} \cdot \text{mol}^{-0.5}$.

For any anion-cation interaction, Pitzer assumes that the term B in Eq. 2.20 has an ionic strength dependent form as:

$$B_{Ma} = \beta_{Ma}^{(0)} + \beta_{Ma}^{(1)} g(\alpha_1 \sqrt{I}) + \beta_{Ma}^{(2)} g(\alpha_2 \sqrt{I}) \quad (2.25)$$

with
$$g(x) = 2[1 - (1 + x)e^{-x}] \quad (2.26)$$

$$C_{ca} = \frac{C_{ca}^\Phi}{(2\sqrt{|z_c z_a|})} \quad (2.27)$$

Φ terms account for interactions between two ions i and j of like charges and is given by:

$$\Phi_{ij} = \theta_{ij} + {}^E\theta_{ij}(I) \quad (2.28)$$

where θ_{ij} is the only adjustable parameter. The term ${}^E\theta_{ij}(I)$ accounts for electrostatic unsymmetric mixing effects that depend only on the charges of ions i and j and the total ionic strength.

In Eq. 2.20 and Eq. 2.21, C_{Ma} and C_{cX} are the third virial coefficients and are assumed to be ionic strength independent. However, some terms containing C_{Ma} parameters have a concentration dependence given by Z as:

$$Z = \sum_i m_i |z_i| \quad (2.29)$$

❖ Activity of water

Water is the solvent of the aqueous solution and its activity a_w can be defined by applying Eq. 2.14 as:

$$\mu_{w(T,P,m_i)} = \mu_{w(T,P)}^0 + RT \ln a_{w(T,P,m_i)} \quad (2.30)$$

According to Hamer [158], the activity of water can be related to the osmotic coefficient by:

$$\Phi = -\frac{1000 \ln a_w}{M_w \sum_i v_i m_i} \quad (2.31)$$

where M_w is the molar mass of water (in $\text{g}\cdot\text{mol}^{-1}$), v_i is the number of ions formed by the complete dissociation of a molecule of solute i and it corresponds to $v_i = v_c + v_a$ for a compound whose formula is $M_{v_c}X_{v_a}$. M and X stand for cation and anion respectively.

❖ Thermodynamic equilibrium and saturation index

There are several types of reactions and they concern the equilibrium between aqueous species and minerals as well as the equilibrium between the aqueous species themselves. Fundamental to any description of equilibria in water is the law of mass action. It states that for a reaction of the generalized type:



the distribution at equilibrium of the species at the left and right side of the reaction, is given by [145]:

$$K(T, P) = \frac{\{C\}^c \{D\}^d}{\{A\}^a \{B\}^b} \quad (2.33)$$

where K is the equilibrium constant for the temperature T and the pressure P . a , b , c and d are the stoichiometric coefficients of the reaction. $\{ \}$ denote the activities of gaseous, solid, or aqueous species in solution, also known as the “effective concentration”. The activity of pure liquid or of solid phases is equal to 1. For a mixture of ideal gases, the activity correspond to the partial pressure P_i of a species i while in the case of real gases, the fugacity has to be considered instead of P_i [159]. The activity of ions or aqueous species is given in Eq. 2.15.

The equilibrium constant can be calculated through the Gibbs free energy following the equation:

$$\Delta G_r = \Delta G_r^0 + RT \ln \frac{(a_C)^c (a_D)^d}{(a_A)^a (a_B)^b} \quad (2.34)$$

where ΔG_r is the change in Gibbs free energy (in $\text{kJ}\cdot\text{mol}^{-1}$) of the reaction, ΔG_r^0 is the standard Gibbs free energy of the reaction. ΔG_r indicates the direction in which the reaction will proceed. In fact, if $\Delta G_r > 0$, the reaction proceeds to the left while the reaction proceeds to the right if $\Delta G_r < 0$. At equilibrium, $\Delta G_r = 0$.

$$\Delta G_r^0(T, P) = c\mu_C^0(T, P) + d\mu_D^0(T, P) - a\mu_A^0(T, P) - b\mu_B^0(T, P) \quad (2.35)$$

And the equilibrium constant $K(T, P)$ of the reaction is defined by:

$$\Delta G_r^0 = -RT \ln K \quad (2.36)$$

Back substitution of Eq. 2.36 in Eq. 2.34 results in:

$$\Delta G_r = -RT \ln K + RT \ln \frac{(a_C)^c (a_D)^d}{(a_A)^a (a_B)^b} \quad (2.37)$$

We can define the ionic activity product (IAP) or Q as:

$$IAP = Q = \frac{(a_C)^c (a_D)^d}{(a_A)^a (a_B)^b} \quad (2.38)$$

$$\Delta G_r = -RT \ln K + RT \ln Q \quad (2.39)$$

$$\Rightarrow \Delta G_r = RT \ln \frac{Q}{K}$$

The equilibrium of the reaction results in:

$$\frac{Q}{K} = 1 \quad (2.40)$$

For homogeneous reactions (i.e. aqueous complexation reactions), thermodynamic equilibrium is assumed to be achieved instantaneously. But it is not always the case for mineral dissolution/precipitation reactions. Therefore, the ratio Q/K is used to define the saturation index (SI) or the degree of saturation of the solution with respect to a mineral. Let's consider that, in reaction (2.32), A is a mineral and B, C and D are aqueous species.

$$SI = \log \left(\frac{Q}{K} \right) \quad (2.41)$$

The degree of saturation, sub-saturation or equilibrium state of a solution with respect to a mineral is only defined by comparing Q to K of the reference solution. It represents the energy difference between the current state and the thermodynamic equilibrium. Depending on its sign, it indicates the amount of energy to release or to capture for reaching thermodynamic equilibrium. Thus, SI makes it possible to define whether the thermodynamic conditions are favourable or not for mineral precipitation. Three scenarios are possible:

- $Q = K$: an equilibrium state is reached and the solution is saturated with respect to the mineral. $SI=0$.
- $Q < K$: the solution is under saturated with respect to the mineral concerned: $SI < 0$. The reaction tries to achieve equilibrium by dissolving all or part of A and consuming B to form species C and D.
- $Q > K$: the solution is super-saturated with respect to A. $SI > 0$. the assemblage $aA + bB$ is more stable than the solution $cC + dD$. The system tends to return to equilibrium by precipitating mineral A and producing species B.

In nature, groundwater is generally not found at the reference conditions of 25 °C and 1 atm pressure. While moderate variations in pressure have little effect on the values of the equilibrium constants of chemical reactions (except when gases are involved), the temperature variations have important effects [145]. For temperatures below about 100 °C, variations of equilibrium constants with temperature are usually calculated with the Van't Hoff equation:

$$\log K_T = \log K_{298} + \frac{\Delta H_r^0}{2.303 R} \left(\frac{1}{298} - \frac{1}{T} \right) \quad (2.42)$$

where ΔH_r^0 is the standard enthalpy of the reaction.

We have presented the basic equations for calculating the thermodynamic properties of electrolytic solutions. For numerical modelling, we have chosen to use the geochemistry software PHREEQC, which is an open source code and is widely used by the geoscience community. It has the advantage of having accessible and modifiable sources.

2.4.2 PHREEQC description and working principle

PHREEQC (pH-Redox-Equilibrium in C language) is a general geochemical solver applicable to many hydrogeochemical environments. It is now in its third version. Like the previous versions, PHREEQC V3 is a computer program written in the C and C++ programming languages. It is designed for simulating a wide variety of aqueous geochemical reactions and is able to simulate transport processes in simple 1D hydrodynamic systems. A complete description of PHREEQC V3 can be found in reference [147]. It is based on the equilibrium chemistry of aqueous solutions. PHREEQC implements several types of aqueous models including ion association approaches like the Debye-Hückel model and the Pitzer specific-ion-interaction model. The Peng-Robinson equation of state has been implemented for calculating the fugacity and, therefore, the solubility of gases at high pressure. PHREEQC has many capabilities, such as:

- Perform aqueous speciation calculations based on the conservation equations of matter, the laws of mass action and the principle of electroneutrality. Perform batch-reaction calculations including mixing of solutions at controlled temperature and pressure.
- Calculate the volume and the density of solutions, and saturation indices.
- Calculate 1D (one-dimensional) transport with reversible and irreversible reactions, which include equilibrium between aqueous, mineral or gas phases.

For its calculations, PHREEQC uses concentrations given in molality (mol.kg^{-1}). Calculations with PHREEQC require an input file (see Fig. B.1 of Appendix B for an example) in where two main informations must be entered, namely: the choice of the database used and the instructions that allow the desired reactions to be carried out. The PHREEQC program can use several databases. The latter each contain information on the thermodynamic properties of chemical species (such as equilibrium constants of chemical reactions, reaction enthalpies, molar volumes, etc.) and their dependence on temperature and pressure. Thus, in relation with its domain of validity (temperature, pressure, salinity, chemical system), the choice of the database depends on the complexity and on the objectives of the simulation. The instructions are represented by "key words" which make it possible to diversify the geochemical study. Within these keywords can be entered information such as the concentrations of the various elements of the chemical system

considered, the temperature, the pressure, the pH, the equilibria between the mineral phases when they are expected, etc. The output file contains several informations: the solution composition, the description of the solution (pH, ionic strength, density of a solution, electrical balance, pressure temperature, osmotic coefficient, etc.), the distribution of species (molality, activity, activity coefficients, etc.) and the saturation indices for the phase.

2.4.3 Diffusive transport modelling in PHREEQC

PHREEQC provides a numerically efficient method for simulating the movement of solutions through a column or 1D flow path with or without the effects of dispersion. The initial composition of the aqueous, gas, and solid phases within the column are specified and the changes in composition due to advection and dispersion and (or) diffusion [145] coupled with reversible and irreversible chemical reactions within the column can be modeled. For modeling a dual porosity medium, stagnant zones can be incorporated in the column. Multicomponent diffusion can be included in advective transport simulations or as a stand-alone diffusion process. In the multicomponent diffusion process, the diffusion coefficients can be coupled to porosity changes that may result from mineral dissolution and precipitation [147].

For the transport processes, the numerical scheme in PHREEQC is for cell-centered concentrations, which means that the composition at a half-cell distance represent the composition of the entire cell. As a result, if 1 is a first cell and 2 the cell that directly follows 1, h_{12} is the distance between the midpoints of cells 1 and 2.

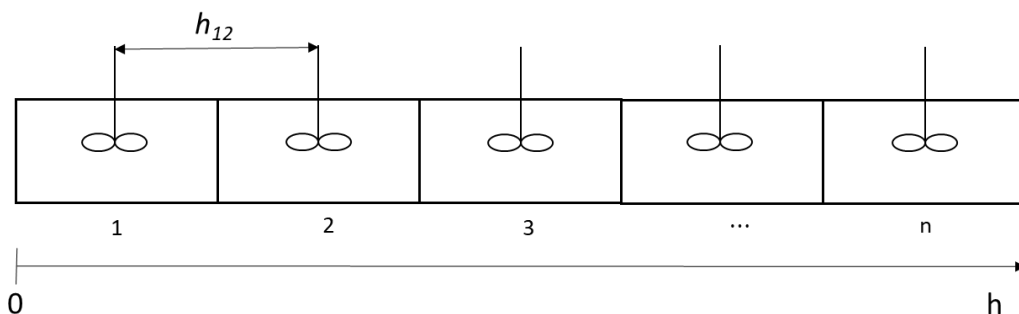


Figure 2.14: Column divided into cells showing a composition is taken at a half-cell distance.

When there is no advection, the transport algorithm can simulate a column or a 1D flow path diffusion. The diffusive reactive transport modelling here requires some important

input. After defining the mesh size and the time step associated with diffusion period, it is required to define the boundary conditions. They are defined for the first and last cell and three types of boundary conditions are allowed at either end of the column (indicated by x_{end}): [147]

- **Constant:** concentration is constant at one or both boundaries: $C(x_{end}, t) = C_0$, also known as first type or Dirichlet boundary condition. C_0 is the concentration outside the column (mol.kg^{-1}).
- **Closed:** Also known as second type or Neumann boundary condition, it means that there is no flux at one or both boundaries. The flow velocity v (m.s^{-1}) is equal to zero ($v = 0$) and $\frac{\partial C(x_{end}, t)}{\partial x} = 0$.
- **Flux:** flux boundary condition at one or both boundaries defined by $C(x_{end}, t) = C_0 + \frac{D_L}{v} \frac{\partial C(x_{end}, t)}{\partial x}$, where D_L is the dispersion coefficient ($\text{m}^2.\text{s}^{-1}$). It is also known as third type or Cauchy boundary condition.

In this study, the simulations are performed with closed boundary conditions. Regarding the diffusion process, the diffusive flux is calculated according to whether homogeneous multicomponent diffusion or heterogeneous multicomponent diffusion is considered:

- **Homogeneous multicomponent diffusion**

Homogeneous multicomponent diffusion is characterised by the fact that all the species involved in the mixture diffuse with a same diffusion coefficient. In this case, the diffusive flux J_i ($\text{mol.m}^{-2}.\text{s}^{-1}$) for a species i is given by:

$$\vec{J}_i = -D_p \times \vec{\nabla} C_i \quad (2.43)$$

where, D_p is the pore-water diffusion coefficient ($\text{m}^2.\text{s}^{-1}$) and $\text{grad}(C_i)$ is the concentration gradient of the species i (mol.m^{-4}). D_p is the same for all species and is not corrected for changes of temperature. D_p is related to the diffusion coefficient of a salt in water by $D_p = D/\tau$. The diffusion coefficient of a salt in water is given by the harmonic mean of the diffusion coefficient of the components of the salt, weighted by their molal concentration as follow:

$$D = \frac{\sum m_i}{\sum \frac{m_i}{D_i}} \quad (2.44)$$

where D_i are the diffusion coefficients of dissolved species i . It results, for a binary salt, the Nernst equation:

$$D = \frac{(Z_{i,+} - Z_{i,-})D_{i,+}D_{i,-}}{Z_{i,+}D_{i,+} - Z_{i,-}D_{i,-}} \quad (2.45)$$

For example, with $D_{Ca^{2+}} = 0.79 \times 10^{-9} \text{ m}^2.\text{s}^{-1}$ and $D_{Cl^-} = 2.03 \times 10^{-9} \text{ m}^2.\text{s}^{-1}$, the diffusion coefficient for CaCl_2 is $D_{CaCl_2} = 1.34 \times 10^{-9} \text{ m}^2.\text{s}^{-1}$ at 25°C . Thus, to maintain overall charge balance, diffusion of Ca^{2+} is accelerated, while Cl^- is impeded somewhat. For the other ionic species of interest, their diffusion coefficients at 25°C are $D_{Na^+} = 1.33 \times 10^{-9} \text{ m}^2.\text{s}^{-1}$ and $D_{SO_4^{2-}} = 1.07 \times 10^{-9} \text{ m}^2.\text{s}^{-1}$ [147].

- **Heterogeneous multicomponent diffusion**

Unlike the previous case, heterogeneous multicomponent diffusion is characterised by the fact that each solute can be given its own diffusion coefficient, allowing it to diffuse at its own rate, but with the constraint that overall charge balance is maintained [89], [106], [160]. A rigorous description of the diffusive motion of charged species requires the inclusion of electrochemical migration as a transport mechanism. In such electrolytic systems, charge-induced ion-ion interactions lead to electrostatic coupling of ionic flows, resulting in coordinated movement of positively and negatively charged species to maintain local charge balance [161]. The relevance of these Coulombic effects has been studied under conservative and reactive transport conditions dominated by macroscopic diffusion and advection, leading to the development of multicomponent diffusion theories [106]. The details of the multicomponent diffusion theories can be found elsewhere [89], [106], [160], [162], [163] so that here we just recall the essential equations. A general equation of ionic diffusion is generally based on the thermodynamic electrochemical potential gradients rather than the concentration gradients. The electrochemical potential of species i is presented in Eq. 2.14, but a general description includes the charge number z_i , the Faraday constant F (96485 J/V/eq) and the electrical potential φ (V) as:

$$\mu_i = \mu_i^0 + RT \ln a_i + z_i F \varphi \quad (2.46)$$

The diffusive flow J_i of a species i in solution as a result of chemical and electrical potential gradients is:

$$J_i = -\frac{u_i RT}{|z_i| F} C_i \nabla(\ln a_i) - \frac{u_i}{|z_i|} C_i z_i \nabla \varphi \quad (2.47)$$

Where u_i ($\text{m}^2 \cdot \text{s}^{-1} \cdot \text{V}^{-1}$) is the mobility which is related to the diffusion coefficient D_i ($\text{m}^2 \cdot \text{s}^{-1}$) of species i by $D_i = \frac{u_i RT}{|z_i| F}$. The gradient of the electrical potential originates from different transport velocities of ions, which creates charge and an associated potential. Eq. 2.47 represents the Nernst-Planck equation for the flow of a charged species and after considering the activity gradient, this equation can also be expressed as:

$$J_i = -D_i \left(1 + \frac{\partial \ln \gamma_i}{\partial \ln C_i} \right) \nabla C_i - \frac{D_i z_i C_i F}{RT} \nabla \varphi \quad (2.48)$$

If there is no electrical current, then $\sum_{i=1}^N z_i J_i = \vec{0}$. Thus $\nabla \varphi$ can be eliminated as an unknown by expressing this gradient term as:

$$\nabla \varphi = -\frac{\sum_{i=1}^N \left[z_i D_i \left(1 + \frac{\partial \ln \gamma_i}{\partial \ln C_i} \right) \nabla C_i \right]}{\frac{F}{RT} \sum_{i=1}^N (z_i^2 D_i C_i)} \quad (2.49)$$

By substituting Eq. 2.49 to Eq. 2.48, the diffusive flow becomes:

$$J_i = -D_i \left(1 + \frac{\partial \ln \gamma_i}{\partial \ln C_i} \right) \nabla C_i + \frac{D_i z_i C_i}{\sum_{j=1}^N (z_j^2 D_j C_j)} \sum_{j=1}^N \left[z_j D_j \left(1 + \frac{\partial \ln \gamma_j}{\partial \ln C_j} \right) \nabla C_j \right] \quad (2.50)$$

where the subscript j is introduced for species to show that they stem from the potential term. Eq. 2.50 clearly demonstrates that the movement of a particular charged species is a function of concentration gradients, diffusion coefficients, activity coefficients, and charge numbers not only of that ion but also of all other charged species in solution [106].

In PHREEQC program, the diffusive flux J_i for a species i for multicomponent diffusion is calculated by: [147]

$$J_i = -D_i \left(\frac{\partial \ln \gamma_i}{\partial \ln C_i} + 1 \right) \text{grad}(C_i) + CBt_i \quad (2.51)$$

where CBt_i is the charge balance term [89]. This term is given in detail in the second term on the right-hand side of Eq. 2.50. D_i is corrected to temperature $T(K)$ of the solutions by:

$$D_i = (D_i)_{298} \times \frac{T}{298} \times \frac{\eta_{298}}{\eta_T} \quad (2.52)$$

Where η is the viscosity of water.

2.5 Conclusion

In this chapter, we have presented the various experimental methods used for the measurement of mass diffusion coefficients of salts in water. Interferometric methods are considered the most precise for measuring diffusion coefficients in liquids. All the previous techniques mentioned above have led to reliable results with uncertainties and accuracies that vary depending on the method used. Each of these techniques has both advantages and disadvantages. However, from a general point of view, precautions should be taken to avoid or minimize the impact of test-beam deflection that could disturb the measurement. One way to overcome test beam deflection is to illuminate the whole system parallel to the concentration gradient as shown in Fig. 2.15.

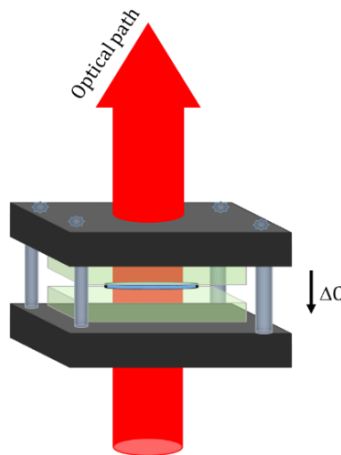


Figure 2.15: Diffusion cell illuminated by a light beam parallel to the concentration gradient.

In this configuration, density fluctuations in the horizontal plane at the interface between the solutions of contrasted concentrations cause light scattering and one can record the intensity fluctuations generated by the interference between the light transmitted through the transparent sample and the scattered light by the tiny fluctuations. This is the physical principle underlying the shadowgraph technique. The fluctuations that are recorded in this way are mostly due to non-equilibrium concentration fluctuations as they are much more (orders of magnitude) intense than equilibrium concentration or temperature fluctuations, present at the same time during a diffusion experiment. In the near field, i.e. not so far from the experimental cell, the superimposition (interference) between the light transmitted (nor deflected neither absorbed) by the system and the light scattered by the non-equilibrium density fluctuations gives rise to a dynamic intensity pattern on a detector plane. In this condition, one can visualise the density fluctuations within the sample and the optical method is called shadowgraphy. The statistical analysis of the latter can provide both the static power spectrum and the time correlation function of the fluctuations. The shadowgraph technique has also been successfully used to visualize from above convection structures parallel to an external vertical temperature gradient [164], but also to study the thermodiffusion phenomenon in binary and ternary mixtures [165]–[170]. Within the framework of this thesis, we propose to measure non-equilibrium fluctuations by shadowgraphy in order to study free diffusion and diffusive reactive transport in saline aqueous solutions. To the best of our knowledge, this has never been done before for measuring mass diffusion coefficients, while free diffusion was previously studied on molecular and colloidal solutions by shadowgraphy to highlight the effect of gravity on concentration non-equilibrium fluctuations (c-NEFs) [171]–[173].

For the interpretation of the experimental results, we propose to use the PHREEQC modelling tool, which is based on the fundamentals of thermodynamics of solutions and provides a numerically efficient method for simulating the movement of solutions through a column or 1D flow path with or without advective flow. When there is no advective flow, only diffusion occurs. Within PHREEQC program, the diffusive flux can be calculated in two different approaches: i) the homogeneous multicomponent diffusion that is characterised by the fact that all the species involved in the mixture diffuse with the same diffusion coefficient. The latter is given by the harmonic mean of the diffusion coefficients of the salt components, weighted by their molar concentration. However, the

diffusion coefficient in this case is not corrected for temperature changes. Thus, when having a temperature gradient, the diffusive behaviour of the system would be very little impacted. Furthermore, the calculation of the diffusive flux of a given specie is only function of the concentration gradient of the species and does not take into account the electrostatic coupling of ionic fluxes. In the case of a single salt in solution or a complex multicomponent system at infinite dilution, the interactions between the charged species may be negligible and this type of modeling can give satisfactory results. However, in the case of a highly concentrated complex multicomponent system, the calculated flux as it stands has limitations. ii) The second approach of calculating the diffusion flux is heterogeneous multicomponent diffusion where the species have individual, temperature-dependent diffusion coefficients, but the ionic fluxes are modified to maintain charge balance during transport. It rigorously describes the diffusive motion of charged species including the electrochemical migration as a transport mechanism. Usually, multicomponent heterogeneous diffusion is considered mainly in porous media than in free media. However, in a complex multicomponent system where we have different layers of electrolytes, it cannot be excluded that heterogeneous multicomponent diffusion can have a significant impact. In this study, we propose to compare these two descriptions of multicomponent diffusion.

The next chapter describes the Shadowgraphy technique and the diffusion cell we have developed to perform the measurement of the diffusion coefficients of salts in water and to study the reactive diffusive transport, as well as the interpretation of the experimental results with the PHREEQC program.

Chapter 3 : Contribution to the study of the multicomponent salts diffusion in water

3.1 Introduction

This chapter describes the Shadowgraphy technique and the diffusion cell we developed to carry out isothermal and non-isothermal diffusion coefficients of salts measurements. Our technique is applied to study: first, the behaviour of each saline solution in water by measuring their Fickian diffusion coefficients. Secondly, the superimposition of two non-reactive salts and finally the superimposition of two reactive salts with and without temperature gradient. The numerical interpretation of the experimental results is performed with PHREEQC program. Complex fluids subjected to non-equilibrium conditions exhibit non-equilibrium fluctuations (NEFs) of the thermodynamic variables [174]–[176]. These conditions can be induced, for example, by applying a concentration or a temperature gradient to a multicomponent fluid mixture [177]. Superimposing two layers at different concentrations of a solution generates an initial gradient of concentration which evolves towards an equilibrium state by mass diffusion, in the absence of convective motions [171]. Free-diffusion transport processes can be investigated by optical techniques and particularly by light scattering thanks to its ability to visualize NEFs without altering the intrinsic properties of the fluid. The transport properties of the fluid can be determined both at atmospheric [165] and at high pressure [169]. In this work, dynamic shadowgraphy has been adopted [171], [178], [179] to study the refractive index fluctuations as generated by the NEFs of the concentration in the case of free-diffusion experiments. It is important to highlight the novelty of using this methodology to determine the transport properties of fluid mixtures in free-diffusion experiments. By shadowgraphy, a large range of fluctuation sizes λ or, conversely, of wave numbers $q = 2\pi/\lambda$, can be investigated at the same time, providing simultaneous reliable measurements of different transport properties, like mass diffusion coefficient.

3.2 Experimental procedure

In this section, we have used two experimental setups that operate on exactly the same principle but differ in the use of the camera sensor. In the shadowgraph setup#1 we use a scientific-CMOS camera (Hamamatsu Digital Camera C13440, ORCA - Flash 4.0) as a

camera sensor. In the shadowgraph setup #2, the camera sensor is the CCD progressive PIKE camera (Allied Vision Technologies, PIKE-F421B). All the experiments with the shadowgraph setup#2 were carried out by Rizwan Minhas during his Master's internship [180]. A more in-depth analysis of its results is presented in this manuscript.

3.2.1 Solutions preparation and characterisation

Mass diffusion coefficients of the molecular binary mixture of triethylene glycol (TEG) and water, at different concentrations and temperature, are already known in the literature [109], [181]. We used this mixture in order to calibrate the experimental setup and the data analysis. Moreover, we collaborated in a study on the TEG/water/ethanol mixture by different experimental techniques [109], our contribution being the determination of the transport properties of the TEG/water at binary boundary limit of the concentration Gibbs ternary triangle by quantitative dynamic shadowgraphy [182]. The published and the submitted articles, respectively named as Paper #1 and Paper #2 can be found in appendix E.

TEG (Sigma-Aldrich, T59455-1L, ReagentPlus®, purity 99%) used without further purification, and degassed de-ionized water (resistivity 18.5 M Ω -cm), retrieved from a Millipore Milli-Q filtration station, were used to prepare around 30 g of every calibrating sample to the required TEG concentration C in mass fraction, using an analytical balance (Sartorius TE313S, resolution 10⁻² g/200 g).

Mass diffusion of the electrolytic binary mixtures of sodium chloride (NaCl) and water, calcium chloride (CaCl₂) and sodium sulfate and water (Na₂SO₄) are well documented in the literature [113], [138]. NaCl (Sigma-Aldrich, 746398-500G, anhydrous, ACS reagent, purity 99%), CaCl₂·2H₂O (PROLABO, 22 313.294, purity 99%), Na₂SO₄ (Sigma-Aldrich, 239313-500G, anhydrous, ACS reagent, purity 99%) were used without further purification. Degassed de-ionized water was used to prepare a volume of 100 ml of every saline solution to the required concentration C in mol.L⁻¹. Using the same balance, the mass of salts required to prepare the solutions in a 100 ml volumetric flask was weighed.

3.2.2 Free-diffusion cell

For the free-diffusion experiments, we used a diffusion cell specifically designed to put into contact two layers of two different liquid mixtures, or two solutions of the same

components at different concentrations. Such a configuration allows creating an initial step concentration gradient at uniform temperature while providing vertical optical access to a central area of the cell, similar to the flowing-junction cell already reported in literature [183]. The diffusion cell consists of a stainless steel annulus (see Fig. 3.1) with internal and external diameters of 30 mm and 80 mm, respectively, and a vertical thickness of $h = 10$ mm. The metallic annulus hosts four holes: two for fluids outlets at 180° in the horizontal plane and at mid-height of the cell in the vertical direction, and two for fluid inlet at 50° in the horizontal plane and at the same height in the vertical direction. In order to avoid the thermal contact between the liquid sample and the interior of the conductive metallic annulus, a polytetrafluoroethylene (Teflon®) ring with an internal and external diameter of 20 mm and 30 mm, respectively, is placed inside the stainless steel annulus (see Fig. 3.1-a). This ring has also four thin holes in correspondence to those present in the metallic annulus to allow the circulation of the fluids. Moreover, the two holes for the fluid inlets are inclined in the vertical direction so that one incoming fluid is steered to the top of the cell, while the other one is steered to the bottom of the cell.

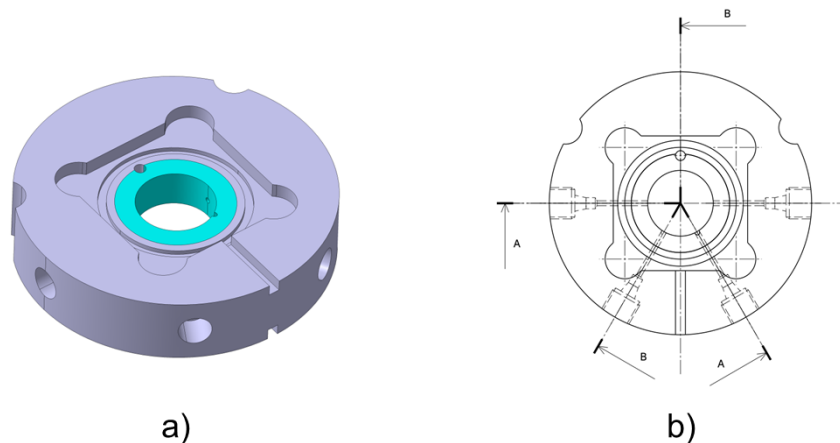


Figure 3.1: a) 3D-drawing of the stainless steel annulus with the Teflon ring in the inner part. b) 2D-drawing of the same, as observed from the top.

The stainless steel annulus is designed to accommodate two square sapphire windows ($8 \times 40 \times 40$ mm³), one on each vertical side with a groove for a Viton® O-ring for sealing. The internal faces of the two sapphire windows are then separated by the metal annulus and kept apart by $h = 10$ mm, thus defining the vertical thickness of the fluid sample. The external surfaces of the two sapphire windows are in contact with two square aluminium plates with a central circular aperture with a diameter $d = 13$ mm. These plates are meant for hosting two temperature sensors so to measure the temperature as close as possible

to the sapphires. The aluminium plates are also in contact with two square Peltier elements (Kryotherm, TB-109-1.4-1.5 CH) which can transport heat by means of a current flow and have the same central circular aperture. The Peltier elements provide/remove the heat necessary to maintain the set-point temperature as driven by two temperature controllers (Wavelength Electronics, LFI-3751) which use a proportional-integrating-derivative feedback system and maintain the temperature of the internal side of each Peltier device constant, with stability better than 1 mK RMS over 1 day. As shown in Fig. 3.2, all these elements are clamped by means of two aluminium blocks (with the same central circular aperture) in which water coming from a thermostatic controlled bath (Huber, ministat 125), circulates in order to remove the Peltier elements excess heat.

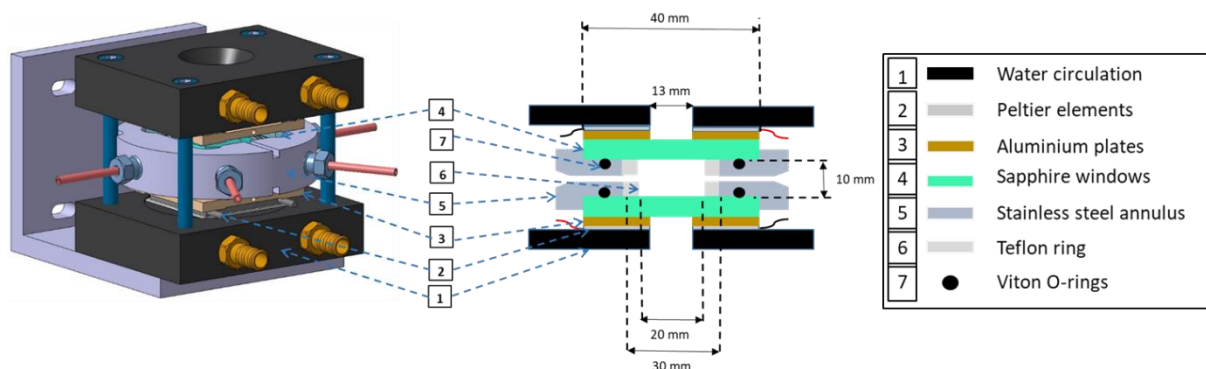


Figure 3.2: 3D drawing of the diffusion cell

External to the stainless steel ring, metallic capillary tubes with external diameter of 1/8 inch and about 50 mm of length (the red stems visible in Fig. 3.2) are connected to each inlet/outlet. These capillary tubes end with a manual valve each (Swagelok, SS-41GS2), as shown in Fig. 3.3. The sample reservoirs are connected to the valves via flexible capillary tube (same external diameter as the metallic capillary tubes).

The cell filling is performed in two main steps. In the first step, the diffusion cell is completely filled with the less dense fluid. In order to do that, the fluid is slowly injected by gravity through the lower part, while air is let out of the outlet pointing to the top. By slightly tilting the cell, the residual air can be completely removed. Attention is paid to avoid any further air inlet while filling the other three capillary tubes. The second step consists in filling the bottom half of the cell with the denser fluid and create a sharp interface between the two fluids. This is achieved by filling the cell simultaneously with the two fluids from the bottom and the top inlets, while the remixed fluid is let out through the two outlets. The two connectors for fluids outlet are connected to two syringes (100

mL), each well attached to a syringe pumps. We use the Fusion 4000 independent dual-channel infusion and withdrawal syringe pump from Chemyx. It can hold syringes from 0.5 mL to 100 mL and can deliver a flow rate from 1×10^{-7} to $170.5 \text{ mL}\cdot\text{min}^{-1}$ in either infuse or withdraw mode. Once half of the cell is filled with the denser fluid (the volume of fluid to be injected into the cell to fill it by half, taking into account the length and the internal diameter of capillary tubes and the dead volumes is calculated beforehand), a relatively flat horizontal interface between the two fluids is formed. The four valves are simultaneously closed and the free-diffusion process starts.

3.2.3 Shadowgraph setups

The shadowgraph optical setups (Fig. 3.3) involves a super luminescent diode (Super Lumen, SLD MS-261-MP2-SM, $\lambda = 675 \pm 13 \text{ nm}$), connected to a single-mode optical fiber. The divergent beam at the output of the fiber is collimated by an achromatic doublet lens (focal length $f = 150 \text{ mm}$, and diameter $\phi = 50.8 \text{ mm}$). The collimated beam passes through the free-diffusion cell, via two linear polarizers that allow adjusting the average transmitted light intensity, and is supposed to be perpendicular to the interface between the two solutions, or parallel to the temperature gradient when applying a thermal gradient. A camera collects the sum of the light scattered by the NEFs plus the transmitted one.

For the shadowgraph setup#1, the detection plane is positioned at a distance of $z = (12.0 \pm 0.5) \text{ cm}$ from the sample central plane. As a camera sensor, we use a scientific-CMOS camera (see section 3.2) whose detector size is $s = 13.3 \text{ mm}$. This camera sensor allows a fast image acquisition frequency, up to 100 Hz at full frame resolution of 2048×2048 square pixels with a pixel side of $l_{pix} = 6.5 \text{ }\mu\text{m}$. Images are acquired in real time by the HCLive (x64) software program installed in a dedicated PC. In order to have both a good stability of acquisition frequency and a quick backup of the images, we use 4 Solid-State Drive (SSD) hard disks in RAID0 configuration.

For the shadowgraph setup#2, the detection plane is positioned at a distance of $z = (10.0 \pm 0.5) \text{ cm}$ from the sample central plane. As a camera sensor, we use a CCD PIKE camera (see section 3.2). The camera attributes were adjusted with 'National Instruments and Measurements' software. This camera allows acquiring a series of raw images spaced at a constant time step by means of in-house

'Lab View' software. This camera is capable of speeds of up to 15 frames per second at full frame resolution of 2048×2048 square pixels with a pixel side of $l_{pix} = 7.4 \mu\text{m}$.

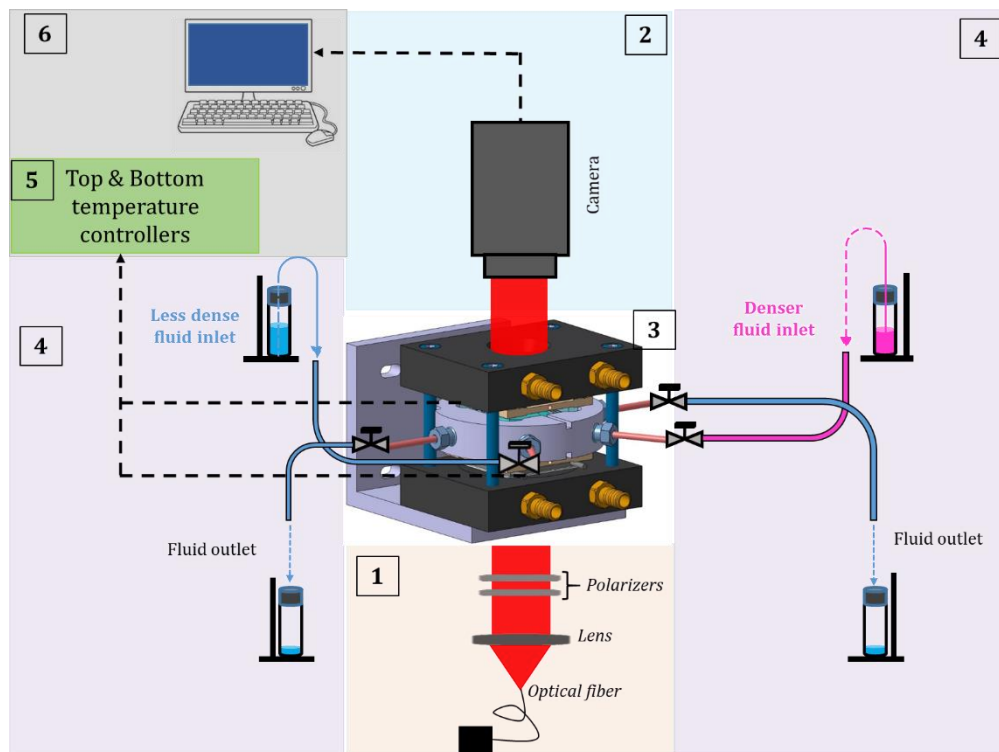


Figure 3.3: Shadowgraph optical setup summarized in six distinct blocks: 1) optical components; 2) Camera; 3) free-diffusion cell; 4) specific filling procedure; 5) temperature controllers; 6) computer equipment.

The analysis of images are described in the forthcoming section, where the analysis of wave vectors are performed in a Fourier space and the range of these accessible wave vectors depends on the number and size of the pixels. The optical path is isolated from air currents by means of rigid tubing. The various optical elements and the diffusion cell are mounted on an optical rail. The entire setup is fixed on an optical table with vibration isolation through air cushion. Both cameras collect the interference between the scattered light and the transmitted one (much more intense) [168], [169]. The image acquisition starts immediately at the end of the cell filling, a few seconds/minutes after closing the valves.

3.2.4 Dynamic near field imaging

The images acquired in the near field consist of an intensity map $I(\vec{x}, t)$, generated by the interference on the camera plane between the portion of the incident beam that has passed undisturbed through the sample and the beams scattered by the refractive index

fluctuations occurring within the sample. Here, \vec{x} and t stand for the position in the image plane and the time lapsed during the acquisition, respectively. Thanks to the interference of different beams, the fluctuations in the fluid density, that are proportional to the fluctuations of the fluid refractive index, are transformed into fluctuations of the light intensity at the detector plane. Therefore, in order to study the dynamics of the density fluctuations in our samples, we calculate the Structure Function (SF) of the light intensity, i.e. of the acquired images, by means of an already proven Differential Dynamic Algorithm (DDA) [184].

The DDA algorithm consists of the following main steps: first, each recorded image $I(\vec{x}, t)$ is normalised by its intensity average $\langle I(\vec{x}, t) \rangle_{\vec{x}}$, in order to remove the source intensity fluctuations and get the normalized image $i(\vec{x}, t) = I(\vec{x}, t) / \langle I(\vec{x}, t) \rangle_{\vec{x}}$ (Fig. 3.4-a). Then, the differences between normalized images at a given time difference Δt (called correlation time) $\Delta i(\vec{x}, t, \Delta t) = i(\vec{x}, t) - i(\vec{x}, t + \Delta t)$ are calculated (Fig. 3.4-b). These Δt 's are, of course, multiples of the time delay dt_{\min} of the recording process, and cannot be larger than the acquisition duration. Next, 2D-Fast Fourier Transforms (FFTs) of the image differences are calculated $\Delta i(\vec{q}, t, \Delta t) = \mathcal{F}(\Delta i(\vec{x}, t, \Delta t))$ and their square moduli $|\Delta i(\vec{q}, t, \Delta t)|^2 = |i(\vec{q}, t) - i(\vec{q}, t + \Delta t)|^2$ are determined (Fig. 3.4-c). Finally, the individual spatial Fourier transforms of the image differences are averaged, first over all times t and second over the modulus of the wave vector \vec{q} over the azimuthal angle. The result $\langle |\Delta i(q, \Delta t)|^2 \rangle$ is the structure function (SF) of the recorded intensity fluctuations. In order to reduce the computational time to calculate the SF out of the image series, we make use of a graphic card with the advantage of the massive parallelization on the Graphic Processing Unit (GPU) and an in-house developed software [184], [185]. This experimental quantity requires a physical model for its interpretation. The details of the theoretical model can be found elsewhere [174], [175]. In the present manuscript, we just recall the essential equations used to fit the SF.

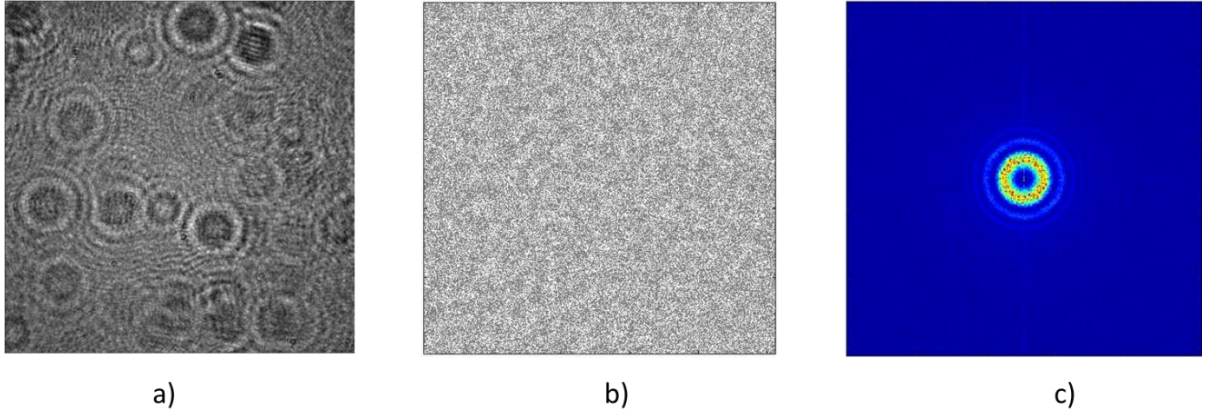


Figure 3.4: Main steps in the evaluation of the SF of the NEFs in a free diffusion experiment of NaCl into water (mean concentration $C_{\text{mean}}=2.7 \text{ mol.L}^{-1}$ and concentration difference between the two superimposed solutions of $\Delta C=2 \text{ mol.L}^{-1}$).

- a) Near field $1024 \times 1024 \text{ pix}^2$ recorded image $I(\vec{x}, t)$.**
b) Difference between two images $\Delta i(\vec{x}, t, \Delta t) = i(\vec{x}, t) - i(\vec{x}, t + \Delta t)$ separated by a correlation time of $\Delta t = 2 \text{ s}$.
c) 2D Fast Fourier transform of image differences $|\Delta i(\vec{q}, t, \Delta t)|^2 = |i(\vec{q}, t) - i(\vec{q}, t + \Delta t)|^2$ averaged over 200 pairs of images each separated by $\Delta t = 2 \text{ s}$.

The circular stains visible on Fig. 3.4-a are due to dust particles located on the optical components within the beam path, or on the protective glass of the camera sensor. Because these external disturbances do not move in time, the differential analysis method is not disturbed. The circular symmetry of the SF on Fig. 3.4-c is due to the isotropic character of the fluctuations.

3.2.5 Structure function analysis

The SF can be related to the power spectrum density fluctuation and the characteristics of the optical system as follows :

$$\langle |\Delta i(q, \Delta t)|^2 \rangle = 2\{T(q)S(q)[1 - ISF(q, \Delta t)] + B(q, \Delta t)\} \quad (3.1)$$

where $T(q)$ is the optical transfer function of the shadowgraph, $S(q)$ the static power spectrum of the fluctuations, the product $A(q) = T(q)S(q)$ is called the static structure factor (independent of the correlation time) and $B(q, \Delta t)$ is the signal background. It includes different contributions like electronic noise due to the camera and all the acquisition chain, and can be modelled by $B(q, \Delta t) = C(q) + E(q) \cdot \Delta t + F(q) \cdot \Delta t^2$. The parabolic term $F(q) \cdot \Delta t^2$ becomes particularly important for the experiments performed in the free-diffusion configuration, where the system is never at the steady state, so that

the background noise becomes time-dependent. The Intermediate Scattering Function $ISF(q, \Delta t)$ corresponds to the dynamic part of the SF, that can be described in many cases as the sum of exponential decays [186]–[188]: $ISF(q, \Delta t) = \sum_i a_i \exp(-\Delta t/\tau_i(q))$, where a_i are the amplitudes of the different modes with $\sum_i a_i = 1$ and $\tau_i(q)$ the wave-number-dependent relaxation times.

During a free-diffusion experiment, the density fluctuations recorded through the shadowgraph are mostly due to concentration-NEFs (c-NEFs) that are much more intense (orders of magnitude) than equilibrium temperature and/or concentration fluctuations present at the same time for the wave number range of our interest. Thus, the ISF is expected to be well described by a single exponential decay for all wave numbers. Thus, the SF is supposed to take the following form:

$$\langle |\Delta i(q, \Delta t)|^2 \rangle = 2 \left\{ A(q) \left[1 - \exp\left(-\frac{\Delta t}{\tau_c(q)}\right) \right] + C(q) + E(q) \cdot \Delta t + F(q) \cdot \Delta t^2 \right\} \quad (3.2)$$

where $\tau_c(q)$ is the decay time of the c-NEFs at wave number q . $A(q)$, $\tau_c(q)$, $C(q)$, $E(q)$ and $F(q)$ are the fitting parameters at each wave number. We use MatLab and an implemented Levenberg-Marquand non-linear least-square fitting routine [189]. At the end of the fitting, we proceed to the analysis of the statics of the fluctuations through the static structure factor $A(q)$, as well as to the analysis of the dynamics of the fluctuations through the decay times $\tau_c(q)$. Below, we will focus on the dynamics of the fluctuations.

3.2.6 Dynamics of the non-equilibrium fluctuations

The details of the theoretical description of the hydrodynamic behaviour of density fluctuations out-of-equilibrium can be found elsewhere [174], [175], so that here we just recall the main expressions useful for the experimental data analysis.

At intermediate and large wave numbers, in the absence of any convective motion, in the presence of the gravity force and in the bulk fluid, the decay time of the c-NEFs is given by:

$$\tau_c(q) = \frac{1}{Dq^2 \left[1 + \left(\frac{q_c}{q}\right)^4 \right]} \quad (3.3)$$

where D is the mass diffusion coefficient and q_c the cut-off wave number which defines the length scale below which the dynamics of the c-NEFs are no longer dominated by diffusion, but rather by buoyancy. The curve of the decay times as a function of wave numbers looks like a bell-shape (in log-log scale) and mirrors the presence of two distinct regimes as already reported in a number of previous publications [165], [171], [172]. The asymptotic behaviour of Eq. 3.3 for wave numbers larger than q_c is $\tau_c(q) = 1/Dq^2$ so that the diffusion coefficient D can be obtained from the fitting of the experimental data points in this region.

During a free-diffusion experiment, the concentration difference between the bottom and the top of the cell is assumed to remain constant until the diffusive process reaches the cell boundaries at the diffusive time $\tau_d = (h/2)^2/\pi D$. For times smaller than τ_d the cut-off wave number is given by the expression [171]–[173]:

$$q_c = \left(\frac{\beta g (C_1 - C_2)}{\nu D \sqrt{4\pi D t}} \right)^{1/4} \quad (3.4)$$

where β is the mass expansion coefficient of the binary mixture, g the gravitational acceleration, and ν the kinematic viscosity of the binary mixture at the mean temperature of the experiment. C_1 and C_2 are the concentrations of the denser and lower component, at the bottom and top layers in the diffusion cell, respectively. The cut-off wave number is time-dependent, following a power law with a $(-1/8 = -0.125)$ exponent.

3.2.7 Images contrast calculation

The appearance of diffraction spots on the shadowgraph images, related to the presence of dust, or convective patterns in particular experimental conditions produces significant variations in the contrasts of the images. This leads to significant variations and strongly quadratic dependencies with respect to time in the calculation of the SF and which prevents an analysis of it. Calculating the contrast of the difference in images is an effective way to remove the contribution of the transmitted beam and reveal the intensity fluctuations. It also deletes the dust contribution and in many cases it has allowed the study the convection [164]. The image contrast is defined as $C(t) = \langle |i(t) - i(t_0)| \rangle_{\vec{x}}$ where $\langle \dots \rangle_{\vec{x}}$ represents the average over the pixels of an image, $i(t) = I(t)/\langle I(t) \rangle_{\vec{x}}$ is an

image normalized by its spatial average, and $i(t_0)$ is a normalized background image, chosen in this work as the first image for each image sequence.

3.3 Free diffusion experiments

3.3.1 Calibration

For the concentration $C = 50\%$ in mass fraction (0.5 w/w) and $C = 0.7$ w/w of TEG in water, free diffusion experiments were performed at the temperatures of 20, 25 and 30 °C. The diffusion cell is first filled with the less dense solution and subsequently, the less dense and the denser solution fills about half of the cell. The valves are closed and the free-diffusion process starts. Series of $N = 2500$ images of 1024×1024 pix² were recorded at frequency rate of $f = 10$ Hz, every 5 minutes over the first 20 minutes of each experiment, and then every 10 minutes. Shadowgraph setup #1, with the s-CMOS camera, was used for this series of measurements (see section 3.2.3). The minimum accessible wave number is given by $q_{min} = 2\pi/L$, L being the side of the image in the real space defined as $L = N_{pix}l_{pix}$. The pixel side of this camera is $l_{pix} = 6.5 \mu\text{m}$. For the acquired images, $L = 0.67$ cm, so that $q_{min} = 9.44 \text{ cm}^{-1}$. The theoretical maximum frequency is $q_{max} = (N_{pix}/2) \cdot q_{min} = 4833 \text{ cm}^{-1}$, N_{pix} being the number of the pixels along one side of the images. In the case of the isothermal diffusion experiment, only one mode is expected to be measured corresponding to the relaxation of c-NEFs in the fluid mixture. The SFs were calculated by the DDA algorithm, as shown in Fig. 3.5 for the average concentration of $C = 0.5$ w/w, a difference of concentration of $\Delta C = 0.2$ w/w between the two superimposed fluid layers, a homogeneous temperature of 25 °C, and 80 minutes after closing the valves.

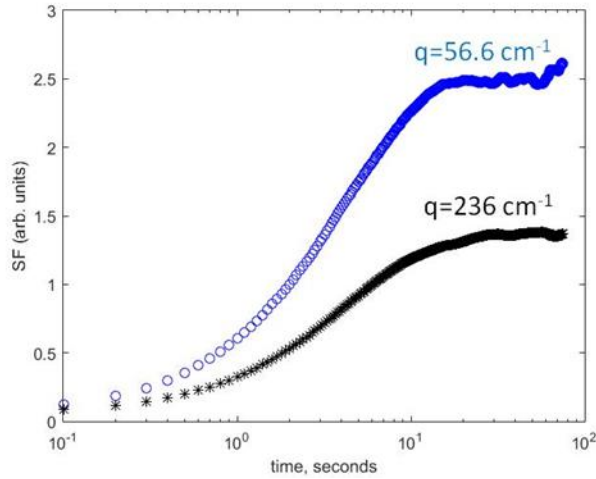


Figure 3.5: Structure function for different wave numbers of the free-diffusion experiment carried out with the binary mixture of TEG/water at the mean concentration of $C = 0.5$ w/w, difference of concentration $\Delta C = 0.2$ w/w between the bottom and top layer solutions, mean temperature of 25°C and 80 minutes after closing the valves.

The SFs show a single exponential decay, as expected, so that data points can be fitted through Eq. 3.2 for the entire range of wave numbers. The resulting values for the parameter $F(q)$ turned out to be negligible and for $E(q)$ one order of magnitude smaller than $C(q)$. In this case, the quantity $A(q)/C(q)$ can be calculated and provides a useful indication of the signal-to-noise ratio of the measurement. In Fig. 3.6 the signal-to-noise ratio is shown for the sample with $C = 0.5$ w/w and the homogeneous temperature $T=25$ °C for images taken 80 minutes after closing the inlet/outlet valves. The data are plotted for three different values of the concentration difference $\Delta C = 0.1, 0.2$ and 0.4 w/w.

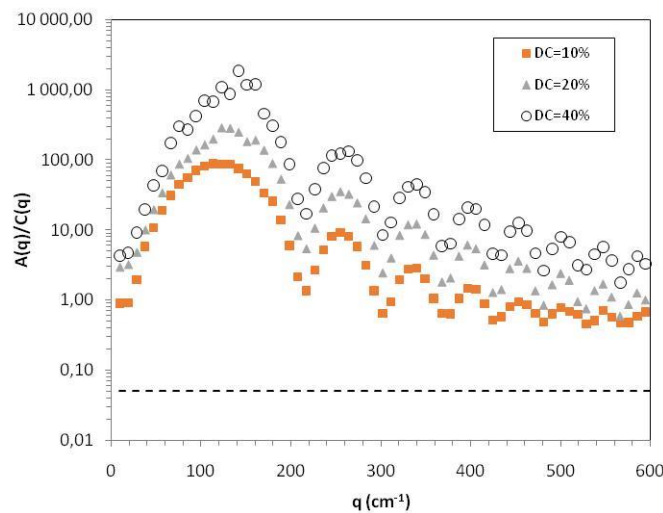


Figure 3.6: Ratio between the static structure factor and the signal background as a function of the wave number for the free-diffusion experiments, carried out with the binary mixture of TEG/water

at mean concentration of $C = 0.5$ w/w, and for different differences of concentration between the bottom and the top layers, at 25 °C and 80 minutes after closing the valves.

The oscillations visible in the graph are related to the shadowgraph transfer function $T(q)$ that vanishes at specific wave number. As visible from Fig. 3.6 the signal also increases with increasing concentration difference and distance for ΔC between 0.1 and 0.2 w/w. However, it is approximately the same in a log-log graph whatever the distance for ΔC between 0.2 and 0.4 w/w, which is coherent with a quadratic dependence of the signal to the concentration difference. The horizontal line visible in Fig. 3.6 stands for the threshold value of 0.05 below which we consider that a shadowgraph measurement cannot provide reliable results [190], [191]. We decided to perform the fitting in the wave number range from 30 to 600 cm^{-1} , thus spanning more than one decade in wave numbers. In Fig. 3.7 we report the decay times obtained from fitting the SFs as a function of the wave number q and for different times after closing the inlet/outlet valves. The graph corresponds to the sample with $C = 0.5$ w/w, $\Delta C = 0.2$ w/w and $T = 25$ °C. As stated before, only one mode can be detected corresponding to the decay of c-NEFs. By fitting the decay times through Eq. 3.3 we can obtain a measurement of the roll off wave number q_c and the mass diffusion coefficient D .

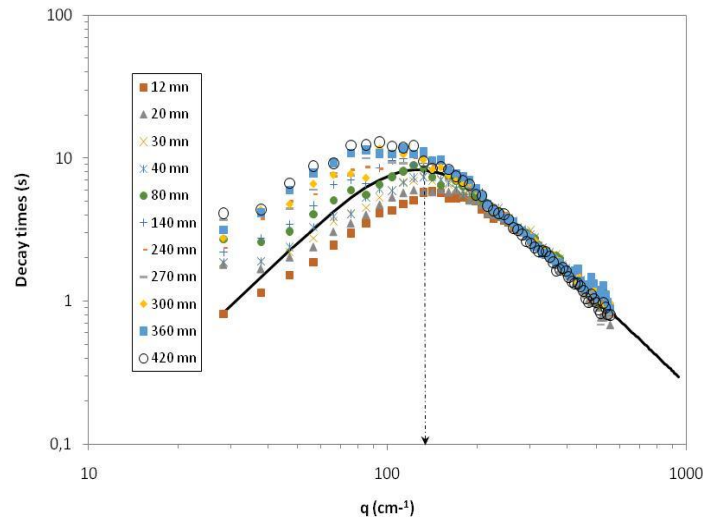


Figure 3.7: Decay times of the c-NEFs as a function of the wave numbers and time after closing the inlet/outlet valves for the free-diffusion experiment carried out with the binary mixture of TEG/water at $C = 0.5$ w/w, difference of concentration $\Delta C = 0.2$ w/w and $T = 25$ °C. The continuous black line corresponds to the curve obtained fitting Eq. 3.3 to data points obtained 80 minutes after starting the free-diffusion experiment.

For all the times, the relaxation time curve has a bell-shape in the log-log plot of τ_c vs q . As already reported in a number of publications, the right part of such curves for large wave

numbers corresponds to the diffusive regime of c-NEFs. All curves collapse onto a single one for large wave numbers, because the mass diffusion coefficient remains constant during the free-diffusion process. This can be clearly observed also in Fig. 3.8-a, where the mass diffusion coefficients obtained after fitting time decays through Eq. 3.3 are shown as a function of normalized time by the diffusive time. Moreover, the diffusion coefficient does not change with respect to the applied concentration difference ΔC . All data shown in Fig. 3.8 are relative to the average concentration $C = 0.5$ w/w and $T = 25$ °C. On the contrary, the position of the maximum of the time constant q_c decreases with time as visible in Fig. 3.8-b.

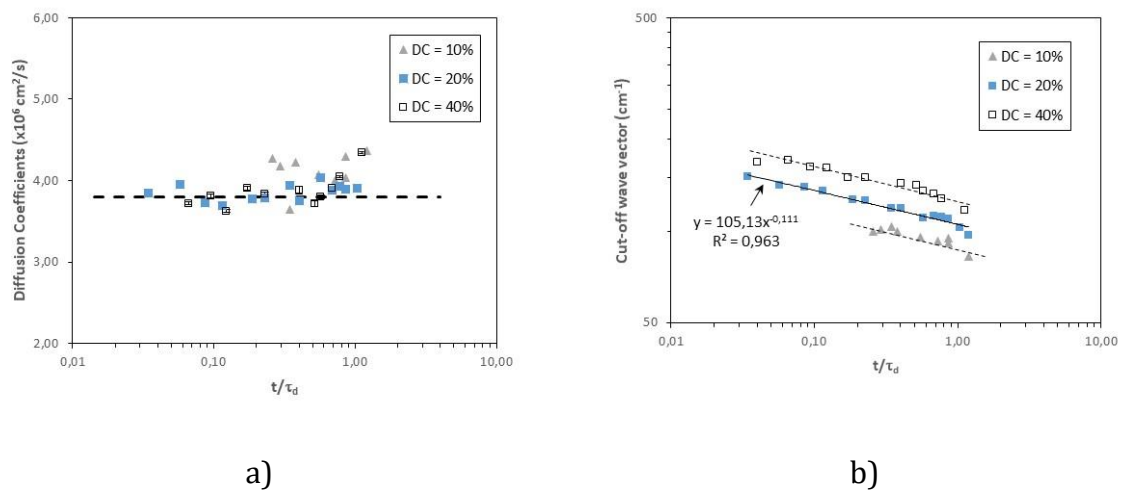


Figure 3.8: a) Mass diffusion coefficient D and b) cut-off wave number q_c as a function of the normalized time for different concentration differences for the free-diffusion experiments carried out with the binary mixture of TEG/water at $C = 0.5$ w/w and $T = 25$ °C.

The values obtained for the mass diffusion coefficient D are nicely centred around the literature value obtained by Optical Beam Deflection (OBD) [109], that is represented by a horizontal dashed line in Fig. 3.8-a. The values obtained for $\Delta C = 0.1$ w/w are somewhat more scattered, which mirrors the smaller signal-to-noise ratio, also visible in Fig. 3.6. Moreover, the measurement error is increased for times close to the diffusive time of the cell, because, again, the signal-to-noise ratio decreases due to the decrease of the concentration gradient. The values obtained for the mass diffusion coefficient remain almost constant as a function of time and do not depend on the concentration difference imposed at the beginning of the experiment. Conversely, the cut-off wave number decreases with time and with the concentration difference according to Eq. 3.4. Fitting data point with a power law and free exponent provides a value of -0.11, rather close to the theoretical value of -0.125.

In Fig. 3.9-a, we report the values of the mass diffusion coefficient and the cut-off wave number as a function of the normalised time and for different values of the homogeneous temperature. In Fig. 3.9-b we report the values of the cut-off wave number as a function of the normalized time in the same conditions. The experiments reported in Fig. 3.9 have been performed with average concentration $C = 0.5$ w/w and concentration difference $\Delta C = 0.2$ w/w.

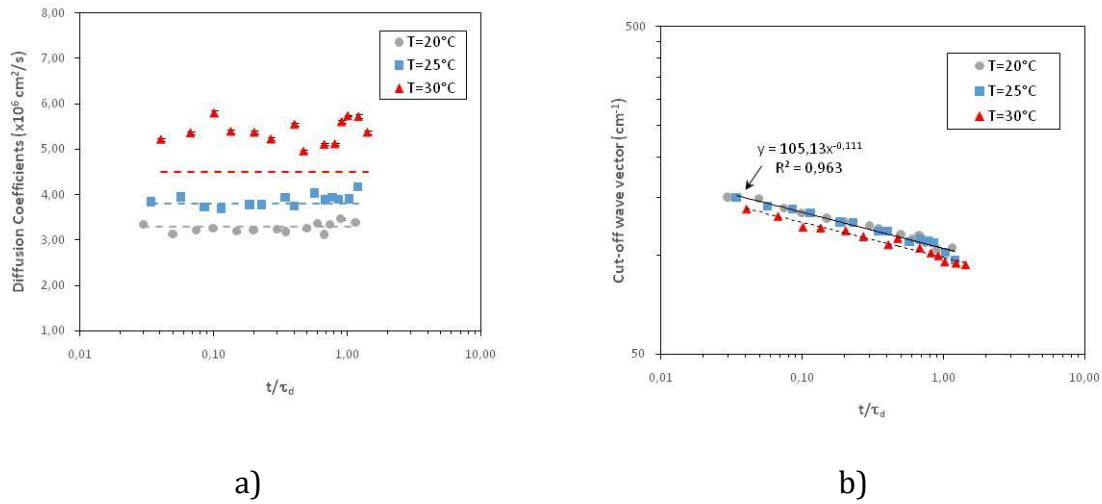


Figure 3.9: a) Mass diffusion coefficient and b) cut-off wave number as a function of the normalized time for different temperatures for the free-diffusion experiments carried out with the binary mixture of TEG/water at $C = 0.5$ w/w and a difference of concentration $\Delta C = 0.2$ w/w.

In Fig. 3.9-a, the horizontal dashed lines provide a visual reference of the values of the mass diffusion coefficient obtained by OBD and reported in the literature [109]. The data points for $T = 20$ and 25 °C are in very good agreement with the literature values, however those obtained at 30 °C show a 10% difference with respect to the literature one. In Fig. 3.9-b we can see that the wave numbers follow a power law dependence upon reduced time with an exponent close to the theoretical value of -0.125 for all the three investigated temperatures.

In Table 3.1 we provide the obtained values of the mass diffusion coefficients as obtained by the free-diffusion experiments carried out with the TEG/water binary mixture at the two average concentrations of $C = 0.5$ and 0.7 w/w, at the three different homogeneous temperatures of $T = 20, 25$ and 30 °C. For the average concentration of $C = 0.7$ w/w, the concentration difference between bottom and top solutions was $\Delta C = 0.2$ w/w.

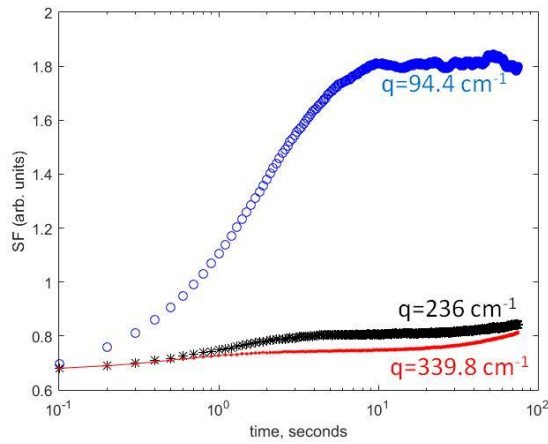
Table 3.1: Mass diffusion coefficients D obtained by free-diffusion experiments carried out with the TEG/water binary mixture at mean concentration C in mass fraction of TEG and homogeneous temperature T .

D ($\times 10^{-6}$ cm ² /s)		
T (°C)	$C = 0.5$ w/w	$C = 0.7$ w/w
20	3.27 ± 0.10	2.15 ± 0.16
25	3.86 ± 0.14	2.32 ± 0.06
30	5.4 ± 0.3	3.00 ± 0.13

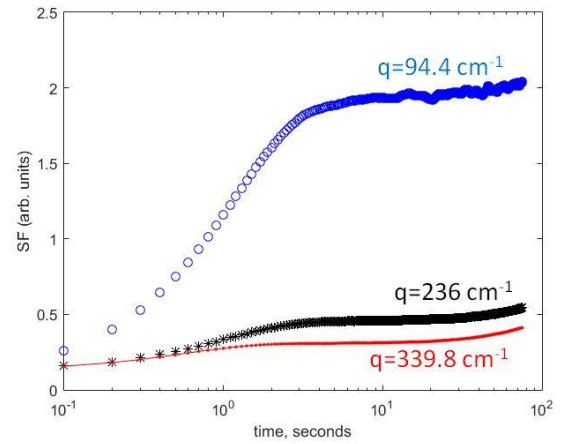
The uncertainties reported in Table 3.1 correspond to the standard deviation with respect to the average value including the measurements obtained at different normalised times. In the case of the measurements performed at $C = 0.5$ w/w, we averaged data obtained for $\Delta C = 0.2$ and 0.4 w/w. The values reported in Table 3.1 show that the diffusion coefficient increases with the temperature for the two TEG concentrations, which is a reasonable behaviour as fluid viscosity typically decreases with increasing temperature and the mass diffusion coefficient is inversely proportional to the fluid viscosity (see Table 1 of the Paper #2 done in appendix E), following the Stokes-Einstein relation.

3.3.2 Electrolyte diffusion coefficient measurements

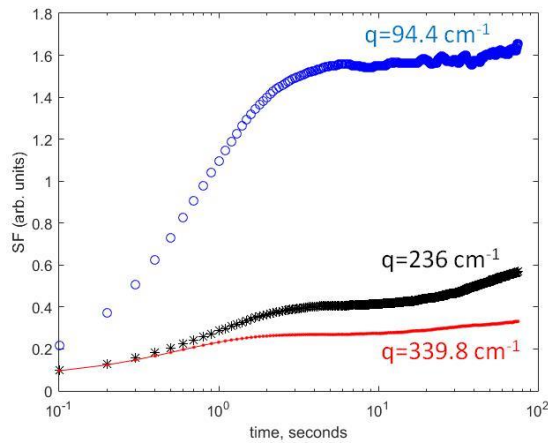
Also as part of the experimental calibration step, free diffusion experiments have been performed at NaCl concentration $C = 2.7$ mol.L⁻¹ in water and 25°C, with the shadowgraph #1. The diffusion cell is first filled with the less dense solution and subsequently, the less dense and the denser solution fills about half of the cell. The valves are closed and the free-diffusion process starts. Series of $N = 2500$ images of 1024×1024 pix² were recorded at a frequency rate of $f = 10$ Hz, every 5 minutes over the first 20 minutes of each experiment, and then every 10 minutes. The SFs were directly calculated by the DDA algorithm, as shown in Fig. 3.10 for different differences of concentration ΔC between the two superimposed fluid layers and 40 minutes after closing the valves.



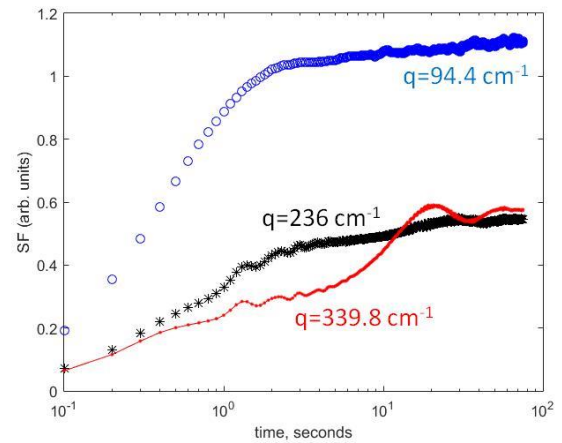
a) $\Delta C = 1 \text{ mol.L}^{-1}$



b) $\Delta C = 2 \text{ mol.L}^{-1}$



c) $\Delta C = 3 \text{ mol.L}^{-1}$



d) $\Delta C = 5.4 \text{ mol.L}^{-1}$

Figure 3.10: Structure function for different wave numbers of the free-diffusion experiment carried out with the binary mixture of NaCl/water at the mean concentration of $C = 2.7 \text{ mol.L}^{-1}$, mean temperature of 25°C , 40 minutes after closing the valves, and different differences of concentration ΔC between the bottom and top layer solutions, that are indicated under the figures.

Until $\Delta C = 3 \text{ mol.L}^{-1}$, the mono-exponential behavior of the SFs can be assumed for most of the wave numbers, except for the larger wave vector where the final plateau does not seem to be reached. However, the latter SF remains consistent with calculations of SFs made on experiments carried out in a transient state. In Fig. 3.10-d it is clearly visible that the mono-exponential behavior of the SF is no longer valid for most of the wave numbers, even showing pronounced oscillations at large wave numbers. This experiment, made at $C = 2.7 \text{ mol.L}^{-1}$ and $\Delta C = 5.4 \text{ mol.L}^{-1}$, corresponds to a solution of NaCl at the limit of solubility, diffusing in pure water. This proximity to the solubility limit can explain the behavior of the SFs for these experimental conditions. Data points until $\Delta C = 3 \text{ mol.L}^{-1}$ were fitted through Eq. 3.2 for the entire range of wave numbers. The resulting values for the parameter $F(q)$ turned out to be four orders of magnitude smaller than $C(q)$, and

parameter $E(q)$ two orders of magnitude smaller. The quantity $A(q)/C(q)$ can provide here also a useful indication of the signal-to-noise ratio of the measurement. In Fig. 3.11 the signal-to-noise ratio is shown for a difference of concentration of $\Delta C = 2 \text{ mol.L}^{-1}$ between the two superimposed fluid layers, and 40 minutes after closing the valves (orange squares in the figure).

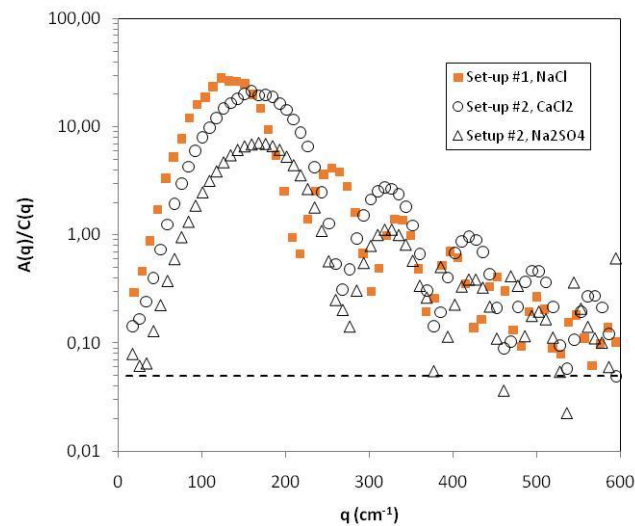


Figure 3.11: Ratio between the static structure factor and the signal background as a function of the wave number for the free-diffusion experiments carried out:

- orange squares for the binary mixture of NaCl/water and the shadowgraph set-up #1 ($C = 2.7 \text{ mol.L}^{-1}$, $\Delta C = 2 \text{ mol.L}^{-1}$, $T = 25^\circ\text{C}$ and 40 minutes after closing the valves);
- open circles for the binary mixture of CaCl_2 /water and the shadowgraph set-up #2 ($C = 0.46 \text{ mol.L}^{-1}$, $\Delta C = 0.8 \text{ mol.L}^{-1}$, $T = 25^\circ\text{C}$ and 40 minutes after closing the valves);
- open triangles for the binary of Na_2SO_4 /water and the shadowgraph set-up #2 ($C = 0.5 \text{ mol.L}^{-1}$, $\Delta C = 0.7 \text{ mol.L}^{-1}$, $T = 25^\circ\text{C}$ and 90 minutes after closing the valves)

The positions of the maximums and minimums correspond to those of Fig. 3.6, which makes sense given that the shadowgraph setup is the same. Compared to Fig. 3.6, the value of the signal-to-noise ratio is lower here. The horizontal line visible in Fig. 3.11 stands for the threshold value of 0.05. Fitting the SFs in the wave number range from 30 to 500 cm^{-1} was performed. In Fig. 3.12 we report the decay times obtained from fitting the SFs as a function of the wave number q and for different times after closing the inlet/outlet valves. The graph corresponds to a sample with $C = 2.7 \text{ mol.L}^{-1}$, $\Delta C = 2 \text{ mol.L}^{-1}$ and $T = 25^\circ\text{C}$.

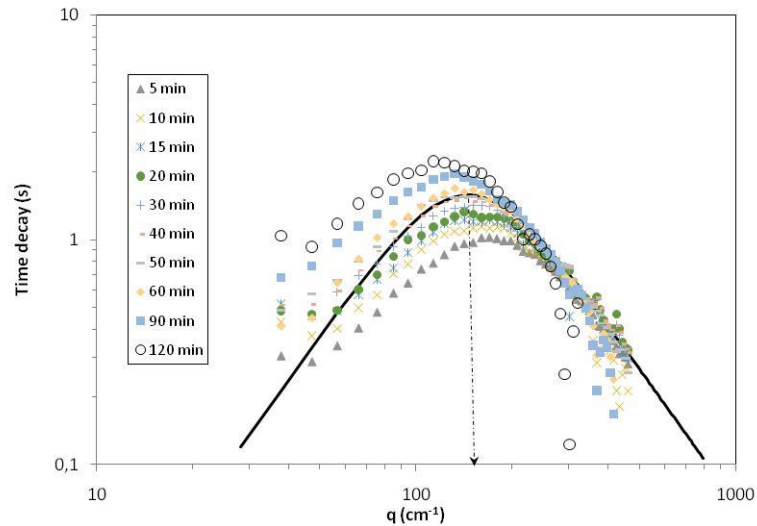


Figure 3.12: Decay times of the c-NEFs as a function of the wave numbers and time after closing the inlet/outlet valves for the free-diffusion experiment carried out with the binary mixture of NaCl/water at $C = 2.7 \text{ mol.L}^{-1}$, difference of concentration $\Delta C = 2 \text{ mol.L}^{-1}$ and $T = 25 \text{ }^\circ\text{C}$. The continuous black line corresponds to the curve obtained fitting Eq. 3.3 to data points obtained 40 minutes after starting the free-diffusion experiment.

For all the times, the relaxation time curve has here also a bell-shape in the log-log plot of τ_c vs. q . All curves collapse onto a single one for large wave numbers, meaning that the mass diffusion coefficient remains constant during the free-diffusion process. However, a downfall of the relaxation times at the last instants and largest wave numbers is observable, probably due to the low value of the signal-to-noise ratio in this region, and which decreases due to the decrease of the concentration gradient in the cell. In Fig. 3.13-a, we plotted the mass diffusion coefficients and in Fig. 3.13-b the q_c as a function of reduced time and for different differences of concentration ΔC between the two superimposed fluid layers, obtained after fitting time decays through Eq. 3.3.

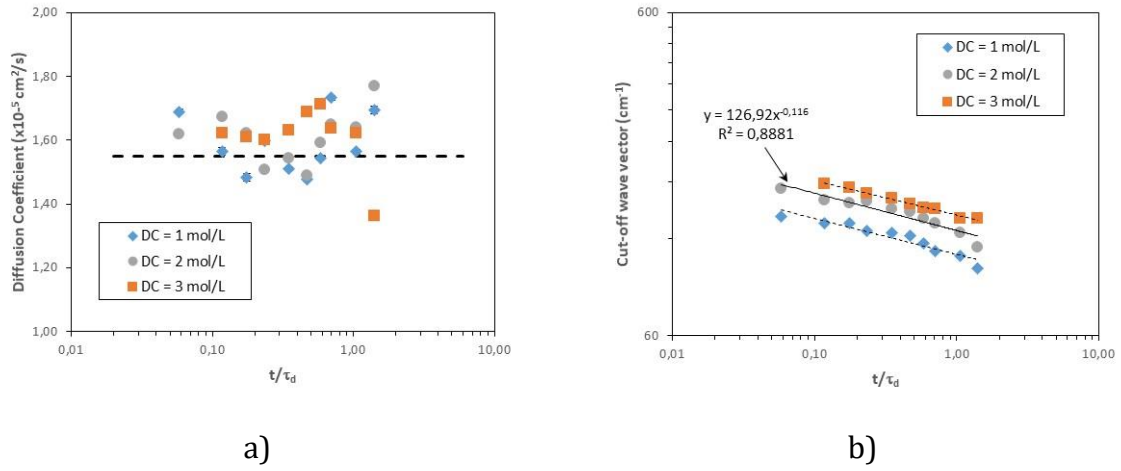


Figure 3.13: a) Mass diffusion coefficient D of NaCl in water and b) cut-off wave number q_c as a function of the normalized time for different concentration differences for the free-diffusion experiments carried out with the binary mixture of NaCl/water at $C = 2.7 \text{ mol.L}^{-1}$ and $T = 25 \text{ }^\circ\text{C}$.

The values obtained for the mass diffusion coefficient D are centred around the literature value obtained by Rayleigh interferometry [113], represented by a horizontal dashed line in Fig. 3.13-a. They are, as for the TEG/water mixture (Fig. 3.8-a), not dependent on the investigated concentration differences imposed at the beginning of the experiment, with an error increased for times close to the diffusive time of the cell, because, again, the signal-to-noise ratio decreases due to the decrease of the concentration gradient in the cell. Conversely, the cut-off wave number q_c decreases with time according to Eq. 3.4 as can be seen in Fig. 3.13-b. Fitting data points with a power law and free exponent gives a lower regression coefficient R^2 compared to the TEG/water mixture (Fig. 3.8-b), but provides a value of -0.116 rather close to the theoretical value of -0.125.

Before performing the free diffusion experiments on the complex configuration of the three superimposed aqueous solutions, preliminary free diffusion experiments were performed on binary $\text{CaCl}_2/\text{water}$ and $\text{Na}_2\text{SO}_4/\text{water}$ systems.

With the same filling procedure as before, free diffusion experiments with CaCl_2 and Na_2SO_4 have been performed with the shadowgraph setup #2 (see section 3.2.3), the main difference being the use of the PIKE camera. Series of $N = 2500$ images of $1024 \times 1024 \text{ pix}^2$ were recorded at frequency rate of $f = 10 \text{ Hz}$, every 5 minutes over the first 20 minutes of each experiment, and then every 10 minutes. As previously stated, the minimum accessible wave number is given by $q_{min} = 2\pi/L$, L being the side of the image in the real space. For the acquired images, $L = 0.75 \text{ cm}$, so that $q_{min} = 8.38 \text{ cm}^{-1}$. The theoretical maximum frequency with the second shadowgraph is $q_{max} = (N_{pix}/2) \cdot q_{min} =$

4291 cm^{-1} , N_{pix} being the number of the pixels along one side of the images. The SFs were calculated by the DDA algorithm, as shown in Fig. 3.14-a for a mean CaCl_2 concentration of $C = 0.46 \text{ mol.L}^{-1}$, a difference of concentration $\Delta C = 0.8 \text{ mol.L}^{-1}$ between the two superimposed fluid layers, and 40 minutes after closing the valves. In Fig. 3.14.b we report resulting calculations for a mean Na_2SO_4 concentration of $C = 1.484 \text{ mol.L}^{-1}$, a difference of concentration $\Delta C = 0.7 \text{ mol.L}^{-1}$ between the two superimposed fluid layers, and 50 minutes after closing the valves.

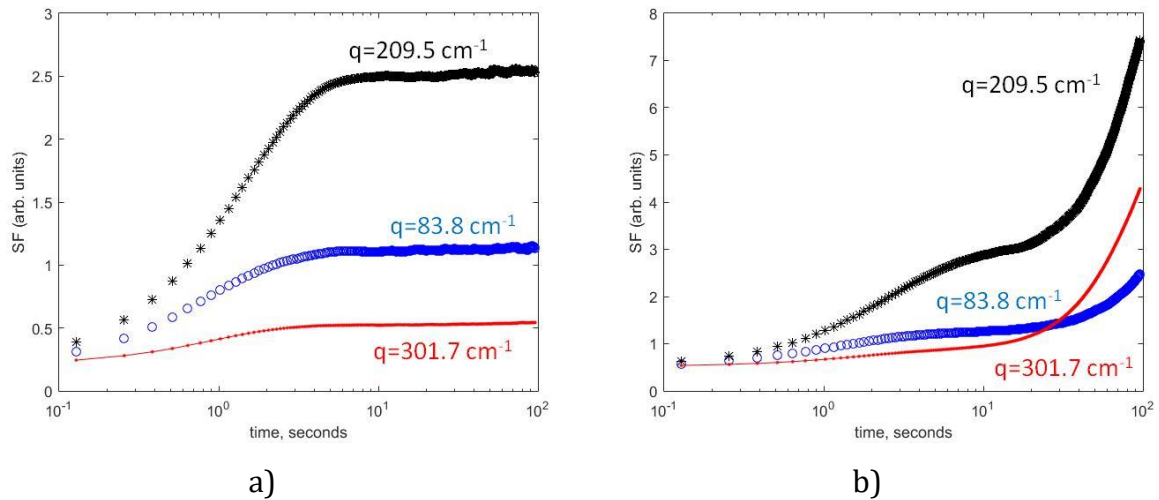


Figure 3.14: Structure function for different wave numbers of the free-diffusion experiment carried out at mean temperature of 25°C with:

- a) the binary mixture of $\text{CaCl}_2/\text{water}$
($C = 0.46 \text{ mol.L}^{-1}$, $\Delta C = 0.8 \text{ mol.L}^{-1}$ and 40 minutes after closing the valves);
- b) the binary mixture of $\text{Na}_2\text{SO}_4/\text{water}$
($C = 1.484 \text{ mol.L}^{-1}$, $\Delta C = 0.7 \text{ mol.L}^{-1}$ and 50 minutes after closing the valves)

In the case of the experiment performed with CaCl_2 the calculated SFs show a mono-exponential behaviour with a well characterised plateau, even for large wave numbers. Conversely, the SFs obtained with the experiment with Na_2SO_4 show clearly visible quadratic dependence with time for all wave numbers (see Fig. 3.14-b). The proximity to the solubility limit of mirabilite ($\text{Na}_2\text{SO}_4 \cdot 10\text{H}_2\text{O}$) for the experiment with Na_2SO_4 can explain the behavior of the SFs. Indeed, for the experiment with CaCl_2 the chosen concentration is far from the solubility limit. To check this hypothesis, we carried out experiments with Na_2SO_4 at mean concentrations of 1 and 0.5 mol.L^{-1} with a difference of concentration $\Delta C = 0.7 \text{ mol.L}^{-1}$ between the two superimposed fluid layers. In Fig. 3.15, we report the SFs calculated 50 minutes after closing the valves.

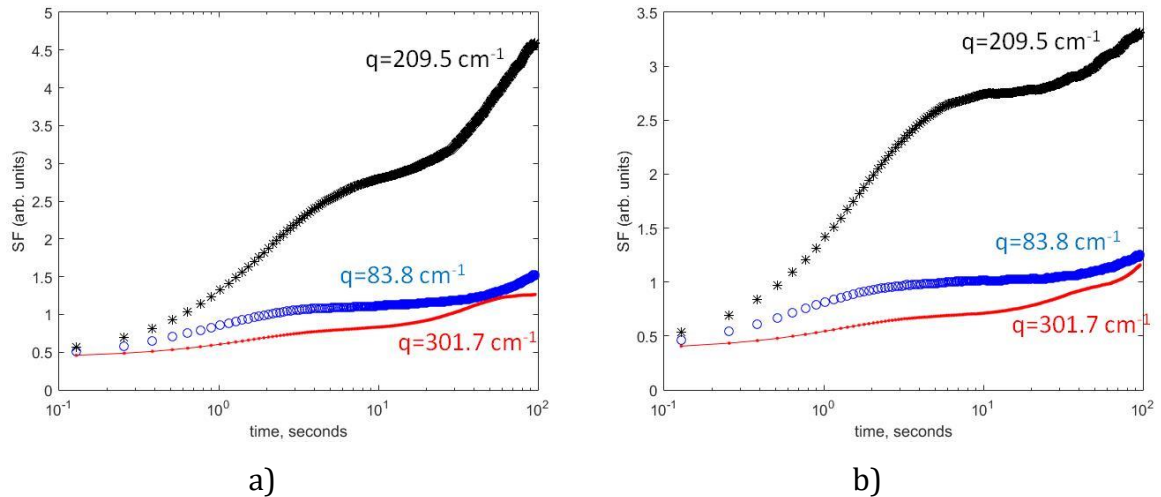
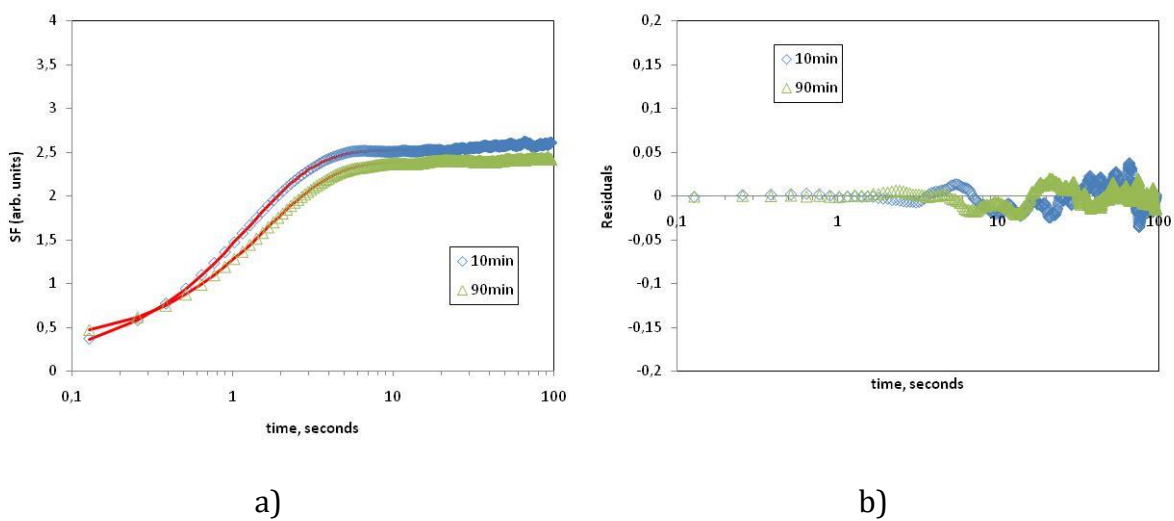


Figure 3.15: Structure function for different wave numbers of the free-diffusion experiment carried out with the binary mixture $\text{Na}_2\text{SO}_4/\text{water}$ at mean temperature of $25\text{ }^\circ\text{C}$, difference of concentration $\Delta C = 0.7\text{ mol.L}^{-1}$ and 50 minutes after closing the valves with: a) $C = 1\text{ mol.L}^{-1}$; b) $C = 0.5\text{ mol.L}^{-1}$.

Although it is attenuated as the average concentration of the experiment decreases, the quadratic dependence of the SFs on time is still visible. Moreover, we noticed that it decreases with time. In Fig. 3.16-a we plot the SFs calculated for the wavenumber $q = 209.5\text{ cm}^{-1}$ and the fits obtained with Eq. 3.2, 10 min and 90 min after closing the valves for the experiment with CaCl_2 . In Fig. 3.16-b we plotted the corresponding residuals. In Fig. 3.16-c and Fig. 3.16-d we reported the analogous results for the experiment with Na_2SO_4 at $C = 0.5\text{ mol.L}^{-1}$.



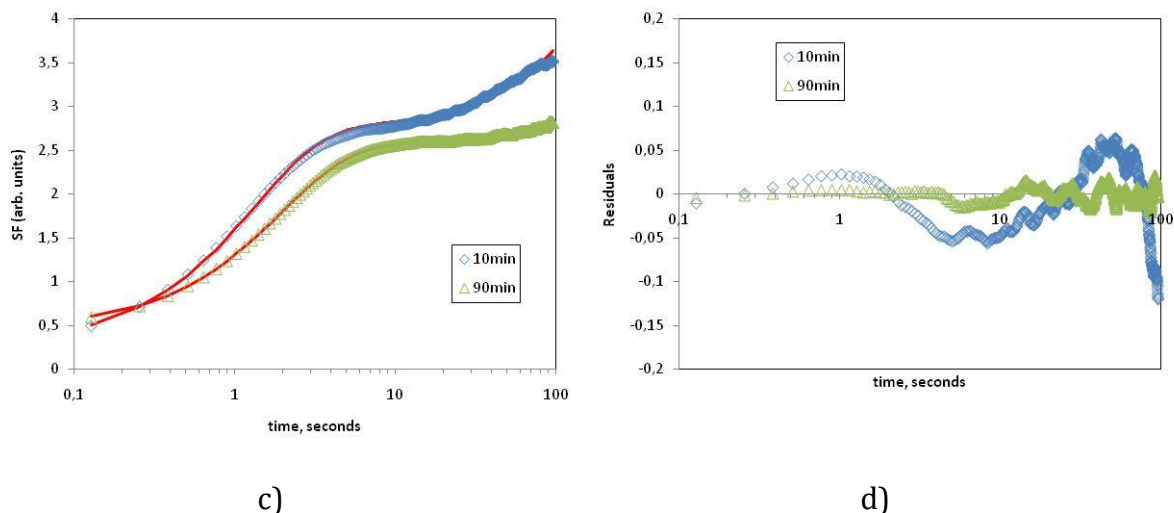


Figure 3.16: Structure function for wave number $q = 209.5 \text{ cm}^{-1}$ and for different moments after closing the valves, carried out with: a) the binary mixture $\text{CaCl}_2/\text{water}$ ($C = 0.46 \text{ mol.L}^{-1}$, $\Delta C = 0.8 \text{ mol.L}^{-1}$, $T = 25^\circ\text{C}$); c) the binary mixture $\text{Na}_2\text{SO}_4/\text{water}$ ($C = 0.5 \text{ mol.L}^{-1}$, $\Delta C = 0.7 \text{ mol.L}^{-1}$, $T = 25^\circ\text{C}$). The continuous red line corresponds to the curve obtained fitting Eq. 3.2 to data points. In b) and d) we report the corresponding residuals between data points and the theoretical model.

From Fig. 3.16-b we can see that the theoretical model of the SF given by Eq. 3.2 allows us to correctly describe the experimental points, especially at the first moments of the image recording, which is the part of the curve during which the SF evolves the most. Although Eq. 3.2 contains a quadratic time dependence term, we can see in Fig. 3.16-d that the experimental points are not correctly described at the beginning of the experiment with Na_2SO_4 , especially at the first moments after closing the valves. Towards the end of the experiment, when the quadratic dependence term on the SF is less pronounced, the fit of the experimental points becomes acceptable for 90 min after closing the valves, as can be seen in Fig. 3.16-d.

The resulting values for the parameter $F(q)$ turned out to be four orders of magnitude smaller than $C(q)$, and parameter $E(q)$ two orders of magnitude smaller. The quantity $A(q)/C(q)$ can provide here also a useful indication of the signal-to-noise ratio of the measurement. In Fig. 3.11, the signal-to-noise ratio is shown for the experiment with CaCl_2 ($C = 0.46 \text{ mol.L}^{-1}$, $\Delta C = 0.8 \text{ mol.L}^{-1}$, $T = 25^\circ\text{C}$) 40 minutes after closing the valves (open circles in the figure) and for the experiment with Na_2SO_4 ($C = 0.5 \text{ mol.L}^{-1}$, $\Delta C = 0.7 \text{ mol.L}^{-1}$, $T = 25^\circ\text{C}$) 90 minutes after closing the valves (open triangles in the figure). The positions of the maximums and minimums nicely correspond for these two experiments, which makes sense given that the shadowgraph setup is the same. Here also the fitting of the SF was performed in the wave number range from 30 to 500 cm^{-1} . In Fig. 3.17, we plot the

mass diffusion coefficients as a function of reduced time and for the two last experiments, obtained after fitting time decays through Eq. 3.3.

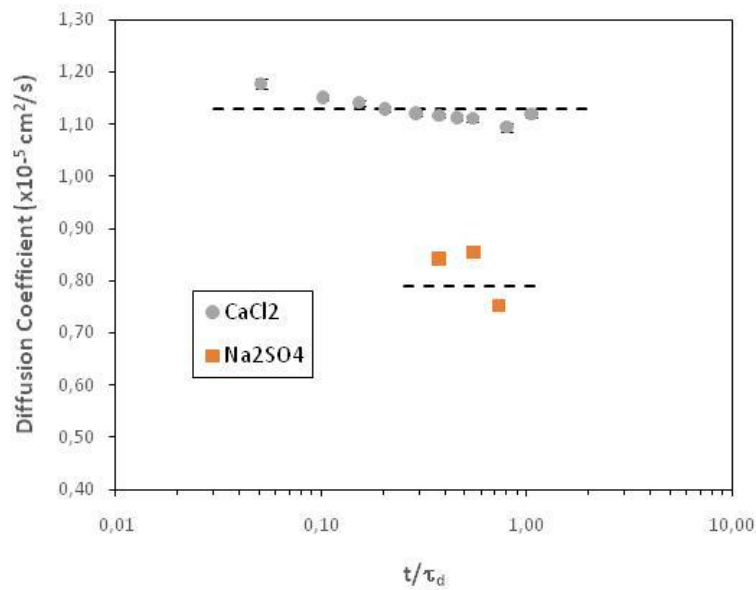


Figure 3.17: Mass diffusion coefficient D as a function of the normalized time for the free-diffusion experiments carried out, circles are for the binary mixture of $\text{CaCl}_2/\text{water}$ ($C = 0.46 \text{ mol.L}^{-1}$, $\Delta C = 0.8 \text{ mol.L}^{-1}$, $T = 25^\circ\text{C}$) and rectangles are for the binary mixture $\text{Na}_2\text{SO}_4/\text{water}$ ($C = 0.5 \text{ mol.L}^{-1}$, $\Delta C = 0.7 \text{ mol.L}^{-1}$, $T = 25^\circ\text{C}$).

The literature values obtained by Rayleigh interferometry [113], [138] are represented by horizontal dashed lines. The agreement is pretty good in both cases.

3.3.3 Non-isothermal conditions

One free-diffusion experiment at NaCl mean concentrations of 2.637 mol.L^{-1} , difference of concentration $\Delta C = 2 \text{ mol.L}^{-1}$ between the two superimposed fluid layers, mean temperature $T = 25^\circ\text{C}$ and imposing a vertical difference of temperature across the cell $\Delta T = +20 \text{ K}$ (heating by the top) was performed with the shadowgraph #2. In Fig. 3.18-a we report the mass diffusion coefficients and in Fig. 3.18-b the q_c as a function of reduced time. We superimposed the results obtained in an equivalent configuration but in isothermal conditions.

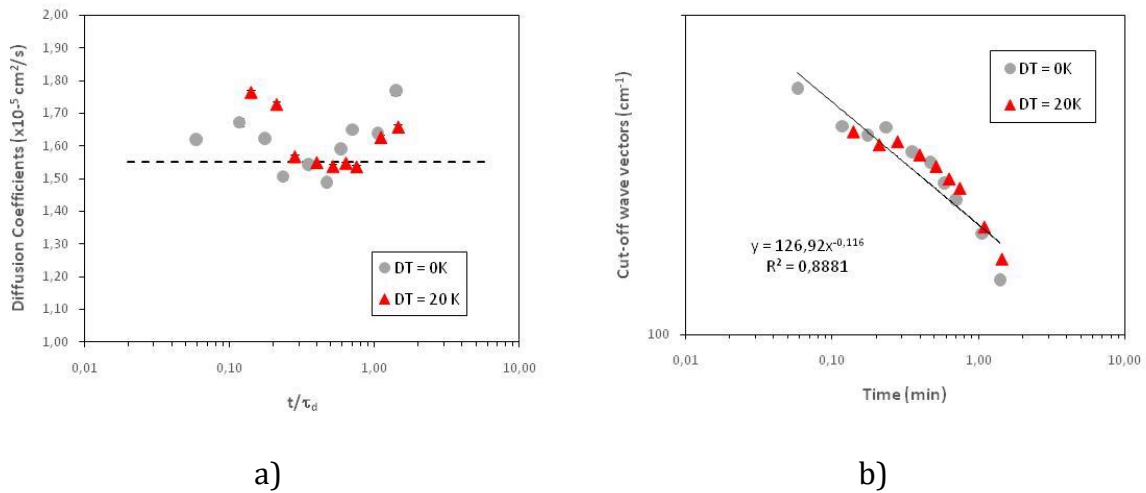


Figure 3.18: a) Mass diffusion coefficient D and b) cut-off wave number q_c as a function of the normalized time for the free-diffusion experiments carried out with the binary mixture of NaCl/water ($C \approx 2.7 \text{ mol.L}^{-1}$, $\Delta C = 2 \text{ mol.L}^{-1}$, $T_{\text{mean}} = 25 \text{ }^\circ\text{C}$). Circles are for the experiment without a difference of temperature and triangles are with a vertical difference of temperature $\Delta T = +20 \text{ K}$ across the cell.

The literature value of the diffusion coefficient for isothermal conditions [113], is represented by a horizontal dashed line in Fig. 3.18-a. Already presented fitting of the q_c in Fig 3.13-b is represented by a solid line in Fig. 3.20-b. The thermal gradient did not have a significant effect on the relaxation mode of the system.

In order to achieve the superimposition of two or three aqueous electrolyte layers and to be mechanically stable in the gravity field, the choice of the concentrations of the solutions must be adjusted. In Fig. 3.19, we plotted the density of NaCl, CaCl_2 and Na_2SO_4 aqueous solutions as a function of the salt concentration at $T = 20^\circ\text{C}$.

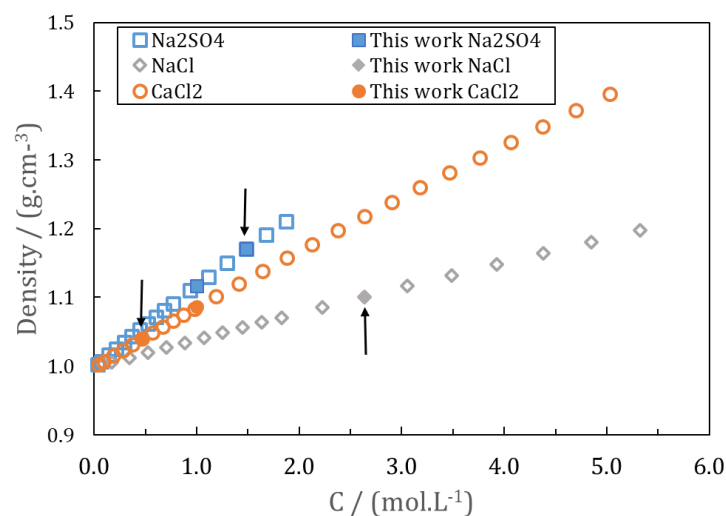


Figure 3.19: Density as a function of the salt concentration in water at $T = 20 \text{ }^\circ\text{C}$, diamonds are for NaCl, circles for CaCl_2 and rectangles for Na_2SO_4 . Open symbols are for literature data [192] and filled symbols are points measured in this work.

Open symbols are for literature data [192]. Additional measurements were performed in the laboratory using a density meter (Anton Paar DMA 5000, see appendix C for more details), and are represented for the temperature of 20 °C by the filled symbols in Fig. 3.19. We therefore chose to superimpose CaCl₂ on Na₂SO₄ with an intermediate layer of NaCl, at respective concentrations of 0.46, 1.484 and 2.637 mol.L⁻¹, and which are indicated by arrows in Fig. 3.19, corresponding to a density distribution of 1.039 < 1.099 < 1.169 g.cm⁻³ respectively.

3.4 Superimposition of two aqueous layers of non-reactive salts

3.4.1 Experimental observations parallel to the gravity

The superimposition of a layer of aqueous CaCl₂ at the concentration of 0.46 mol.L⁻¹ on a layer of aqueous NaCl at the concentration of 2.637 mol.L⁻¹ resulted in the appearance of some diffraction spots on the image differences themselves, as shown in Fig. 3.20-a.

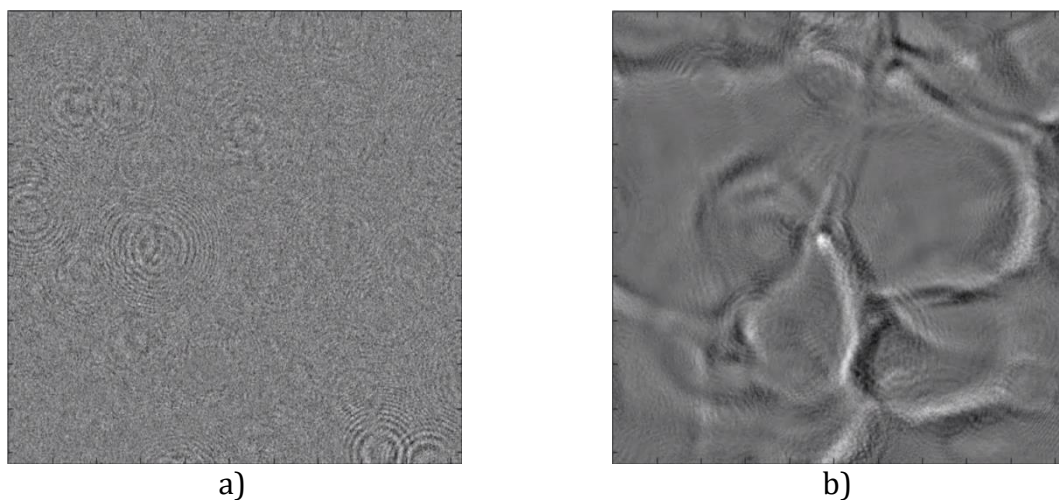


Figure 3.20: Normalized image differences :

- a) 20 minutes after closing the valves when a layer of a CaCl₂ solution (0.46 mol.L⁻¹) is brought in contact with a NaCl solution (2.637 mol.L⁻¹) at the homogenous temperature of 25 °C;
- b) 5 minutes after closing the valves when a layer of a NaCl solution (2.637 mol.L⁻¹) is brought in contact with a Na₂SO₄ solution (1.484 mol.L⁻¹) at the homogenous temperature of 25 °C.

These diffraction spots were less frequent as time goes by, leading towards the end of the experiment to an evolution of the image contrast compatible with that produced by fluctuations in a free diffusion process, as shown in Fig. 3.21-a. As an example in Fig. 3.21 we give a difference of images and the evolution of the contrast of the images 40 minutes

after closing the valves in a free-diffusion experiment with the binary mixture $\text{CaCl}_2/\text{water}$ ($C = 0.46 \text{ mol.L}^{-1}$, $\Delta C = 0.8 \text{ mol.L}^{-1}$, $T = 25 \text{ }^\circ\text{C}$). In Fig. 3.21-a only the fluctuations are visible and in Fig. 3.21-b we note a slight increase in contrast as a function of time.

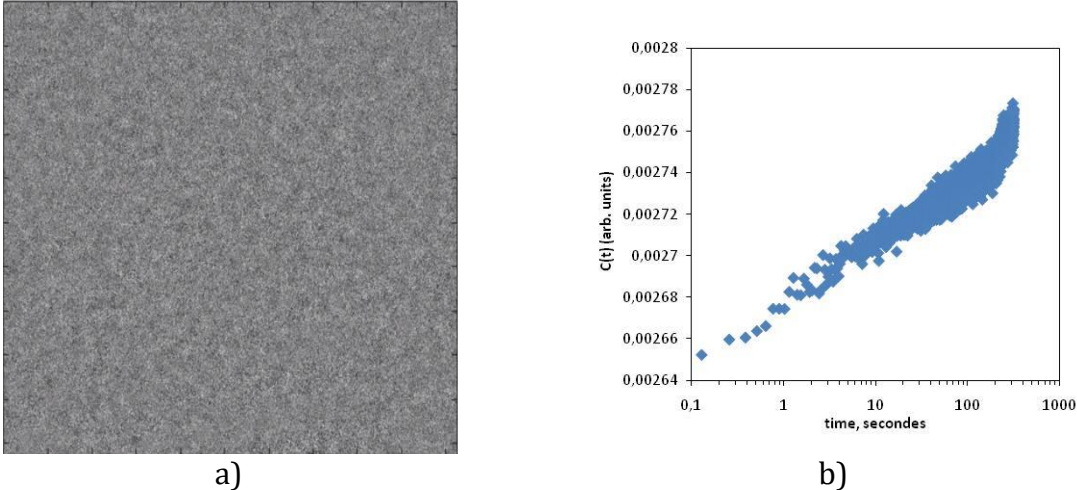


Figure 3.21: a) Normalized image differences and b) contrast of shadowgraph image sequence 40 minutes after closing the valves in a free-diffusion experiment with the binary mixture $\text{CaCl}_2/\text{water}$ ($C = 0.46 \text{ mol.L}^{-1}$, $\Delta C = 0.8 \text{ mol.L}^{-1}$, $T = 25 \text{ }^\circ\text{C}$).

The results obtained when a layer of aqueous Na_2SO_4 at the concentration of 1.484 mol.L^{-1} was brought into contact with a layer of aqueous NaCl at the concentration of 2.637 mol.L^{-1} proved to be very different from previous cases. At the very first moments, convection patterns are clearly visible as shown in Fig. 3.20-b. As shown in Fig. 3.22-b, the contrast of the images shows a strong variation at the first instants (an order of magnitude higher compared to the case of the $\text{CaCl}_2/\text{NaCl}$ salt pair Fig. 3.22-a.), and then shows a smooth variation of the contrast characteristic of the fluctuations once the convection has dissipated.

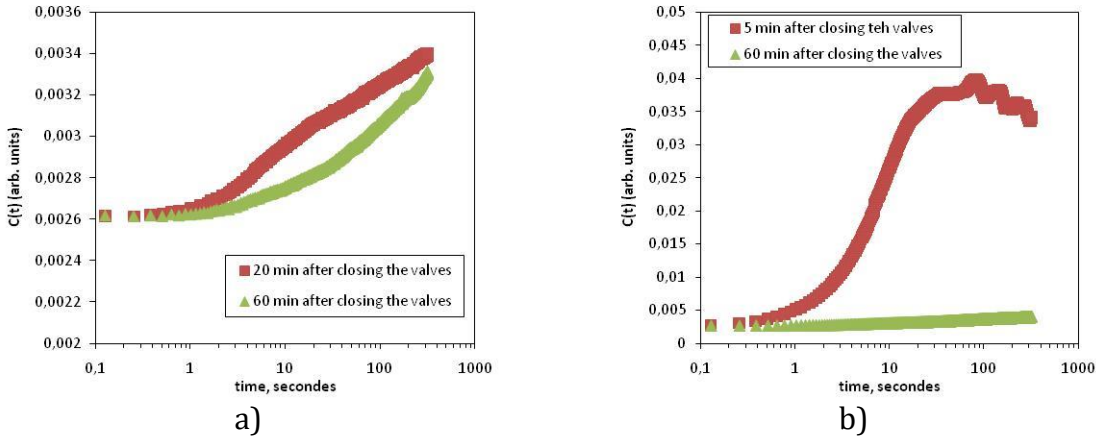


Figure 3.22: Contrast of shadowgraph image sequences $C(t)$ as a function of time and for different moments after closing the valves:

- a) when a layer of a CaCl_2 solution (0.46 mol.l^{-1}) is brought in contact with a NaCl solution (2.637 mol.l^{-1}) at the homogenous temperature of 25°C ;
- b) when a layer of a NaCl solution (2.637 mol.l^{-1}) is brought in contact with a Na_2SO_4 solution (1.484 mol.l^{-1}) at the homogenous temperature of 25°C .

According to these results, the relative mixing of CaCl_2 in NaCl cannot be fully characterised as diffusive. For the moment, we do not have an explanation of the origin of these diffraction spots. In contrast, the relative dissolution of NaCl in Na_2SO_4 can be unambiguously characterised as convective. In the following paragraph, we propose to give a numerical interpretation of the results obtained.

3.4.2 Numerical modelling

The objective, here, is to reproduce numerically in a 1D column the diffusion experiments that involved two superimposed layers of different aqueous electrolytes. For its calculations, PHREEQC uses concentrations given in molality (mol.kg^{-1}) summarised in Table 3.2. The correspondences between molarity and molality are presented in appendix A.

Table 3.2: Concentration of saline solutions in molality at $T = 25^\circ\text{C}$ and $P = 1 \text{ atm}$

	C (mol.l^{-1})	ρ (g.cm^{-3})	Molar mass (g.mol^{-1})	m (mol.kg^{-1})
CaCl_2	0.469	1.038962	110.98	0.475
NaCl	2.637	1.098622	58.44	2.792
Na_2SO_4	1.484	1.168653	142.04	1.548

For the mesh (see Fig. 3.23), the column has a height of $h = 0.01 \text{ m}$ as our experimental diffusion cell, which is subdivided into 20 cells ($5 \times 10^{-4} \text{ m}$) of equal length in order to have detailed information on the phenomena that may occur in the column. The saline solutions at the top and bottom of the column are exactly at the midheight of the column, so that each saline solution is distributed over 10 cells whose total height is $5 \times 10^{-3} \text{ m}$.

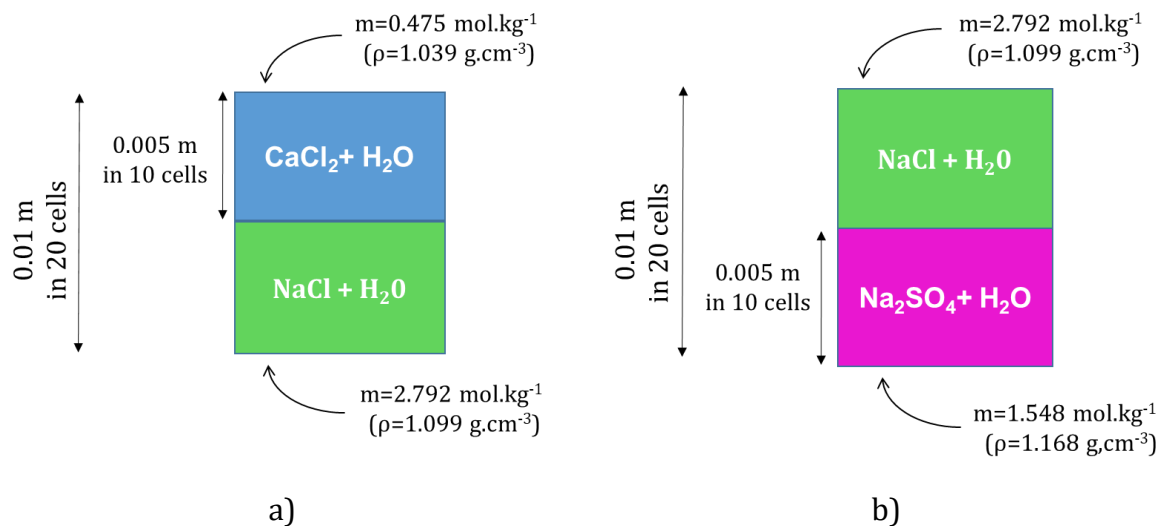


Figure 3.23: Mesh of the column for the numerical modelling of the superimposition of two aqueous layers of non-reactive salts. a) Superimposition of a layer of a CaCl_2 solution (0.46 mol.L^{-1}) with a layer of NaCl solution (2.637 mol.L^{-1}). b) Superimposition of layer of NaCl solution (2.637 mol.L^{-1}) with a layer of a Na_2SO_4 solution (1.484 mol.L^{-1}).

The closed boundary conditions is applied. The initial conditions of the simulation are represented in Fig. 3.24. The activity model used is the interaction model based on the Pitzer formalism, which is suitable for our complex chemical system with high salinity. An example of input file for the numerical modelling of the superimposition of a layer of a CaCl_2 solution (0.46 mol.L^{-1}) with a layer of NaCl solution (2.637 mol.L^{-1}) is shown in Fig. B.2 of appendix B.

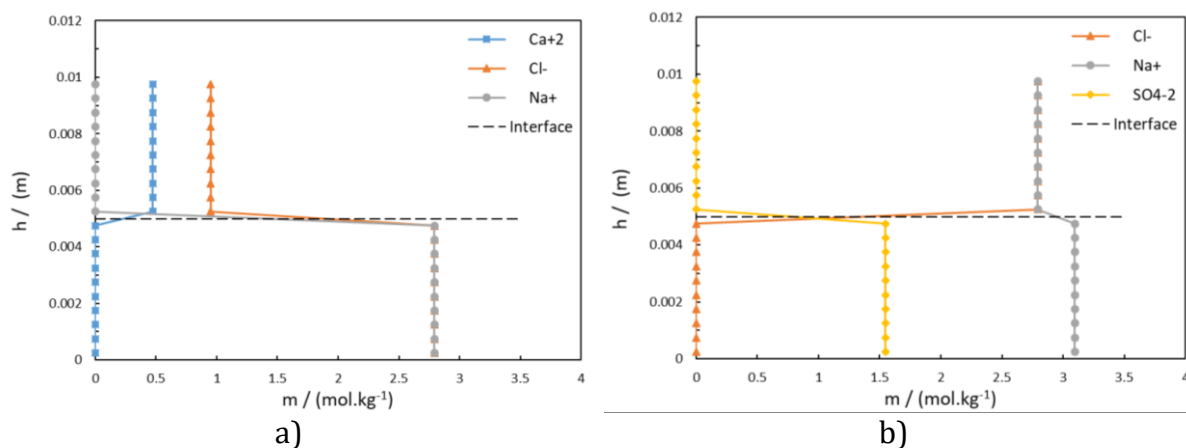


Figure 3.24: Concentration profiles representing the initial conditions of simulation of the diffusion column at the homogenous temperature of $25 \text{ }^\circ\text{C}$ and 1 atm : a) when a layer of a CaCl_2 solution (0.46 mol.L^{-1}) is brought in contact with a NaCl solution (2.637 mol.L^{-1}). b) when a layer of a NaCl solution (2.637 mol.L^{-1}) is brought in contact with a Na_2SO_4 solution (1.484 mol.L^{-1}).

Fig. 3.24-a shows the initial condition when a layer of CaCl_2 solution (top of the column) is brought in contact with a NaCl solution (bottom of the column). Each ionic species is represented individually, knowing that in the case of CaCl_2 , there are twice as many Cl^- ions in solution and therefore the Cl^- concentration is twice that of Ca^{2+} in the top part of

the column. Along the same lines, Fig. 3.24-b shows the initial condition when a layer of NaCl solution (top of the column) is brought in contact with a Na₂SO₄ solution (bottom of the column). In the case of Na₂SO₄, there are twice as many Na⁺ ions in solution and therefore the Na⁺ concentration is twice that of SO₄²⁻. Each couple of electrolytes is allowed to diffuse over time and the diffusive flux is calculated with both homogeneous and heterogeneous multicomponent diffusion for comparison. As explained in section 2.4.3, the diffusion coefficient defined for calculations in the case of the homogeneous multicomponent diffusion is given by the harmonic mean of the diffusion coefficient of the components of the salt, weighted by their molal concentration. Using Eq. 2.44, the harmonic mean of the diffusion coefficient when a layer of CaCl₂ solution is brought in contact with a layer of NaCl solution is $D = 1.543 \times 10^{-9} \text{ m}^2 \cdot \text{s}^{-1}$ while is $D = 1.411 \times 10^{-9} \text{ m}^2 \cdot \text{s}^{-1}$ when a layer of NaCl solution is brought in contact with a layer of Na₂SO₄ solution.

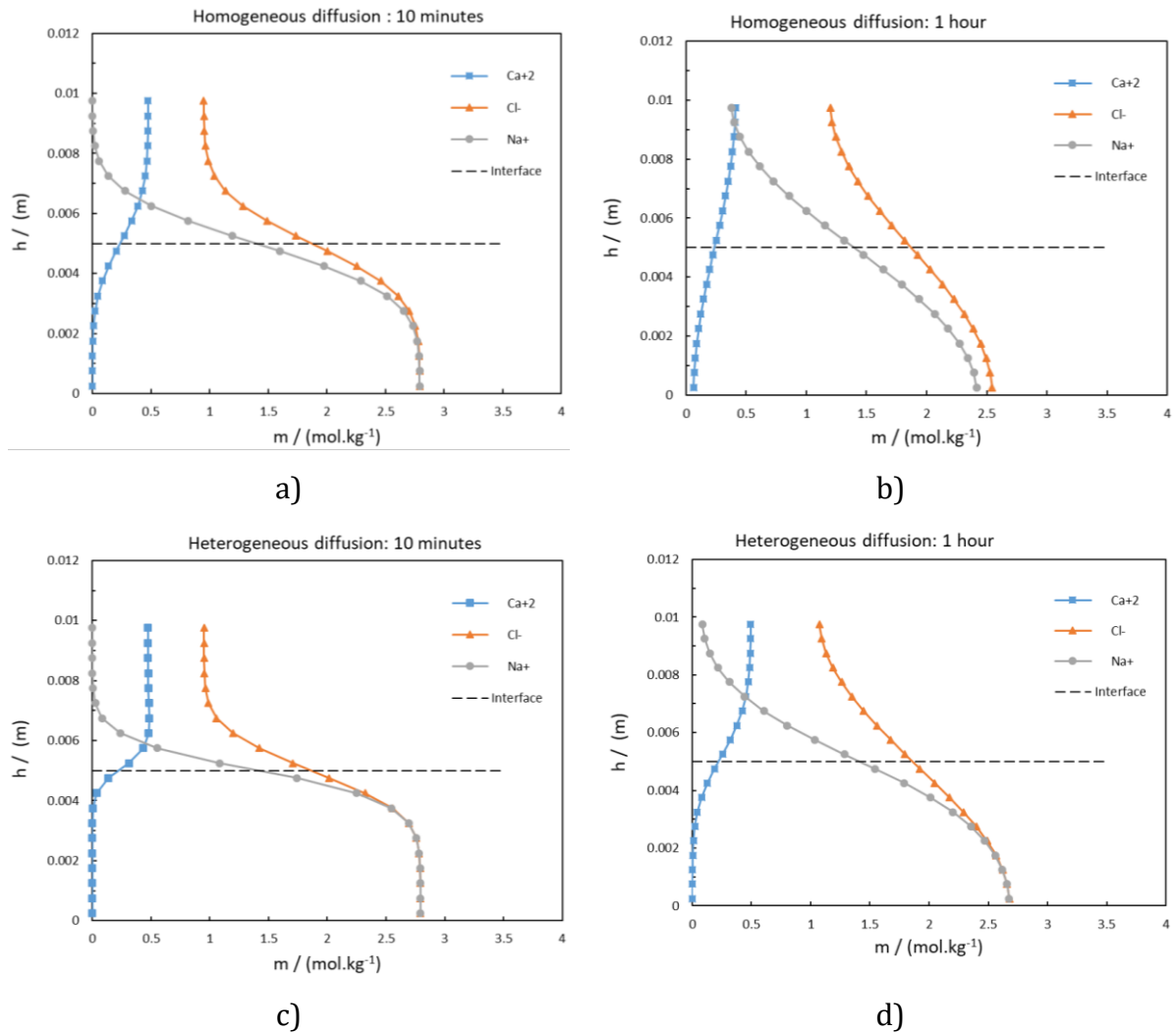


Figure 3.25: Evolution of the molality of ions when a layer of a CaCl_2 solution (0.46 mol.L^{-1}) is brought in contact with a NaCl solution (2.637 mol.L^{-1}) at the homogenous temperature of $25 \text{ }^\circ\text{C}$ in the case of a) Homogeneous multicomponent diffusion after 10 minutes of diffusion, b) Homogeneous multicomponent diffusion after 1 hour of diffusion, c) Heterogeneous multicomponent diffusion after 10 minutes of diffusion and d) Heterogeneous multicomponent diffusion after 1 hour of diffusion

Fig. 3.25 is a comparison between homogeneous and heterogeneous multicomponent diffusion of the superimposition of a layer of CaCl_2 at the concentration of 0.46 mol.L^{-1} on a layer of NaCl at the concentration of 2.637 mol.L^{-1} along the column after 10 and 60 minutes. The results show an intuitively expected behaviour of the concentration of ions in both cases, i.e. as time goes by, the diffusion goes from the most concentrated area to the least concentrated area over the diffusion process comparing with the initial state in Fig. 3.24-a. However, for a same diffusion time, 1 hour for example (Fig. 3.25-b and Fig. 3.25-d), the distribution of ionic species seems to reach the equilibrium state faster in the case of homogeneous diffusion than in the case of heterogeneous diffusion. This is clearly visible on Fig. 3.26 that illustrates the evolution of the ionic strength over the column for

different moments after the beginning of the diffusion. In Fig. 3.26-a, we are close to the equilibrium state after 10 hours (600 minutes) whereas for the same instant in the case of heterogeneous diffusion the diffusion process still evolves as shown in Fig. 3.26-b.

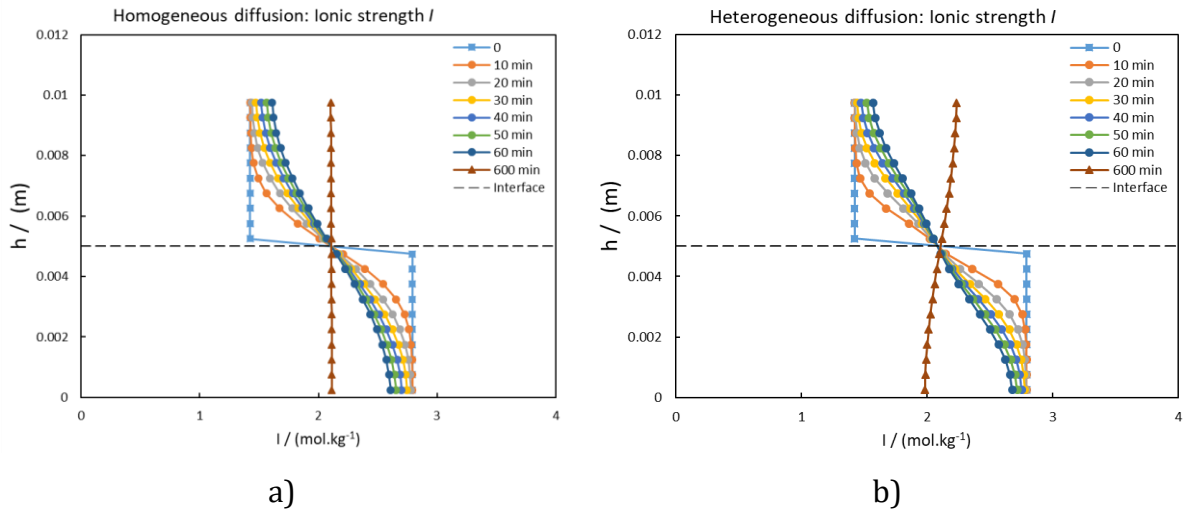


Figure 3.26: Evolution of the ionic strength over the column as a function of time when a layer of a CaCl_2 solution (0.46 mol.L^{-1}) is brought in contact with a NaCl solution (2.637 mol.L^{-1}) at the homogenous temperature of $25 \text{ }^\circ\text{C}$ in the case of a) Homogeneous multicomponent diffusion and b) Heterogeneous multicomponent diffusion.

Fig. 3.27 illustrates the evolution of the density of the solution along the column as the diffusion process evolves. Whether in the case of homogeneous multicomponent diffusion (Fig. 3.27-a) or heterogeneous multicomponent diffusion (Fig. 3.27-b), the evolution of the solution density along the column over time does not reveal any instability that could justify the presence of diffraction spots observed experimentally during the mixing process.

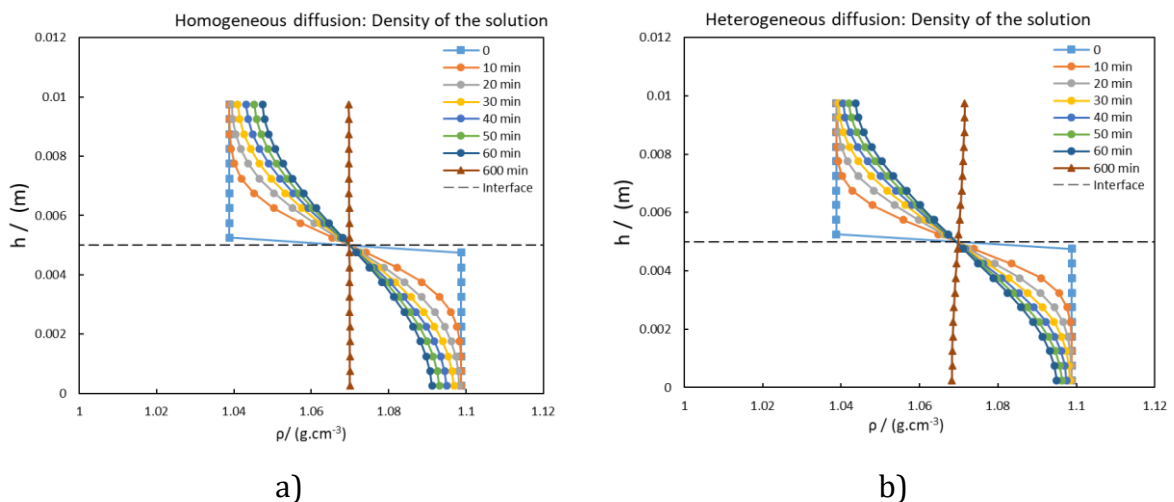


Figure 3.27: Evolution of the density of the solution over the column as a function of time when a layer of a CaCl_2 solution (0.46 mol.L^{-1}) is brought in contact with a NaCl solution (2.637 mol.L^{-1}) at

the homogenous temperature of 25 °C in the case of a) Homogeneous multicomponent diffusion and b) Heterogeneous multicomponent diffusion.

Homogeneous and heterogeneous multicomponent diffusion obtained when a layer of NaCl at the concentration of 2.637 mol.L⁻¹ is brought into contact with a layer of Na₂SO₄ at the concentration of 1.484 mol.L⁻¹ represented on Fig. 3.28 proved to be very different.

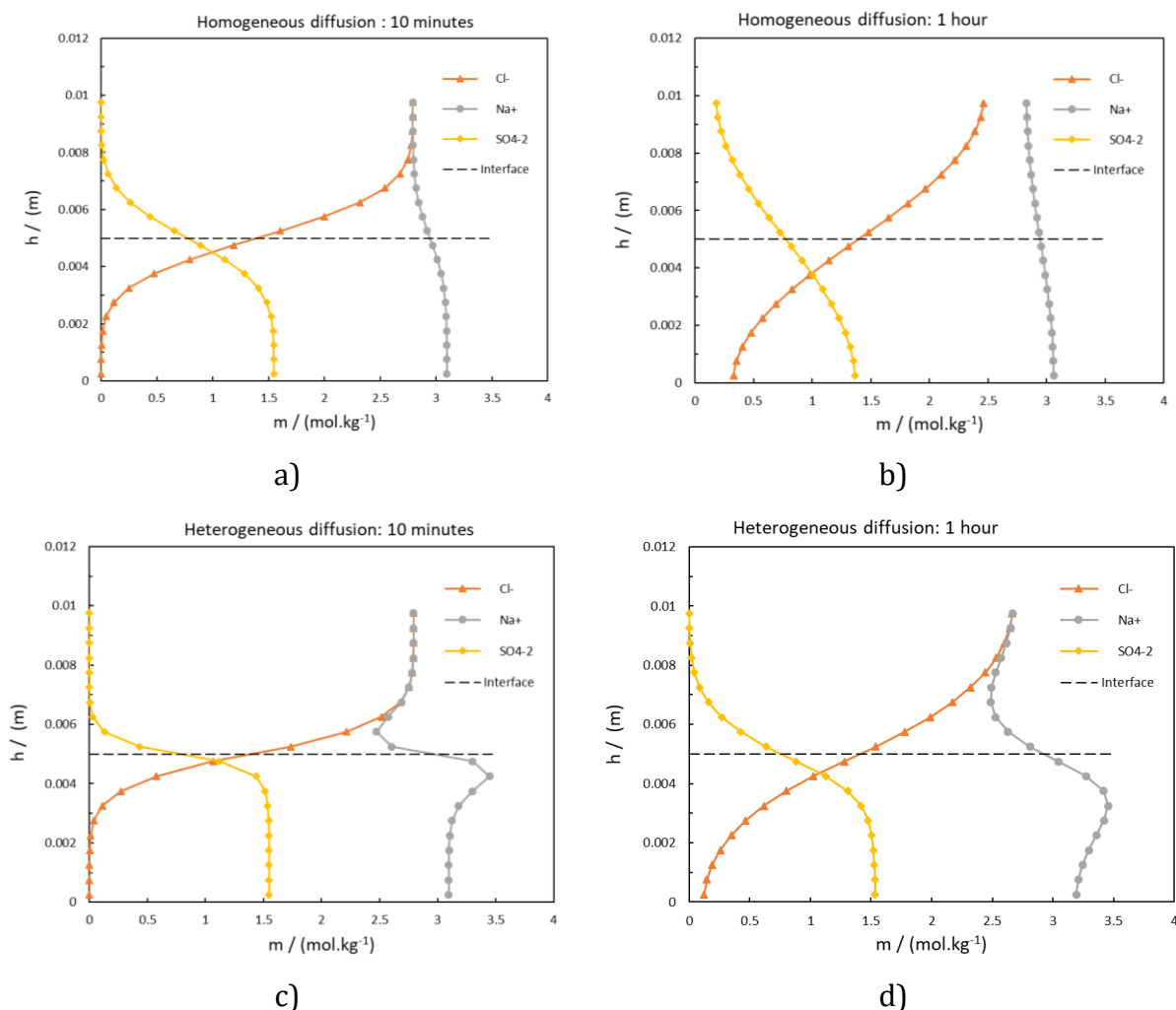


Figure 3.28: Evolution of the molality of ions when a layer of a NaCl solution (2.637 mol.L⁻¹) is brought in contact with a Na₂SO₄ solution (1.484 mol.L⁻¹) at the homogenous temperature of 25 °C in the case of a) Homogeneous multicomponent diffusion after 10 minutes of diffusion, b) Homogeneous multicomponent diffusion after 1 hour of diffusion, c) Heterogeneous multicomponent diffusion after 10 minutes of diffusion and d) Heterogeneous multicomponent diffusion after 1 hour of diffusion

In the case of homogeneous multicomponent diffusion, the evolution of the concentration inside the column after 10 minutes (Fig. 3.28-a) and 1 hour (Fig. 3.28-b) shows an intuitively expected behaviour: for each species, ions move from the more concentrated region towards the less concentrated one. This is also clearly visible on the evolution of the ionic strength over the column for different instants in Fig. 3.29-a. The results obtained for heterogeneous multicomponent diffusion inside the column after 10 minutes

(Fig. 3.28-c) and 1 hour (Fig. 3.28-d) present a non-intuitive behaviour, especially for the evolution of the concentration of the Na^+ ions. We observe that the Cl^- and SO_4^{2-} ions diffuse from the more concentrated area to the less concentrated area. However, for Na^+ ion, it is observed that in the first 10 minutes, before following the expected evolution, its concentration decreases in the upper part of the column instead of increasing, to become overconcentrated in the bottom part of the column, where it is initially most concentrated. This can be explained by the fact that Cl^- ions, which have a high diffusion velocity, carry with them, the Na^+ ions when diffusing downward, in order to respect the electroneutrality principle. It is also possible that there is a play of charges during the diffusion, due to the valence of the ions that could affect the behaviour of the system. This overconcentration of Na^+ ions towards the bottom of the column would have an impact on the evolution of the ionic strength as visible on Fig. 3.29-b.

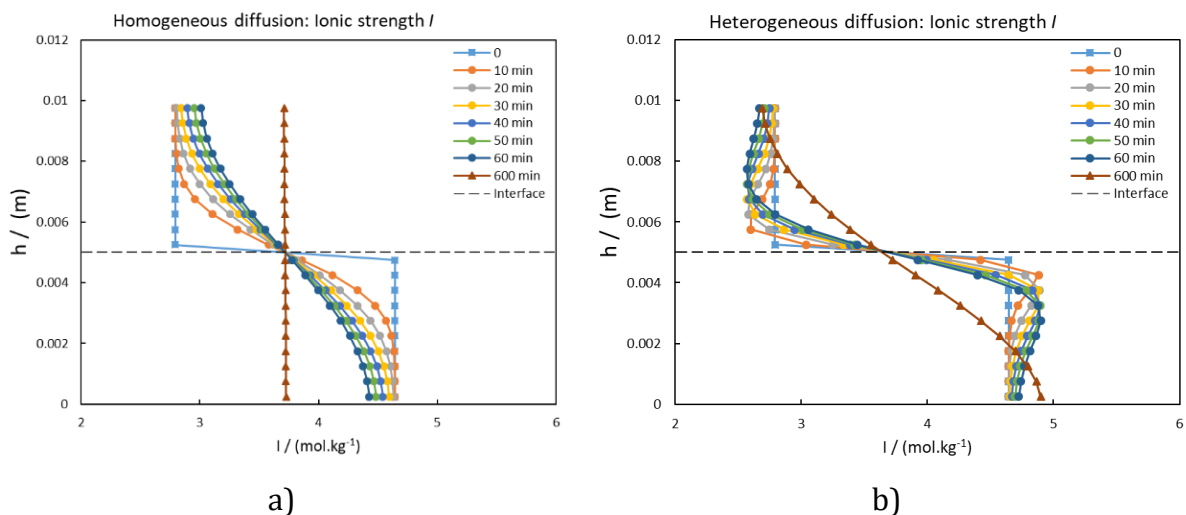


Figure 3.29: Evolution of the ionic strength profile as a function of time when a layer of a NaCl solution (2.637 mol.L^{-1}) is brought in contact with a Na_2SO_4 solution (1.484 mol.L^{-1}) at the homogenous temperature of $25 \text{ }^\circ\text{C}$ in the case of a) Homogeneous multicomponent diffusion and b) Heterogeneous multicomponent diffusion.

Fig. 3.30 illustrates the evolution of the density of the solution along the column as the diffusion process evolves. In the case of homogeneous multicomponent diffusion (Fig. 3.30-a), the evolution of the solution density along the column over time does not reveal any instability. However, in the case of multicomponent diffusion (Fig. 3.30-b), the evolution of the density of the solution along the column over time reveals an inversion of the density of the solution in the lower half of the column during a certain time before

the onset of the expected evolution. This unexpected result is in very consistent with the convection patterns observed experimentally for this system (Fig. 3.20-b) since the inversion densities should initiate downward advective flows of the denser fluid and the corresponding upward advective flows of the lighter fluid. These flows were not included in the numerical simulations performed in this study because of the no-flow option classically imposed in a priori diffusive-only closed systems.

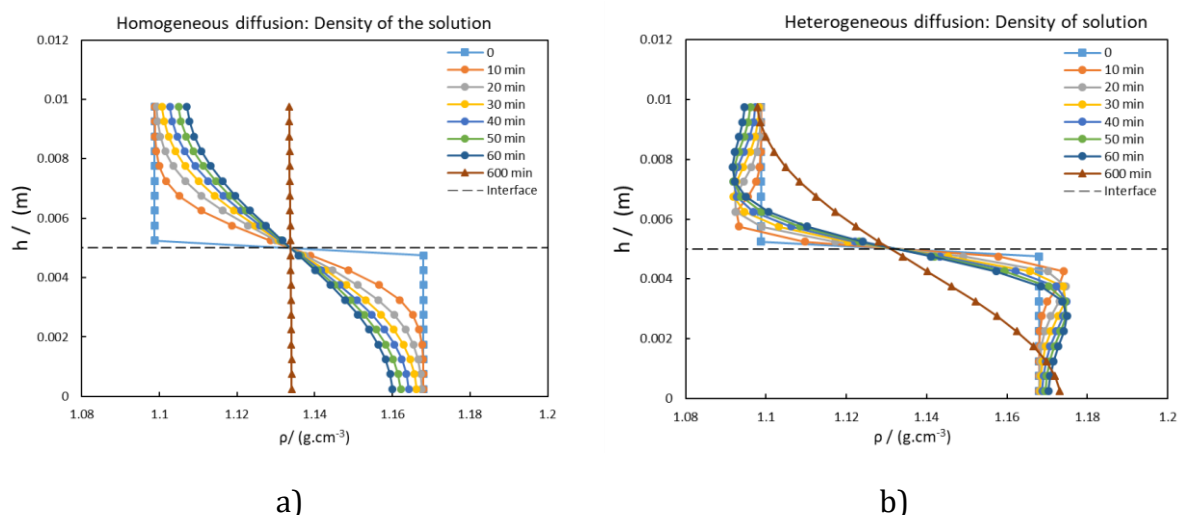


Figure 3.30: Evolution of the density of the solution over the column as a function of time when a layer of a NaCl solution (2.637 mol.L^{-1}) is brought in contact with a Na_2SO_4 solution (1.484 mol.L^{-1}) at the homogenous temperature of $25 \text{ }^\circ\text{C}$ in the case of a) Homogeneous multicomponent diffusion and b) Heterogeneous multicomponent diffusion.

3.5 Superimposition of two aqueous layers of reactive salts

When a CaCl_2 aqueous solution is brought into contact with a Na_2SO_4 aqueous solution, the diffusive mixing is expected to provoke the precipitation of gypsum, whose chemical composition is $\text{CaSO}_4 \cdot 2\text{H}_2\text{O}$. In the following sections, it is proposed to monitor the dynamics of such a process using the shadowgraph technique and to simulate it numerically for interpreting the observations.

3.5.1 Experimental observations parallel to the gravity

Using the same shadowgraph technique (shadowgraph setup#2), the reactive transport is investigated by superimposing three saline solutions in the same free-diffusion cell as shown previously on Fig. 1.18. The intermediate solution is meant to act as a buffer solution between the two reactive aqueous salt solutions. In this context, the cell is first filled with a solution of NaCl ($\rho = 1.099 \text{ g.cm}^{-3}$) with a concentration of 2.637 mol.L^{-1} . Once the filling of NaCl is completed, the solution of Na_2SO_4 ($\rho = 1.169 \text{ g.cm}^{-3}$) at a concentration

of 1.484 mol.L^{-1} is injected from the bottom, while the solution of CaCl_2 ($\rho = 1.039 \text{ g.cm}^{-3}$) at a concentration of 0.46 mol.L^{-1} is injected from the top by means of two outlets connected with the syringe pumps at a flow rate of $2 \times 1 \text{ mL/min}$. The two inlet reservoirs are kept at a same level in order to equalize the flow of the two saline solutions. Once the required amounts ($3/8$ of the cell) of Na_2SO_4 and CaCl_2 have been injected from the bottom and the top, respectively, all the inlets and outlets are closed immediately. The diffusion then starts, while an isothermal or non-isothermal state is maintained between the cell by means of temperature controllers.

The thickness a of the intermediate layer (Fig. 1.18) is therefore $1/4$ of the cell. The thicknesses of the top and bottom layers are $l_1 = l_2 = 3/8 \text{ cm}$, with a precision given by:

$$\Delta l_i = \frac{4}{\pi d^2} \Delta V_{asp} \quad (3.5)$$

where $d = 20 \text{ mm}$ is the internal diameter of the cell and V_{asp} are the volumes aspirated by the syringes of the syringe pump. The precision on the aspirated volumes, ΔV_{asp} , is estimated to be 0.5 mL , which gives $\Delta l_1 \approx 0.2 \text{ mm}$ and $\Delta a \approx 0.4 \text{ mm}$. The relative uncertainty on the thickness of the intermediate layer is therefore estimated to be 16% . The onset time of the precipitation is estimated with the formula:

$$t_p = \frac{a^2}{\pi D} \approx 34 \text{ min} \quad (3.6)$$

where $D = 9.73 \times 10^{-6} \text{ cm}^2/\text{s}$. We have estimated the D value assuming a homogeneous diffusion and calculating it with an harmonic mean of the diffusion coefficients of the salts, weighted by their molal concentrations. The accuracy of the precipitation time is estimated by:

$$\Delta t_p = 2t_p \frac{\Delta a}{a} \approx 10 \text{ min.} \quad (3.7)$$

Taking into account the experimental set-up used and the filling method practiced, we estimate the time of appearance of gypsum in the cell to range between 20 and 40 minutes.

In Fig. 3.31-a, we report the contrast of the images as a function of time and for different moments after closing the valves for the isothermal case at 25 °C.

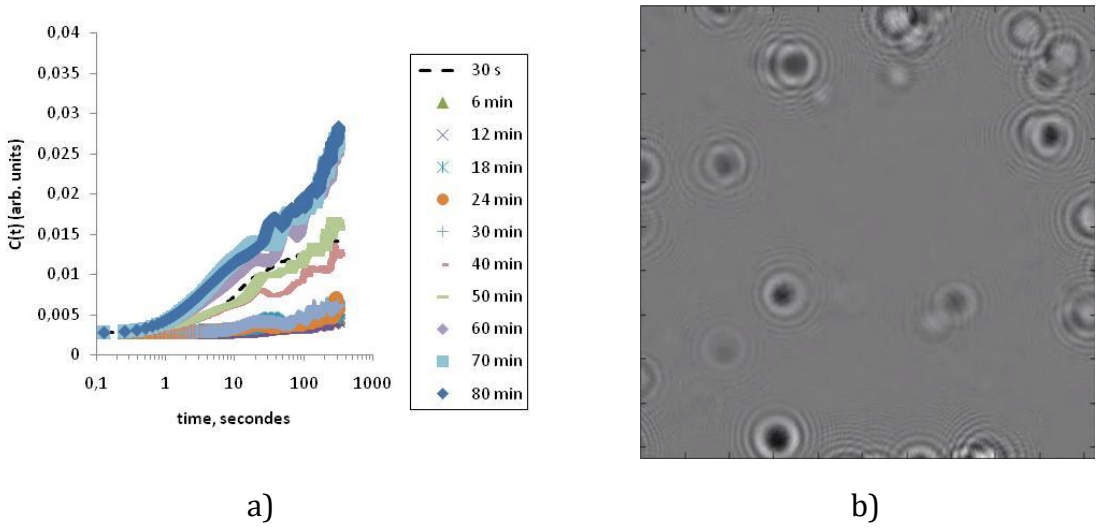


Figure 3.31: a) Contrast of shadowgraph image sequences $C(t)$ as a function of time and for different moments after closing the valves in the case of the superimposition of the three layers at homogenous temperature of 25°C; b) normalized image differences 50 minutes after closing the valves.

In the early stages, a strong variation in the contrast of the images is associated to convection patterns (dashed ligne in Fig. 3.31-a), a result that is consistent with the observations made on the relative dissolution of NaCl in Na₂SO₄. Then the contrast decreases very quickly. It increases sharply again after 40 minutes. This rapid variation in contrast is associated with the appearance of diffraction spots as shown in Fig. 3.31-b that we associate with the onset of precipitation.

As shown in Fig. 3.32, direct observation of the shadowgraph images reveals that a solid phase appears from the cell periphery after 1h, and which grows inwards the cell.

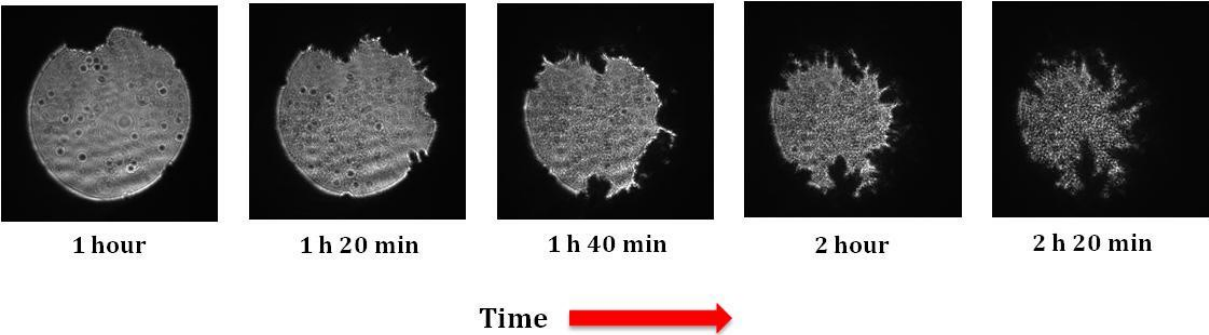


Figure 3.32: Full resolution shadowgraph images 1 hour to 2h20 after closing the valves in the case of the superimposition of the three layers at homogenous temperature of 25 °C.

When a vertical and positive thermal gradient is applied, convection patterns appear at the first moments with a variable intensity (dashed lines in Fig. 3.33-a, b and c). The onset time of precipitation t_p , which corresponds to an increase in the contrast of the images associated to the sudden appearance of diffraction spots, is indicated on Figs. 3.33-a, b, c and d.

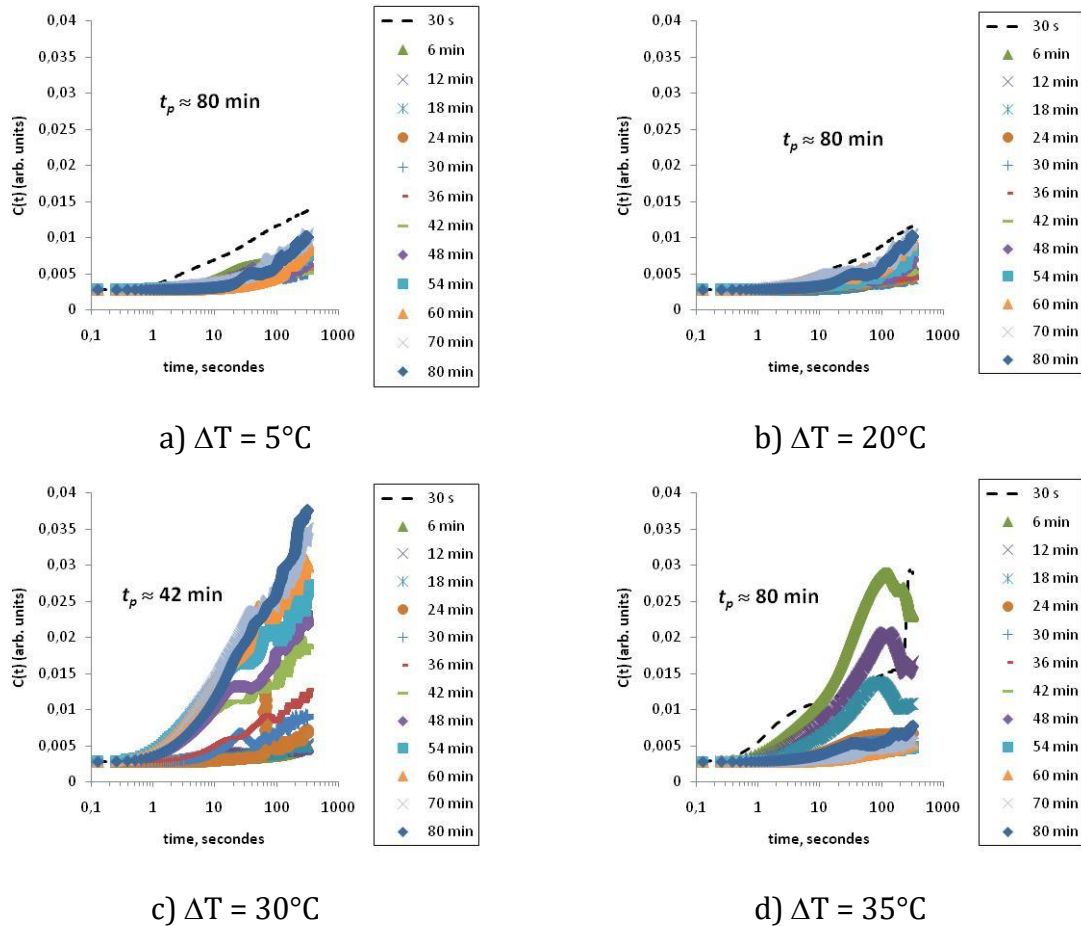


Figure 3.33: a) Contrast of shadowgraph image sequences $C(t)$ as a function of time and for different moments after closing the valves in the case of the superimposition of the three layers with a vertical difference of temperature ΔT across the cell.

For $\Delta T = 20^\circ\text{C}$, the experiments were repeated twice. The results are shown in Fig. 3.34.

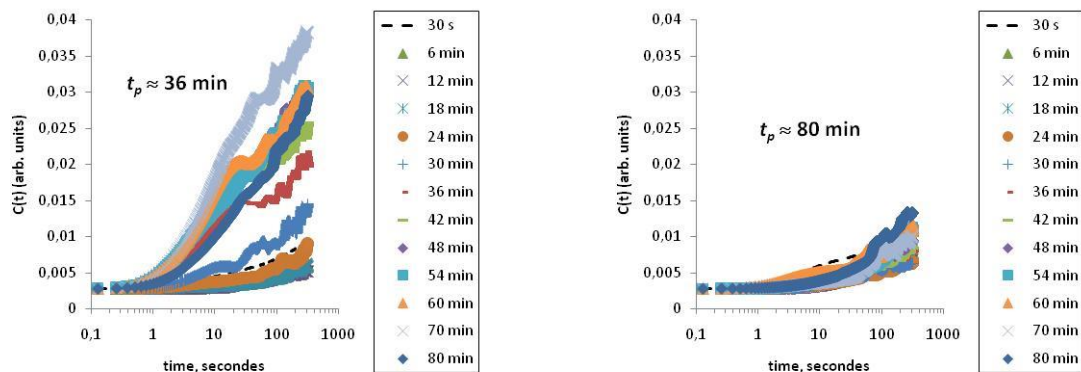


Figure 3.34: Repetition of the superimposition of the three layers with a vertical difference of temperature $\Delta T = 20^\circ\text{C}$ across the cell (contrast of shadowgraph image sequences $C(t)$ as a function of time and for different moments after closing the valves).

Regardless of the thermal gradient applied, the onset time of precipitation all ranged between 40 and 80 min. On the basis of the observations made, by analysing the evolution of the image contrast as a function of time, we can conclude that the applied thermal gradient did not have a noticeable influence on the onset time of precipitation. Moreover, it can be noted that the precipitation times measured experimentally are systematically higher than the precipitation times predicted on the basis of a calculation assuming homogeneous diffusion (see Eq. 3.6).

3.5.2 Numerical modelling

To remain roughly in the same proportions as the experimental configuration, we defined the mesh as represented in Fig. 3.35. The column has a height of $h = 0.01$ m as our experimental diffusion cell, which is subdivided into 20 cells (5×10^{-4} m) of equal length in order to have detailed information on the phenomena that may occur in the column. Inside the column, the superimposition of the 3 layers is organised as follows: the top of the column is filled with the aqueous solution of CaCl_2 ($\rho = 1.039 \text{ g.cm}^{-3}$) at a concentration of $0.475 \text{ mol.kg}^{-1}$ and the bottom of the column is filled with the solution Na_2SO_4 ($\rho = 1.169 \text{ g.cm}^{-3}$) at a concentration of $1.548 \text{ mol.kg}^{-1}$. Each layer of solution is distributed over 7 cells whose total height is 3.5×10^{-3} m. The buffer solution (NaCl , $\rho = 1.099 \text{ g.cm}^{-3}$ with a concentration of $2.792 \text{ mol.kg}^{-1}$) is set between the two reactive aqueous salts solutions and is distributed over 6 cells whose total height is 3×10^{-3} m.

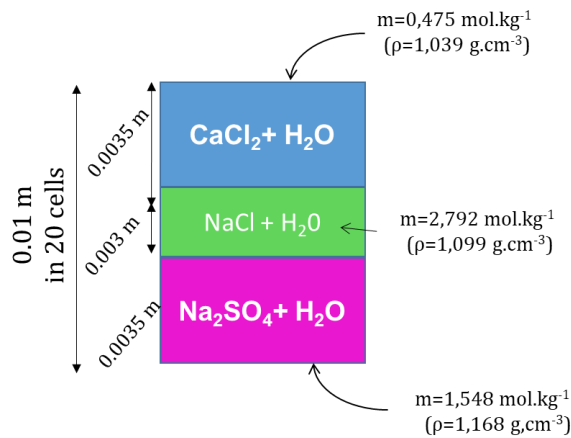


Figure 3.35: Mesh of the numerical modelling of the superimposition of a layer of a CaCl_2 solution (0.46 mol.L^{-1}) with a layer of a Na_2SO_4 solution (1.484 mol.L^{-1}) separated by a layer of NaCl solution (2.637 mol.L^{-1}).

The closed boundary conditions is applied. The activity model used is the interaction model based on the Pitzer formalism, which is suitable for our complex chemical system with high salinity. The diffusive flux is calculated with both homogeneous and heterogeneous multicomponent diffusion for comparison. The diffusion coefficient defined for calculations in the case of the homogeneous multicomponent diffusion is $D = 1.40 \times 10^{-9} \text{ m}^2 \cdot \text{s}^{-1}$. The appropriate parameters to account for gypsum precipitation from a numerical point of view are the saturation index and the amount the mineral (gypsum) formed over time.

For the isothermal case at homogenous temperature of 25 °C, the results are shown in Fig. 3.36.

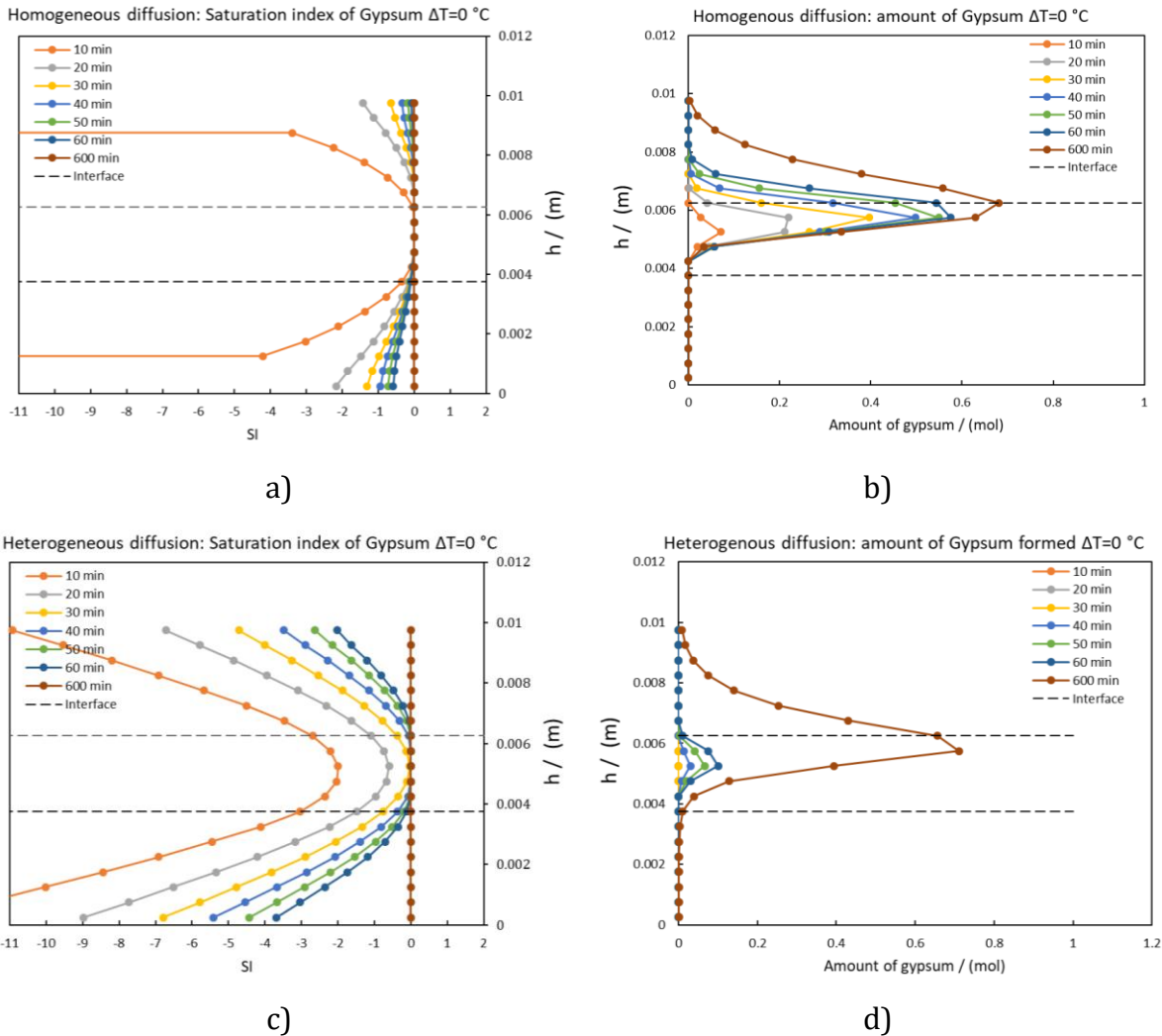


Figure 3.36: Evolution of the profile of the saturation index of gypsum as a function of time at 25 °C and isothermal case $\Delta T = 0$ °C a) homogeneous multicomponent diffusion, c) heterogeneous multicomponent diffusion. Evolution of the total amount of precipitated Gypsum along the column as a function of time: b) homogeneous multicomponent diffusion, d) heterogeneous multicomponent diffusion.

The dashed lines represent the interface where the buffer solution (NaCl) was initially present. Of course, this interface evolves with time. The saturation index in the case of homogeneous and heterogeneous multicomponent diffusion presents an asymmetric behaviour with respect to the interface as can be seen on Fig. 3.36-a and c. According to these curves, one can note that gypsum precipitates much more quickly in the case of homogeneous multicomponent diffusion than in the case of heterogeneous multicomponent diffusion. This is clearly visible in Fig. 3.36-b and d, which represent the quantity of gypsum formed along the column when the solution becomes supersaturated with the mineral phase. We can see that gypsum starts to precipitate after 10 minutes in the case of homogeneous multicomponent diffusion, whereas the precipitation appears after 40 minutes in the case of heterogeneous multicomponent diffusion. The latter is rather in agreement with the experimental observations.

When a positive thermal gradient is applied, the diffusive flux calculated via the homogeneous multicomponent diffusion presents some limits because, in PhreeqC, the diffusion coefficient is not corrected for changes of temperature. Therefore, an impact of the thermal gradient is not expected in the case of homogeneous multicomponent diffusion. In the case of heterogeneous multicomponent diffusion, the diffusion coefficient is temperature corrected according to Eq. 2.52.

Before applying any temperature gradient to the column, it is important to know the transition temperature between gypsum ($\text{CaSO}_4 \cdot 2\text{H}_2\text{O}$) and anhydrite (CaSO_4) for the studied system. Indeed, in contact with an aqueous solution, gypsum can dehydrate and turn into anhydrite above a transition temperature whose value depends not only on the type of electrolyte involved, but also on the salinity. This has been shown experimentally in the context of CO_2 storage by Pironon *et al.* [193]: the evaporation of water into the rich sCO_2 phase increases the salinity of the solution and provokes gypsum dehydration at temperatures lower than in pure water. Therefore, in order to know this transition temperature, we studied the curve of the saturation indices of these two minerals as a function of the temperature for each saline solution used in the diffusion column.

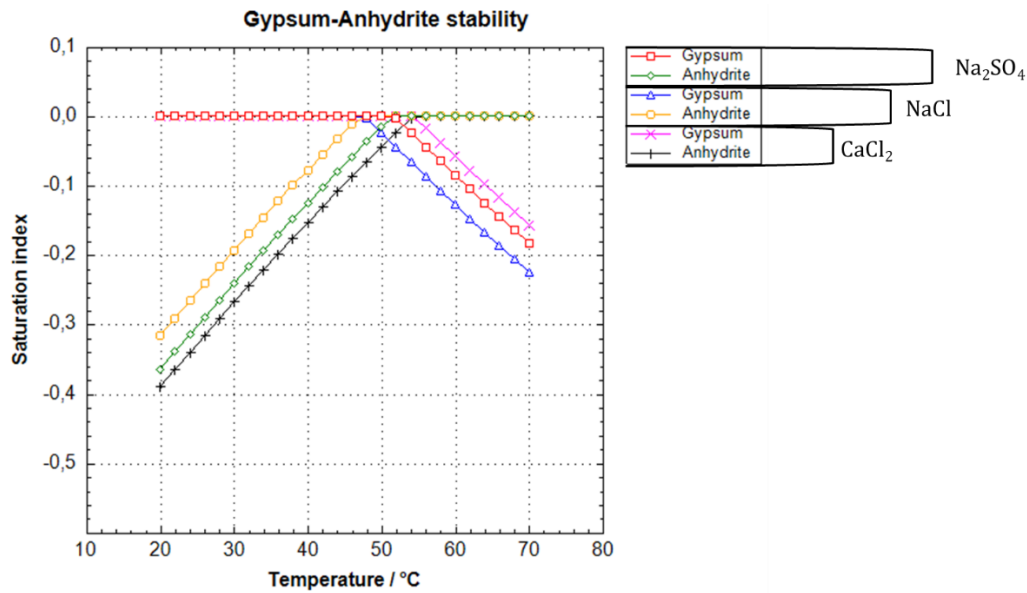
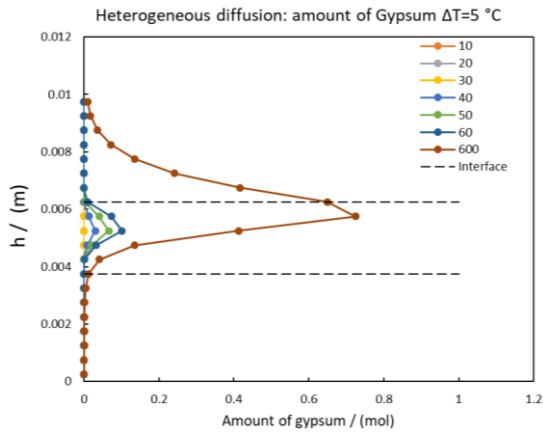


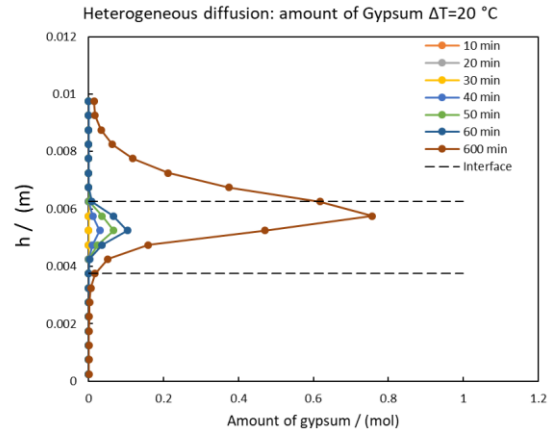
Figure 3.37: Saturation indices of gypsum and anhydrite in binary aqueous Na_2SO_4 , NaCl and CaCl_2 solutions at equilibrium with the most stable of the two phases over the temperature range 20 to 70 °C. The size of the boxes on the right side of the chart is indicative of the salinity of the aqueous solutions.

According to Fig. 3.37, the transition temperature between gypsum and anhydrite decreases with the increase of the concentration. In fact, for the solution of CaCl_2 at a concentration of $0.475 \text{ mol.kg}^{-1}$, the transition temperature, represented by intersection of the magenta and black lines, is around 54 °C. For the solution of Na_2SO_4 at a concentration of $1.548 \text{ mol.kg}^{-1}$, the transition temperature, represented by the intersection of the red and green lines, is around 52 °C. For the solution NaCl at a concentration of $2.792 \text{ mol.kg}^{-1}$, the transition temperature, represented by the intersection of the blue and yellow lines, is around 48 °C. The chemical system of interest is at an average temperature of 25 °C. Applying temperature gradients of $\Delta T = 5, 20, 30$ or 35 °C does not shift the system outside the stability domain of gypsum.

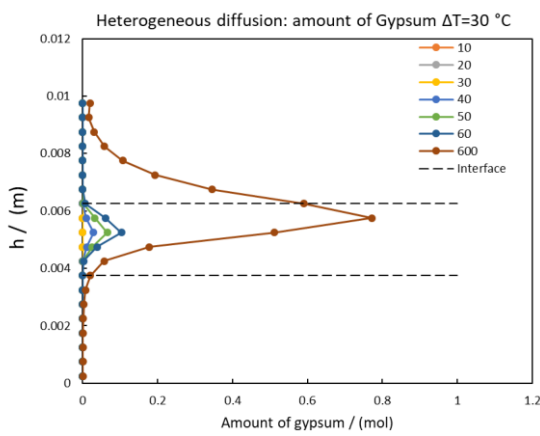
To observe whether there are relevant effects of the temperature gradient in the case of heterogeneous multicomponent diffusion, one representative parameter is the quantity of gypsum formed along the column represented in Fig. 3.38.



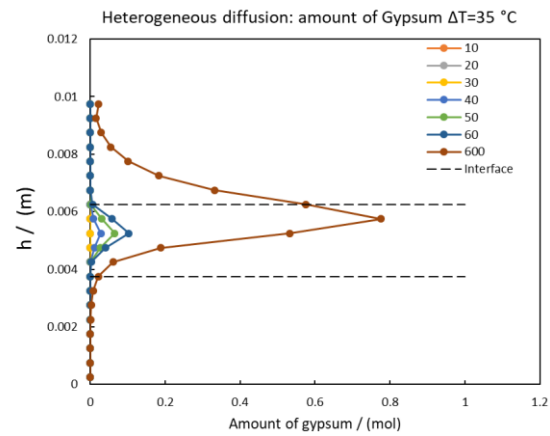
a) $\Delta T = 5^{\circ}\text{C}$



b) $\Delta T = 20^{\circ}\text{C}$



c) $\Delta T = 30^{\circ}\text{C}$



d) $\Delta T = 35^{\circ}\text{C}$

Figure 3.38: Evolution of the total amount of Gypsum precipitated along the column as a function of time in the case of heterogeneous multicomponent diffusion for different temperature gradients.

From Fig. 3.38, we observe that whatever the temperature gradient applied, the precipitation of gypsum appears after about 40 minutes as we observed in the case of isothermal diffusion. Furthermore, the amount of gypsum that forms at any given time is almost the same, regardless of the temperature gradient. Based on these results, we can conclude that the applied thermal gradient did not have a noticeable influence on the precipitation of gypsum. This result is in good agreement with the experimental observations.

3.5.3 Experimental observations perpendicular to the gravity

The experimental setup works like interferometric techniques but is still based on the shadowgraphy technique like in the previous configuration. The difference lies in the path of the light beam that passes through the diffusion cell in a lateral way, perpendicular to the gravity, in order to have a lateral visualization of what is happening in the diffusion cell. The principle scheme is illustrated in Fig. 3.39.

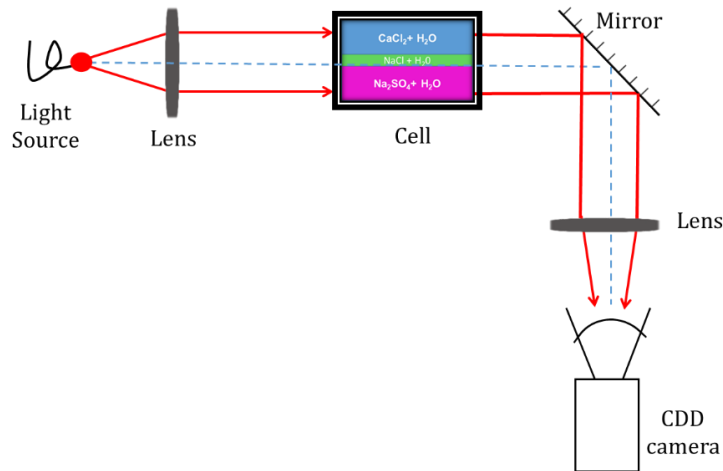


Figure 3.39: working principle of the transversal configuration of the shadowgraphic device.

In this configuration, the entire light beam passes horizontally through the diffusion cell, and, unlike interferometric methods, there is neither a beam splitter nor a reference beam. A super-luminescent diode (Super Lumen, SLD- MS-261-MP2-SM, $\lambda = 675 \pm 13 \text{ nm}$) is connected to a single-mode optical fiber. The divergent beam at the output of the fiber is collimated by an achromatic doublet lens (focal length $f = 150 \text{ mm}$, and diameter $\phi = 50.8 \text{ mm}$). After passing through the diffusion cell the light beam is reflected on a mirror and is re-collimated by a second converging lens to form a shadowgram captured by a CCD PIKE camera.

A new diffusion cell (Fig. 3.40) was specifically designed to fit with this configuration. Like the previous diffusion cell sketched in Fig. 3.2, this cell allows putting into contact two layers of two different liquid mixtures or two solutions made of the same compounds at different concentrations, thus creating an initial step concentration gradient at uniform temperature while providing horizontal optical access to a central area. The diffusion cell in Fig. 3.40 consists of a metal cylinder with internal and external diameters of 15 mm and 25 mm, respectively, and a vertical thickness of $h = 10 \text{ mm}$. This metal cylinder hosts four

holes: two for fluid inlets at 180° in the vertical plane and at mid-height of the cell in the vertical direction and two for fluids outlets at 180° in the horizontal plane and at mid-height of the cell in the vertical direction. This cell does not allow temperature gradients to be imposed. The metal cylinder is designed to accommodate two sapphire windows, one on each horizontal side with a groove for a Viton® O-ring to prevent leakage. All the elements are clamped with two aluminium blocks (with the same central circular aperture). The two connectors for fluids outlet are connected to 2 syringes, each well attached to a syringe pumps.

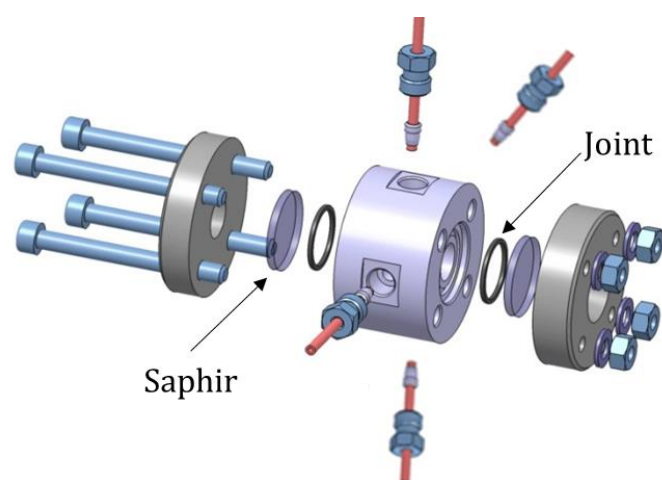
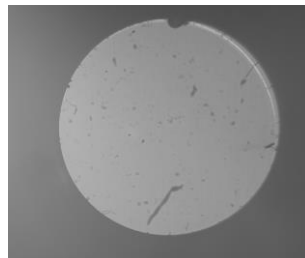


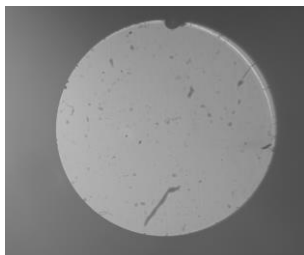
Figure 3.40: 3D drawing of the diffusion cell for the transversal configuration of the shadowgraphic device.

The filling of this diffusion cell is performed at a controlled rate using syringe pumps that act as outlet reservoirs, and contain NaCl solution. First, the syringe pumps infuse the buffer solution of NaCl ($\rho = 1.099 \text{ g.cm}^{-3}$) with a concentration of 2.637 mol.L^{-1} until the cell is completely filled (Fig. 3.41-a). The two inlet reservoirs (containing CaCl_2 and Na_2SO_4) are kept at a same level with the syringe pumps in order to equalize the flow of the two saline solutions (Fig. 3.41-b). Then, the syringe pumps withdraw the NaCl solution initially present in the cell at a flow rate of $2 \times 1 \text{ mL.min}^{-1}$, allowing the simultaneous injection of CaCl_2 ($\rho = 1.039 \text{ g.cm}^{-3}$) at a concentration of 0.46 mol.L^{-1} from the top and the solution of Na_2SO_4 ($\rho = 1.169 \text{ g.cm}^{-3}$) at a concentration of 1.484 mol.L^{-1} from the bottom (Fig. 3.41-d). Because, the length of the capillary tubes of the inlet reservoir is not the same, CaCl_2 solutions arrives first in the cell (Fig. 3.41-c). After each syringe has aspirated 2 mL more of NaCl solution, the valves are closed (Fig. 3.41-e) and we obtain a well stratified superimposition of the 3 layers, clearly visible in Fig. 3.41-f. The layer of the buffer solution being thick, we reduce it by further aspiration of 3 ml of NaCl solution by each syringe pump. (Fig. 3.41-g). It is important to note that the total volume aspirated

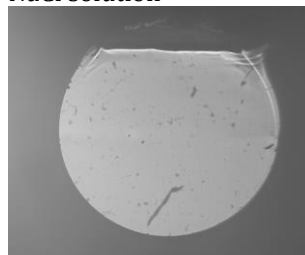
from the syringe pumps does not correspond to the total volume directly aspirated from the diffusion cell. The volume of capillary tubes and dead volumes must be taken into account to have the real volume of each layer of solution in the diffusion cell. Few minutes later after closing the valves, we observe some dark spots (kind of crystals) in the view field, only located in the upper part of the cell (Fig. 3.41-h). If we refer to the solutions involved and to the temperature and pressure conditions (25 °C and 1 atm), we can assume that these crystals correspond to Gypsum precipitates. Few minutes later, the precipitate of Gypsum is more and more visible and appears preferentially in the upper part of the cell (Fig. 3.41-i). The day after the mixture has reached its equilibrium state, a part of the Gypsum formed falls into the bottom of the cell (Fig. 3.41-j).



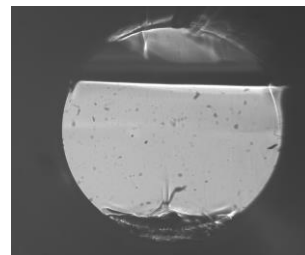
a) Cell completely filled with NaCl solution



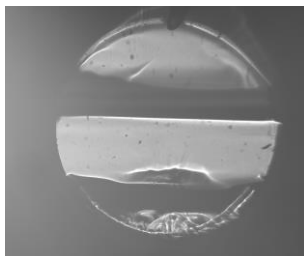
b) the four valves are open to allow the circulation of fluids



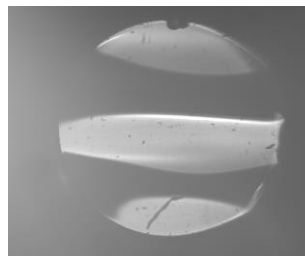
c) Arrival of CaCl_2 solution from the top: 1ml were aspirated



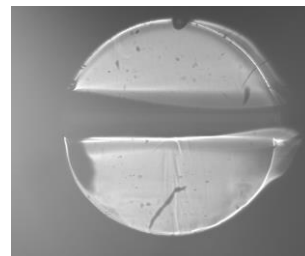
d) Arrival of Na_2SO_4 solution from the bottom: 1ml were aspirated



e) 2x2ml aspirated; All the valves are closed



f) Few minutes later: 3 layers of solutions



g) The valves are opened, then aspiration of 2x3ml

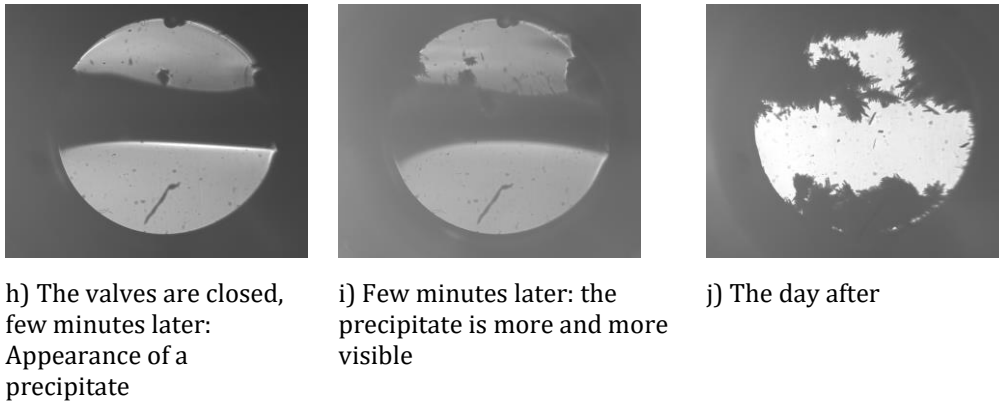


Figure 3.41: Full resolution shadowgraph images after closing the valves in the case of the superimposition of the three layers at homogenous temperature of 25 °C.

In the following paragraph, we propose to give a numerical interpretation of the results obtained experimentally.

3.5.4 Numerical modelling

The conditions of the simulation are the same as in the previous case. The main difference lies in the description of the mesh. In the present case, the thickness of the buffer solution is thinner while the thickness of the layers of CaCl_2 and Na_2SO_4 solution are greater than in the previous case. Here, the top of the column is filled with the aqueous solution of CaCl_2 and the bottom of the column is filled with the solution of Na_2SO_4 . Each solution is distributed over 9 cells whose total height is 4.5×10^{-3} m. The buffer solution is set between two reactive aqueous salts solutions and is distributed over 2 cells whose total height is 1×10^{-3} m. Fig. 3.42 shows the initial concentration profile, where three layers of aqueous CaCl_2 , NaCl and Na_2SO_4 solutions are superimposed in a 1D column at homogenous temperature and pressure of 25 °C and 1 atm, respectively. The dashed lines delimitate the buffer solution interface located between the two reactive aqueous saline solutions.

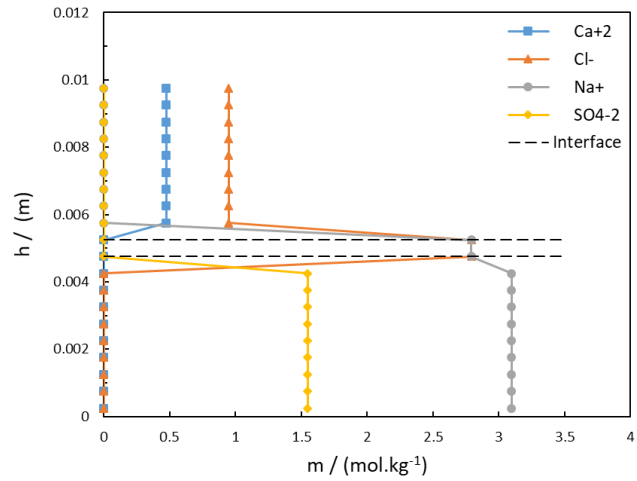
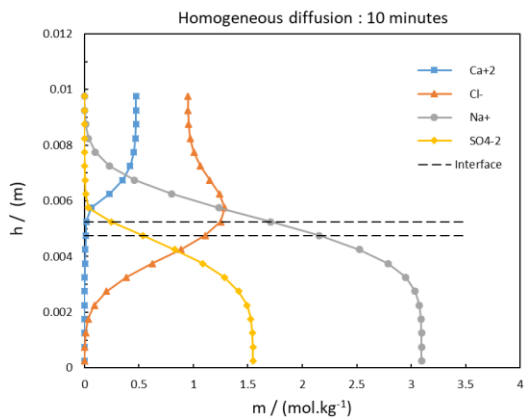
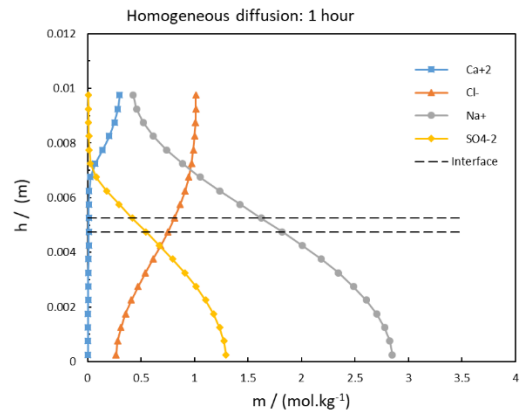


Figure 3.42: Initial concentration profile within the simulated column, at the homogenous temperature of 25 °C and 1 atm.

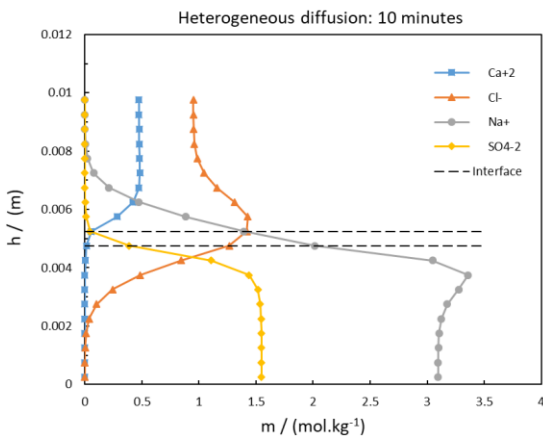
The system is allowed to diffuse over time and the diffusive flux is calculated with both homogeneous and heterogeneous multicomponent diffusion for comparison.



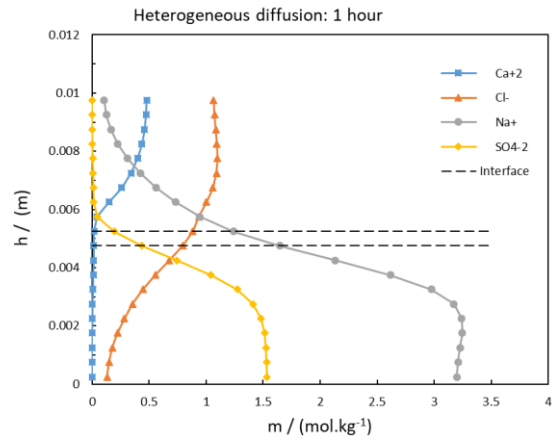
a)



b)



c)



d)

Figure 3.43: Evolution of the molality of ions when layers of binary aqueous CaCl_2 , NaCl and Na_2SO_4 solutions are superimposed at the homogenous temperature of 25 °C in the case of a)

Homogeneous multicomponent diffusion after 10 minutes of diffusion, b) Homogeneous multicomponent diffusion after 1 hour of diffusion, c) Heterogeneous multicomponent diffusion after 10 minutes of diffusion and d) Heterogeneous multicomponent diffusion after 1 hour of diffusion

Fig. 3.43 is a comparison between homogeneous and heterogeneous multicomponent diffusion of the superimposition of the three layers of binary aqueous CaCl_2 , NaCl and Na_2SO_4 solutions along the column after 10 and 60 minutes of diffusion. The evolution of the concentrations follows an intuitively expected behaviour in the case of homogenous diffusion while it follows a non-intuitive behaviour in the case of heterogeneous multicomponent diffusion in comparison with the initial state in Fig. 3.42. This is directly related to the superimposition of two non-reactive salts described in section 3.4.2. One can note that in all the cases, the concentration of Ca^{2+} ions decreases well in the upper part of the column where it was initially present, but tends to vanish close to and below the initial location of the upper interface as the diffusion process evolves. This means that the Ca^{2+} reacts with SO_4^{2-} , which, in comparison, is in excess in the medium. This is the reason why the concentration of SO_4^{2-} increases in the upper part of the cell while that of Ca^{2+} tends to vanish. Moreover, we can see that, after 10 minutes of diffusion, the point of equal concentration between Ca^{2+} and SO_4^{2-} is at the upper limit of the interface but closer to the interface in the case of heterogeneous multicomponent diffusion (Fig. 3.43-c) than in the case of homogeneous multicomponent diffusion (Fig. 3.43-a). This point of equal concentration further moves upwards after 1 hour, and remains closer to the interface in the case of heterogeneous multicomponent diffusion (Fig. 3.43-d) than in the case of homogeneous multicomponent diffusion (Fig. 3.43-b). This is already indicative of the location where we expect to have the formation of the gypsum in both cases.

For a same diffusion time, 1 hour for example (Fig. 3.43-b and Fig. 3.43-d), the diffusion of ionic species reaches the equilibrium state faster in the case of homogeneous diffusion than in the case of heterogeneous diffusion. This is clearly visible in Fig. 3.44 that illustrates the evolution of the ionic strength along the column for different moments after the beginning of the diffusion. Fig. 3.44-a, shows that the system is close to the equilibrium state after 10 hours (600 minutes) in the case of homogeneous diffusion. In contrast, Fig. 3.44-b shows that the diffusion process still evolves for the same instant in the case of heterogeneous diffusion. Therefore, according to the behaviour of the ionic strength, heterogeneous multicomponent diffusion slows down the simulated diffusion process compared to homogeneous diffusion.

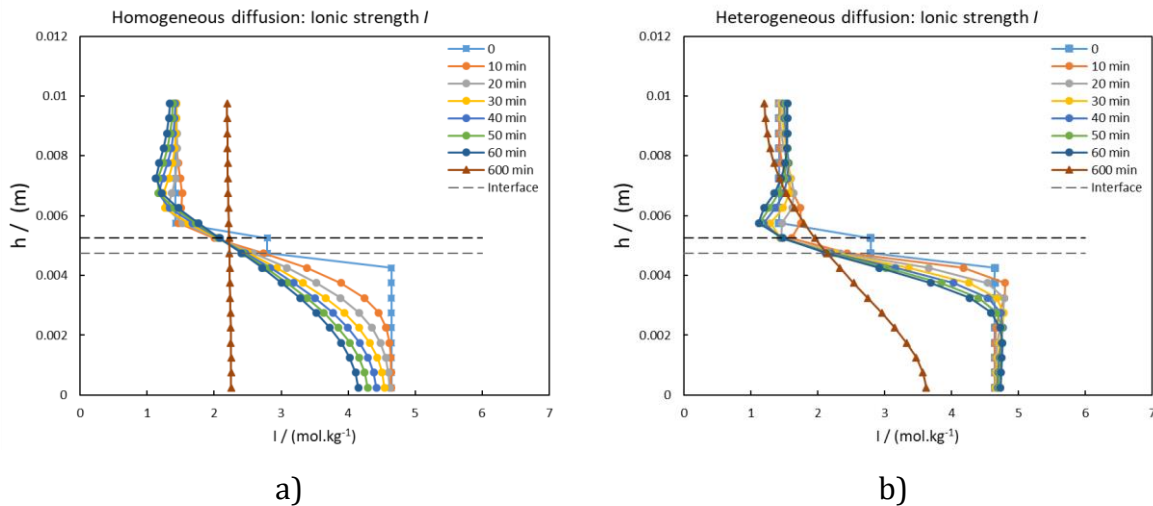
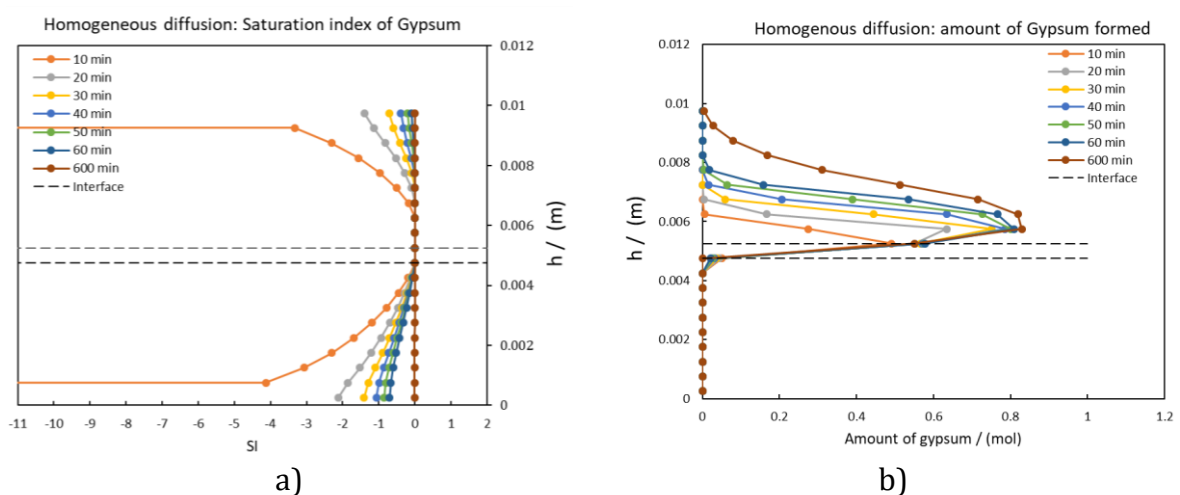


Figure 3.44: Evolution of the ionic strength profile as a function of time when layers of binary aqueous CaCl_2 , NaCl and Na_2SO_4 solution are superimposed at the homogenous temperature of 25°C in the case of a) homogeneous multicomponent diffusion and b) heterogeneous multicomponent diffusion.

It is interesting to note that the ionic strength presents an asymmetric behaviour with respect to the initial ionic strength both in homogeneous and heterogeneous multicomponent diffusion conditions. The presence of those 3 saline solutions offers a lot of degrees of freedom to each ionic species. The evolution of the ionic strength therefore depends on the way in which the ions move. It is important to remember that the ionic strength depends on the molality but also on the square of the charge of each species.

To have a precise location where the gypsum precipitates, the appropriate parameters are the saturation index and the amount the mineral (gypsum) formed over time.



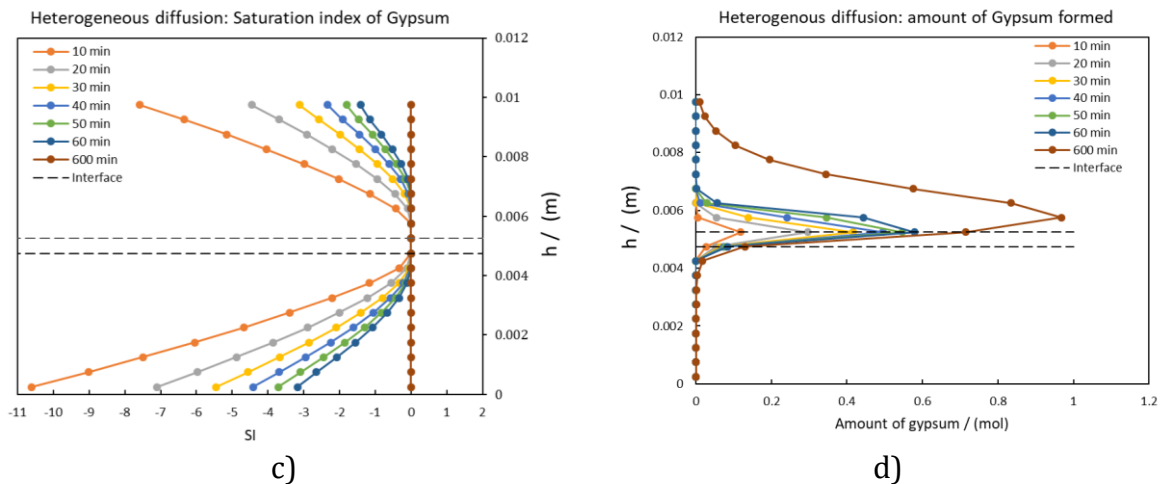


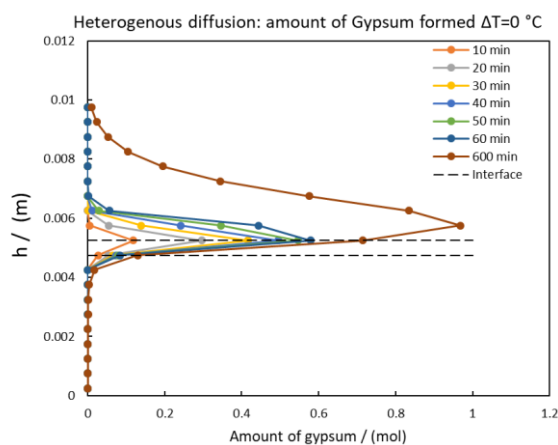
Figure 3.45: Evolution of the profile of the saturation index of gypsum as a function of time a) homogeneous multicomponent diffusion, c) heterogeneous multicomponent diffusion. Evolution of the total amount of pure Gypsum in the pure phase assemblage along the column as a function of time: b) homogeneous multicomponent diffusion, d) heterogeneous multicomponent diffusion.

The saturation index in the case of homogeneous and heterogeneous multicomponent diffusion presents an asymmetric behaviour with respect to the interface as can be seen on Fig. 3.45-a and c. According to these curves, one can note that the precipitation of gypsum is preferentially located in the upper part of the column as we observed experimentally in Fig. 3.41. However, from Fig. 3.45-a and c, gypsum seems to precipitate also in the lower part of the column after 600 minutes ($SI \approx 0$ along the whole column). It is actually not the case, and it is simply due to an effect of scale. This is clearly visible in Fig. 3.45-b and d, which represents the quantity of gypsum formed along the column when the solution becomes supersaturated with the mineral phase. It is easily visible that gypsum preferentially precipitates in the upper part of the column whether in homogeneous (Fig. 3.45-b) or heterogeneous (Fig. 3.45-d) multicomponent diffusion conditions. However, as observed with the evolution of the molalities, the precipitation of gypsum is closer to the interface in the case of heterogeneous multicomponent diffusion than in the other case. Moreover, the quantity of the mineral formed is greater in homogeneous diffusion than in heterogeneous diffusion over a period of one hour. Nevertheless, the amount of mineral formed in the case of homogeneous diffusion slows down towards the end as equilibrium is approached.

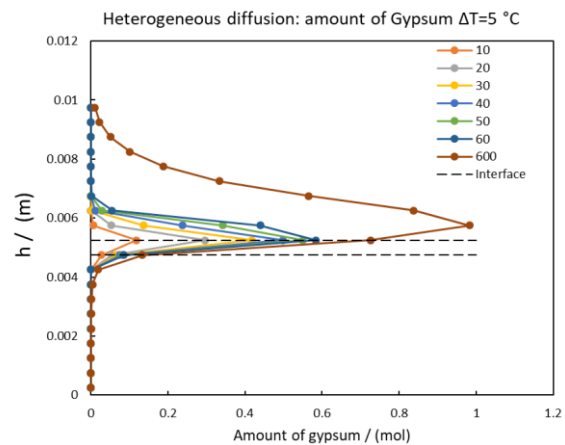
Whether in homogeneous or heterogeneous multicomponent diffusion, the gypsum precipitates preferentially in the upper part of the column. This result is in very good agreement with the experimental observations. It is therefore difficult to decide which of these conditions is preferable. However, we have previously shown that the results

obtained with heterogeneous multicomponent diffusion were consistent with the instabilities found in the diffusion cell since the constitutive equations (Eq. 2.48 to 2.52) better describe the interactions between all ionic species involved. Heterogeneous multicomponent diffusion has a significant effect on the simulated behaviour of the system despite being in a free (but static) aqueous system. In a real complex multicomponent system with other minerals, the consequences can be a shift of the level of the precipitation of a given mineral, leading to a possible modification of a reaction path. The results show that it would be necessary to be very precise on the sensitive areas where the system is very reactive because there can be non-intuitive behaviour. Heterogeneous multicomponent diffusion therefore has a significant particular interest.

For this configuration, the temperature gradient was not imposed and the reactions occurred under isothermal conditions at homogeneous temperature of 25 °C. However, it would be interesting to know if with a thinner layer of buffer solution, the temperature gradient could have a significant impact on the system. As already explained, applying temperature gradients of $\Delta T = 5, 20$ or 30 °C does not shift the system outside the stability domain of gypsum. To observe whether or not there are relevant effects of the temperature gradient, one representative parameter is the quantity of gypsum formed along the column.



a) $\Delta T = 0$ °C



b) $\Delta T = 5$ °C

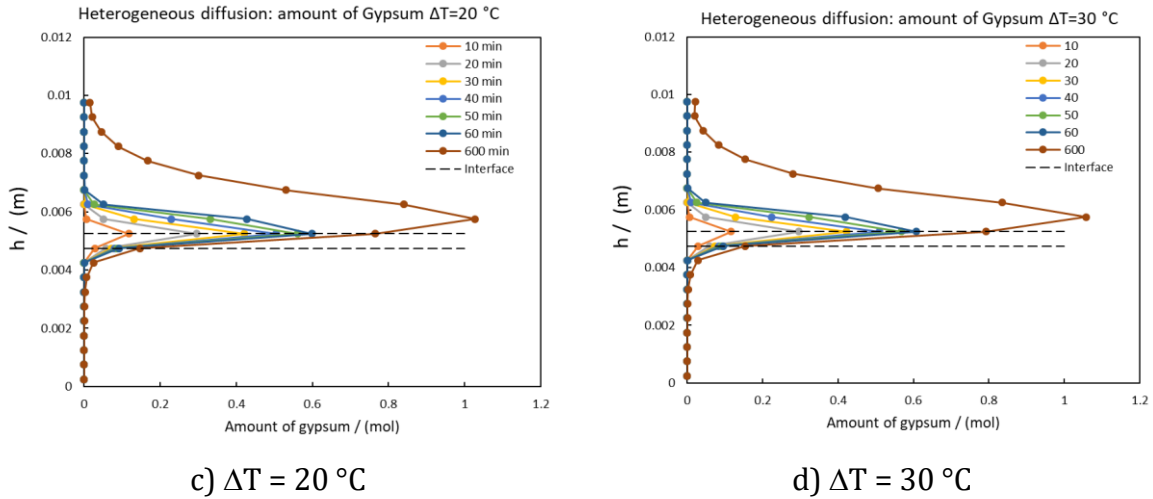


Figure 3.46: Evolution of the total amount of pure Gypsum in the pure phase assemblage over the column as a function of time in the case of heterogeneous multicomponent diffusion for different temperature gradient.

Fig. 3.46 shows that whatever the temperature gradient that is applied to the column, this does not seem to have a significant influence on the precipitation of the gypsum, and this over a period of up to one hour of diffusion. Over time, a slight effect on gypsum precipitation can be noticed: the greater the temperature gradient, the greater the quantity of mineral formed at greater times. But, this strongly depends on the thickness of the the buffer solution.

3.6 Conclusion

We have developed a diffusion cell that allows superimposing vertically 2 to 3 layers of salt solutions of different concentrations and different chemical composition, and studying the mass transport phenomena that take place in the cell. The characterization technique lies on the analysis of the light scattered by the NEFs that establish during the diffusion process of the solutes. The cell was installed in an optical shadowgraphy device. Two Peltier elements placed at each vertical end of the cell allow regulating the temperature and applying a vertical thermal gradient parallel to the gravity field. Series of shadowgraphy images are recorded as a function of time for a fixed acquisition frequency. The SF of the images is then calculated at different times during the diffusion process. The analysis setup and methodology was calibrated using the molecular solution of TEG and water, and aqueous solutions of NaCl, CaCl₂ and Na₂SO₄. In order to obtain a mono-exponential behaviour and a constant background level of the SFs, it was found preferable to consider solutes concentrations away from the saturation with respect to

the solid salts. A subsequent fitting of the decay times of the c-NEFs allowed us to calculate the diffusion coefficients of the dissolved salts in water, which are in good agreement with the literature data. The effect of external temperature gradient is also considered in case of free-diffusion experiments of NaCl/water and approximately same results were obtained as compared to the isothermal free-diffusion experiments for the same NaCl/water mixture, suggesting that the thermal gradient does not have a significant effect on the relaxation mode of the system.

A superimposition of two aqueous layers of non-reactive and reactive salts was possible in the diffusion cell and the dynamics of the relaxation was studied by the shadowgraphy technique. The numerical interpretation of the results was performed using the PHREEQC modelling tool. The diffusive flux is calculated by two methods: First, a homogeneous multicomponent diffusion that is characterised by the fact that all the species involved in the mixture diffuse with a same diffusion coefficient (not corrected for changes of temperature). Second, a heterogeneous multicomponent diffusion was considered, where the species have individual temperature-dependent diffusion coefficients and coupled interactions with the others dissolved salts.

The dynamics of relaxation of the system formed by the diffusion of an aqueous solution of CaCl_2 into an aqueous solution of NaCl resulted in the appearance of some diffraction spots on the image differences. The numerical modelling with PHREEQC software, either considering homogeneous or heterogeneous multicomponent diffusion, does not reveal any instability (due to vertical inversion of density) that could justify the presence of diffraction spots observed experimentally during the mixing process. As for the diffusion of an aqueous solution of NaCl into an aqueous solution of Na_2SO_4 , the dynamics of relaxation of the system observed experimentally clearly present the formation of convection patterns at the very early moments, and that fade with time. Numerical simulations assuming heterogeneous multicomponent diffusion allowed explaining the observed convective instability by revealing a density inversion near the interface in the early instants, before following the expected evolution.

For the superimposition of two reactive salts, a layer of an aqueous solution of CaCl_2 was brought into contact with a layer of an aqueous solution of sodium sulfate, separated by an intermediate layer of an aqueous solution of NaCl in order to delay the appearance of gypsum. For the experimental observations parallel to the gravity, we observed that the precipitation time strongly depends on the thickness of the the buffer solution which

controls the diffusion distance that ions have to cross. For a buffer thickness of 1/4 cm, we estimated with a homogenous diffusion hypothesis the time of appearance of gypsum in the cell to be between 20 and 40 minutes. This range of the estimated precipitation time seems to be large. This is due to the fact that our cell is relatively small. Therefore, from one experiment to another, if the volume drawn in varies slightly, there will be a large uncertainty because the precipitation time varies with the square of the thickness of the buffer solution. We observed a strong variation in the contrast of the images in the early stages, which is associated to convection patterns. This result was consistent with the observations made when superimposing two non-reactive salts of NaCl and Na₂SO₄. When applying thermal gradients of $\Delta T = 5, 20, 30$ and 35 °C perpendicularly to the interface, the onset time of precipitation all ranged between 40 and 80 min. The analysis of the evolution of the contrast of the image as a function of time revealed that the thermal gradient did not have a noticeable influence on the onset time of precipitation. For this experiment, the numerical interpretation shows that the precipitation of gypsum appears after about 10 minutes in the case of homogeneous multicomponent diffusion whereas it appears after about 40 minutes in the case of heterogeneous multicomponent diffusion. Results obtained with the latter approach are consistent with the convection patterns that have been observed experimentally. Moreover, as we observed experimentally, the numerical interpretation reveals that the temperature gradient did not have a noticeable influence on the precipitation of gypsum.

As for the location where the gypsum is formed in this system of three electrolyte layers, experimental observations perpendicular to the gravity (lateral observations), by the shadowgraphy technique, showed that the precipitation takes place in the initial layer of CaCl₂ solution, close to the interface with the NaCl solution. The numerical modelling of this configuration has made it possible to account for the experimental observations both in the case of homogeneous and heterogeneous multicomponent diffusion of this configuration. However, from a general point of view, heterogeneous multicomponent diffusion well account the behaviour of electrolytes in solution in a multicomponent system. Indeed, it integrates all the interactions between the species, unlike homogeneous multicomponent diffusion that only depends on the concentration gradient and on the diffusion coefficient. In a complex multicomponent system, with large concentrations, either in free or in porous medium, we recommend to consider the heterogeneous

multicomponent diffusion. Thus, for the next chapter, only the heterogeneous multicomponent diffusion is considered.

Chapter 4 : Numerical modelling of the reactive transport process induced by the CO₂ storage in a deep saline aquifer

4.1 Conceptual scheme

This chapter aims to apply the results obtained in the previous chapter to a more realistic and more complex context that is sketched in the conceptual diagram presented in Fig. 1.15 of chapter 1. As a reminder, our conceptual scheme is based on the principle that we consider in the porous medium a preferential flow of the injected CO₂ in the pores characterized by a high permeability, and which are in contact with pores of lower permeability that contain brine trapped in the pore space. With a continuous evaporation of brine in the injected CO₂ stream, the salt concentration is expected to increase at the evaporation front inducing backflows (capillary effects) of the brine with salt diffusion and geochemical reactions. Indeed, this will generate a high concentration gradient in the weakly permeable porous media and will lead to a “retro diffusion” process. Over time, when the salt concentration eventually reaches the solubility threshold of a given mineral, the latter may precipitate at the evaporation front [194]. The results we obtained in the previous chapters, namely the significance of the heterogeneous multicomponent diffusion at cm scale, is applied to a formation water representative of the saline solutions found in real deep reservoirs intended for CO₂ storage. In this context, stronger constraints are brought by the local mineralogy. Our study more specifically focuses on the deep carbonate reservoir of the Dogger aquifer (Paris Basin, France).

The geology of the Dogger aquifer is well established and its petrophysical characteristics have been taken from the literature [195]. This aquifer has already been the subject of several studies. Particularly, André *et al.* [50] studied the physical and chemical impact of CO₂ injection on the properties of the carbonate Dogger aquifer through numerical simulations using the reactive transport code TOUGHREACT [196], [197]. Their work focused on the evaluation of the evolution of the geochemical reactivity induced by injection of CO₂ both in time and space, at the interface between the supercritical CO₂-rich phase and the brine phase. However, in their study, the geometry of the Dogger aquifer was modelled on a very large scale with a mesh made with a thickness of 20 m and a

maximum radial extent of 100 km. In this thesis, our interest is rather on the transport phenomena at the pore scale. Therefore, this chapter focuses on reactive transport phenomena at the interface between the supercritical CO₂ and the brine of the Dogger aquifer. The simulations of the transport at the pore scale presented in this part is performed using the PHREEQC program already described in Chapter 2. In the previous chapter, we demonstrated that the heterogeneous multicomponent diffusion approach is well suited to describe the behaviour of the complex multicomponent the system of interest. Therefore, only heterogeneous multicomponent diffusion is taken into account in order to simulate the 1D-flow path diffusion.

Moreover, we have studied the effect of a strong temperature gradient on the diffusion phenomena via laboratory experiments and numerical simulations. By imposing different temperature gradients of $\Delta T = 5, 20, 30$ and 35 °C on a cell/column of 1 cm, the temperature gradient did not seem to have a significant effect on the behaviour of the system. This was observed both experimentally with shadowgraphy and numerically with PHREEQC. Futhermore, in an aquifer like the Dogger, we would not expect to have a strong temperature gradient during CO₂ injection at the pore scale. Nevertheless, even if there is a strong thermal gradient at the pore scale under reservoir conditions, this cannot be maintained over time. To demonstrate this assertion, we determined the evolution of the temperature profile in the Dogger aquifer whose initial reservoir temperature is 75 °C and which would be in contact with a flow of CO₂ whose temperature is set to 40 °C. To solve this problem, we consider a heat transfer by conduction in a simple mono-dimensional system when the temperature at one side of a system (here, the reservoir) is suddenly changed (arrival of the cold supercritical CO₂) from its initial value and kept constant at this side.

This is a configuration of a transient nature where there will be a heat transfer between the boundary and the initial system to gradually achieve an equilibrium temperature in the system over time as a function of distance. The solution to this problem of conduction from a limit at constant temperature is defined by the following equation: [198], [199]

$$\frac{T - T_i}{T_0 - T_i} = \operatorname{erfc}\left(\frac{x}{2 \cdot \sqrt{\alpha \cdot t}}\right) \quad (4.1)$$

where T_0 (°C) is the temperature imposed at the limit (40 °C), T_i (°C) is the initial temperature of the system (75 °C), T (°C) is the temperature at a distance x (m) from the system limit at a time t (s) after the temperature change at the limit, and α is the thermal diffusivity of the system (m^2/s). The thermal diffusivity is the ratio between the volume heat capacity $\rho \cdot c$ (ρ and c stand for density and specific heat of the rock, respectively) and the overall thermal conductivity λ , and is defined by [200] :

$$\alpha = \frac{\lambda}{\rho c} \quad (4.2)$$

This solution (Eq. 4.1) makes it possible to represent the temperature distribution as a function of distance for different instants or as a function of time for different distances. In order to draw the temperature profile, it is therefore necessary to calculate the thermal diffusivity α . The physical rock properties of the Dogger are well known, with a formation heat conductivity of $2.51 \text{ W}(\text{m } ^\circ\text{C})^{-1}$, a rock grain specific heat of $920 \text{ J}(\text{kg } ^\circ\text{C})^{-1}$ and a rock grain density of $2600 \text{ kg}\cdot\text{m}^{-3}$ [50]. This leads to a thermal diffusivity of $0.758 \times 10^{-6} \text{ m}^2\cdot\text{s}^{-1}$ according to Eq. 4.2. The thermal properties in a two-phase (solid and pore fluid) system can also be calculated using different models:

- The geometric-mean model originally introduced in 1924 by Lichtenecker [201], is used for the calculation of the matrix thermal conductivity λ_{ma} from the thermal conductivity of the mineral constituents and the calculation of the water-saturated bulk thermal conductivity λ_b using the matrix thermal conductivity λ_{ma} and the porosity ϕ of the medium according to the equations :[200]

$$\lambda_{ma} = \prod_1^n \lambda_i^{V_i} \quad (4.3)$$

where λ_i and V_i are the thermal conductivity and the volume fraction of a mineral i respectively. The thermal conductivity is a function of temperature and varies inversely with temperature [202], [203].

$$\lambda_b = \lambda_{ma}^{1-\phi} \lambda_p^\phi \quad (4.4)$$

where λ_p is the thermal conductivity of the pore-filling fluid.

- The arithmetic-mean model, originally introduced by Voigt in 1928 [204] and Reuss in 1929 [205], is used to calculate the matrix specific heat capacity $\rho_{ma}c_{ma}$ from the mineral constituents, as well as to calculate the saturated bulk specific heat capacity $\rho_b c_b$ using the matrix specific heat capacity and the porosity ϕ of the medium according to the equations :[200]

$$\rho_b c_b = V_{ma} \rho_{ma} c_{ma} + V_p \rho_p c_p \quad (4.5)$$

where V is the volume fraction, ρ is the density and c is the specific heat capacity for the rock matrix 'ma', for the pore-filling fluid 'p', and for each mineral component 'i', respectively.

By adding this value to Eq. 4.1, we can therefore plot the evolution of the temperature T as a function of the distance over time represented by Fig. 4.1 below

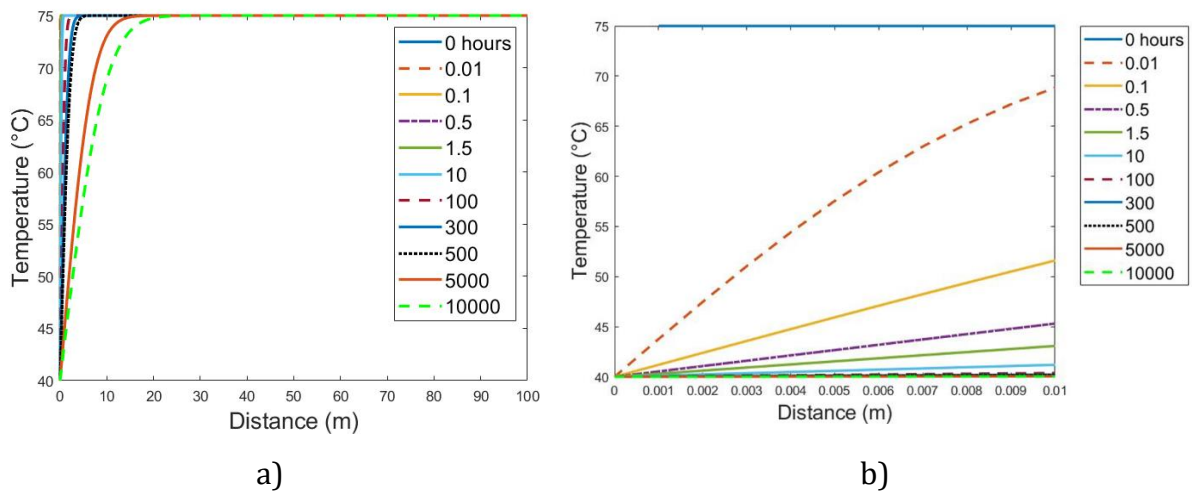


Figure 4.1: Evolution of the temperature profile of the Dogger aquifer as a function of distance for different times with Eq. 4.1 which a thermal diffusivity of $0.758 \times 10^{-6} \text{ m}^2 \cdot \text{s}^{-1}$.

Fig. 4.1 represents the evolution of the temperature as a function of distance for different times. At $t = 0$, the initial temperature of the reservoir is $75 \text{ }^\circ\text{C}$. Because the temperature of the flowing CO_2 at the left limit of the system is 40°C , a very strong temperature gradient is set up from the first few centimeters (Fig. 4.1-a). This gradient evolves and fades over time. However, if we perform a zoom to size at the pore scale over a distance of 1 cm (Fig. 4.1b), we observe that the thermal diffusion is quite fast. Indeed, after 10 hours, the temperature evolves linearly with distance, according to a low gradient, barely $1 \text{ }^\circ\text{C} \cdot \text{m}^{-1}$. Compared to mass diffusion, the thermal diffusion sets up very quickly and the temperature gradient is negligible at the pore scale. Consequently, one cannot envisage a

strong gradient that would be maintained at the pore scale and which would generate the coupling of the thermal gradient with the diffusive transport phenomena. In this chapter, we will only focus on reactive pore-scale mass transport at constant temperature.

4.2 Dogger Aquifer properties

4.2.1 Mineralogy of the basin

The Paris basin is made up of sedimentary layers with large aquifers present at different depths, especially the Dogger aquifer which dates from the Jurassic. The Dogger aquifer extends over more than 15.000 km² and at approximately 1700 m deep, with a temperature ranging from 55 to 85 °C. The physical and geochemical properties of the Dogger aquifer zone on which our study relates has been already described in the literature [50], [195], so that here we just recall the main parameters used in the model. It has a mean porosity of 0.12 and the permeability is assumed to be spatially homogeneous at 10⁻¹³ m². The initial temperature and pressure for water formation are 75 °C and 180 bars respectively. The mineralogy of the basin consists mainly of carbonates (85% in volume fraction of calcite, disordered dolomite and siderite) with alumino-silicates (Albite and K-Feldspar) and Illite. This initial mineral composition is given in volume fraction. However, the PHREEQC program uses the amount of substance (in mol). To convert the volume fraction %V_i to the amount n_i of a mineral phase i , the following equation applies:

$$n_i = \frac{\%V_i \cdot V_T}{V_{m,i}} \quad (4.6)$$

Where V_T is the total volume of minerals, and $V_{m,i}$ is the molar volume of each mineral phase. The porosity of the basin being 0.12, it means that for a rock volume of 1 L, we have 0.12 L volume of empty pores and 0.88 L volume of minerals. The aqueous speciation with PHREEQC program gives a volume of empty pores (or volume of water formation) of $V_{\text{pore}} = 1.0194$ L in each cell of the simulation column. It means that the corresponding total volume of mineral phases is 7.4754 L in each cell. Therefore, the mineral composition is given in Table 4.1 below:

Table 4.1: Dogger aquifer mineralogy, amount of each mineral per 1.0194 L of saline water and list of minerals not initially present in the reservoir (amount = 0 mole) but likely to precipitate.

Mineral composition (chemical formula)	Volume fraction	Amount of substance (mol)
Calcite (CaCO_3)	0.70	141.81
Disordered dolomite ($\text{CaMg}(\text{CO}_3)_2$)	0.10	11.59
Siderite (FeCO_3)	0.05	12.80
Illite ($(\text{K},\text{H}_3\text{O})(\text{Al},\text{Mg},\text{Fe})_2(\text{Si},\text{Al})_4\text{O}_{10} [(\text{OH})_2,(\text{H}_2\text{O})]$)	0.05	2.69
Albite ($\text{NaAlSi}_3\text{O}_8$)	0.05	3.37
K-Feldspar or Microcline ($\text{K}(\text{AlSi}_3)\text{O}_8$)	0.05	3.43
Kaolinite ($\text{Al}_2\text{Si}_2\text{O}_5(\text{OH})_4$)	0.00	0.00
Chalcedony (SiO_2)	0.00	0.00
Magnesite (MgCO_3)	0.00	0.00
Dawsonite ($\text{NaAlCO}_3(\text{OH})_2$)	0.00	0.00
Anhydrite (CaSO_4)	0.00	0.00
Halite (NaCl)	0.00	0.00

Given the mineralogy and the chemical composition of the formation water, some minerals are likely to precipitate as secondary phases during CO_2 injection, namely Halite, Anhydrite, Kaolinite, Magnesite, Dawsonite and Chalcedony.

4.2.2 Composition of the water formation

The Dogger aquifer contains water with salinity ranging from 5 to 35 g.kg^{-1} . For our simulations, the chemical composition of the water formation from the Dogger aquifer in the region of Fontainebleau has a salinity of 5 g.kg^{-1} . It was determined by Michard and Bastide [206] and is given in Table 4.2. In our simulation, this water formation is initially at equilibrium with the primary minerals given in Table 4.1.

Table 4.2: Chemical composition of water from the Dogger aquifer in the region of Fontainebleau (concentration are in ppm [50]).

Temperature	75
pH	6.70
Alkalinity	427.0
Na	1794.0
K	35.2
Ca	148.0
Mg	55.9

Al	0.002
Fe	1.0
Cl	2485.0
SO ₄	633.6
SiO ₂	41.4
HS	11.9

4.3 Simulation conditions and some limitations of the PHREEQC and associated thermodynamic databases

Our simulation strategy considers a 1 cm 1D-column closed at boundaries, meaning that there is no flux at boundaries (see section 2.4.3). As a reminder, the numerical scheme in PHREEQC is for cell-centered concentrations, which means that the composition at a half-cell distance represent the composition of the entire cell. The system is made of a column with a length of 0.01 m that contains the water formation given in Table 4.2 together with the mineralogy of the reservoir (Table 4.1). The mesh for the numerical modelling is shown in Fig. 4.2. The column is divided into 10 cells of equal length and identical geochemical composition. The first cell of 0.001 m is directly in contact with the constant composition of CO₂-rich gas phase that we impose.

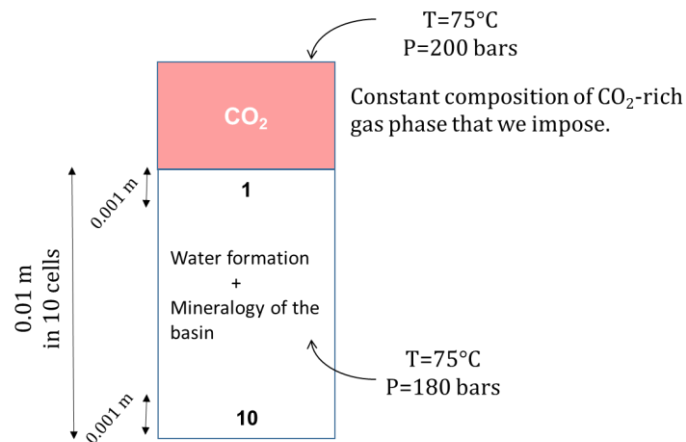


Figure 4.2: Mesh for the numerical modelling for evaporation, diffusion and precipitation of salt within the Dogger aquifer.

The salinity of the water is moderate (5 g.kg⁻¹) leading to an ionic strength of about 0.10 mol.kg⁻¹. For this latter value, the activity model based on the Debye-Hückel formalism as well as the one based on the Pitzer formalism can be used for reactive transport modeling. However, with the continuous evaporation, the formation water becomes highly saline, with an ionic strength that reaches up to 7 mol.kg⁻¹! Therefore, the Debye-Hückel coefficient activity model is not valid anymore and the Pitzer formalism is the one we will

use to cover all the salinity conditions. In the PHREEQC program, the Pitzer formalism is used in combination with the database "pitzer.dat". However, the latter presents some serious limitations.

First, the siderite mineral, which is part of the mineralogy of the Dogger aquifer reservoir, was initially absent from this database, which we modified accordingly. We took the thermodynamic properties of this mineral from the Thermoddem thermodynamic database, devoted to geochemical modelling for environmental studies in natural and industrial contexts [207]. This database is suitable for dilute solutions and can be used with PHREEQC. The thermodynamic properties of siderite selected in the Thermoddem database include the verification that its solubility, which is a function of the physical parameters such as the temperature, is well described in accordance with experimental data that were acquired in dilute solutions. However, by including siderite in the Pitzer database, it is possible that its solubility is not very well described for concentrated solutions. Given that Siderite is present at 5% in the mineralogical assemblage of the Dogger reservoir, and also for kinetic reasons (see next section), we assume that even if the solubility of siderite turns out to be poorly described at high concentration, it will not have a significant impact on the behaviour of the system and on the interpretation of the results.

The chemical composition of the water formation contains the aluminium element. However, Al is not included in Pitzer's parametrization because there is no data allowing to obtain a reliable parametrization close to neutrality (pH ~ 7). In fact, it is possible to reach high concentrations of aluminium ions Al^{3+} in an acidic medium, and of aluminium hydroxides ($\text{Al}(\text{OH})_4^-$) in a basic medium. This allows having enough information to determine the Pitzer parametrization for these extreme pH conditions. However, the solubility of Gibbsite becomes very low in the area close to the neutrality where the concentrations of aluminium are limited to a fraction of micromoles per litre of solution [208], [209]. Since alumino-silicate and clay minerals have slow reaction kinetics, their impact will be limited in the context of our study and therefore that of Al element on the overall behavior of the system.

The sulphur element S can exist in different degrees of oxidation that are linked together by electron transfers. In sulphate ions SO_4^{2-} , sulphur has an oxidation degree of +VI: the sulphur atom lost 6 electrons. In hydrogen sulphide ions HS^- , sulphur has an oxidation

degree of -II: the sulphur atom gained 2 electrons. Both redox states were identified in the Dogger water formation. Yet, the only sulphur redox state implemented in the Pitzer database associated with in the PHREEQC program is the sulphate, with the redox state of +VI. Sulphides are implemented as a distinct element, Sg, in order to describe the solubility of hydrogen sulphide (H₂Sg). It turns out that the redox couple between sulphides and sulphates (HS⁻/SO₄²⁻) cannot be described when using the Pitzer.dat database. As a result, HSg⁻ species cannot interact with sulphate ions and therefore the chemistry of the system cannot be modified by any electron exchange between HSg⁻ and SO₄²⁻.

4.4 Description of the simulation model

The water formation at 75 °C and 180 bars is initially at equilibrium with calcite, dolomite, and siderite. As we mentioned above, the Aluminium element is not included in the Pitzer database. Therefore, all the aluminosilicates (Albite, K-Feldspar, and Kaolinite), clay (Illite) and Dawsonite mineral phases (hydroxy-carbonate of sodium and aluminium) have been removed from the model mineral assemblage. Calcite is assumed to react at equilibrium, meaning that it can precipitate as soon as conditions are favourable. Halite, anhydrite, chalcedony and magnesite are not initially present in the system but are allowed to precipitate as secondary mineral phases. Besides, with these conditions of temperature and pressure and the duration of the injection of CO₂, Magnesite is not allowed to precipitate. Indeed, Magnesite is thermodynamically the stable Mg-carbonate mineral in a wide range of temperatures [210], but some recent studies on magnesite growth kinetics have confirmed that the precipitation rate of this anhydrous magnesium carbonate is very sluggish, and that it has only been synthesized at temperatures above 80 °C [211], [212]. In fact, for temperatures below 80 °C, a variety of hydrated magnesium carbonate phases tend to form, mainly hydromagnesite, and nesquehonite [210], [213]. An explanation is widely ascribed to the highly hydrated character of the Mg²⁺ cation and the resulting slow rate of exchange of water molecules between the Mg²⁺ hydration shell and the bulk solution [214], [215].

In our simulation, dolomite and siderite are considered as primary mineral phases that can only dissolve. Dolomite is also a Mg-carbonate mineral and like Magnesite, the strong hydration of Mg²⁺ ion and its slow dehydration rate is also used as an explanation for the failure to grow anhydrous dolomite [215]. In addition, dolomite is a double carbonate

with the Ca^{2+} cation, which ordered incorporation into an anhydrous crystal structure also has to be accomplished. As a result, anhydrous dolomite precipitate at rather elevated temperatures, which even exceed the temperatures necessary to form magnesite. [215], [216]. As for siderite, it is a Fe-carbonate mineral which is very poorly soluble and which precipitates at low temperature [214]. However, in inhibitor-free aqueous conditions at surface temperature and pressure, the growth rate of siderite is nearly 7-orders of magnitude slower than that of calcite at their respective supersaturation. [217]. This is due to the fact that Fe^{2+} ion has a larger ionic radius than that of Ca^{2+} , resulting in a lower dehydration frequency of Fe^{2+} ion. Siderite is therefore characterized by a rather slow precipitation kinetics compared to calcite.

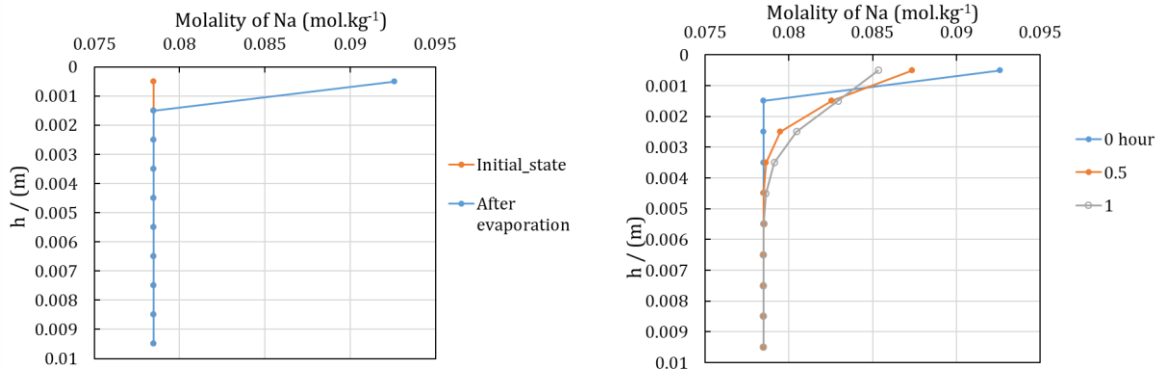
After being equilibrated with the minerals, the initial formation water was first pre-equilibrated with the pure dry CO_2 phase at temperature and pressure of 75 °C and 200 bars respectively, resulting in a CO_2 -saturated solution with a concentration of 1.1981 mol.kg⁻¹ CO_2 . At the interface between the supercritical CO_2 and the aqueous solution (i.e. the first cell of the column), the CO_2 dissolves in the water formation. At this interface, the pH of the water decreases from 6.7 to a value of 3.99. After being in contact with the dry CO_2 gas phase, the water is slowly vaporized and this evaporation process eventually leads to salt precipitation. Many parameters, such as the salinity, injection flow rate, capillary pressure, aqueous phase mobility and temperature have been identified as the main sensitive parameters governing salt precipitation process, the most controversial results being reported for the effect of the CO_2 injection rate. [77] It has been clearly shown that all these parameters affect the evaporation rate. However, in the literature there is a lack of information on the rate of evaporation of brine in the CO_2 stream under reservoir conditions.

In our simulations, we estimated an evaporation rate taken from the work of Veran-Tissoires et Prat [218]. In their study, they focus on an evaporation-wicking situation, where the porous medium remains fully saturated all along the evaporation process. A porous medium is exposed to evaporation at its top surface and is in contact with a sodium chloride saturated aqueous solution at its bottom, which has an initial salt mass fraction of 25 %, taking into account that the saturation mass fraction is about 26 % at 25 °C. One of their objectives was to highlight the dynamic aspect of efflorescence structure growth. In their work, the authors experimentally measured the evaporation rate of pure water. For a distance δ of 15 mm between the packing surface and the rim of the hollow cylinder,

and a vertical distance L_s of 22 mm between the free surface in the reservoir and the surface of the porous medium, they found that water evaporates at a rate of $J_{exp} = 1.80 \times 10^{-8} \text{ kg.s}^{-1}$. The porous medium is formed by a pack of glass beads of mean size d_b in a 50 mm long hollow cylinder of inner radius $r_w=19$ mm. The porosity of the medium was 0.36. This leads to a radius of free pores of $r_p=11.4$ mm. This results in a flow per free water surface of $8.82 \text{ mol.h}^{-1}.\text{m}^{-2}$. In our simulation, we have a surface of free water of 1 m^2 . Therefore, we can use an evaporation rate close to the one found by Veran-Tissoires and Prat. In our simulation, the evaporation rate is set constant to $10 \text{ mol.h}^{-1}.\text{m}^{-2}$.

4.5 Modelling procedure with the PHREEQC program

A simulation cycle has a duration of one hour and must include, from a phenomenological point of view, the process of evaporation of the formation water in the CO_2 stream and at the same time the process of diffusion that comes from the concentration gradient within the brine as a result of evaporation. In fact, the evaporation strongly concentrates the solution at the CO_2 -brine interface. This leads to a retrodiffusion process, i.e. diffusion towards the bottom of the reservoir. However, there is no command in the PHREEQC program making it possible to carry out this cycle directly in a single step. We therefore decomposed the simulation cycle into two stages as represented in Fig. 4.3. The first step is represented in Fig. 4.3-a. It consists in a simulation of evaporation of water together with a physical transport of water from the bottom to the top of the column in order to compensate the evaporation. Indeed, we have a pore volume of 1.0194 L that is the same over the entire column and is supposed to remain constant and constantly saturated with water over time. Evaporation of water at the first cell reduces its water mass and therefore modifies the pore water volume. The compensation of the water loss in this cell is carried out by taking a fraction of solution from the cell below. In practice, this physical transport represents the capillary backflow, which corresponds to a displacement of water that tends to regain the porosity occupied by the gas phase. As evaporation gives rise to an overconcentration in the first cell of the column, one is obliged to stop the process of evaporation and displacement of the solution to leave place for the second step. The latter corresponds to the diffusion of ions for the same equivalent time associated with evaporation and displacement of water, in accordance with the evaporation rate determined in the previous section.



a)

b)

Figure 4.3: Concentration profile of Na in the column for one cycle of evaporation whose modelling procedure is exemplified by a) the first step corresponding to the evaporation together with the physical transport of aqueous solution. b) the second step corresponding to the diffusion process.

The Fig. 4.3 represents one cycle of simulation. The brine contains different ionic species but here we only represent the behaviour of Na⁺ as an example. In Fig. 4.3-a above, one can see that the evaporation takes place in the cell directly in contact with the CO₂ flow. In Fig. 4.3-b, one can clearly see the retrodiffusion effect. Over time, the concentration of Na⁺ decreases at the top of the column while slowly increases in the cells below due to diffusion. The cycle thus continues over time, knowing that the initial state of new cycle corresponds to the final state of the previous cycle and starts with a new evaporation step, followed by a diffusion step. The result for two successive cycles is represented in Fig. 4.4 below:

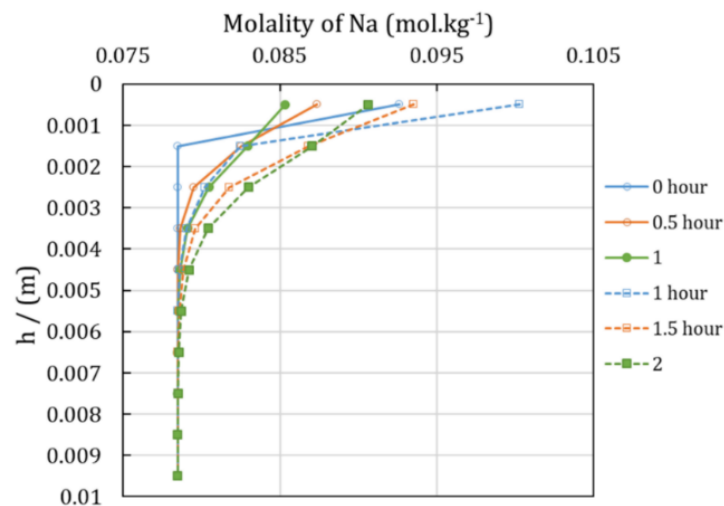


Figure 4.4: Concentration profiles of Na in the column during two successive cycles of simulation

The figure above is a detailed description of the simulation results, but we are interested in the final states of each simulation cycle. Therefore, in the following parts, we will only represent the final states of successive 1 hour-long cycles.

In Fig. 4.5 below are represented the evolution of the concentration profiles of Sodium, Chloride, Calcium and sulfate ionic as a function of the depth up to 20 hours after imposing a constant partial pressure of CO₂ gas phase in contact with the pore solution.

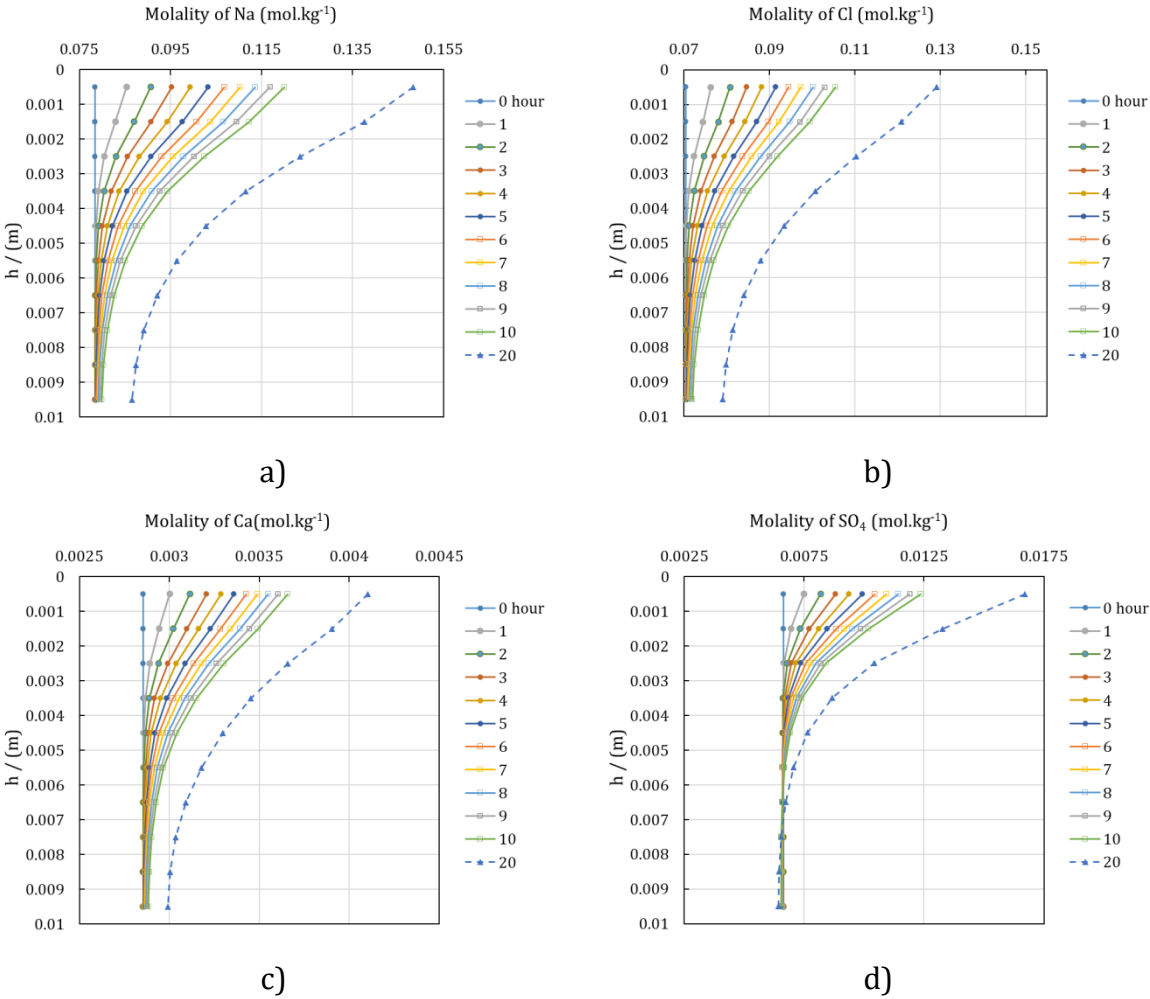


Figure 4.5: Evolution of the concentration profiles of a) Na, b) Cl, c) Ca and d) SO₄ ions over 20 hours. In legend is the time given in hour.

Based on the final states, we can observe that the concentration profiles of all the ionic species in the solution increases over time at the brine-CO₂ interface while retrodiffusion takes place in the porous matrix. The same behaviour is observed for the other chemical species that are not represented here but are present in the formation water.

The increase of the concentration of ionic species in the medium leads to the increase of the ionic strength as represented on Fig. 4.6 below:

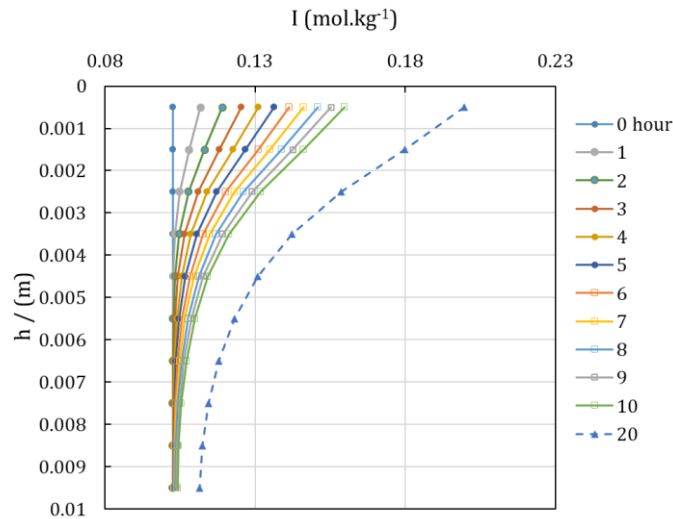


Figure 4.6: Evolution of ionic strength I over 20 hours. In legend is the time given in hour.

From Fig. 4.6, we can see that the ionic strength increases at the bottom part of the column over time. This is directly related to the increase of the concentration of chemical species in the solution as shown on Fig. 4.5. However, the latter phenomenon is only visible on a small scale, i.e. from the pore scale up to some centimeters. In fact, if we extend the column length to 3 cm (0.03 m), the concentration in the rest of the reservoir remains constant, and therefore so does the ionic strength, as shown below:

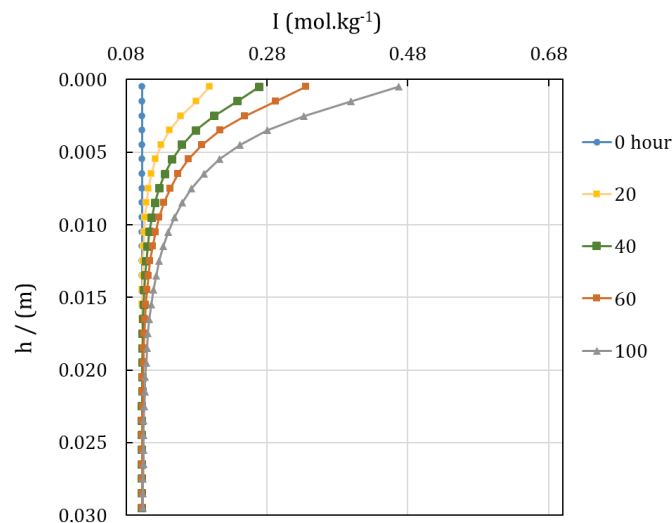


Figure 4.7: Evolution of the of ionic strength I over 100 hours in a 3 cm-long column. In legend, the time is in hour.

On Fig. 4.7, we observe that, the ionic strength of the water formation increases at the brine-CO₂ interface, related to the increase of the concentration of ionic species due to evaporation. The retrodiffusion occurs significantly over about 1 cm and beyond this distance; the concentration remains constant in the rest of the host reservoir even over a

period of 100 hours. This result shows that the mass diffusion is a phenomenon, which can have a significant impact at the pore scale. However, it is possible to envisage that for very long times the concentration increases at the bottom of the column but this will not be significant.

Like the ionic strength, the increase of the concentration in the formation water increases the saturation indices of minerals over time as represented below:

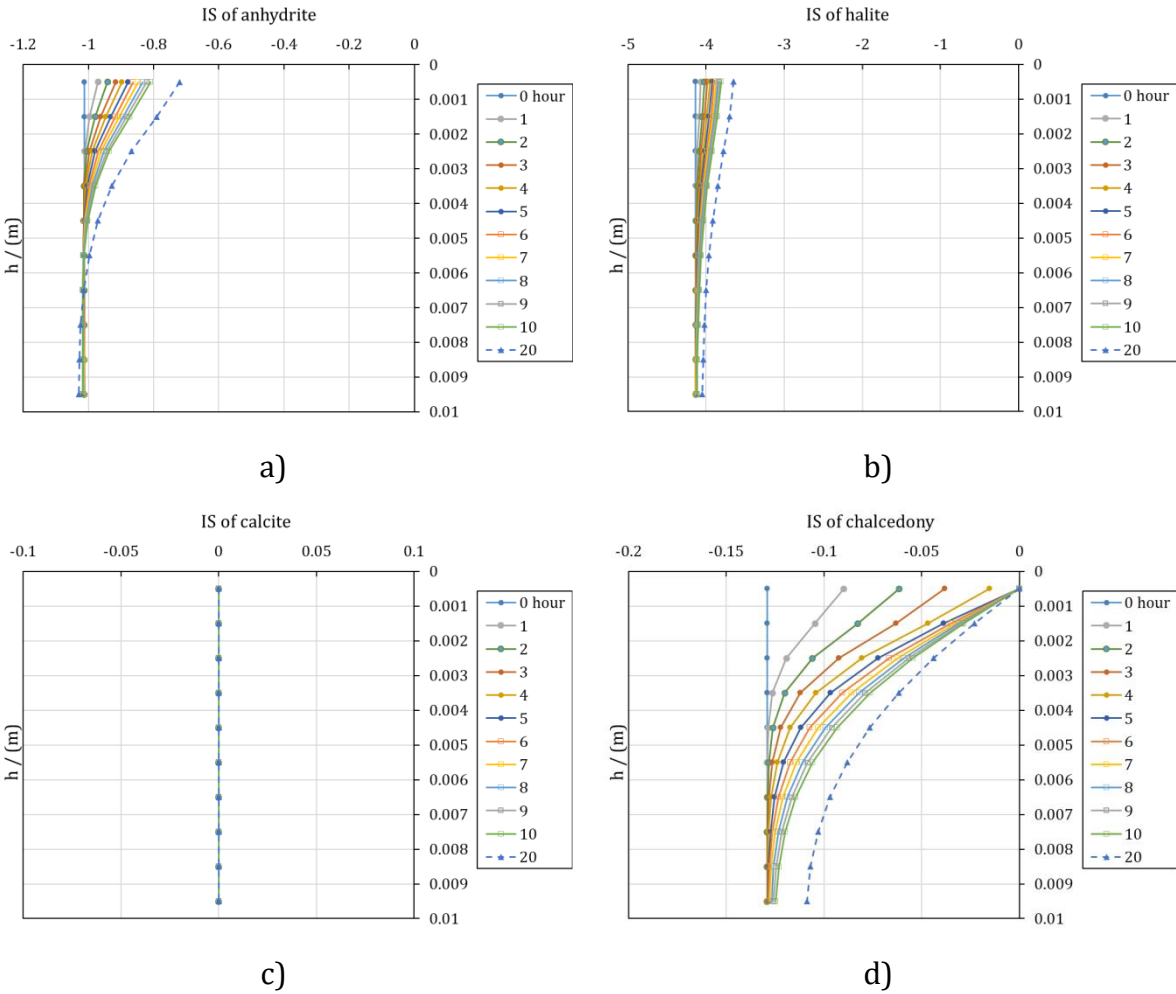


Figure 4.8: Evolution of saturation indices of a) anhydrite, b) halite, c) calcite and d) chalcedony over 20 hours. In legend is the time given in hour.

As concentrations increase, saturation index values may become positive or zero as soon as the precipitation conditions of a mineral are favourable.

4.6 Results and discussion

4.6.1 Evolution of the net volume of minerals

The medium contains an initial pore volume of 1.0194 L. As mentioned above, this volume is the same over the entire column and is supposed to remain constant. However, as the minerals precipitate, the volume of solution in the pore formation will decrease, as it will be progressively occupied by the minerals that precipitate into the solution. As a result, when the volume of mineral formed due to precipitation will be equal to the initial volume of the solution, then the porosity will be completely clogged. Therefore, we are interested by comparing the net volume of minerals formed to the initial volume of the pore solution. The total net volume of minerals formed corresponds to the total volume of minerals at the final state minus the total volume of minerals at the initial state ($V_T = V_{f, \text{minerals}} - V_{i, \text{minerals}}$). The total volume of minerals at the initial state is 7.4754 L in each cell. However, due to the code limitations, some minerals are not taken into account by the Pitzer formalism as explained in section 4.3 and 4.4. Therefore, the initial volume of the reactive minerals is $V_{i, \text{minerals}} = 6.358$ L. With the PHREEQC software, there is a command that directly gives the volume of each mineral in the final state as well as the total volume of the minerals in the final state.

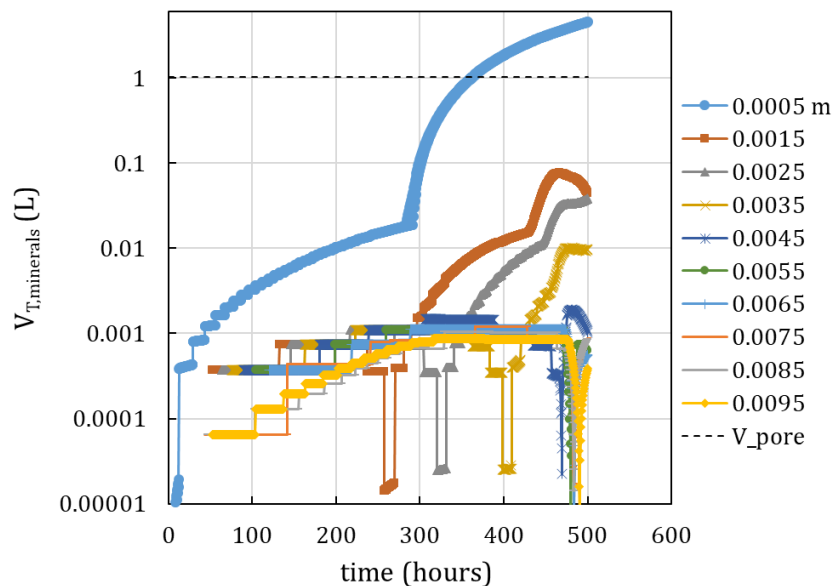


Figure 4.9: Log-linear evolution of the total net volume of minerals as a function of time for different depths in the column in. The black dashed-line represents the initial volume of pore solution. In the legend, the distance are in meter.

Fig. 4.9 represents the spatio-temporal evolution of the total net volume of minerals. The dashed black line represents the initial volume of the pore solution $V_{\text{pore}} = 1.0194 \text{ L}$. The simulation is performed over a period of 500 hours. We observe that over time, we increase minerals volume meaning that precipitation occurs. One can also note that the net volume of minerals is more important in the first cell that has a height of 1 mm. This means that the precipitation occurs massively in this first cell. As mentioned earlier, minerals can only grow in a free volume and when the volume of the minerals is equal to the initial volume of the pore solution, the porosity has been completely clogged because the minerals have no place to grow more (as observed experimentally in Peysson *et al.* [194]). Thus, if the evolution of the porosity was formally correlated with the evolution of the net volume of mineral precipitation, an evaporation rate of 10 mol/hour would result in the clogging of the porosity after about 360 hours (15 days). Consequently, the simulations can be stopped at this time, and any further evolution of the system may result in erroneous interpretation because it may not take place. If we consider a slower evaporation rate, for example of the order of 1 mol/hour, we can push the simulations up to about 150 days before the clogging of the porosity. However, in the practical case, it is possible that, during their growth, the minerals leave a “mini” porosity between grains where water can still percolate and reach the larger pore where the CO_2 -rich phase flows. Eventually, this could give rise to the efflorescence phenomenon (at the pore scale) [219], or the subflorescence phenomenon at a larger scale. We will therefore perform our simulation up to 400 hours and study the behaviour of the ionic species up to 400 hours and look at the mineral that contributes to the clogging of the porosity.

4.6.2 Evolution of the ionic strength and the molality of ionic species

With the continuous evaporation, the ionic strength increases over time as the solution becomes more saline (see Fig. 4.10) and the highest concentrations are in the first cell, which corresponds to the place where the precipitation occurs massively (see Fig. 4.11).

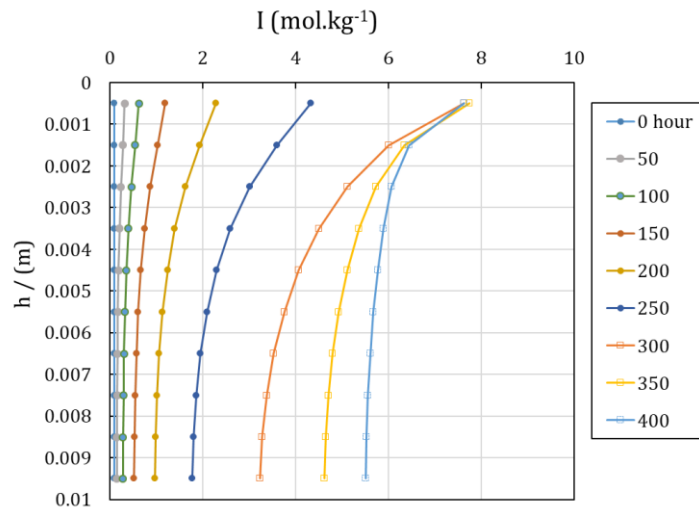
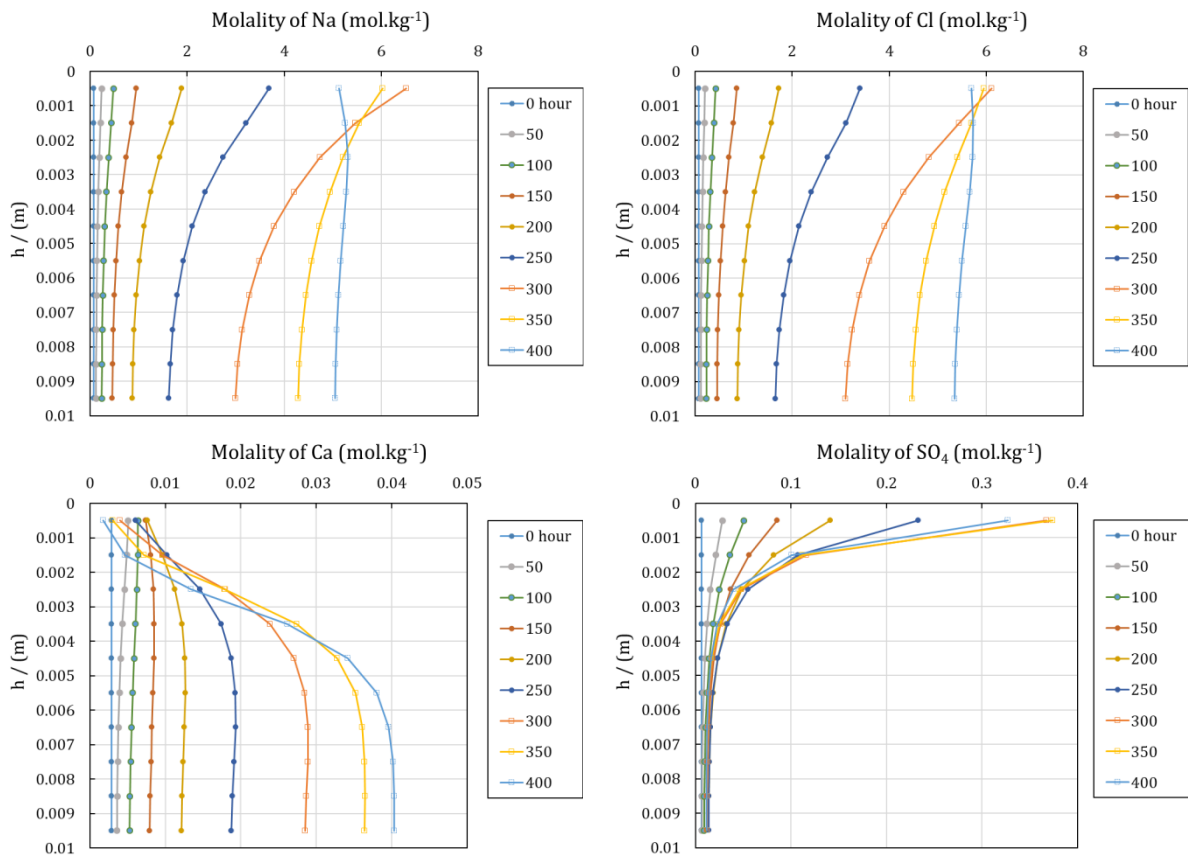


Figure 4.10: Evolution of ionic strength I over 400 hours. In legend is the time given in hour.



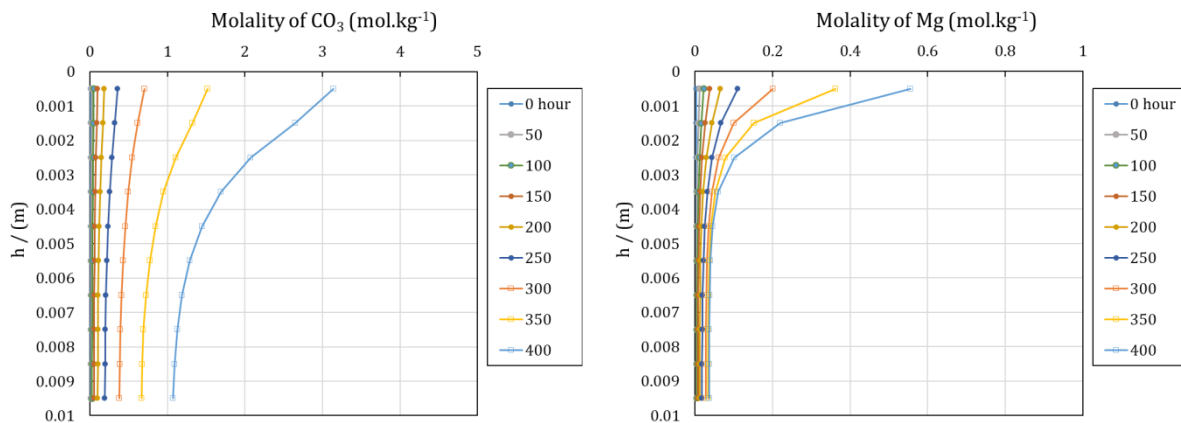


Figure 4.11: Evolution of the concentration profiles of ionic species over 400 hours. From the top to bottom at the left side: Na, Ca, and CO₃. From top to bottom at the right side: Cl, SO₄ and Mg. In legend is the time given in hour.

We observe a regular increase of the concentration of sulfate, carbonate and Magnesium species. Regarding the behaviour of Na and Cl, we observe that after about 350 hours, their concentration no longer increases significantly, related to the precipitation of halite whose solubility limit is around 6.4 mol.kg⁻¹ at a mean temperature of 75 °C. As for the behaviour of calcium, we observe a decrease in its concentration in the first cell from 250 hours. This is due to the fact that there is the precipitation of two minerals, namely calcite (CaCO₃) and anhydrite (CaSO₄), that consume calcium during their precipitation while the concentration of carbonate and sulfate continues to increase with evaporation. The ionic strength represents the contribution of all the ionic species in solution and it can be seen that Na and Cl are the main contributors to the increase of this parameter. This already tells us that there is a significant amount of potentially halite being formed as a result of precipitation.

4.6.3 Evolution of the amount of minerals

The amount of mineral is directly related to the saturation index of each mineral. In fact, if there is an amount of a mineral that forms at a given place, it means that the saturation index of the mineral has become positive or zero at this place. Among the minerals likely to precipitate, saturation with respect to halite, anhydrite and chalcedony is achieved, while being saturated with respect to calcite.

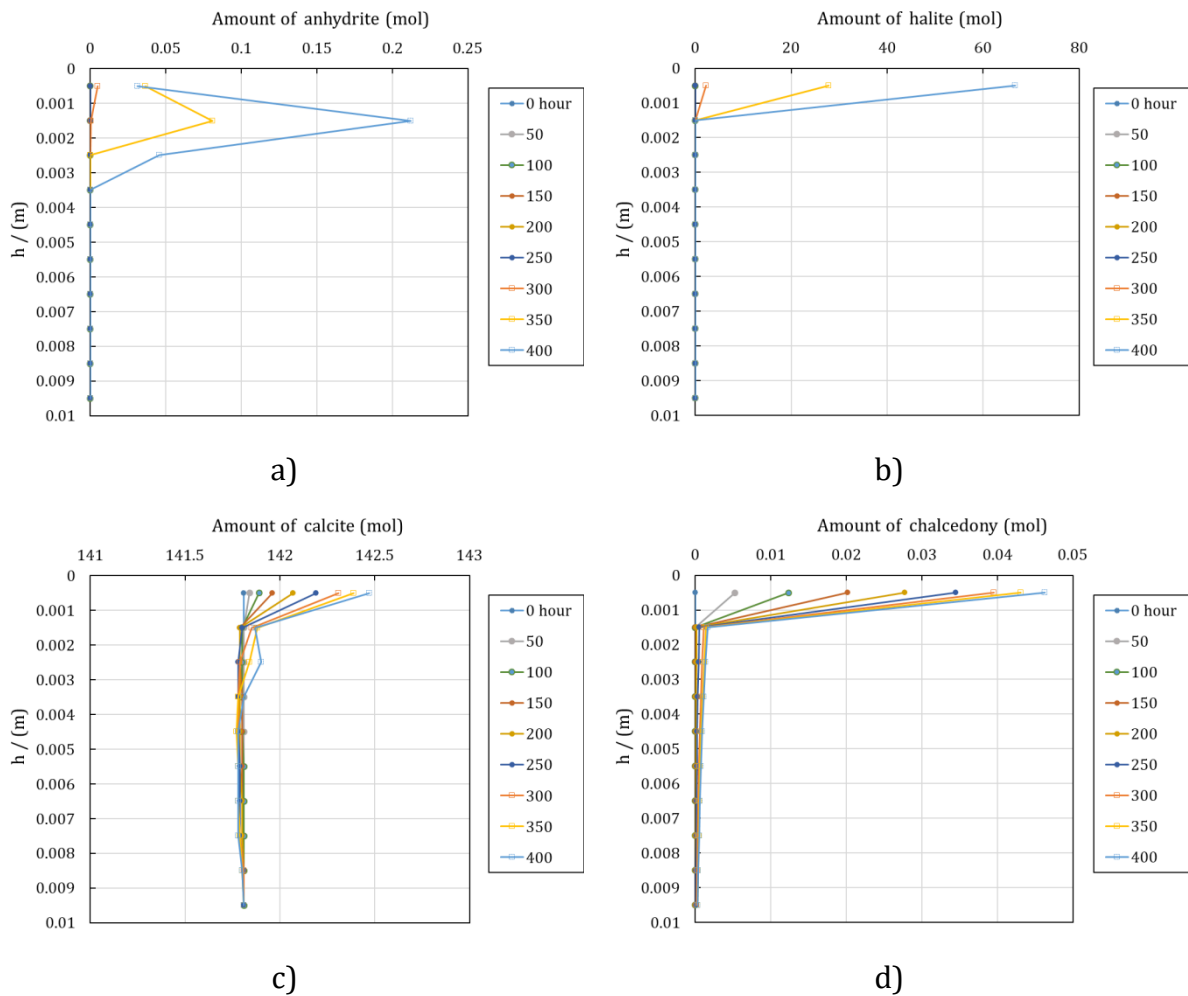


Figure 4.12: Evolution of the amount of minerals likely to precipitate over 400 hours: a) anhydrite, b) halite, c) calcite and d) chalcedony.

From Fig. 4.12, one can note the effect of diffusive transport on precipitation. For a given diffusion time, calcite and chalcedony precipitate first (after 50 hours) while anhydrite and halite appear much later (after 300 hours). However, we observe that calcite and chalcedony have a less important contribution on the behaviour of the system. Moreover, we observe that all the reactivity is mainly concentrated at the level of the first cell as also observed by Peysson *et al.* [194]. This means that the transport of ions by diffusion (retro diffusion) does not compensate the concentration increase due to evaporation, probably due to the fact that the evaporation rate is high. For the adopted conditions in our tests and explorations, the amount of halite becoming more and more important with evaporation and is only formed in the first cell. The anhydrite is formed over 3 mm with a preferential location at the level of the second cell, i.e. 2 mm from the CO₂-brine interface. All this indicates that halite is the mineral that contributes most to clogging. To confirm this, we examine the formed volume of each mineral.

4.6.4 Evolution of the total net volume of each mineral

With the PHREEQC software, there is a command that directly gives the volume of each mineral in the final state. The latter can also be calculated knowing the initial amount and the molar volume of each mineral.

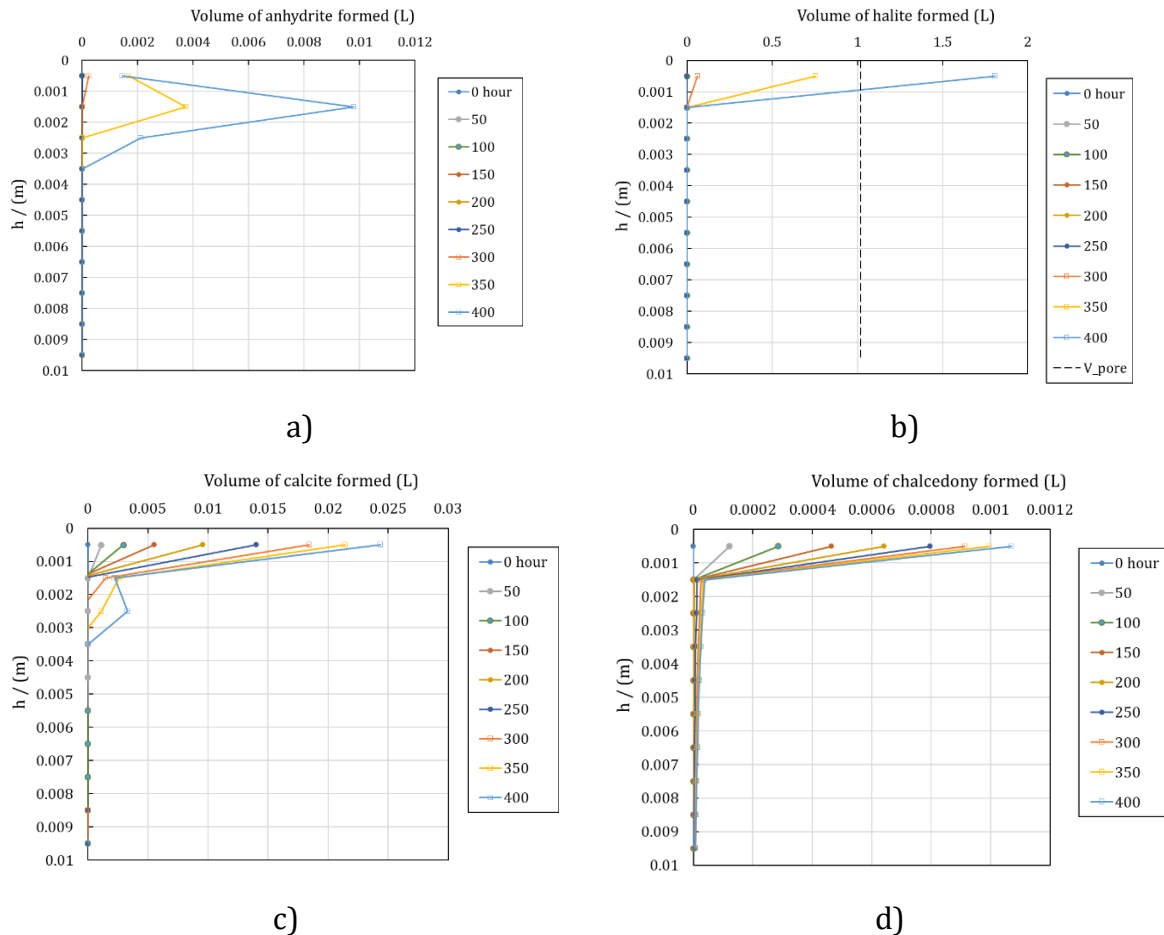


Figure 4.13: Evolution of volume of a) anhydrite b) halite c) calcite and d) chalcedony as a function of time. The black dashed-line represents the initial volume of pore solution

Halite only precipitates at the first cell (over 1 mm). Calcite and chalcedony also precipitate in the first cell and contribute to the clogging of the porosity but only minimally. The contribution of anhydrite at the level of the first cell remains negligible and appears rather significantly at the level of the second cell, over 2 mm from the CO₂-brine interface. A small amount of precipitate is observed to form in the rest of the reservoir due to the diffusion but it remains undersaturated in mineral. Beyond 3 mm, no precipitate is formed. A summarise of the results is given in Fig. 4.14:

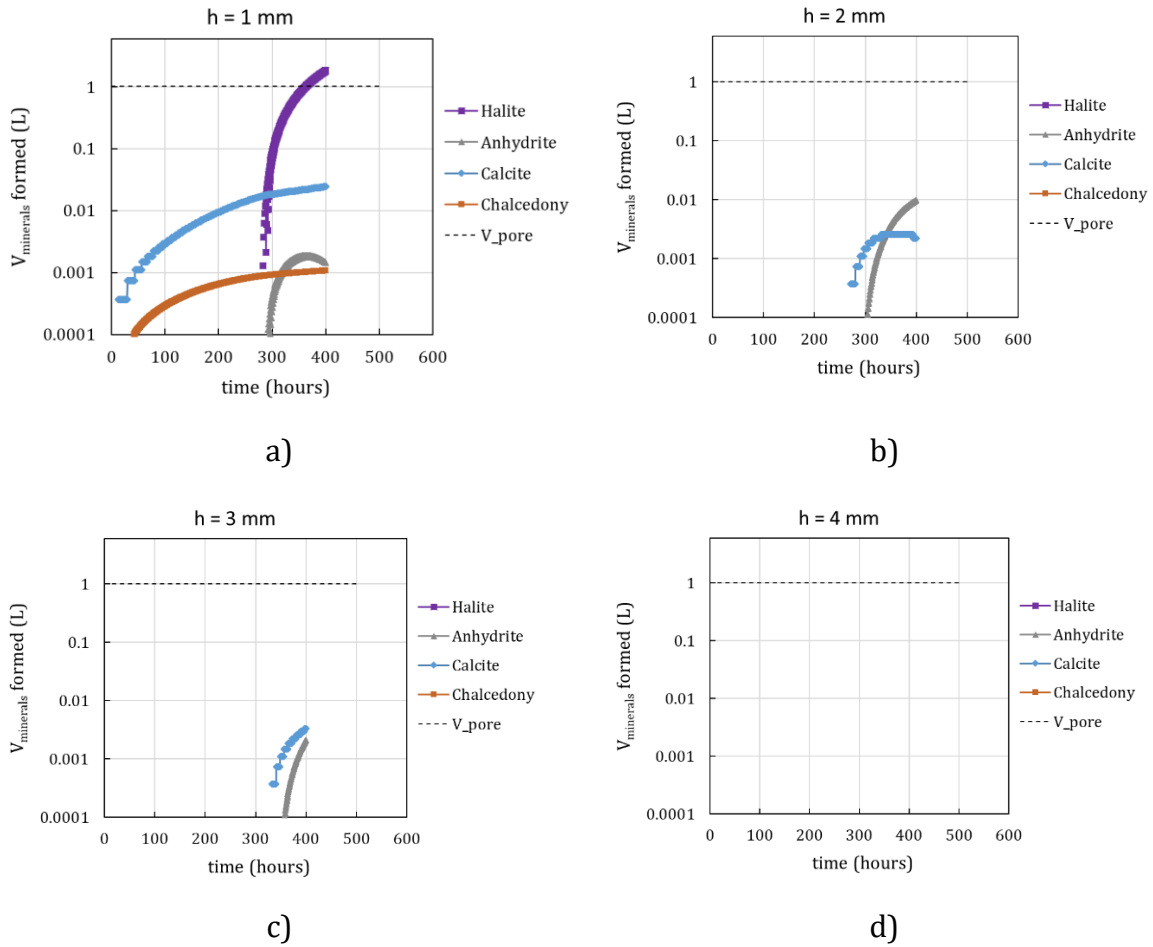


Figure 4.14: Log-linear evolution of volume of each mineral allowed to precipitate as a function of time for different distance: a) 1 mm b) 2 mm c) 3 mm and d) 4 mm. The black dashed-line represents the initial volume of pore solution.

Halite is only formed at the evaporation front over 1 mm and is the main responsible of clogging of the porosity (Fig. 4.14-a). Anhydrite and calcite precipitate over 3 mm (Fig. 4.14-a,b, and c) with a preferential location at 2 mm from the CO₂-brine interface for anhydrite (Fig. 4.14-b) and at 1 mm from the CO₂-brine interface for calcite. Above 3 mm, no mineral precipitates (Fig. 4.14-d).

4.7 Conclusion

In this chapter, we have studied, at pore scale, 3 main phenomena that are encountered in CO₂ storage conditions in deep saline aquifers: i) evaporation of brine into the CO₂ stream. We have shown it is a phenomenon that affects all ionic species in solution and has a significant effect within 3 mm of the evaporation front. An extrapolation of these results to the reservoir scale suggests that this phenomenon would have a significant effect over a distance of 3 m from the CO₂ near-well injection. For this purpose, Peysson

et al. [194] experimentally investigate the drying effects, salt precipitation and capillary forces at core scale and a numerical interpretation was investigated by André *et al.*[73]. At core scale, they highlighted the phenomena of precipitation and evaporation in the near-well injection zone. Numerical interpretation showed that evaporation is a phenomenon that affects the first 5 m of the CO₂ near-well injection and consequently precipitation as well. This is in good agreement with our observations. ii) Diffusive reactive transport which is the major force in the evolution of the thermodynamic properties we have studied. We have shown that diffusion (retrodiffusion) does not compensate the concentration increase due to evaporation. However, in reservoir conditions, this depends strongly on the CO₂ injection flow and the evaporation rate of the brine in the CO₂ injection flow. Peysson *et al.* [194] and André *et al.*[73] highlighted the influence of the CO₂ injection flow, and the impact of capillary backflow which, depending on whether they are more or less important, will have a different clogging effect. iii) The precipitation of salts is given by "universal" thermodynamic constraints that organise the appearance/disappearance of mineral phases. In this study we have considered that all reactions are at equilibrium, assuming that we have an infinite velocity. Indeed, in this context, the minerals react instantaneously i.e. as soon as the saturation index is slightly higher than zero ($IS > 0$) the minerals precipitate and otherwise the minerals dissolve ($IS < 0$). However, for a better analysis of the results, it is important to introduce a kinetic limitation of precipitation and/or dissolution whose rate parameters of water-mineral interaction kinetics have been provided by Palandri *et al.* [220]. The precipitation kinetics is defined as the speed at which the minerals will precipitate. Thus, by introducing a kinetic limitation, one could have a complete reorganisation of the appearance/disappearance of minerals, knowing that temperature is a parameter that also affects the kinetic laws. It is therefore possible to achieve a supersaturation state of minerals ($IS > 0$), depending on whether the rate of evaporation is high or the solution is highly concentrated, while having small amounts of minerals being formed. This could contribute to reorganise the order of appearance of minerals and their contribution to the clogging of the porosity.

In this chapter, we have also shown that higher salinity gives rise to higher amounts of salt precipitation and therefore leads to higher porosity reduction. Our simulation shows that even a moderately salted brine can precipitate minerals during its evaporation having a major impact on the reservoir hydraulic properties, particularly the porosity. As

the pore space is invaded by precipitating minerals, the reaction paths for evaporation and diffusion become increasingly reduced. As a result, the morphology of the crystals that form may be altered and therefore a change of the geometric properties of the pore network and petrophysical properties. In our study, salt precipitation occurs in a local form and is related to the capillary drying regime. Since the porosity is clogged at the first cell, there is no more evaporation. However, in the practical case, it is possible that, during their growth, the minerals leave a “mini” porosity between grains where water can still percolate and reach the larger pore where the CO₂-rich phase flows. Some studies performed at the pore by Kim *et al.* [76], and Miri *et al.*[92] on the salt crystallization have revealed that although salt crystals precipitate at different rates, they can grow in both the liquid and gas phases. The precipitates occupy the space initially available to the flow leading to the reduce of the porosity of the medium. Even a moderate change in porosity due to salt precipitation can have a significant effect on permeability. If salinity and temperature are considered as sensitive parameters that can influence the salt precipitation, the CO₂ injection flow rate is a key parameter. Therefore, modelling the mechanism of salt precipitation at the reservoir scale would require taking into account the evaporation rate as a function of the CO₂ injection rate, the change in porosity at the interface, and the kinetics of precipitation of mineral including a possible efflorescence in the draining pore.

General conclusion

The injection of supercritical CO₂ into deep saline aquifers has been recognized as one of the most promising ways to mitigate atmospheric CO₂ emissions and thus respond to the growing challenges of climate change. Deep saline aquifers are made of porous rocks saturated with highly saline water unusable for domestic needs and unfit for consumption. In addition, they have a huge storage capacity that can raise to several gigatons, making them the most suitable reservoir for CO₂ storage. However, the injection of sCO₂ in these porous medium considerably disturbs the equilibrium state of the medium. Indeed, it is known to trigger several phenomena in the near well zone, in particular a salt precipitation associated to heat and mass exchanges. This influence the evolution of the porosity and permeability, and therefore injectivity of the reservoir and the safety of the storage. This thesis project aimed at studying the transport phenomena inducing salt precipitation associated with a thermal gradient, and at understanding the physico-chemical processes at the interface between brine and sCO₂ in a case of a real reservoir.

In order to achieve the objectives, the study was based on experimental and numerical approaches in isothermal and non-isothermal conditions. From an experimental point of view, the target was to study in free medium, the chemical reactivity between an aqueous solution of CaCl₂ and an aqueous solution of Na₂SO₄ to obtain the precipitation of gypsum (CaSO₄·2H₂O). We have developed a diffusion cell that allow to superimpose vertically 2 to 3 layers of salt solutions of different concentrations and different chemical composition, and to study the mass transport phenomena that take place in the cell. The characterization technique is based on the analysis of the light scattered by the NEFs that establish during the diffusion process of the solutes. The cell was installed in an optical shadowgraphy device. The analysis setup and methodology was calibrated using first a molecular binary mixture of TEG/water and then the aqueous solutions of NaCl, CaCl₂ and Na₂SO₄. A subsequent fitting of the decay times of the c-NEFs allowed us to calculate the diffusion coefficients of TEG/water as well as the dissolved salts in water. Our results are in good agreement with the literature data. This is very innovative because the measurement of the diffusion coefficients in a free-diffusion process by the shadowgraphy technique had never been done before to the best of our knowledge. However, we found

that for electrolyte solutions, it was better to consider solutes concentrations far from the saturation with respect to the solid salts in order to obtain a mono-exponential behaviour and a constant background level of the SFs. The free-diffusion of NaCl in water, with and without the thermal gradient at a mean temperature of 25 °C, suggested that the thermal gradient does not have a significant effect on the relaxation mode of the system.

A superimposition of two aqueous layers of non-reactive and reactive salts was possible in the diffusion cell and the dynamics of the relaxation was studied by the shadowgraphy technique. The dynamics of relaxation of the system formed by the diffusion of an aqueous solution of CaCl₂ into an aqueous solution of NaCl resulted in the appearance of some diffraction spots on the contrasts of the images, whereas the appearance of convection patterns was obvious for the diffusion of an aqueous solution of NaCl into an aqueous solution of Na₂SO₄. The numerical interpretation of the results was provided using the PHREEQC modelling tool. Considering heterogeneous multicomponent diffusion allowed explaining the observed convective instability by revealing a density inversion near the interface.

As for the superimposition of two reactive salts, a layer of an aqueous solution of CaCl₂ was brought into contact with a layer of an aqueous solution of Na₂SO₄, separated by an intermediate layer of an aqueous solution of NaCl in order to delay the appearance of gypsum. With the experimental observations parallel to the gravity, we observed that the precipitation time strongly depends on the thickness of the the buffer solution which controls the diffusion distance that ions have to cross. A strong variation in the contrast of the images in the early stages was obvious, which was associated to convection patterns. When applying a thermal gradient perpendicular to the interface, the analysis of the evolution of the contrast of the image as a function of time revealed that, the thermal gradient did not have a noticeable influence on the onset time of precipitation. These same results were obtained by numerical simulation considering heterogeneous multicomponent diffusion calculation. In summary of this study, we were able to carry out laboratory experiments and interpret the different phenomena by numerical modelling. This integrated approach highlights the mutual benefits gained both at the experimental and theoretical levels. From a numerical point of view, heterogeneous multicomponent diffusion is well suited to describe the behaviour of electrolytes in solution in a multicomponent system without advective fluid flow. Indeed, it integrates all the interactions between the aqueous species and helped explaining non-intuitive phenomena

such as the local inversion of density, which can be a source of physical instability responsible for the onset of digitation within the liquid aqueous phase. In a complex multicomponent system either in free or in porous medium, we recommend to consider the heterogeneous multicomponent diffusion.

This major result (even if obtained at ambient temperature and atmospheric pressure) was applied to saline solutions representative of real reservoirs (Dogger aquifer), where stronger constraints were brought by the mineralogy and a condition of constant composition of CO₂ gas phase in contact with the water formation was introduced. Three main phenomena that are encountered in CO₂ storage conditions in deep saline aquifers were studied at cm scale, namely: i) the evaporation of brine into the CO₂ stream that was shown to affect all ionic species in solution, ii) the diffusive reactive transport which is the major driving force in the evolution of the thermodynamic properties, and iii) the precipitation of salts is given by "universal" thermodynamic constraints that organise the appearance/disappearance of mineral phases. We have shown that higher salinity gives rise to higher amounts of salt precipitation and therefore leads to higher porosity reduction. Even a moderately salted brine can precipitate minerals during its evaporation having a major impact on the reservoir hydraulic properties, particularly the porosity. An introduction of a kinetic constraint is necessary and can contribute to reorganise the order of appearance of minerals and the magnitude of their contribution to the clogging of the porosity.

In this thesis, all experimental measurements were carried out in a free medium, at a mean temperature of 25 °C and at atmospheric pressure. However, the diffusion cell developed during this thesis allows reaching average temperatures up to 60 °C and pressures up to 200 bar. Since we are now able to generate and study salt precipitation phenomena, a perspective would be to use the diffusion cell developed during the thesis to work under reservoir conditions and study the precipitation of other minerals like carbonates. Another perspective would also be to develop techniques for analysing the precipitates that form, for example by X-ray diffraction (XRD). We used a cell with a thickness of 1 cm. A small variation in the volume of solution injected into the cell gives very large uncertainties. To reduce these uncertainties, one can move to a larger cell. In this cell, one could even add a porous medium. Numerically, PHREEQC is a powerful geochemical modelling tool. It would be very important to add kinetic aspects in our

simulation scripts. Moreover, PHREEQC offers the possibility to do either advective or diffusive transport mechanisms. We could consider coupling of PHREEQC with other software in order to have a good description of the permeability-porosity heterogeneities.

Bibliography

- [1] M. R. Mansouri Daneshvar, M. Ebrahimi, and H. Nejadsoleymani, 'An overview of climate change in Iran: facts and statistics', *ENVIRONMENTAL SYSTEMS RESEARCH*, vol. 8, Mar. 2019, doi: 10.1186/s40068-019-0135-3.
- [2] IPCC, 'IPCC Special Report on Carbon Dioxide Capture and Storage. Cambridge University Press, UK', 2005.
- [3] T. M. Letcher, 'Why do we have global warming?', in *Managing Global Warming*, Elsevier, 2019, pp. 3–15. doi: 10.1016/B978-0-12-814104-5.00001-6.
- [4] M. Jafari, S. C. Cao, and J. Jung, 'Geological CO₂ sequestration in saline aquifers: Implication on potential solutions of China's power sector', *Resources, Conservation and Recycling*, vol. 121, pp. 137–155, Jun. 2017, doi: 10.1016/j.resconrec.2016.05.014.
- [5] WMO, *WMO statement on the state of the global climate in 2019*. 2020. [Online]. Available: https://library.wmo.int/doc_num.php?explnum_id=10211
- [6] C. Le Quéré *et al.*, 'Temporary reduction in daily global CO₂ emissions during the COVID-19 forced confinement', *Nature Climate Change*, vol. 10, no. 7, pp. 647–653, Jul. 2020, doi: 10.1038/s41558-020-0797-x.
- [7] K. Caldeira *et al.*, 'A Portfolio of Carbon Management Options', 2004, pp. 103–129.
- [8] K. S. Lackner, D. P. Butt, and C. H. Wendt, 'Progress on binding CO₂ in mineral substrates', *Energy Conversion and Management*, vol. 38, pp. S259–S264, Jan. 1997, doi: 10.1016/S0196-8904(96)00279-8.
- [9] J. Lipponen, K. Burnard, B. Beck, J. Gale, and B. Pegler, 'The IEA CCS Technology Roadmap: One Year On', *Energy Procedia*, vol. 4, pp. 5752–5761, 2011, doi: 10.1016/j.egypro.2011.02.571.
- [10] A. Rojey and T. A. Torp, 'Éditorial: "la capture et le stockage géologique du co₂: perspectives"', *Oil & Gas Science and Technology*, vol. 60, no. 3, pp. 441–448, May 2005, doi: 10.2516/ogst:2005026.
- [11] R. FARRET, 'Captage et stockage géologique du CO₂ : retour d'expérience et perspectives', rapport INERIS DRS-17-164859-08281A, Nov. 2017.
- [12] J. C. White, G. Williams, A. Chadwick, A.-K. Furre, and A. Kiær, 'Sleipner: The ongoing challenge to determine the thickness of a thin CO₂ layer', *International Journal of Greenhouse Gas Control*, vol. 69, pp. 81–95, Feb. 2018, doi: 10.1016/j.ijggc.2017.10.006.
- [13] H. Kongsjorden, O. Kårstad, and T. A. Torp, 'Saline aquifer storage of carbon dioxide in the Sleipner project', *Waste Management*, vol. 17, no. 5, pp. 303–308, Jan. 1998, doi: 10.1016/S0956-053X(97)10037-X.
- [14] T. A. Torp and J. Gale, 'Demonstrating storage of CO₂ in geological reservoirs: The Sleipner and SACS projects', *Energy*, vol. 29, no. 9, pp. 1361–1369, Jul. 2004, doi: 10.1016/j.energy.2004.03.104.
- [15] J.-Q. Shi, C. Imrie, C. Sinayuc, S. Durucan, A. Korre, and O. Eiken, 'Snøhvit CO₂ Storage Project: Assessment of CO₂ Injection Performance Through History Matching of the Injection Well Pressure Over a 32-months Period', *Energy Procedia*, vol. 37, pp. 3267–3274, Jan. 2013, doi: 10.1016/j.egypro.2013.06.214.
- [16] P. S. Ringrose *et al.*, 'The In Salah CO₂ Storage Project: Lessons Learned and Knowledge Transfer', *Energy Procedia*, vol. 37, pp. 6226–6236, Jan. 2013, doi: 10.1016/j.egypro.2013.06.551.

- [17] J. Logan, J. Venezia, and K. Larsen, 'OPPORTUNITIES AND CHALLENGES FOR CARBON CAPTURE AND SEQUESTRATION', p. 8, 2007.
- [18] O. Hansen *et al.*, 'Snøhvit: The History of Injecting and Storing 1 Mt CO₂ in the Fluvial Tubåen Fm', *Energy Procedia*, vol. 37, pp. 3565–3573, 2013, doi: 10.1016/j.egypro.2013.06.249.
- [19] R. FARRET, P. GOMBERT, and A. THORAVAL, 'Etat des connaissances sur les risques liés au stockage géologique du CO₂, Rapport n°2 : les risques en phase de stockage à long terme', rapport INERIS DRS-12-126009-01377A, 2012.
- [20] P. GOMBERT and A. THORAVAL, 'Etat des connaissances sur les risques liés au stockage géologique du CO₂. Rapport n°1 : les risques en phase d'injection', rapport INERIS DRS-08-95145-11842A du 06/10/2009, 2009.
- [21] V. Vilarrasa and J. Rutqvist, 'Thermal effects on geologic carbon storage', *Earth-Science Reviews*, vol. 165, pp. 245–256, Feb. 2017, doi: 10.1016/j.earscirev.2016.12.011.
- [22] S. Bachu, 'Sequestration of CO₂ in geological media: criteria and approach for site selection in response to climate change', *Energy Conversion and Management*, vol. 41, no. 9, pp. 953–970, Jun. 2000, doi: 10.1016/S0196-8904(99)00149-1.
- [23] S. Bachu, 'Sequestration of CO₂ in geological media in response to climate change: road map for site selection using the transform of the geological space into the CO₂ phase space', *Energy Conversion and Management*, vol. 43, no. 1, pp. 87–102, Jan. 2002, doi: 10.1016/S0196-8904(01)00009-7.
- [24] M. Bentham and Mg. Kirby, 'CO₂ Storage in Saline Aquifers', *Oil & Gas Science and Technology*, vol. 60, no. 3, pp. 559–567, May 2005, doi: 10.2516/ogst:2005038.
- [25] P. GOMBERT and A. THORAVAL, 'Etat des connaissances sur les risques liés au stockage géologique du CO₂ Rapport n°1 : les risques en phase d'injection', Rapport d'étude INERIS DRS-08-95145-11842B, Mar. 2010.
- [26] S. Holloway and D. Savage, 'The potential for aquifer disposal of carbon dioxide in the UK', *Energy Conversion and Management*, vol. 34, no. 9–11, pp. 925–932, Sep. 1993, doi: 10.1016/0196-8904(93)90038-C.
- [27] B. Hitchon, W. D. Gunter, T. Gentzis, and R. T. Bailey, 'Sedimentary basins and greenhouse gases: a serendipitous association', *Energy Conversion and Management*, vol. 40, no. 8, pp. 825–843, May 1999, doi: 10.1016/S0196-8904(98)00146-0.
- [28] L. Wickstrom, E. Slucher, M. Baranoski, and D. Mullett, 'Geologic Assessment of the Burger Power Plant and Surrounding Vicinity for Potential Injection of Carbon Dioxide', Jan. 2008.
- [29] H. Emami-Meybodi, H. Hassanzadeh, C. P. Green, and J. Ennis-King, 'Convective dissolution of CO₂ in saline aquifers: Progress in modeling and experiments', *International Journal of Greenhouse Gas Control*, vol. 40, pp. 238–266, Sep. 2015, doi: 10.1016/j.ijggc.2015.04.003.
- [30] S. Bachu, 'Screening and ranking of sedimentary basins for sequestration of CO₂ in geological media in response to climate change', *Env Geol*, vol. 44, no. 3, pp. 277–289, Jun. 2003, doi: 10.1007/s00254-003-0762-9.
- [31] S. Bachu and J. J. Adams, 'Sequestration of CO₂ in geological media in response to climate change: capacity of deep saline aquifers to sequester CO₂ in solution', *Energy Conversion and Management*, vol. 44, no. 20, pp. 3151–3175, Dec. 2003, doi: 10.1016/S0196-8904(03)00101-8.

- [32] U. Zahid, Y. Lim, J. Jung, and C. Han, 'CO₂ Geological Storage: A Review on Present and Future Prospects', *Korean Journal of Chemical Engineering*, vol. 28, Mar. 2011, doi: 10.1007/s11814-010-0454-6.
- [33] S. Benson *et al.*, 'Chapter 5 - Underground geological storage. IPCC Special Report on CO₂ capture and sequestration.', 2005, pp. 197–265.
- [34] S. Garcia, S. Kaminska, and M. Mercedes Maroto-Valer, 'Underground carbon dioxide storage in saline formations', *Proceedings of the Institution of Civil Engineers - Waste and Resource Management*, vol. 163, no. 2, pp. 77–88, May 2010, doi: 10.1680/warm.2010.163.2.77.
- [35] M. A. Hesse, F. M. Orr, and H. A. Tchelepi, 'Gravity currents with residual trapping', *Journal of Fluid Mechanics*, vol. 611, pp. 35–60, Sep. 2008, doi: 10.1017/S002211200800219X.
- [36] G. P. D. De Silva, P. G. Ranjith, and M. S. A. Perera, 'Geochemical aspects of CO₂ sequestration in deep saline aquifers: A review', *Fuel*, vol. 155, pp. 128–143, Sep. 2015, doi: 10.1016/j.fuel.2015.03.045.
- [37] S. Iglauer, 'Dissolution Trapping of Carbon Dioxide in Reservoir Formation Brine – A Carbon Storage Mechanism', in *Mass Transfer - Advanced Aspects*, H. Nakajima, Ed. InTech, 2011. doi: 10.5772/20206.
- [38] S. M. V. Gilfillan *et al.*, 'Solubility trapping in formation water as dominant CO₂ sink in natural gas fields', *Nature*, vol. 458, no. 7238, pp. 614–618, Apr. 2009, doi: 10.1038/nature07852.
- [39] H. Messabeb, F. Contamine, P. Cézac, J. P. Serin, and E. C. Gaucher, 'Experimental Measurement of CO₂ Solubility in Aqueous NaCl Solution at Temperature from 323.15 to 423.15 K and Pressure of up to 20 MPa', *J. Chem. Eng. Data*, vol. 61, no. 10, pp. 3573–3584, Oct. 2016, doi: 10.1021/acs.jced.6b00505.
- [40] H. Messabeb, F. Contamine, P. Cézac, J. P. Serin, C. Pouget, and E. C. Gaucher, 'Experimental Measurement of CO₂ Solubility in Aqueous CaCl₂ Solution at Temperature from 323.15 to 423.15 K and Pressure up to 20 MPa Using the Conductometric Titration', *J. Chem. Eng. Data*, vol. 62, no. 12, pp. 4228–4234, Dec. 2017, doi: 10.1021/acs.jced.7b00591.
- [41] M. Poulain *et al.*, 'Experimental Measurements of Carbon Dioxide Solubility in Na–Ca–K–Cl Solutions at High Temperatures and Pressures up to 20 MPa', *Journal of Chemical and Engineering Data*, vol. 64, no. 6, p. 2497, 2019, doi: 10.1021/acs.jced.9b00023.
- [42] P. F. dos Santos, L. André, M. Ducouso, F. Contamine, and P. Cézac, 'Experimental Measurement of CO₂ Solubility in Aqueous Na₂SO₄ Solution at Temperatures between 303.15 and 423.15 K and Pressures up to 20 MPa', *J. Chem. Eng. Data*, vol. 65, no. 6, pp. 3230–3239, Jun. 2020, doi: 10.1021/acs.jced.0c00230.
- [43] P. F. dos Santos *et al.*, 'An improved model for CO₂ solubility in aqueous Na⁺–Cl[–]–SO₄^{2–} systems up to 473.15 K and 40 MPa', *Chemical Geology*, vol. 582, p. 120443, Nov. 2021, doi: 10.1016/j.chemgeo.2021.120443.
- [44] O. Bouc, G. Bellenfant, D. Fauconnier, D. Guyonnet, and N. Jacquemet, 'Critères de sécurité pour le stockage géologique du CO₂', p. 227, 2006.
- [45] F. Yang, B. Bai, D. Tang, D.-N. Shari, and W. David, 'Characteristics of CO₂ sequestration in saline aquifers', *Pet. Sci.*, vol. 7, no. 1, pp. 83–92, Mar. 2010, doi: 10.1007/s12182-010-0010-3.
- [46] A. G. Ilgen and R. T. Cygan, 'Mineral dissolution and precipitation during CO₂ injection at the Frio-I Brine Pilot: Geochemical modeling and uncertainty analysis',

- International Journal of Greenhouse Gas Control*, vol. 44, pp. 166–174, Jan. 2016, doi: 10.1016/j.ijggc.2015.11.022.
- [47] N. Kampman, M. Bickle, M. Wigley, and B. Dubacq, 'Fluid flow and CO₂-fluid-mineral interactions during CO₂-storage in sedimentary basins', *Chemical Geology*, vol. 369, pp. 22–50, Mar. 2014, doi: 10.1016/j.chemgeo.2013.11.012.
- [48] P. Newell and A. G. Ilgen, 'Chapter 1 - Overview of Geological Carbon Storage (GCS)', in *Science of Carbon Storage in Deep Saline Formations*, P. Newell and A. G. Ilgen, Eds. Elsevier, 2019, pp. 1–13. doi: 10.1016/B978-0-12-812752-0.00001-0.
- [49] L. André, M. Azaroual, and A. Menjoz, 'Numerical Simulations of the Thermal Impact of Supercritical CO₂ Injection on Chemical Reactivity in a Carbonate Saline Reservoir', *Transp Porous Med*, vol. 82, no. 1, pp. 247–274, Mar. 2010, doi: 10.1007/s11242-009-9474-2.
- [50] L. André, P. Audigane, M. Azaroual, and A. Menjoz, 'Numerical modeling of fluid-rock chemical interactions at the supercritical CO₂-liquid interface during CO₂ injection into a carbonate reservoir, the Dogger aquifer (Paris Basin, France)', *Energy Conversion and Management*, vol. 48, no. 6, pp. 1782–1797, Jun. 2007, doi: 10.1016/j.enconman.2007.01.006.
- [51] M. Azaroual *et al.*, 'Behaviour of the CO₂ injection well and the near wellbore during carbon dioxide injection in saline aquifers', Sep. 2012, p. Session V: Carbon Dioxide Storage II. Accessed: Sep. 07, 2021. [Online]. Available: <https://hal-brgm.archives-ouvertes.fr/hal-00755073>
- [52] I. Gaus *et al.*, 'Geochemical and solute transport modelling for CO₂ storage, what to expect from it?', *International Journal of Greenhouse Gas Control*, vol. 2, no. 4, pp. 605–625, Oct. 2008, doi: 10.1016/j.ijggc.2008.02.011.
- [53] A. Kopp, A. Ebigbo, A. Bielinski, H. Class, and R. Helmig, 'Numerical simulation of temperature changes caused by CO₂ injection in geological reservoirs', vol. 59, 2009, pp. 439–456. doi: 10.1306/13171255St593391.
- [54] E. Jobard, J. Sterpenich, J. Pironon, J. Corvisier, M. Jouanny, and A. Randi, 'Experimental simulation of the impact of a thermal gradient during geological sequestration of CO₂: The COTAGES experiment', *International Journal of Greenhouse Gas Control*, vol. 12, pp. 56–71, Jan. 2013, doi: 10.1016/j.ijggc.2012.11.001.
- [55] W. S. Han, K.-Y. Kim, E. Park, B. McPherson, S.-Y. Lee, and M.-H. Park, 'Modeling of Spatiotemporal Thermal Response to CO₂ Injection in Saline Formations: Interpretation for Monitoring', *Transport in Porous Media*, vol. 93, Jul. 2012, doi: 10.1007/s11242-012-9957-4.
- [56] W. S. Han, G. A. Stillman, M. Lu, C. Lu, B. J. McPherson, and E. Park, 'Evaluation of potential nonisothermal processes and heat transport during CO₂ sequestration', *Journal of Geophysical Research*, vol. 115, no. B7, Jul. 2010, doi: 10.1029/2009JB006745.
- [57] V. Vilarrasa, S. Olivella, J. Carrera, and J. Rutqvist, 'Long term impacts of cold CO₂ injection on the caprock integrity', *International Journal of Greenhouse Gas Control*, vol. 24, pp. 1–13, May 2014, doi: 10.1016/j.ijggc.2014.02.016.
- [58] C. Lu, W. S. Han, S.-Y. Lee, B. J. McPherson, and P. C. Lichtner, 'Effects of density and mutual solubility of a CO₂-brine system on CO₂ storage in geological formations: "Warm" vs. "cold" formations', *Advances in Water Resources*, vol. 32, no. 12, pp. 1685–1702, Dec. 2009, doi: 10.1016/j.advwatres.2009.07.008.

- [59] M. A. Nomeli, N. Tilton, and A. Riaz, 'A new model for the density of saturated solutions of CO₂-H₂O-NaCl in saline aquifers', *International Journal of Greenhouse Gas Control*, vol. 31, pp. 192–204, Dec. 2014, doi: 10.1016/j.ijggc.2014.10.006.
- [60] M. Abbaszadeh, S. Shariatipour, and A. Ifelebuegu, 'The influence of temperature on wettability alteration during CO₂ storage in saline aquifers', *International Journal of Greenhouse Gas Control*, vol. 99, p. 103101, Aug. 2020, doi: 10.1016/j.ijggc.2020.103101.
- [61] C. Cottin, H. Bodiguel, and A. Colin, 'Drainage in two-dimensional porous media: From capillary fingering to viscous flow', *Physical review. E, Statistical, nonlinear, and soft matter physics*, vol. 82, p. 046315, Oct. 2010, doi: 10.1103/PhysRevE.82.046315.
- [62] F. Osselin, 'Thermochemical-based poroelastic modelling of salt crystallization, and a new multiphase flow experiment : how to assess injectivity evolution in the context of CO₂ storage in deep aquifers', phdthesis, Université Paris-Est, 2013. Accessed: Jun. 08, 2021. [Online]. Available: <https://pastel.archives-ouvertes.fr/tel-00958697>
- [63] R. Lenormand, E. Touboul, and C. Zarcone, 'Numerical Models and Experiments on Immiscible Displacement in Porous Media', *Journal of Fluid Mechanics*, vol. 189, pp. 165–187, Apr. 1988, doi: 10.1017/S0022112088000953.
- [64] R. Lenormand, 'Liquids in Porous-Media', *Journal of Physics: Condensed Matter*, vol. 2, p. SA79, Jan. 1999, doi: 10.1088/0953-8984/2/S/008.
- [65] R. Lenormand and C. Zarcone, 'Capillary fingering: Percolation and fractal dimension', *Transp Porous Med*, vol. 4, no. 6, pp. 599–612, Dec. 1989, doi: 10.1007/BF00223630.
- [66] S. Cao, B. Bate, J. Hu, and J. Jung, 'Engineering Behavior and Characteristics of Water-Soluble Polymers: Implication on Soil Remediation and Enhanced Oil Recovery', *Sustainability*, vol. 8, no. 3, p. 205, Feb. 2016, doi: 10.3390/su8030205.
- [67] S. Morais, 'Applications des laboratoires géologiques sur puce pour les problématiques du stockage du CO₂', phdthesis, Université de Bordeaux, 2016. Accessed: Nov. 19, 2021. [Online]. Available: <https://tel.archives-ouvertes.fr/tel-01500101>
- [68] C. Gniese *et al.*, 'Relevance of Deep-Subsurface Microbiology for Underground Gas Storage and Geothermal Energy Production', in *Geobiotechnology II*, vol. 142, A. Schippers, F. Glombitza, and W. Sand, Eds. Berlin, Heidelberg: Springer Berlin Heidelberg, 2013, pp. 95–121. doi: 10.1007/10_2013_257.
- [69] T. O. Okyay and D. F. Rodrigues, 'Biotic and abiotic effects on CO₂ sequestration during microbially-induced calcium carbonate precipitation', *FEMS Microbiology Ecology*, vol. 91, no. fiv017, Mar. 2015, doi: 10.1093/femsec/fiv017.
- [70] J. R. Thompson, A. J. E. Freedman, K. C. Peet, and J. Ajo-Franklin, 'Field Observations, Experimental Studies, and Thermodynamic Modeling of CO₂ Effects on Microbial Populations', in *Science of Carbon Storage in Deep Saline Formations*, Elsevier, 2019, pp. 263–290. doi: 10.1016/B978-0-12-812752-0.00012-5.
- [71] Y. Cinar and A. Riaz, 'Carbon dioxide sequestration in saline formations: Part 2—Review of multiphase flow modeling', *Journal of Petroleum Science and Engineering*, vol. 124, pp. 381–398, Dec. 2014, doi: 10.1016/j.petrol.2014.07.023.
- [72] K. Pruess and N. Müller, 'Formation dry-out from CO₂ injection into saline aquifers: 1. Effects of solids precipitation and their mitigation', *Water Resources Research*, vol. 45, no. 3, 2009, doi: <https://doi.org/10.1029/2008WR007101>.

- [73] L. André, Y. Peysson, and M. Azaroual, 'Well injectivity during CO₂ storage operations in deep saline aquifers – Part 2: Numerical simulations of drying, salt deposit mechanisms and role of capillary forces', *International Journal of Greenhouse Gas Control*, vol. 22, pp. 301–312, Mar. 2014, doi: 10.1016/j.ijggc.2013.10.030.
- [74] N. Muller, R. Qi, E. Mackie, K. Pruess, and M. J. Blunt, 'CO₂ injection impairment due to halite precipitation', *Energy Procedia*, vol. 1, no. 1, pp. 3507–3514, Feb. 2009, doi: 10.1016/j.egypro.2009.02.143.
- [75] Y. Wang *et al.*, 'Halite Precipitation and Permeability Assessment During Supercritical CO₂ Core Flood. In: International Symposium of the Society of Core Analysis, Halifax, pp. 4–7.', 2010.
- [76] M. Kim, A. Sell, and D. Sinton, 'Aquifer-on-A-Chip: Understanding pore-scale salt precipitation dynamics during CO₂ sequestration', *Lab on a chip*, vol. 13, Mar. 2013, doi: 10.1039/c3lc00031a.
- [77] R. Miri and H. Hellevang, 'Salt precipitation during CO₂ storage—A review', *International Journal of Greenhouse Gas Control*, vol. 51, pp. 136–147, Aug. 2016, doi: 10.1016/j.ijggc.2016.05.015.
- [78] M. Azaroual, K. Pruess, and C. Fouillac, 'Feasibility of using supercritical CO₂ as heat transmission fluid in the EGS integrating the carbon storage constraints.', *ENGINE – ENhanced Geothermal Innovative Network for Europe Workshop 2, Exploring high temperature reservoirs: new challenges for geothermal energy Volterra, 1-4 April 2007, Italy*.
- [79] S. Morais *et al.*, 'Monitoring CO₂ invasion processes at the pore scale using geological labs on chip', *Lab Chip*, vol. 16, no. 18, pp. 3493–3502, Aug. 2016, doi: 10.1039/C6LC00830E.
- [80] J. Joseph, N. S. K. Gunda, and S. Mitra, 'On-chip porous media: Porosity and permeability measurements', *Chemical Engineering Science*, vol. 99, pp. 274–283, Aug. 2013, doi: 10.1016/j.ces.2013.05.065.
- [81] Y. Zhao, Y. Song, Y. Liu, H. Liang, and B. Dou, 'Visualization and Measurement of CO₂ Flooding in Porous Media Using MRI', *Ind. Eng. Chem. Res.*, vol. 50, no. 8, pp. 4707–4715, Apr. 2011, doi: 10.1021/ie1013019.
- [82] C. Zhang, M. Oostrom, J. W. Grate, T. W. Wietsma, and M. G. Warner, 'Liquid CO₂ Displacement of Water in a Dual-Permeability Pore Network Micromodel', *Environ. Sci. Technol.*, vol. 45, no. 17, pp. 7581–7588, Sep. 2011, doi: 10.1021/es201858r.
- [83] C. Zhang, M. Oostrom, T. W. Wietsma, J. W. Grate, and M. G. Warner, 'Influence of Viscous and Capillary Forces on Immiscible Fluid Displacement: Pore-Scale Experimental Study in a Water-Wet Micromodel Demonstrating Viscous and Capillary Fingering', *Energy Fuels*, vol. 25, no. 8, pp. 3493–3505, Aug. 2011, doi: 10.1021/ef101732k.
- [84] E. Ozgur and F. Gümrah, 'Analytical and Numerical Modeling of CO₂ Sequestration in Deep Saline Aquifers', *Energy Sources, Part A: Recovery, Utilization, and Environmental Effects*, vol. 32, no. 7, pp. 674–687, Jan. 2010, doi: 10.1080/15567030802606145.
- [85] B. Bijeljic and M. Blunt, 'Pore-scale modeling and continuous random walk analysis of dispersion in porous media', *Water Resources Research - WATER RESOUR RES*, vol. 42, Jan. 2006, doi: 10.1029/2005WR004578.
- [86] J. Bear, *Dynamics of Fluids In Porous Media*. American Elsevier Publishing Company, 1972.

- [87] Papa Ousmane Mangane, 'Caractérisation des changements dans les propriétés de réservoir carbonaté induits par une modification dans la structure des pores lors d'une injection de CO₂: application au stockage géologique du CO₂', Université Montpellier 2, 2013.
- [88] F. Gjetvaj, 'Experimental characterization and modeling non-Fickian dispersion in aquifers', Theses, Université Montpellier, 2015. Accessed: Aug. 05, 2021. [Online]. Available: <https://tel.archives-ouvertes.fr/tel-02049304>
- [89] C. A. J. Appelo and P. Wersin, 'Multicomponent Diffusion Modeling in Clay Systems with Application to the Diffusion of Tritium, Iodide, and Sodium in Opalinus Clay', *Environ. Sci. Technol.*, vol. 41, no. 14, pp. 5002–5007, Jul. 2007, doi: 10.1021/es0629256.
- [90] L. André, M. Azaroual, Y. Peysson, and B. Bazin, 'Impact of porous medium desiccation during anhydrous CO₂ injection in deep saline aquifers: Up scaling from experimental results at laboratory scale to near-well region', *Energy Procedia*, vol. 4, pp. 4442–4449, Jan. 2011, doi: 10.1016/j.egypro.2011.02.398.
- [91] M. G. Lima, P. Schädle, C. P. Green, D. Vogler, M. O. Saar, and X.-Z. Kong, 'Permeability Impairment and Salt Precipitation Patterns During CO₂ Injection Into Single Natural Brine-Filled Fractures', *Water Resources Research*, vol. 56, no. 8, p. e2020WR027213, 2020, doi: 10.1029/2020WR027213.
- [92] R. Miri, R. van Noort, P. Aagaard, and H. Hellevang, 'New insights on the physics of salt precipitation during injection of CO₂ into saline aquifers', *International Journal of Greenhouse Gas Control*, vol. 43, pp. 10–21, Dec. 2015, doi: 10.1016/j.ijggc.2015.10.004.
- [93] R. C. Jones and W. H. Furry, 'The Separation of Isotopes by Thermal Diffusion', *Rev. Mod. Phys.*, vol. 18, no. 2, pp. 151–224, Apr. 1946, doi: 10.1103/RevModPhys.18.151.
- [94] J. E. Powers and C. R. Wilke, 'Separation of liquids by thermal diffusion', *AIChE J.*, vol. 3, no. 2, pp. 213–222, Jun. 1957, doi: 10.1002/aic.690030216.
- [95] C. Soret, 'Sur l'état d'équilibre que prend au point de vue de sa concentration une dissolution saline primitivement homogène dont deux parties sont portées à des températures différentes.', *Archives des sciences physiques et naturelles [de la Bibliothèque Universelle]*, vol. 3, 1879.
- [96] C. Ludwig, *Diffusion zwischen ungleich erwärmten Orten gleich zusammengesetzter Lösung*. Aus der K.K. Hof- und Staatsdruckerei, in Commission bei W. Braumüller, Buchhändler des K.K. Hofes und der K. Akademie der Wissenschaften, 1856.
- [97] pierre costeseque, 'Sur la migration sélective des isotopes et des éléments par thermodiffusion dans les solutions. Applications de l'effet thermogravitationnel en milieu poreux ; observations expérimentales et conséquences géochimiques', Theses, Université Paul Sabatier - Toulouse, 1982. Accessed: Jun. 16, 2021. [Online]. Available: <https://hal.archives-ouvertes.fr/tel-02004870>
- [98] P. Costeseque, C. P. F. Jp, and S. J, 'ON THE IMPORTANCE OF THERMAL DIFFUSION IN THE FORMATION OF BRINES IN GEOTHERMAL SYSTEMS.', 1977, Accessed: Jun. 16, 2021. [Online]. Available: <http://pascal-francis.inist.fr/vibad/index.php?action=getRecordDetail&idt=PASCALGEODEBRGM7820147432>
- [99] J. L. Dandurand, J. P. Fortuné, R. Pérami, J. Schott, and F. Tollon, 'On the importance of mechanical action and thermal gradient in the formation of metal-bearing deposits', *Mineral. Deposita*, vol. 7, no. 4, pp. 339–350, Dec. 1972, doi: 10.1007/BF00208364.

- [100] C. Soullaine and H. A. Tchelepi, 'Micro-continuum Approach for Pore-Scale Simulation of Subsurface Processes', *Transp Porous Med*, vol. 113, no. 3, pp. 431–456, Jul. 2016, doi: 10.1007/s11242-016-0701-3.
- [101] T. Beuvier *et al.*, 'Implementation of in situ SAXS/WAXS characterization into silicon/glass microreactors', *Lab on a Chip*, vol. 15, no. 9, pp. 2002–2008, 2015, doi: 10.1039/C5LC00115C.
- [102] J. F. Torres, A. Komiya, E. Shoji, J. Okajima, and S. Maruyama, 'Development of phase-shifting interferometry for measurement of isothermal diffusion coefficients in binary solutions', *Optics and Lasers in Engineering*, vol. 50, no. 9, pp. 1287–1296, Sep. 2012, doi: 10.1016/j.optlaseng.2012.03.006.
- [103] B. S. Krumgalz, 'Temperature Dependence of Mineral Solubility in Water. Part 3. Alkaline and Alkaline Earth Sulfates', *Journal of Physical and Chemical Reference Data*, vol. 47, no. 2, p. 023101, Jun. 2018, doi: 10.1063/1.5031951.
- [104] N. Møller, 'The prediction of mineral solubilities in natural waters: A chemical equilibrium model for the Na-Ca-Cl-SO₄-H₂O system, to high temperature and concentration', *Geochimica et Cosmochimica Acta*, vol. 52, pp. 821–837, Apr. 1988, doi: 10.1016/0016-7037(88)90354-7.
- [105] I. W. Duedall, 'Seawater: an explanation of differential isothermal compressibility measurements in terms of hydration and ion-water interactions', *Progress in Oceanography*, vol. 7, no. 3, pp. 91–133, Jan. 1977, doi: 10.1016/0079-6611(77)90001-5.
- [106] M. Muniruzzaman and M. Rolle, 'Multicomponent Ionic Transport Modeling in Physically and Electrostatically Heterogeneous Porous Media With PhreeqcRM Coupling for Geochemical Reactions', *Water Resour. Res.*, vol. 55, no. 12, pp. 11121–11143, Dec. 2019, doi: 10.1029/2019WR026373.
- [107] R. B. Bird, W. E. Stewart, and E. N. Lightfoot, 'The Role of Transport Phenomena in Chemical Engineering Teaching and Research: Past, Present, and Future', in *History of Chemical Engineering*, vol. 190, W. F. Furter, Ed. WASHINGTON, D. C.: AMERICAN CHEMICAL SOCIETY, 1980, pp. 153–165. doi: 10.1021/ba-1980-0190.ch009.
- [108] R. Kita, S. Wiegand, and J. Luettmer-Strathmann, 'Sign change of the Soret coefficient of poly(ethylene oxide) in water/ethanol mixtures observed by thermal diffusion forced Rayleigh scattering', *J. Chem. Phys.*, vol. 121, no. 8, pp. 3874–3885, Aug. 2004, doi: 10.1063/1.1771631.
- [109] M. Schraml *et al.*, 'The Soret coefficients of the ternary system water/ethanol/triethylene glycol and its corresponding binary mixtures', *Eur. Phys. J. E*, vol. 44, no. 10, p. 128, Oct. 2021, doi: 10.1140/epje/s10189-021-00134-6.
- [110] J. M. Ortiz de Zárate and J. V. Sengers, 'Finite-size effects in hydrodynamic fluctuations', in *Hydrodynamic Fluctuations in Fluids and Fluid Mixtures*, Elsevier, 2006, pp. 113–140. doi: 10.1016/B978-044451515-5/50006-5.
- [111] A. Vailati and M. Giglio, 'Nonequilibrium fluctuations in time-dependent diffusion processes', *Phys. Rev. E*, vol. 58, no. 4, pp. 4361–4371, Oct. 1998, doi: 10.1103/PhysRevE.58.4361.
- [112] Crocchio Fabrizio, 'Dynamics of Non Equilibrium Fluctuations in Free Diffusion', Università degli Studi di Milano Dipartimento di Fisica Laboratorio di Ottica e Microgravità, Italy, 2005.
- [113] J. A. Rard and D. G. Miller, 'The mutual diffusion coefficients of NaCl-H₂O and CaCl₂-H₂O at 25°C from Rayleigh interferometry', *J Solution Chem*, vol. 8, no. 10, pp. 701–716, Oct. 1979, doi: 10.1007/BF00648776.

- [114] T. Triller, 'Diffusive properties of the system water/ethanol/triethylene glycol in microgravity and ground conditions', Doctoral thesis, 2018. Accessed: Aug. 09, 2021. [Online]. Available: <https://epub.uni-bayreuth.de/3861/>
- [115] D. R. Caldwell and S. A. Eide, 'Soret coefficient and isothermal diffusivity of aqueous solutions of five principal salt constituents of seawater', *Deep Sea Research Part A. Oceanographic Research Papers*, vol. 28, no. 12, pp. 1605–1618, Dec. 1981, doi: 10.1016/0198-0149(81)90100-X.
- [116] D. R. Caldwell and S. A. Eide, 'Separation of seawater by Soret diffusion', *Deep Sea Research Part A. Oceanographic Research Papers*, vol. 32, no. 8, pp. 965–982, Aug. 1985, doi: 10.1016/0198-0149(85)90039-1.
- [117] J.-L. Dandurand and J. Schott, 'Stabilité de la magnésite et de la dolomite ; interprétation des résultats de mise en solution et de synthèse par thermodiffusion', *bulmi*, vol. 100, no. 2, pp. 94–99, 1977, doi: 10.3406/bulmi.1977.7121.
- [118] D. G. Miller, 'Application of Irreversible Thermodynamics to Electrolyte Solutions. I. Determination of Ionic Transport Coefficients lij for Isothermal Vector Transport Processes in Binary Electrolyte Systems^{1,2}', *J. Phys. Chem.*, vol. 70, no. 8, pp. 2639–2659, Aug. 1966, doi: 10.1021/j100880a033.
- [119] H. S. Harned and A. L. Levy, 'The Differential Diffusion Coefficient of Calcium Chloride in Dilute Aqueous Solutions at 25°', *J. Am. Chem. Soc.*, vol. 71, no. 8, pp. 2781–2783, Aug. 1949, doi: 10.1021/ja01176a053.
- [120] R. A. Robinson and R. H. Stokes, *Electrolyte solutions: the measurement and interpretation of conductance, chemical potential and diffusion in solutions of simple electrolytes*, 2. ed. (rev.), 5. impr. London: Butterworths, 1959.
- [121] R. A. Robinson and C. L. Chia, 'The Diffusion Coefficient of Calcium Chloride in Aqueous Solution at 25°', *J. Am. Chem. Soc.*, vol. 74, no. 11, pp. 2776–2777, Jun. 1952, doi: 10.1021/ja01131a021.
- [122] M. Capobianchi, T. F. Irvine Jr, N. K. Tutu, and G. Alanson Greene, 'A new technique for measuring the Fickian diffusion coefficient in binary liquid solutions', *Experimental Thermal and Fluid Science*, vol. 18, no. 1, pp. 33–47, Sep. 1998, doi: 10.1016/S0894-1777(98)10006-7.
- [123] J. Lielmezs, 'External transverse magnetic field effect on electrolyte diffusion in alkali chloride-water solutions', *Thermochimica Acta*, vol. 19, no. 3, pp. 249–266, Jun. 1977, doi: 10.1016/0040-6031(77)80001-4.
- [124] E. A. Hollingshead and A. R. Gordon, 'The Differential Diffusion Constant of Calcium Chloride in Aqueous Solution', *J. Chem. Phys.*, vol. 9, no. 2, pp. 152–153, Feb. 1941, doi: 10.1063/1.1750867.
- [125] J. R. Vinograd and J. W. McBain, 'Diffusion of Electrolytes and of the Ions in their Mixtures', *J. Am. Chem. Soc.*, vol. 63, no. 7, pp. 2008–2015, Jul. 1941, doi: 10.1021/ja01852a063.
- [126] D. Ambrosini, D. Paoletti, and N. Rashidnia, 'Overview of diffusion measurements by optical techniques', *Optics and Lasers in Engineering*, vol. 46, no. 12, pp. 852–864, Dec. 2008, doi: 10.1016/j.optlaseng.2008.06.008.
- [127] H. J. V. Tyrrell and K. R. Harris, *Diffusion in liquids: a theoretical and experimental study*. Butterworth-Heinemann, 2013.
- [128] R. Riquelme, I. Lira, C. Perez-Lopez, J. Rayas, and R. Rodriguez-Vera, 'Interferometric measurement of a diffusion coefficient: Comparison of two methods and uncertainty analysis', *Journal of Physics D: Applied Physics*, vol. 40, p. 2769, Apr. 2007, doi: 10.1088/0022-3727/40/9/015.

- [129] J. H. Bruning, D. R. Herriott, J. E. Gallagher, D. P. Rosenfeld, A. D. White, and D. J. Brangaccio, 'Digital Wavefront Measuring Interferometer for Testing Optical Surfaces and Lenses', *Appl. Opt.*, *AO*, vol. 13, no. 11, pp. 2693–2703, Nov. 1974, doi: 10.1364/AO.13.002693.
- [130] Z. Guo, S. Maruyama, and A. Komiya, 'Rapid yet accurate measurement of mass diffusion coefficients by phase shifting interferometer', *J. Phys. D: Appl. Phys.*, vol. 32, no. 9, pp. 995–999, Jan. 1999, doi: 10.1088/0022-3727/32/9/309.
- [131] Y. Nimdeo, Y. Joshi, and K. Muralidhar, 'Measurement of Mass Diffusivity Using Interferometry through Sensitivity Analysis', *Industrial & Engineering Chemistry Research*, vol. 53, p. 19338, Dec. 2014, doi: 10.1021/ie502601h.
- [132] L. G. Longsworth, 'Experimental Tests of an Interference Method for the Study of Diffusion', *J. Am. Chem. Soc.*, vol. 69, no. 10, pp. 2510–2516, Oct. 1947, doi: 10.1021/ja01202a077.
- [133] G. Kegeles and L. J. Gosting, 'The Theory of an Interference Method for the Study of Diffusion', *J. Am. Chem. Soc.*, vol. 69, no. 10, pp. 2516–2523, Oct. 1947, doi: 10.1021/ja01202a078.
- [134] J. F. Torres Alvarez, 'A study of heat and mass transfer in enclosures by phase-shifting interferometry and bifurcation analysis.', Ecole Centrale de Lyon, 2014.
- [135] J. R. Hall, B. F. Wishaw, and R. H. Stokes, 'The Diffusion Coefficients of Calcium Chloride and Ammonium Chloride in Concentrated Aqueous Solutions at 25°', *J. Am. Chem. Soc.*, vol. 75, no. 7, pp. 1556–1560, Apr. 1953, doi: 10.1021/ja01103a011.
- [136] V. Vitagliano and P. A. Lyons, 'Diffusion Coefficients for Aqueous Solutions of Sodium Chloride and Barium Chloride', *Journal of the American Chemical Society*, vol. 78, no. 8, pp. 1549–1552, Apr. 1956, doi: 10.1021/ja01589a011.
- [137] Y. C. Chang and A. S. Myerson, 'The diffusivity of potassium chloride and sodium chloride in concentrated, saturated, and supersaturated aqueous solutions', *AIChE J.*, vol. 31, no. 6, pp. 890–894, Jun. 1985, doi: 10.1002/aic.690310603.
- [138] J. A. Rard and D. G. Miller, 'The mutual diffusion coefficients of Na₂SO₄-H₂O and MgSO₄-H₂O at 25°C from Rayleigh interferometry', *J Solution Chem*, vol. 8, no. 10, pp. 755–766, Oct. 1979, doi: 10.1007/BF00648779.
- [139] F. A. Gonçalves and J. Kestin, 'The Viscosity of NaCl and KCl Solutions in the Range 25–50°C', *Berichte der Bunsengesellschaft für physikalische Chemie*, vol. 81, no. 11, pp. 1156–1161, 1977, doi: 10.1002/bbpc.19770811108.
- [140] F. A. Gonçalves and J. Kestin, 'The Viscosity of CaCl₂ Solutions in the Range 20–50°C', *Berichte der Bunsengesellschaft für physikalische Chemie*, vol. 83, no. 1, pp. 24–27, 1979, doi: 10.1002/bbpc.19790830105.
- [141] P. von Debye and E. Hückel, 'Zur Theorie der Elektrolyte: I. Gefrierpunktserniedrigung und verwandte Erscheinungen; II. Das Grenzgesetz für die elektrische Leitfähigkeit (On the theory of electrolytes: I. Lowering of the freezing point and related phenomena; II. The limiting laws for the electrical conductivity)', *Phys. Z*, vol. 24, p. 185, 1923.
- [142] L. O. R. Fuoss and L. Onsager, 'Irreversible processes in electrolytes', *J. phys. Chem*, vol. 36, pp. 2689–2778, 1932.
- [143] K. S. Pitzer, *Activity coefficients in electrolyte solutions*. 1991.
- [144] A. L. Thadée, 'Étude des saumures naturelles et industrielles : Approche expérimentale et par modélisation de l'extraction du lithium par évaporation', These de doctorat, Pau, 2017. Accessed: Aug. 19, 2021. [Online]. Available: <http://www.theses.fr/2017PAUU3012>

- [145] C. A. J. Appelo and D. Postma, *Geochemistry, groundwater and pollution*, 2nd edition. Boca Raton London New York: CRC Press, Taylor & Francis Group, 2005.
- [146] D. Parias, I. Paspaliaris, and E. Balomenos, 'Modeling Chemical Equilibrium of Electrolyte Solutions', *Mineral Processing and Extractive Metallurgy Review*, vol. 27, pp. 1–60, Jan. 2006, doi: 10.1080/08827500500339299.
- [147] D. L. Parkhurst and C. A. J. Appelo, *Description of input and examples for PHREEQC version 3—A computer program for speciation, batch-reaction, one-dimensional transport, and inverse geochemical calculations: U.S. Geological Survey Techniques and Methods, book 6, chap. A43, 497 p., available only at <https://pubs.usgs.gov/tm/06/a43/>*. 2013.
- [148] K. S. Pitzer, 'Thermodynamics of electrolytes. I. Theoretical basis and general equations', *J. Phys. Chem.*, vol. 77, no. 2, pp. 268–277, Jan. 1973, doi: 10.1021/j100621a026.
- [149] K. S. Pitzer and G. Mayorga, 'Thermodynamics of electrolytes. II. Activity and osmotic coefficients for strong electrolytes with one or both ions univalent', *J. Phys. Chem.*, vol. 77, no. 19, pp. 2300–2308, Sep. 1973, doi: 10.1021/j100638a009.
- [150] C. Harvie, N. Møller, and J. Weare, 'The prediction of mineral solubilities in natural waters: The Na-K-Mg-Ca-H-Cl-SO₄-OH-HCO₃-CO₃-CO₂-H₂O system to high ionic strengths at 25°C', *Geochimica Et Cosmochimica Acta - GEOCHIM COSMOCHIM ACTA*, vol. 48, pp. 723–751, Apr. 1984, doi: 10.1016/0016-7037(84)90098-X.
- [151] A. Lassin, C. Christov, L. Andre, and M. Azaroual, 'A thermodynamic model of aqueous electrolyte solution behavior and solid-liquid equilibrium in the Li-H-Na-K-Cl-OH-H₂O system to very high concentrations (40 molal) and from 0 to 250 °C', *American Journal of Science*, vol. 315, no. 3, pp. 204–256, Mar. 2015, doi: 10.2475/03.2015.02.
- [152] K. S. Pitzer, Ed., *Activity Coefficients in Electrolyte Solutions*, 2nd ed. Boca Raton: CRC Press, 2017. doi: 10.1201/9781351069472.
- [153] K. S. Pitzer and J. J. Kim, 'Thermodynamics of electrolytes. IV. Activity and osmotic coefficients for mixed electrolytes', *J. Am. Chem. Soc.*, vol. 96, no. 18, pp. 5701–5707, Sep. 1974, doi: 10.1021/ja00825a004.
- [154] K. S. Pitzer and G. Mayorga, 'Thermodynamics of electrolytes. III. Activity and osmotic coefficients for 2–2 electrolytes', *J Solution Chem*, vol. 3, no. 7, pp. 539–546, Jul. 1974, doi: 10.1007/BF00648138.
- [155] J. F. Zemaitis and American Institute of Chemical Engineers, Eds., *Handbook of aqueous electrolyte thermodynamics: theory & application*. New York, N.Y: Design Institute for Physical Property Data sponsored by the American Institute of Chemical Engineers, 1986.
- [156] A. Lach, L. André, A. Lassin, M. Azaroual, J.-P. Serin, and P. Cézac, 'A new Pitzer parameterization for the binary NaOH-H₂O and ternary NaOH-NaCl-H₂O and NaOH-LiOH-H₂O systems up to NaOH solid salt saturation, from 273.15 to 523.15 K and at saturated vapour pressure', *Journal of Solution Chemistry*, vol. 44, no. 7, Jul. 2015, doi: 10.1007/s10953-015-0357-6.
- [157] A. R. Felmy and J. H. Weare, 'The prediction of borate mineral equilibria in natural waters: Application to Searles Lake, California', *Geochimica et Cosmochimica Acta*, vol. 50, no. 12, pp. 2771–2783, Dec. 1986, doi: 10.1016/0016-7037(86)90226-7.
- [158] W. J. Hamer and Y. Wu, 'Osmotic Coefficients and Mean Activity Coefficients of Uni-univalent Electrolytes in Water at 25°C', *Journal of Physical and Chemical Reference Data*, vol. 1, no. 4, pp. 1047–1100, Oct. 1972, doi: 10.1063/1.3253108.

- [159] C. Kervévan, M. Azaroual, and P. Durst, 'Improvement of the Calculation Accuracy of Acid Gas Solubility in Deep Reservoir Brines: Application to the Geological Storage of CO₂', *Oil & Gas Science and Technology*, vol. 60, no. 2, pp. 357–379, Mar. 2005, doi: 10.2516/ogst:2005022.
- [160] R. B. Bird and D. J. Klingenberg, 'Multicomponent diffusion—A brief review', *Advances in Water Resources*, vol. 62, pp. 238–242, Dec. 2013, doi: 10.1016/j.advwatres.2013.05.010.
- [161] S. Ben-Yaakov, 'Diffusion of sea water ions—I. Diffusion of sea water into a dilute solution', *Geochimica et Cosmochimica Acta*, vol. 36, no. 12, pp. 1395–1406, Dec. 1972, doi: 10.1016/0016-7037(72)90069-5.
- [162] B. Boudreau, 'Multicomponent ionic diffusion in porewaters: Coulombic effects revisited', *Earth and Planetary Science Letters*, vol. 222, pp. 653–666, May 2004, doi: 10.1016/S0012-821X(04)00152-9.
- [163] A. C. Lasaga, 'The treatment of multi-component diffusion and ion pairs in diagenetic fluxes', *American Journal of Science*, vol. 279, no. 3, pp. 324–346, Mar. 1979, doi: 10.2475/ajs.279.3.324.
- [164] F. Croccolo, F. Scheffold, and A. Vailati, 'Effect of a Marginal Inclination on Pattern Formation in a Binary Liquid Mixture under Thermal Stress', *Phys. Rev. Lett.*, vol. 111, no. 1, p. 014502, Jul. 2013, doi: 10.1103/PhysRevLett.111.014502.
- [165] F. Croccolo, H. Bataller, and F. Scheffold, 'A light scattering study of non equilibrium fluctuations in liquid mixtures to measure the Soret and mass diffusion coefficient', *The Journal of Chemical Physics*, vol. 137, no. 23, p. 234202, Dec. 2012, doi: 10.1063/1.4771872.
- [166] F. Croccolo, C. Giraudet, H. Bataller, R. Cerbino, and A. Vailati, 'Shadowgraph Analysis of Non-equilibrium Fluctuations for Measuring Transport Properties in Microgravity in the GRADFLEX Experiment', *Microgravity Science and Technology*, vol. 28, May 2016, doi: 10.1007/s12217-016-9501-1.
- [167] H. Bataller, C. Giraudet, F. Croccolo, and J. M. Ortiz de Zárate, 'Analysis of Non-Equilibrium Fluctuations In A Ternary Liquid Mixture', *Microgravity Sci. Technol.*, vol. 28, no. 6, pp. 611–619, Dec. 2016, doi: 10.1007/s12217-016-9517-6.
- [168] H. Bataller, T. Triller, B. Pur, W. Köhler, J. M. Ortiz de Zárate, and F. Croccolo, 'Dynamic analysis of the light scattered by the non-equilibrium fluctuations of a ternary mixture of polystyrene-toluene-n-hexane', *Eur. Phys. J. E*, vol. 40, no. 3, p. 35, Mar. 2017, doi: 10.1140/epje/i2017-11522-8.
- [169] C. Giraudet, H. Bataller, and F. Croccolo, 'High-pressure mass transport properties measured by dynamic near-field scattering of non-equilibrium fluctuations', *The European Physical Journal E*, vol. 37, no. 11, Nov. 2014, doi: 10.1140/epje/i2014-14107-1.
- [170] C. Giraudet, H. Bataller, Y. Sun, A. Donev, J. M. O. de Zárate, and F. Croccolo, 'Slowing-down of non-equilibrium concentration fluctuations in confinement', *EPL*, vol. 111, no. 6, p. 60013, Sep. 2015, doi: 10.1209/0295-5075/111/60013.
- [171] F. Croccolo, D. Brogioli, A. Vailati, M. Giglio, and D. S. Cannell, 'Nondiffusive decay of gradient-driven fluctuations in a free-diffusion process', *Physical Review E*, vol. 76, no. 4, Oct. 2007, doi: 10.1103/PhysRevE.76.041112.
- [172] F. Croccolo, D. Brogioli, A. Vailati, M. Giglio, and D. S. Cannell, 'Use of dynamic schlieren interferometry to study fluctuations during free diffusion', *Appl. Opt.*, vol. 45, no. 10, pp. 2166–2173, Apr. 2006, doi: 10.1364/AO.45.002166.
- [173] F. Croccolo, D. Brogioli, A. Vailati, M. Giglio, and D. S. Cannell, 'Effect of Gravity on the Dynamics of Nonequilibrium Fluctuations in a Free-Diffusion Experiment',

- Annals of the New York Academy of Sciences*, vol. 1077, no. 1, pp. 365–379, Sep. 2006, doi: 10.1196/annals.1362.030.
- [174] F. Croccolo, J. M. Zárate, and J. V. Sengers, ‘Non-local fluctuation phenomena in liquids’, *The European Physical Journal E*, vol. 39, Dec. 2016, doi: 10.1140/epje/i2016-16125-3.
- [175] J. M. Ortiz de Zárate and J. V. Sengers, *Hydrodynamic fluctuations in fluids and fluid mixtures*. Amsterdam: Elsevier, 2006.
- [176] A. Vailati and M. Giglio, ‘Giant fluctuations in a free diffusion process’, *Nature*, vol. 390, no. 6657, pp. 262–265, Nov. 1997, doi: 10.1038/36803.
- [177] E. Bouty, ‘CH. SORET. — Sur l’état d’équilibre que prend, au point de vue de sa concentration, une dissolution saline primitivement homogène, dont deux parties sont portées à des températures différentes; Archives de Genève, 3e periode, t. II, p. 48; 1879’, *J. Phys. Theor. Appl.*, vol. 9, no. 1, pp. 331–332, 1880, doi: 10.1051/jphysap:018800090033101.
- [178] F. Croccolo and D. Brogioli, ‘Quantitative Fourier analysis of schlieren masks: the transition from shadowgraph to schlieren’, *Applied optics*, vol. 50, no. 20, pp. 3419–3427, 2011.
- [179] S. P. Trainoff and D. S. Cannell, ‘Physical optics treatment of the shadowgraph’, *Physics of Fluids*, vol. 14, no. 4, pp. 1340–1363, Mar. 2002, doi: 10.1063/1.1449892.
- [180] R. Minhas, ‘Experimental investigation of the reactive transport in the CO₂ storage process in deep saline aquifers by shadowgraphy.’, Internship report, Master of Mechanics and Physics in Porous Media, 2021.
- [181] J. C. Legros *et al.*, ‘Investigation of Fickian diffusion in the ternary mixtures of water–ethanol–triethylene glycol and its binary pairs’, *Phys. Chem. Chem. Phys.*, vol. 17, no. 41, pp. 27713–27725, Oct. 2015, doi: 10.1039/C5CP04745E.
- [182] A. T. Ndjaka *et al.*, ‘Mass diffusion and Soret coefficient measurements of triethylene glycol/water binary mixtures by dynamic shadowgraphy’, *The European Physical Journal E*, submitted 2021.
- [183] F. Croccolo, D. Brogioli, and A. Vailati, ‘Cylindrical flowing-junction cell for the investigation of fluctuations and pattern-formation in miscible fluids’, *Review of Scientific Instruments*, vol. 90, no. 8, p. 085109, Aug. 2019, doi: 10.1063/1.5112778.
- [184] G. Cerchiari, F. Croccolo, F. Cardinaux, and F. Scheffold, ‘Note: Quasi-real-time analysis of dynamic near field scattering data using a graphics processing unit’, *Review of Scientific Instruments*, vol. 83, no. 10, p. 106101, Oct. 2012, doi: 10.1063/1.4755747.
- [185] M. Norouzsadeh, M. Chruga, G. Cerchiari, and F. Croccolo, ‘The modern structurator: increased performance for calculating the structure function’, *Eur. Phys. J. E*, vol. 44, no. 12, p. 146, Dec. 2021, doi: 10.1140/epje/s10189-021-00146-2.
- [186] F. Croccolo, L. García-Fernández, H. Bataller, A. Vailati, and J. M. Ortiz de Zárate, ‘Propagating modes in a binary liquid mixture under thermal stress’, *Physical Review E*, vol. 99, no. 1, Jan. 2019, doi: 10.1103/PhysRevE.99.012602.
- [187] J. M. O. D. Ortiz de Zarate, C. Giraudet, H. Bataller, and F. Croccolo, ‘Non-equilibrium fluctuations induced by the Soret effect in a ternary mixture’, *European Physical Journal E: Soft matter and biological physics*, vol. 37, no. 8, p. Article number 77, Pages 1-7, Aug. 2014, doi: 10.1140/epje/i2014-14077-2.
- [188] L. García-Fernández, P. Fruton, H. Bataller, J. M. Ortiz de Zárate, and F. Croccolo, ‘Coupled non-equilibrium fluctuations in a polymeric ternary mixture’, *The European Physical Journal E*, vol. 42, no. 9, Sep. 2019, doi: 10.1140/epje/i2019-11889-4.

- [189] D. J. Higham and N. J. Higham, 'MATLAB Guide', *Third Edition*. SIAM, 2016.
- [190] M. Safari, M. Vorontsova, R. Poling-Skutvik, P. Vekilov, and J. Conrad, 'Differential dynamic microscopy of weakly scattering and polydisperse protein-rich clusters', *Physical Review E*, vol. 92, Oct. 2015, doi: 10.1103/PhysRevE.92.042712.
- [191] K. He, M. Spannuth, J. C. Conrad, and R. Krishnamoorti, 'Diffusive dynamics of nanoparticles in aqueous dispersions', *Soft Matter*, vol. 8, no. 47, pp. 11933–11938, Nov. 2012, doi: 10.1039/C2SM26392K.
- [192] D. R. Lide, *CRC Handbook of Chemistry and Physics, 84th Edition*. CRC Press, 2003.
- [193] J. Pironon *et al.*, 'Dehydration of Gypsum Under Dry CO₂ Injection', *Energy Procedia*, vol. 37, pp. 4575–4582, Dec. 2013, doi: 10.1016/j.egypro.2013.06.365.
- [194] Y. Peysson, L. André, and M. Azaroual, 'Well injectivity during CO₂ storage operations in deep saline aquifers—Part 1: Experimental investigation of drying effects, salt precipitation and capillary forces', *International Journal of Greenhouse Gas Control*, vol. 22, pp. 291–300, Mar. 2014, doi: 10.1016/j.ijggc.2013.10.031.
- [195] J. Rojas *et al.*, 'Caractérisation et modélisation du réservoir géothermique du Dogger, bassin parisien, France. Rapport final CCE, EN 3G-0046-F(CD), BRGM R 30 IRG SGN 89, 1989.'
- [196] T. Xu, J. Apps, and K. Pruess, 'Mineral sequestration of carbon dioxide in a sandstone-shale system', *Chemical Geology*, vol. 217, pp. 295–318, Apr. 2005, doi: 10.1016/j.chemgeo.2004.12.015.
- [197] T. Xu and K. Pruess, 'Modeling Multiphase Non-isothermal Fluid Flow and Reactive Geochemical Transport in Variably Saturated Fractured Rocks: 1. Methodology', *American Journal of Science*, vol. 301, no. 1, pp. 16–33, Jan. 2001, doi: 10.2475/ajs.301.1.16.
- [198] H. S. Carslaw and J. C. Jaeger, *Conduction of heat in solids*, 2nd ed. Oxford [Oxfordshire] : New York: Clarendon Press ; Oxford University Press, 1986.
- [199] R. Lefebvre, 'Cours sur l'Écoulement multiphase en milieux poreux. Chapitre 5 : Transfert de chaleur dans les milieux poreux. Course title: CE 470, Université de Montréal'. Automne 2006.
- [200] S. Fuchs, N. Balling, and A. Förster, 'Calculation of thermal conductivity, thermal diffusivity and specific heat capacity of sedimentary rocks using petrophysical well logs', *Geophysical Journal International*, vol. 203, no. 3, pp. 1977–2000, Dec. 2015, doi: 10.1093/gji/ggv403.
- [201] K. von Lichtenecker, 'Der elektrische Leitungswiderstand künstlicher und natürlicher Aggregate', *Physikalische Zeitschrift*, vol. 25, no. 8, pp. 169–181, 1924.
- [202] C. Clauser and E. Huenges, 'Rock Physics and Phase Relations. A Handbook of Physical Constants', vol. 3, 1995, pp. 105–126.
- [203] K. Horai and G. Simmons, 'Thermal conductivity of rock-forming minerals', *Earth and Planetary Science Letters*, vol. 6, no. 5, pp. 359–368, Jan. 1969, doi: 10.1016/0012-821X(69)90186-1.
- [204] W. Voigt, *Lehrbuch der Kristallphysik (mit Ausschluss der Kristalloptik)*. Vieweg+Teubner Verlag, 1966. doi: 10.1007/978-3-663-15884-4.
- [205] A. Reuss, 'Berechnung der Fließgrenze von Mischkristallen auf Grund der Plastizitätsbedingung für Einkristalle.', doi: 10.1002/ZAMM.19290090104.
- [206] G. Michard and J.-P. Bastide, 'Etude géochimique de la nappe du dogger du bassin parisien', *Journal of Volcanology and Geothermal Research*, vol. 35, no. 1, pp. 151–163, Sep. 1988, doi: 10.1016/0377-0273(88)90012-1.

- [207] P. Blanc *et al.*, 'Thermoddem: A geochemical database focused on low temperature water/rock interactions and waste materials', *Applied Geochemistry*, vol. 27, pp. 2107–2116, Oct. 2012, doi: 10.1016/j.apgeochem.2012.06.002.
- [208] H. M. May, P. A. Helmke, and M. L. Jackson, 'Gibbsite solubility and thermodynamic properties of hydroxy-aluminum ions in aqueous solution at 25°C', *Geochimica et Cosmochimica Acta*, vol. 43, no. 6, pp. 861–868, Jun. 1979, doi: 10.1016/0016-7037(79)90224-2.
- [209] M. Sivakumar and M. M. Emamjomeh, 'Electrochemical method for fluoride removal: Measurement, Speciation and Mechanisms', pp. 1–8, 2005.
- [210] P. Bénézech, G. D. Saldi, J.-L. Dandurand, and J. Schott, 'Experimental determination of the solubility product of magnesite at 50 to 200°C', *Chemical Geology*, vol. 286, no. 1, pp. 21–31, Jun. 2011, doi: 10.1016/j.chemgeo.2011.04.016.
- [211] G. D. Saldi, G. Jordan, J. Schott, and E. H. Oelkers, 'Magnesite growth rates as a function of temperature and saturation state', *Geochimica et Cosmochimica Acta*, vol. 73, no. 19, pp. 5646–5657, Oct. 2009, doi: 10.1016/j.gca.2009.06.035.
- [212] G. D. Saldi, J. Schott, O. S. Pokrovsky, Q. Gautier, and E. H. Oelkers, 'An experimental study of magnesite precipitation rates at neutral to alkaline conditions and 100–200°C as a function of pH, aqueous solution composition and chemical affinity', *Geochimica et Cosmochimica Acta*, vol. 83, pp. 93–109, Apr. 2012, doi: 10.1016/j.gca.2011.12.005.
- [213] L. Hopkinson, P. Kristova, K. Rutt, and G. Cressey, 'Phase transitions in the system MgO–CO₂–H₂O during CO₂ degassing of Mg-bearing solutions', *Geochimica Et Cosmochimica Acta - GEOCHIM COSMOCHIM ACTA*, vol. 76, Jan. 2012, doi: 10.1016/j.gca.2011.10.023.
- [214] P. Bénézech, A. Stefánsson, Q. Gautier, and J. Schott, 'Mineral Solubility and Aqueous Speciation Under Hydrothermal Conditions to 300 °C – The Carbonate System as an Example', *Reviews in Mineralogy and Geochemistry*, vol. 76, no. 1, pp. 81–133, Jan. 2013, doi: 10.2138/rmg.2013.76.4.
- [215] M. Lindner, G. D. Saldi, S. Carrocci, P. Bénézech, J. Schott, and G. Jordan, 'On the growth of anhydrous Mg-bearing carbonates – Implications from norsethite growth kinetics', *Geochimica et Cosmochimica Acta*, vol. 238, pp. 424–437, Oct. 2018, doi: 10.1016/j.gca.2018.07.013.
- [216] S. Kaczmarek and B. Thornton, 'The effect of temperature on stoichiometry, cation ordering, and reaction rate in high-temperature dolomitization experiments', *Chemical Geology*, vol. 468, Aug. 2017, doi: 10.1016/j.chemgeo.2017.08.004.
- [217] C. Z. Jiang and N. J. Tosca, 'Growth kinetics of siderite at 298.15 K and 1 bar', *Geochimica et Cosmochimica Acta*, vol. 274, pp. 97–117, Apr. 2020, doi: 10.1016/j.gca.2020.01.047.
- [218] S. Veran-Tissoires and M. Prat, 'Evaporation of a sodium chloride solution from a saturated porous medium with efflorescence formation', *J. Fluid Mech.*, vol. 749, pp. 701–749, Jun. 2014, doi: 10.1017/jfm.2014.247.
- [219] G. W. Scherer, 'Stress from crystallization of salt', *Cement and Concrete Research*, vol. 34, no. 9, pp. 1613–1624, Sep. 2004, doi: 10.1016/j.cemconres.2003.12.034.
- [220] J. Palandri and Y. Kharaka, 'A Compilation of Rate Parameters of Water-Mineral Interaction Kinetics for Application to Geochemical Modeling', vol. 1068, p. 71, Mar. 2004.

Appendices

Appendix A: Macroscopic properties of electrolytes

❖ Molar volume

The molar volume V_m of a substance is the occupied volume V (in liter) divided by the amount of the substance n (in mol) at a given temperature and pressure as:

$$V_m = \frac{V}{n} = \frac{M}{\rho} \quad (\text{B.1})$$

Where M is the molar mass in $\text{g}\cdot\text{mol}^{-1}$ and ρ the mass density of the substance.

❖ Mol fraction or molar fraction

The molar fraction x_i of a component i is a dimensionless quantity defined as the ratio between the amount of matter of i , n_i , divided by the total amount of all the components in a mixture n_{tot} , as:

$$x_i = \frac{n_i}{n_{tot}} \quad (\text{B.2})$$

In a mixture which contains N component, the sum of all the mol fractions is equal to 1 as:

$$n_{tot} = \sum_{i=1}^N n_i \quad \text{and} \quad \sum_{i=1}^N x_i = 1 \quad (\text{B.3})$$

❖ Mass fraction

The mass fraction of w_i of a component i is a dimensionless quantity defined as the ratio of the mass of the component i , $m_{s,i}$, to the total mass of the mixture $m_{s,tot}$ as:

$$w_i = \frac{m_{s,i}}{m_{s,tot}} \quad \text{with} \quad \sum_{i=1}^N w_i = 1 \quad (\text{B.4})$$

❖ Molar concentration or molarity

The molarity of a solution C is the concentration of a solute in a solution and is defined as the ratio between the amount of a solute n divided by the volume of the solution (or mixture) V as:

$$C = \frac{n}{V} \quad (\text{B.5})$$

The unit of C is usually in mol.L^{-1} . A solution with a concentration of 2 mol.L^{-1} is said to be 2 molar, commonly designated as 2 M. The mass concentration C_m has the same definition like molarity with in the numerator the mass of the solute m_s instead of the amount n . For a pure component, the mass concentration is equal to its density ρ . C_m (in g.L^{-1}) is related to molarity by:

$$C_m = C \cdot M \quad (\text{B.6})$$

❖ Molality

The molality m_i corresponds to the amount of solute (in mol) contained in 1 Kg of solvent, m_{solvent} and is defined as:

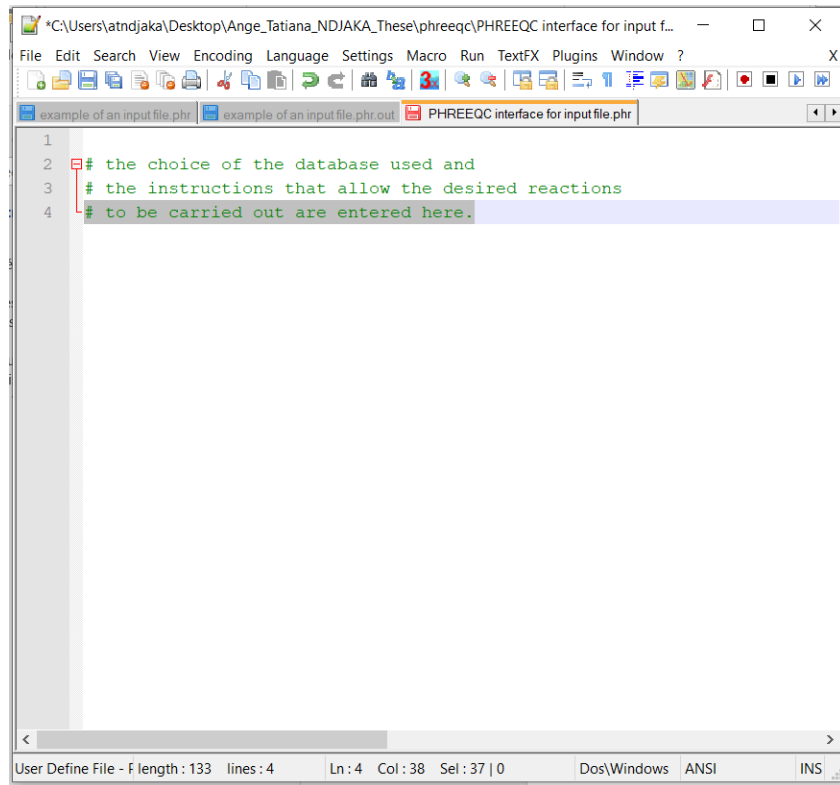
$$m_i = \frac{n_{\text{solute}}}{m_{\text{solvent}}} \quad (\text{B.7})$$

Where m_i is expressed in mol.kg^{-1} . The molality is widely used in models to describe the properties of electrolytic solutions. We work with aqueous solution, the solvent is usually water. The molarity C is related to the molality by:

$$C = \frac{m_i \times \rho_{\text{solution}}}{1 + (m_i \times M_{\text{solute}})} \quad (\text{B.8})$$

Where C is the molarity in mol.L^{-1} , ρ_{solution} is the density of the solution in (kg.L^{-1}), and M_{solute} is the molar mass of the solute (kg.mol^{-1}).

Appendix B: Example of an input file in PHREEQC program



```
1
2 # the choice of the database used and
3 # the instructions that allow the desired reactions
4 # to be carried out are entered here.
```

User Define File - F length : 133 lines : 4 Ln : 4 Col : 38 Sel : 37 | 0 Dos\Windows ANSI INS

Figure B.1: Graphical interface of PHREEQC for the description of an input file.

```

*Users\atndjaka\Desktop\Ange_Tatiana_NDJAKA_These\phreeqc\example of an input file.phr - Notepad++
File Edit Search View Encoding Language Settings Macro Run TextFX Plugins Window ?
example of an input file.phr example of an input file.phr.out PITZER.DAT
1 DATABASE c:\phreeqc\database\PITZER.DAT
2 TITLE Diffusion du CaCl2 in NaCl
3
4 SELECTED_OUTPUT 1; -reset false; -file diffusion_CaCl2_in_NaCl.txt
5
6 -step
7 -high_precision
8 -solution
9 -ionic_strength
10 -percent_error
11 -pH
12 -molalities Ca+2 Cl- Na+
13 -totals Cl Ca S Na
14 -temperature
15 -saturation_indices Gypsum
16 -equilibrium_phases Gypsum
17 -time
18 -user_punch
19
20 USER_PUNCH
21 -headers Distance Diff_Ca Diff_Cl Diff_Na Diff_SO4 density
22 -start
23 1 punch DIST
24 6 punch DIFF_C("Ca+2")
25 7 punch DIFF_C("Cl-")
26 8 punch DIFF_C("Na+")
27 9 punch DIFF_C("SO4-2")
28 10 punch rho
29 -end
30
31 SOLUTION 1-10
32 temperature 25
33 units mol/kgw
34 density 1 calculate
35 Na 2.792
36 Cl 2.792
37 EQUILIBRIUM_PHASES 1-10
38 Gypsum 0 0
39 END
40
41 SOLUTION 11-20
42 temperature 25
43 units mol/kgw
44 density 1 calculate
45 Cl 0.9504
46 Ca 0.4752
47 EQUILIBRIUM_PHASES 11-20
48 Gypsum 0 0
49 END
50
51 TRANSPORT
52 -cells 20
53 -lengths 0.0005
54 -shifts 136
55 -time_step 10 min
56 -flow_direction diffusion_only
57 -boundary_conditions closed closed
58 -print_cells 1-20
59 -print_frequency 1
60 -punch_cells 1-20
61 -punch_frequency 1
62 -diffusion_coefficient 1.543e-9
63 -multi_d true 1e-9 1 0 0 true #multi_d true for heterogeneous multicomponent diffusion
64 -porosities 1
65 -warnings true
66
67 END
User Define File - Phreeqc length : 1229 lines : 67 Ln : 6 Col : 17 Sel : 0 | 0 Dos\Windows ANSI INS

```

Figure B.2: Input file for the numerical modelling of the the superimposition of a layer of a CaCl₂ solution (0.475 mol.kg⁻¹) with a layer of NaCl solution (2.792 mol.kg⁻¹).

Appendix C: Measurement of the densities of saline solution with the density meter (Anton Paar DMA 5000)

For each salt solution of given average concentration, the density is measured at an average temperature of $T = 20, 25$ and 30 °C. For each average temperature, the measurements are repeated three times for repeatability purpose. The density value obtained is therefore the average of the measurements.

Table A.1: Values of density of solutions of CaCl_2 , NaCl and Na_2SO_4 as a function of concentration and temperature.

Salts	C (mol.L ⁻¹)	T ₁ (°C)	ρ ₁ (g.cm ⁻³)	T ₂ (°C)	ρ ₂ (g.cm ⁻³)	T ₃ (°C)	ρ ₃ (g.cm ⁻³)	ρ _{mean} (g.cm ⁻³)	St. dev. ρ	T _{mean} (°C)
NaCl	2.637	20.001	1.100931	20.001	1.100931	20.003	1.100933	1.100932	0.000001	20.002
		24.999	1.098618	24.996	1.098624	24.997	1.098624	1.098622	0.000003	24.997
		29.995	1.096600	29.996	1.096594	29.996	1.096591	1.096595	0.000003	29.996
Na ₂ SO ₄	1.000	20.001	1.117065	20.000	1.117067	19.999	1.117066	1.117066	0.000001	20.000
		24.999	1.115184	25.001	1.115181	25.000	1.115181	1.115182	0.000001	25.000
		30.002	1.113010	30.002	1.113009	30.002	1.113007	1.113009	0.000001	30.002
	1.484	20.003	1.171019	20.001	1.171022	20.001	1.171023	1.171021	0.000002	20.002
		24.996	1.168657	24.999	1.168655	25.001	1.168646	1.168653	0.000004	24.999
		29.997	1.166546	29.998	1.166541	30.000	1.166538	1.166542	0.000003	29.998
CaCl ₂	1.000	20.000	1.086021	20.001	1.086020	20.001	1.086019	1.086020	0.000001	20.001
		24.996	1.084527	25.000	1.084525	25.001	1.084526	1.084526	0.000001	24.999
		30.000	1.082683	30.000	1.082681	30.001	1.082680	1.082681	0.000001	30.000
	0.469	20.001	1.039984	20.001	1.039981	20.001	1.039983	1.039983	0.000001	20.001
		24.999	1.038962	24.996	1.038963	24.998	1.038961	1.038962	0.000001	24.998
		30.001	1.036913	30.002	1.036917	30.002	1.036921	1.036917	0.000003	30.002

Appendix D: Spreading of Scientific Knowledge

- ❖ **A.T. Ndjaka**, M. Burtin, P. Fruton, L. García-Fernández, F. Croccolo, H. Bataller, “*Diffusion and Soret coefficients measurement of the triethylene glycol and water binary mixture by dynamic Shadowgraphy*”, oral presentation @ 26th ELGRA Biennial symposium, 24-27 septembre 2019, Granada (Spain).
- ❖ **P. Fruton, A.T. Ndjaka**, L. García-Fernández, H. Bataller, F. Croccolo, “*Shadowgraph investigation of free diffusion of glycerol and water under micro gravity conditions using a cylindrical Flowing Junction cell*”, poster presentation @ 26th ELGRA Biennial symposium, 24-27 septembre 2019, Granada (Spain).
- ❖ **A.T. Ndjaka**, A. Lassin, M. Azaroual, F. Croccolo, H. Bataller, “*Experimental development to observe the impact of thermal gradients and chemical reactions on the diffusion of salts in water*”, oral presentation @ winter seminar HUB Newpores, Kick-Off Meeting and scientific presentations, 20 fevrier 2020, Bidart (France)
- ❖ **A.T. Ndjaka**, P. Fruton, A. Lassin, M. Azaroual, W. Köhler, F. Croccolo, and H. Bataller “*Dynamic Shadowgraphy measurements of the diffusion and Soret coefficients in triethylene glycol - water binary mixtures*”, oral presentation @14th International Meeting on Thermodiffusion (IMT14) , 25-27 May 2021 - Trondheim, Norway. (Remotely)
- ❖ **A.T. Ndjaka**, D.E. Bouyou Bouyou, R. Minhas, A. Lassin, M. Azaroual, F. Croccolo, H. Bataller, “*Experimental development to observe the impact of thermal gradients and chemical reactions on the diffusion of salts in water*” oral presentation @Biot-Bažant Conference on Engineering Mechanics and Physics of Porous Materials, 1-3 June 2021, Northwestern University, Evanston, IL, USA. (Remotely)
- ❖ **A.T. Ndjaka**, P. Fruton, A. Lassin, M. Azaroual, W. Köhler, F. Croccolo, and H. Bataller “*Dynamic Shadowgraphy measurements of the diffusion and Soret coefficients in triethylene glycol - water binary mixtures*”, oral presentation @Twenty-first symposium on thermophysical properties, June 20-25, 2021, Boulder, CO, USA. (Remotely)

Appendix E: Publications

❖ Paper #1: published paper


M. Schraml, H. Bataller, C. Bauer, M. M. Bou-Ali, F. Croccolo, E. Lapeira, A. Mialdun, P. Möckel, **A. T. Ndjaka**, V. Shevtsova, and W. Köhler. The Soret coefficients of the ternary system water/ethanol/triethylene glycol and its corresponding binary mixtures. *Eur. Phys. J. E Soft Matter*. 2021 Oct 18;44(10):128.

❖ Paper #2: submitted paper

A. T. Ndjaka, L. Garcia-Fernández, D.E. Bouyou Bouyou, A. Lassin, M. Azaroual, F. Croccolo, and H. Bataller. *Eur. Phys. J. E* submitted (2021).



The Soret coefficients of the ternary system water/ethanol/triethylene glycol and its corresponding binary mixtures

M. Schraml¹, H. Bataller², C. Bauer¹, M. M. Bou-Ali³, F. Croccolo², E. Lapeira³, A. Mialdun⁴, P. Möckel¹, A. T. Ndjaka^{2,5}, V. Shevtsova^{3,6}, and W. Köhler^{1,a} 

¹ Physikalisches Institut, Universität Bayreuth, 95440 Bayreuth, Germany

² Université de Pau et des Pays de l'Adour, E2S UPPA, CNRS, TotalEnergies, LFCR UMR5150, Anglet, France

³ Mondragon Unibertsitatea, 20500 Arrasate-Mondragon, Spain

⁴ MRC, CP 165/62, Université libre de Bruxelles (ULB), 50, Ave. F.D. Roosevelt, B-1050 Brussels, Belgium

⁵ BRGM, Orléans, France

⁶ Ikerbasque, Basque Foundation for Science, Bilbao, Spain

Received 22 July 2021 / Accepted 2 October 2021 / Published online 18 October 2021

© The Author(s) 2021

Abstract Thermodiffusion in ternary mixtures is considered prototypic for the Soret effect of truly multicomponent systems. We discuss ground-based measurements of the Soret coefficient along the binary borders of the Gibbs triangle of the highly polar and hydrogen bonding ternary DCMIX3-system water/ethanol/triethylene glycol. All three Soret coefficients decay with increasing concentration, irrespective of the choice of the independent component, and show a characteristic sign change as a function of temperature and/or composition. With the exception of triethylene glycol/ethanol at high temperatures, the minority component always migrates toward the cold side. All three binaries exhibit temperature-independent fixed points of the Soret coefficient. The decay of the Soret coefficient with concentration can be related to negative excess volumes of mixing. The sign changes of the Soret coefficients of the binaries allow to draw far-reaching conclusions about the signs of the Soret coefficients of the corresponding ternary mixtures. In particular, we show that at least one ternary composition must exist, where all three Soret coefficients vanish simultaneously and no steady-state separation is observable.

1 Introduction

The Soret effect describes a thermodiffusive flow and the subsequent establishment of a composition gradient in a multicomponent fluid mixture subjected to a temperature gradient. Although most liquid mixtures of practical relevance, be it biological systems or crude oil reservoirs [1], can contain a large number of constituents, research has mainly dealt with binary mixtures. It is only recently that the focus has begun to shift to ternaries as prototypes of truly multicomponent mixtures. In the following, we will discuss ground-based measurements on the binaries of the ternary system that has been investigated during the third mission of the DCMIX microgravity project. The DCMIX project of the European Space Agency (ESA) and the Russian Space Agency (Roscosmos) has established a basis of microgravity experiments on ternary liquid mixtures subjected to a temperature gradient that can serve as convection-free references for ground experiments [2].

DCMIX consists of four individual campaigns, named DCMIX1 to DCMIX4, onboard the International Space Station (ISS). The five ternary samples of DCMIX1 were mixtures of dodecane, isobutyl benzene, and tetralin of different compositions. No undue complications were expected for this system, whose corresponding binaries were already very well characterized [3]. The focus of DCMIX2 was on mixtures of toluene, methanol, and cyclohexane, which exhibit a miscibility gap and a critical point [4]. DCMIX4 had exploratory character and contained, among additional DCMIX2-mixtures, polymer solutions, and a nanofluid [5].

The here presented work deals with the DCMIX3-system water (H₂O), ethanol (ETH), and triethylene glycol (TEG) [6]. These molecules are highly polar, and the prevailing hydrogen bonding leads to much more complex interactions than the dominating dispersion interactions of the DCMIX1- and DCMIX2-mixtures. A consequence of these strong interactions is large negative excess volumes of mixing.

The aim of the following work is the investigation of diffusion and thermodiffusion along the three binary borders of the ternary Gibbs triangle of the DCMIX3 system. One of these binaries, ETH/H₂O, has already

^a e-mail: werner.koehler@uni-bayreuth.de (corresponding author)

been characterized in the literature [7,8]. It shows a remarkable sign change of the Soret coefficient and is known for instabilities and oscillatory convection in double-diffusive convection experiments [9,10]. A thorough characterization of the binaries is of great importance, as they define the values to which the transport coefficients of the ternary mixtures extrapolate in the limit of vanishing concentration of either one of the components. Since their measurement does not require complicated two-color experiments with the inversion of a potentially ill-conditioned contrast factor matrix, they can be obtained with a very good accuracy by means of, e.g., single color optical techniques. Other than for ternaries, convection can usually be avoided for binary mixtures in a Soret cell. The proper strategy is to select the direction of the temperature gradient such that the solutal separation leads to a stable stratification with the higher density at the bottom of the cell. If this requires heating from below, the stability requirement is that the thermal Rayleigh number must not exceed its critical value.

In the last part of our work, we show how the information gathered for the binaries around the perimeter of the ternary Gibbs triangle can be used to infer properties of the ternary Soret coefficients. In particular, we show that the sign changes of the Soret coefficients of the binaries lead to the existence of a singular point inside the Gibbs triangle where all three ternary Soret coefficients vanish simultaneously.

2 Experimental

2.1 Optical beam deflection

The majority of the measurements were performed by means of the well-established optical beam deflection (OBD) technique [7,8,11,12]. The design of the instrument is similar to the one described in Ref. [13] with only slight modifications. The sample is inside a Soret cell with a vertical temperature gradient defined by two horizontal copper plates that are kept at a temperature difference of typically 1 K with a stability of better than 10 mK. The lateral confinement consists of an optical glass frame and thin Teflon gaskets that together define the height of the fluid slab of $h = 1.43$ mm. The path length inside the liquid is 10.00 mm. The refractive index gradient in the cell contains contributions from both the temperature and the concentration gradient, which can be separated on the basis of their very different characteristic time constants. The total refractive index gradient is read by deflection of a laser beam of $\lambda = 637$ nm at a distance of 1.325 m behind the Soret cell, whose position is detected by a line camera.

High quality ethanol (VWR LOT 19B064011, 99.96%), triethylene glycol (Acros 99%, LOT A0389346) and de-ionized and filtrated water (resistivity 18.5 M Ω cm, PAK-filter 0.22 μ m) retrieved from a Millipore Milli-Q filtration station were used to prepare typically 3–4 g of every sample to the required composition in mass frac-

tions using an analytical balance (Sartorius BP 211 D, ± 0.5 mg).

Refractive indices were measured over the entire composition range for typically ten intermediate concentrations by means of an Abbe refractometer (Anton Paar, Abbemat WR-MW). The temperature dependence of the refractive index was determined interferometrically as described in Ref. [14] with the proper correction for the temperature dependence of the refractive index of the glass windows of the cell given in Ref. [8]. Based on these measurements, the refractive indices are parameterized by polynomials in the concentration c of the first component and the temperature $\vartheta = T - 273.15$ K in Centigrade:

$$n(c, T) = (1 \ \vartheta) \begin{pmatrix} a_{00} & a_{01} & a_{02} & a_{03} \\ a_{10} & a_{11} & a_{12} & a_{13} \end{pmatrix} \begin{pmatrix} 1 \\ c \\ c^2 \\ c^3 \end{pmatrix}. \quad (1)$$

The matrix coefficients a_{ij} are tabulated in Table 1. Excess volumes were computed from density measurements with an Anton Paar DSA 5000 density meter.

2.2 Optical digital interferometry and counter-flow cell

Diffusion and Soret coefficients of selected temperatures and compositions were also measured by means of optical digital interferometry (ODI) and the diffusion coefficients at the two dilute limits of TEG/ETH with a counter-flow cell (CFC). Similar to OBD, the ODI instrument uses the Soret cell and optical diagnostics. It differs by the cell size and by the approach to the interpretation of the optical signal. The Soret cell used in the ODI setup has a square glass frame with an inner size of 18.00 \times 18.00 mm². The frame is clamped between two metal plates with intermediate seals made of a special thermally conductive rubber. The total diffusion path (plate-to-plate distance) is equal to $h = 6.26$ mm. This relatively large cell height limits the measurements to mixtures with a positive Soret coefficient and a corresponding stable separation. The temperature difference applied to the cell depended on the mixture under investigation. The separation in TEG/H₂O-mixture was studied at $\Delta T = 4.00$ K, while the applied temperature difference was 6.00 K for the TEG/ETH-mixture with its smaller optical signal. The stability of the temperature regulation, estimated as the standard deviation of ΔT records, is around 1 mK. The refractive index gradients appearing in the liquid inside the cell due to thermal or solutal inhomogeneities are sensed by an expanded and collimated laser beam of $\lambda = 532$ nm, directed into a Mach–Zehnder interferometer, with the cell being placed in one arm of the interferometer. The optical phase variation is then extracted from the raw interference fringe patterns using a 2-D Fourier transform technique. The temporal and spatial variation of the refractive index along the diffusion path

Table 1 Parameterization of the refractive indices of TEG/ETH and TEG/H₂O for $\lambda = 633$ nm and for $\lambda = 532$ nm according to Eq. (1)

a_{ij}	Units	633 nm		532 nm	
		TEG/ETH	TEG/H ₂ O	TEG/ETH	TEG/H ₂ O
a_{00}		1.36974	1.3337	1.37223	1.33714
a_{10}	10^{-4} K^{-1}	-4.4696	-0.7593	-4.1728	-0.9207
a_{01}		0.06618	0.11976	0.07283	0.11942
a_{11}	10^{-4} K^{-1}	3.2519	-3.1494	1.3316	-2.1410
a_{02}		0.02639	0.04861	0.02124	0.05002
a_{12}	10^{-4} K^{-1}	-2.1476	-1.5595	-0.5566	-2.8940
a_{03}		-	-0.04041	-	-0.04054
a_{13}	10^{-4} K^{-1}	-	2.2465	-	2.6673

is fitted to different analytical solutions describing the Soret separation in this geometry, allowing to simultaneously extract both diffusion and Soret coefficients. More information on the instrument and the image processing can be found in Refs. [15, 16].

The isothermal diffusion at dilute limits was measured by a similar interferometer using the same data extraction approach. The counter-flow cell for the diffusion study is a metal frame with rectangular opening of $20.0 \times 5.0 \text{ mm}^2$ clamped between two optical windows using PTFE gaskets. The liquid filled space between the inner surfaces of the windows is 5.00 mm. Two inlets located at the top and the bottom of the cell allow injection of two solutions of slightly different concentrations; the heavier one is injected from the bottom to avoid instability. Two outlets located symmetrically on lateral walls at the mid-height of the cell, at 10.0 mm ensure the formation of a sharp interface between both solutions during injection. After the injection stop and sealing of the ports, the interface elution due to diffusion is monitored in time along the diffusion path. More details of the instrument and the data extraction are available in Refs. [17, 18].

Some chemicals (TEG and ETH) used for the experiments conducted with ODI and CFC setups were equivalent by grade and manufacturer to ones used in the OBD experiments, while extra pure deionized water was purchased from Acros Organics (LOT A0396624).

2.3 Nonequilibrium fluctuations and shadowgraphy

Additional measurements for TEG/H₂O-mixtures at selected compositions and temperatures were performed by means of the dynamic shadowgraphy technique (SG), which is based on optical detection of nonequilibrium fluctuations (NEFs). These measurements are described in full detail in Ref. [19] and will only briefly be summarized. The results are included here, since they are based on somewhat different principles and very nicely align with the OBD and ODI experiments.

A fluid submitted to a gradient of temperature or concentration shows thermal and/or solutal nonequilibrium fluctuations that happen at all wavelengths, whose amplitude can be orders of magnitude larger than that

of the equilibrium ones and whose size can grow up to macroscopic scales [20, 21], so that they are usually referred to as ‘giant’ fluctuations [21–23]. The associated refractive index fluctuations generate scattered beams that interfere with the transmitted one. The light intensity modulations can be collected by a pixelated sensor and analyzed in order to extract thermo-physical properties of the fluid [24].

The employed shadowgraph setup is similar to the one described in Ref. [25]. A Soret cell of 25 mm diameter contains the liquid sample that is vertically confined by two horizontal square sapphire windows at a distance of $h = 2$ mm. Their temperatures are regulated by two Peltier elements with a central circular aperture of 13 mm in diameter. Contrary to OBD and ODI, the observation is not perpendicular to but rather along the direction of the temperature gradient.

Thermodiffusion experiments were performed at mean temperatures of 20, 25, and 30 °C with a temperature difference of 20 K between the two sapphire windows. The temperature gradient was anti-parallel to gravity for $c = 0.3$ (heating from above) and parallel for $c = 0.5$ and 0.7 (heating from below). Once the steady state is achieved, a typical experiment consists of recording a series of images for a given acquisition frame rate. The analysis of each image series is performed by means of the Differential Dynamic Algorithm through a custom program taking advantage of GPU parallel execution [26, 27] in order to extract the structure function of the images [25]. The fit of a model temporal correlation function to the structure function allows to extract the decay times of the nonequilibrium fluctuations of the concentration and eventually obtain an indirect measurement of the mass diffusion and the Soret coefficients of the mixture [19, 25].

We also carried out free isothermal diffusion experiments for $c = 0.5$ and 0.7 using a stainless steel annulus with thickness of $h = 10.0$ mm. Two inlets and two outlets allow the superimposition of two fluid layers of equal thickness and different concentration. Once the two layers are in place, the diffusion process is followed by recording series of images in time. Details of this cell and of the filling procedure are also given in Ref. [19]. The reported diffusion coefficients measured by SG are

mean values from the isothermal measurements and the experiments with a temperature gradient.

3 Results and discussion

3.1 The binary borders

We report and discuss results for all three binary borders of the ternary DCMIX3 system consisting of H₂O, ETH, and TEG. The results for the binaries TEG/H₂O and TEG/ETH are new, the system ETH/H₂O has previously been studied by Kolodner et al. [7] and in our laboratory [8]. The numerical values of the transport coefficients of ETH/H₂O can be found in these two original publications and will not be repeated here. The discussion and the numerical fits will focus on the OBD-measurements, which represent a complete and internally consistent data set. The results obtained by the other experimental techniques, which are generally in good agreement but over a more limited parameter range, will be compared and discussed where appropriate.

All OBD-measurements have been evaluated following the protocol described in, e.g., Refs. [8, 28]. The experiment starts with an isothermal, homogeneous sample to which a constant temperature gradient is applied at $t = 0$ by ramping the temperature of one plate up and the temperature of the opposite plate down by the same amount of typically $\delta T/2 = 0.5$ K, thereby keeping the mean sample temperature constant. Assuming sufficient time scale separation, the rise time of the temperature gradient can be neglected. The formation of the concentration gradient is described on the basis of the extended diffusion equation for the mass fraction $c(x, t)$ of the first component:

$$\frac{\partial c}{\partial t} = D \nabla^2 c + D_T c(1 - c) \nabla^2 T. \tag{2}$$

Both the diffusion coefficient D and the thermodiffusion coefficient D_T are assumed constant within the 1-Kelvin-temperature variation in the cell. The Soret coefficient $S_T = D_T/D$ determines the concentration gradient in the nonequilibrium steady state. For sufficiently small Soret coefficients $S_T \ll 1/\delta T$, as prevalent in our experiments, the product $c(1 - c)$ can be assumed constant. The transient beam deflection signal is fitted by an analytic solution of Eq. (2) to obtain D from the characteristic time constant $\tau = h^2/D$. For D_T and S_T , the beam deflections need additionally be transformed from the refractive index to the concentration space by means of the optical contrast factors $(\partial n/\partial T)_{p,c}$ and $(\partial n/\partial c)_{p,T}$.

The focus of our discussion is on the Soret coefficients, but we also document the diffusion coefficients for reference. Our measured diffusion coefficients for TEG/H₂O and TEG/ETH are tabulated as functions of concentration and temperature in Tables 2 and 3,

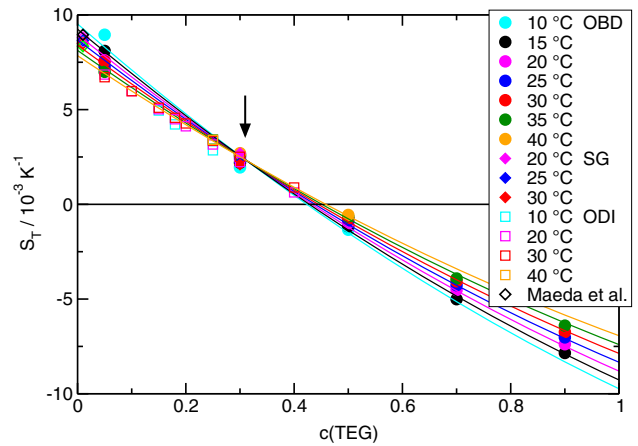


Fig. 1 OBD-measurement (filled circles) of the Soret coefficient of TEG/H₂O for different temperatures as a function of TEG-concentration c . The filled diamonds at $c = 0.3$ were obtained by SG and the open squares by ODI. The data at the lowest concentration of $c = 0.01$ are calculated according to Maeda et al. [31] as $S_T = 9.4 \times 10^{-3} \text{ K}^{-1} - 3.0 \times 10^{-5} \text{ K}^{-2} T$ (open diamonds). The solid lines represent a simultaneous fit of Eq. (4) to all OBD-data

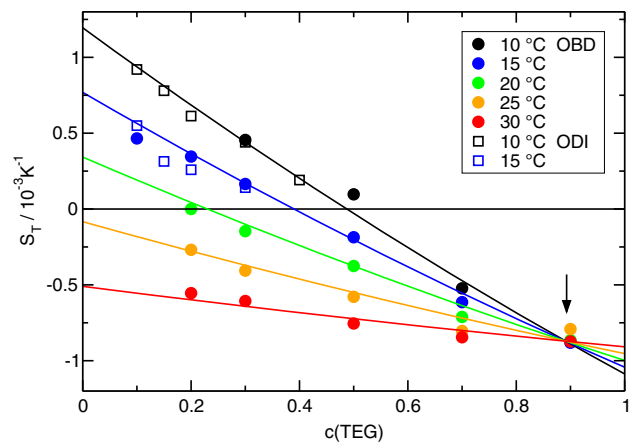


Fig. 2 Soret coefficient of TEG/ETH for different temperatures as a function of TEG-concentration c

respectively. The corresponding Soret coefficients can be found in Tables 4 and 5.

The Soret coefficients of the three binaries are plotted in Figs. 1, 2, and 3. For ETH/H₂O (Fig. 3), we have used only data that were measured in our own laboratory. As shown in Ref. [8], they perfectly agree with older results of Kolodner et al. [7] and also with data over a smaller parameter range by Wiegand et al. [29] and Zhang et al. [30]. Our OBD-, SG- and ODI-data for the Soret coefficient of TEG/H₂O are compared with results from Ref. [31] at the lowest concentration. In the following, the prominent features that are common to all three mixtures shall be discussed.

The first obvious observation is the sign change of the Soret coefficients of all three systems as a function of concentration and/or temperature. Such sign changes, where the components invert their thermodif-

Table 2 Diffusion coefficients of TEG/H₂O as a function of TEG-concentration c and temperature as obtained by OBD, SG, and ODI. SG-data from Ref. [19]

	c	$D [10^{-10} \text{ m}^2/\text{s}]$						
		10 °C	15 °C	20 °C	25 °C	30 °C	35 °C	40 °C
OBD	0.05	4.6(.2)	5.9(.2)	5.9(.2)	7.2(.2)	7.6(.3)	8.9(.3)	
	0.3	3.4(.2)	4.1(.2)	4.7(.2)	5.2(.3)	6.2(.3)	7.0(.3)	7.8(.4)
	0.5	2.3(.1)	2.7(.1)	3.3(.2)	3.8(.2)	4.5(.2)	5.2(.3)	6.0(.3)
	0.7		1.4(.1)	1.9(.1)	2.4(.1)	2.9(.1)	3.4(.2)	4.1(.2)
	0.9		0.9(.1)	1.2(.1)	1.6(.1)	1.9(.1)	2.4(.1)	
SG	0.3			4.79(.12)	5.46(.15)	6.4(.3)		
	0.5			3.3(.1)	3.86(.14)	5.4(.3)		
	0.7			2.09(.12)	2.33(.06)	2.86(.13)		
ODI	0.05			6.2(.3)		8.0(.2)		
	0.1			6.0(.3)		7.6(.2)		
	0.15	4.1(.2)		5.6(.3)		7.2(.2)		
	0.18	4.0(.2)		5.4(.3)		6.9(.2)		
	0.2			5.3(.3)		6.0(.2)		
	0.25	3.6(.2)		4.9(.2)		6.4(.2)		8.2(.2)
	0.3			4.5(.2)		5.9(.1)		
0.4			3.6(.2)		4.9(.1)			

Table 3 Diffusion coefficients of TEG/ETH as a function of TEG-concentration c and temperature as obtained by OBD, ODI, and CFC

	c	$D [10^{-10} \text{ m}^2/\text{s}]$				
		10 °C	15 °C	20 °C	25 °C	30 °C
OBD	0.2		4.7(.2)		4.9(.2)	5.4(.3)
	0.3	2.6(.1)	3.2(.2)	3.7(.2)	4.1(.2)	4.6(.2)
	0.5	1.6(.1)	2.0(.1)	2.5(.1)	3.1(.2)	3.4(.2)
	0.7	1.3(.1)	1.5(.1)	1.8(.1)	2.0(.1)	2.5(.1)
	0.9		0.81(.05)	0.99(.05)	1.2(.1)	1.3(.1)
ODI	0.1	3.39(.09)	4.3(.3)			
	0.15	3.1(.2)	3.9(.4)			
	0.2	3.05(.06)				
	0.3	3.0(.2)				
	0.4	2.5(.1)				
CFC	0.0015	4.9(.1)	5.54(.09)	5.88(.09)	6.5(.2)	7.0(.2)
	0.998		0.62(.03)	0.74(.04)		1.03(.09)

fusive migration direction, have been reported in the literature also for colloids [32] but they are rare for molecular systems.

The second observation is the direction of the sign change. All Soret coefficients decrease with concentration. They are positive for small and become negative for large c . Only for TEG/ETH at the two highest temperatures, $S_T(c)$ is always negative, but the decreasing nature of $S_T(c)$ is still preserved (Fig. 2). Keeping in mind that the given Soret coefficient is the one of the first component and that S_T changes its sign when the numbering of the components is reversed, this means that the minority component always migrates to the cold side in the two dilute limits. Accordingly, the majority component goes to the hot side. It is important to understand that swapping of the components changes the sign of S_T and, thus, does not change the

decaying nature of the curves with positive Soret coefficients for small and negative ones for large concentrations.

The third observation relates to the temperature dependence of the Soret coefficient. For every mixture, there exists a temperature-independent fixed point of S_T at a certain concentration c_f . In TEG/H₂O, it is at $c_f \approx 0.31$ with a positive value of S_T , in TEG/ETH it is at $c_f \approx 0.89$ with a negative S_T and in ETH/H₂O it is at $c_f \approx 0.29$ with a vanishing Soret coefficient $S_T(c_f) \approx 0$. The fixed points are marked in the figures by arrows. In any case, the curves $S_T(c)$ for different temperatures pivot around the fixed point in a way such that S_T decreases with increasing temperature for $c < c_f$ and increases for $c > c_f$. Together with the general decrease in S_T with increasing c , this implies that S_T approaches $S_T(c_f)$ with increasing temperature. There are also sign

Table 4 Soret coefficient of TEG/H₂O as a function of TEG-concentration c and temperature as obtained by OBD, SG, and ODI. SG-data from Ref. [19]

	c	S_T [10^{-3} 1/K]						
		10 °C	15 °C	20 °C	25 °C	30 °C	35 °C	40 °C
OBD	0.05	9.0(.5)	8.1(.4)	7.6(.4)	7.3(.3)	7.6(.3)	7.0(.3)	
	0.3	2.0(.1)	2.2(.1)	2.4(.1)	2.5(.1)	2.6(.2)	2.6(.2)	2.7(.2)
	0.5	-1.34(.05)	-1.16(.07)	-1.00(.06)	-0.85(.05)	-0.74(.04)	-0.65(.04)	-0.56(.03)
	0.7		-5.0(.3)	-4.5(.3)	-4.3(.2)	-4.1(.2)	-3.9(.2)	
	0.9		-7.8(.5)	-7.4(.4)	-7.0(.4)	-6.7(.4)	-6.4(.4)	
SG	0.3			2.3(.3)	2.3(.3)	2.0(.4)		
ODI	0.05			6.9(0.3)		6.7(.3)		
	0.1			6.0(.4)		6.0(.2)		
	0.15	5.0(.3)		5.0(.3)		5.1(.3)		
	0.18	4.2(.2)		4.5(.2)		4.6(.2)		
	0.2			4.1(.2)		4.3(.3)		
	0.25	2.9(.1)		3.2(.1)		3.4(.2)		3.4(.2)
	0.3			2.2(.1)		2.5(.1)		
	0.4			0.63(.06)		0.89(.04)		

Table 5 Soret coefficient of TEG/ETH as a function of TEG-concentration c and temperature as obtained by OBD and ODI

	c	S_T [10^{-3} 1/K]				
		10 °C	15 °C	20 °C	25 °C	30 °C
OBD	0.1		0.47(.02)			
	0.2		0.36(.01)	0	-0.27(.01)	-0.56(.02)
	0.3	0.47(.02)	0.16(.01)	-0.14(.01)	-0.39(.02)	-0.59(.03)
	0.5	0.09(.01)	-0.20(.01)	-0.39(.02)	-0.57(.03)	-0.74(.04)
	0.7	-0.52(.03)	-0.60(.07)	-0.7(.1)	-0.8(.2)	-0.8(.2)
	0.9		-0.88(.04)	-0.87(.04)	-0.79(.03)	-0.87(.04)
ODI	0.1	0.92(.03)	0.55(.06)			
	0.15	0.78(.07)	0.31(.05)			
	0.2	0.61(.04)	0.26(.03)			
	0.3	0.44(.02)	0.14(.01)			
	0.4	0.191(.005)				

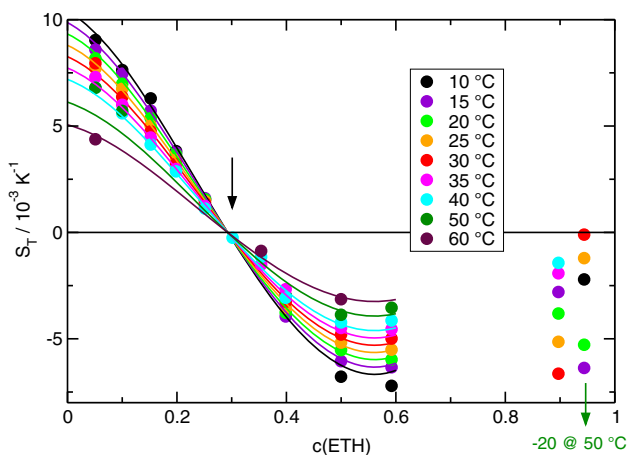


Fig. 3 Soret coefficient of ETH/H₂O for different temperatures as a function of ETH-concentration c . Data from Ref. [8]

changes of S_T as a function of temperature at certain concentrations, e.g., for TEG/ETH around $c = 0.3$ (Fig. 2). No such temperature-induced sign changes are observed for ETH/H₂O, where the temperature-independent fixed point coincides with $S_T(c_f) = 0$.

A temperature-independent fixed point of the Soret coefficient has also been observed for other systems. In Ref. [33] it has been suggested to write the Soret coefficient as a composition-dependent function $\alpha(c)$ multiplied by a temperature-dependent amplitude $\beta(T)$ plus a constant offset S_T^f that is identified with the Soret coefficient at the fixed point:

$$S_T(c, T) = \alpha(c)\beta(T) + S_T^f. \tag{3}$$

This equation with polynomials for $\alpha(c)$ and $\beta(T)$ has already been used for the ETH/H₂O-system, both with the concentration measured in mole [33] and in mass fractions [8]. Following the same idea, the Soret coefficients are fitted by

$$S_T(c, T) = \sum_{i=0}^4 a_i c^i (1 + b_1 \vartheta) + S_T^f. \quad (4)$$

As in Eq. (1), $\vartheta = T - 273.15$ K is the temperature in Centigrade. The fits have been performed to the OBD-measurements, which represent a complete and experimentally consistent data set. The SG- and ODI-results are additionally plotted in Figs. 1 and 2 and are in very good agreement with the OBD-data. The fit parameters for all three systems are summarized in Table 6. As already mentioned, b_1 is always negative and $\beta(T)$ decreases with increasing temperature. For mixtures of benzene and cyclohexane, the Soret coefficient at the fixed point could be identified with the isotopic contribution, which is related to differences of molar mass and moment of inertia, and the term $\alpha(c)\beta(T)$ with the so-called chemical contribution [33]. Despite the similar structure of $S_T(c, T)$, such an assignment is not possible for the here considered hydrogen bonding mixtures.

Although we cannot provide a fully quantitative description of our results, it is worth pointing out another relationship for the composition dependence of S_T . In Ref. [34], it is shown that the Soret coefficient can be split into contributions from the pure components, S_T^{pur} , and a mixing term S_T^{mix} . Only the latter is responsible for the concentration dependence. According to Morozov's theory [35], it is related to the excess volume of mixing V^E by

$$S_T^{mix} \approx C \frac{\partial V^E}{\partial x_1}, \quad (5)$$

with x_1 being the mole fraction of the first component and $C < 0$ a constant that depends on the solvent compressibility.

Since V^E vanishes at the two ends of the concentration axis and typically goes through an extremum in between, a positive excess volume corresponds to a situation with a negative second derivative, $\partial^2 V^E / \partial x_1^2 < 0$. Because of the negative constant $C < 0$, this relates to the situation of a Soret coefficient that increases with c , and vice versa for a negative excess volumes [34]. All three mixtures show a decreasing Soret coefficient, albeit the situation is not fully clear for ETH/H₂O at high ETH concentrations. A few data points above $c \sim 0.9$ might hint at an increase in S_T at higher concentrations, but they show a large scatter and are very unreliable because of the vanishing solutal contrast factor $(\partial n / \partial c)_{p, T}$, which changes sign around $c = 0.8$. They were already excluded from the fit in Ref. [8]. With their inclusion, the Soret coefficient would no longer decrease monotonously, but the overall picture remained unchanged: there would still be the temperature-invariant fixed point with the sign change and an overall decrease in S_T from the left to the right.

Figure 4 shows the excess volumes for all three mixtures at 25 °C as obtained from density measurements of the pure substances and the mixtures performed with an Anton Paar DSA 5000 M densitometer. All three are negative, which is, indeed, in agreement with the

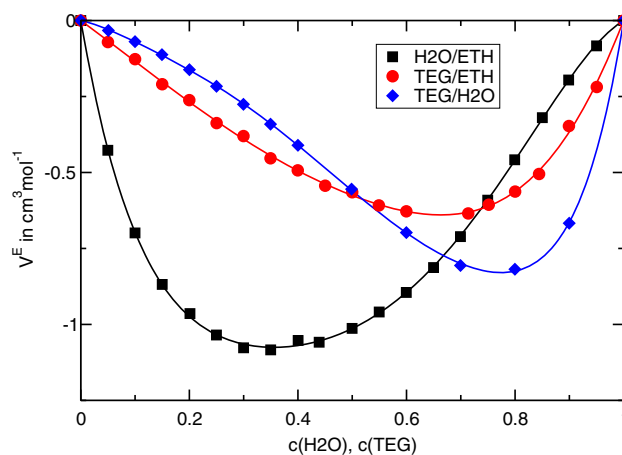


Fig. 4 Excess volumes of mixing V^E for the three mixtures TEG/H₂O, TEG/ETH, and ETH/H₂O at 25 °C

observation of decreasing Soret coefficients. We want to repeat here, that a decreasing $S_T(c)$ remains decreasing under reversal of the components.

3.2 The ternary Gibbs triangle

The knowledge of the signs of the Soret coefficients along all three binary borders allows, within certain assumptions, predictions about the signs of the Soret coefficients inside the ternary Gibbs triangle. In the following, we will use the primed Soret coefficients $S'_{T,i}$, which are the established notation for ternaries. They are defined by the concentration gradients in the Soret equilibrium, $\nabla c_i = -S'_{T,i} \nabla T$, and are related to their unprimed counterparts in the case of binary mixtures by $S'_{T,i} = c_i(1 - c_i)S_{T,i}$ [36]. An in-depth discussion of frame-invariant Soret coefficients has been given by Ortiz de Zárate [37].

Figure 5 shows the Gibbs triangle with colors assigned to the three compounds: magenta for H₂O, orange for ETH, and green for TEG. The color code along the binary borders marks the concentration range, where the respective component is thermophilic, i.e., has a negative Soret coefficient and enriches at the hot side for a mean temperature of 25 °C. These regions are directly taken from Figs. 1, 2, and 3. The coincidence of the color code of the axes with the color of the respective component near the corners reflects our finding that, as a rule, the majority component migrates to the hot and the minority component to the cold side. The concentration of the sign change along the H₂O/ETH-axis, i.e., where the color changes from magenta to orange, is temperature independent (Fig. 3) and the sign change along the TEG/H₂O-axis depends only weakly on temperature (Fig. 1). The sign change concentration for TEG/ETH, on the other hand, shows a pronounced temperature dependence and shifts from $c_{TEG} \approx 0.5$ at 10 °C to $c_{TEG} \approx 0$ at 25 °C, for which Fig. 5 is drawn. Very close to the selected temperature of 25 °C, the Soret coefficient of TEG in TEG/ETH-

Table 6 Fit parameters for the Soret coefficients according to Eq. (4). The values for ETH/H2O are from Ref. [8]

	TEG/H2O	TEG/ETH	ETH/H2O
a_0	0.00777	0.00292	0.0115
a_1	-0.0268	-0.00370	-0.0154
a_2	0.00604	0.000471	-0.1453
a_3	-	-	0.2378
a_4	-	-	-0.0652
b_1 [K ⁻¹]	-0.00719	-0.02921	-0.00931
S_T^f [K ⁻¹]	0.00231	-0.00087	0.0

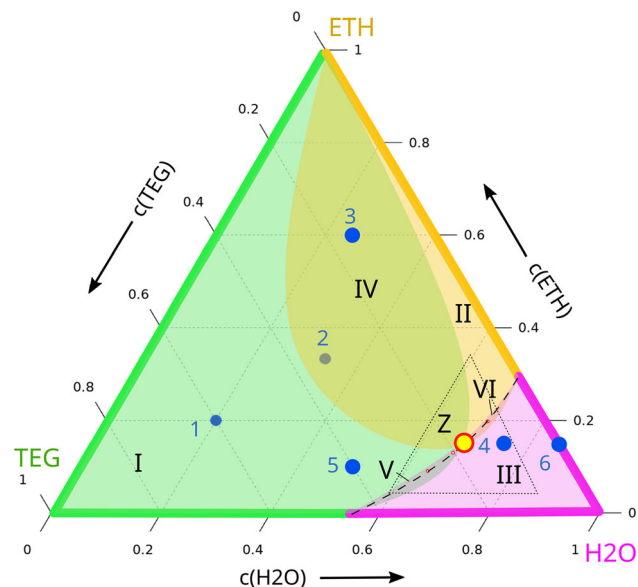


Fig. 5 Signs of the Soret coefficients within the ternary Gibbs triangle at 25 °C. The colored regions denote thermophilic behavior with negative Soret coefficients of the respective components. The dots 1–6 indicate the compositions of the DCMIX3 samples. Point Z marks the intersection of the boundaries of the three colored regions, where all three Soret coefficients vanish simultaneously. The steady-state optical signal vanishes along the dashed line (see Fig. 6). The regions I to VI are explained in the text. The triangle near the H2O corner indicates the zoom-region shown in Fig. 6

mixtures remains negative over the entire composition range and just vanishes in the limit $c_{TEG} \approx 0$, corresponding to $c_{ETH} \approx 1$. Thus, the green color along this axis extends just up to the ETH-corner. Already at a slightly lower temperature, the green color would stop short of the ETH-corner. The following discussion does, however, not depend on these peculiar details.

Since Soret coefficients are smooth and continuous functions of the composition, and since the ternaries extrapolate to the corresponding binaries near the axes, we can draw some conclusions about the signs of the Soret coefficients of the ternaries inside the Gibbs triangle.

Let us begin with TEG. Its Soret coefficient vanishes at the ETH-corner and at the concentration of

the sign change along the TEG/H2O-axis. These two points must be connected by a continuous line through the Gibbs triangle, defined as the locus where the Soret coefficient of TEG, the third component, changes sign, hence $S'_{T,3} = 0$. Together with the green sections of the axes, this line encompasses the green composition range where TEG is thermophilic. Outside, it is thermophobic. Of course, the shape of the green region inside the Gibbs triangle is only a sketch and could be more to the left or more to the right. The orange and the magenta regions can be constructed along the same rules.

From Ref. [38], it is known that both ETH (component 2) and TEG (component 3) have negative Soret coefficients at point 2, whereas the one of H2O (component 1) is positive. Hence, composition 2 must be inside both the green and the orange but outside the magenta region.

Only one negative Soret coefficient exists within regions I, II, and III. Compositions with two negative Soret coefficients define the intersection regions IV, V, and VI. Additional rules follow from mass conservation, which requires

$$S'_{T,1} + S'_{T,2} + S'_{T,3} = 0 . \tag{6}$$

An immediate consequence is that the intersection of all three colors must be of size zero, since all three Soret coefficients cannot be negative at the same time. For the same reason also three positive Soret coefficients are not possible and every composition must belong to either one or two colors.

Because composition 2 is both green and orange, the boundaries of these two regions must intersect in point Z in a similar way as drawn in Fig. 5. Since this intersection is defined by $S'_{T,2} = S'_{T,3} = 0$, Eq. (6) immediately requires $S'_{T,1} = 0$, and the boundary of the magenta region must also pass through the intersection point Z.

Thus, the sign changes of the Soret coefficients of the binaries and the knowledge of their signs at one composition (point 2) inside the ternary diagram allows us to draw far-reaching conclusions about the signs of the Soret coefficients of the ternaries and to prove that at least one composition Z must exist, where all three Soret coefficients vanish simultaneously and no steady-state separation will be observed in a temperature gradient.

Zones V and VI in Fig. 5 are very narrow, meaning that the Soret coefficients that correspond to the

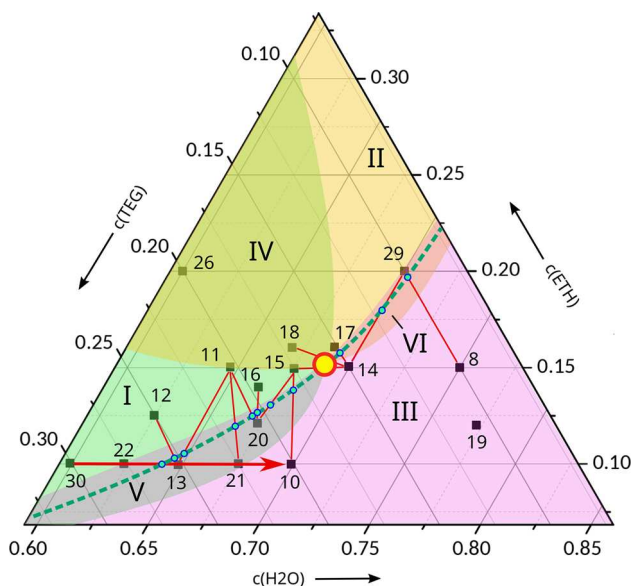


Fig. 6 Construction of the dotted line in Fig. 5 with vanishing steady-state amplitude of the solutal OBD-signal at 25 °C. The numbers reflect the chronological order of the measurements

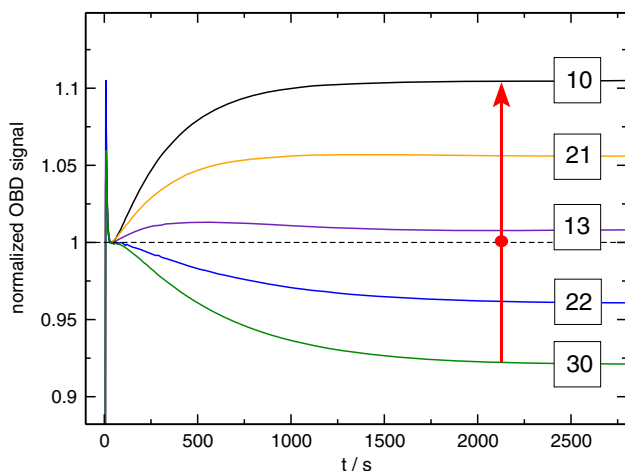


Fig. 7 Solutal OBD-signals for measurements 30, 22, 13, 21, and 10 from Fig. 6 as indicated by red arrow. The steady-state amplitude vanishes between points 22 and 13, close to the latter

two respective overlapping colors (TEG/H₂O in zone V and ETH/H₂O in zone VI) are very close to their sign change compositions. Since two small Soret coefficients automatically imply, according to Eq. (6), also a small Soret coefficient of the third component, the OBD-signals in zones V and VI should be very small. Since H₂O has the smallest refractive index, the OBD-signal is even expected to change its sign along paths through zones I–V–III or II–VI–III.

Indeed, such a sign change within zones V and VI is observed experimentally at the dashed line in Fig. 5. This line has been constructed by measuring the OBD-signal with a single color at a large number of compo-

sitions around the expected sign change compositions. Then, pairs of compositions with different signs of their solutal OBD-amplitudes are identified. The sign change compositions are determined by linear interpolation of the two amplitudes along the connecting line in the Gibbs triangle.

Figure 6 illustrates this procedure. The composition pairs with different signs of the OBD-amplitudes are connected with thin red lines along which the compositions of asymptotically vanishing solutal OBD-signals are determined. Together with the sign changes of the Soret coefficients of the adjacent binaries, they define the dashed lines in Figs. 5 and 6.

The normalized solutal signals along the line through compositions 30–22–13–21–10 are shown in Fig. 7. The sign change occurs between compositions 22 and 13, very close to the latter. We attribute the positive amplitudes below the dashed line mainly to the negative Soret coefficient of H₂O in zones III, V, and VI. The composition with vanishing signal close to composition 13 is, however, not identical to point Z, where all three Soret coefficients vanish. A close inspection of the solutal signal of composition 13 in Fig. 7 reveals a superposition of a fast contribution with a small positive and a slow one with a small negative amplitude.

Thus, although the solutal steady-state optical signal asymptotically vanishes along the dashed line, it is still a superposition of two, albeit small, contributions with different signs that correspond to the two eigenmodes with different eigenvalues of the diffusion matrix. As a consequence, the vanishing asymptotic signals can still show transient amplitudes for finite times. The strict requirement for an asymptotically vanishing solutal amplitude of the optical signal reads

$$\left(\frac{\partial n}{\partial c_1}\right)_{p,T} S'_{T,1} + \left(\frac{\partial n}{\partial c_2}\right)_{p,T} S'_{T,2} = 0. \quad (7)$$

Because of the dispersion of the optical contrast factors, the precise position of the dashed line through regions V VI, with the exception of point Z, is expected to depend slightly on the employed detection wavelength. In principle, Eq. (7) could also be satisfied by a very peculiar combination of large Soret coefficients and matching optical contrast factors. Since this can be excluded at the two binary limits, and since the component separation necessarily needs to be small with changing signs within the narrow overlap regions V and VI, we consider it safe to exclude such unlikely coincidences.

Because of the vanishing solutal steady-state signal on the dashed line, it is very difficult to pin down the precise locus of point Z. Its position can be shifted along the dashed line and even the extreme positions at the two binary axes cannot be ruled out completely. They would still be compatible with our arguments. On the other hand, there are neither experimental observations nor theoretical arguments that would support such a very special assumption.

The sample from DCMIX3 cell number 3 with a composition of 0.25/0.6/0.15 (H₂O/ETH/TEG) provides

Table 7 Ternary thermodiffusion and Soret coefficients of DCMIX3 sample 3 at 25 °C. Thermodiffusion coefficients $D'_{T,i}$ measured by TGC. Soret coefficients $S'_{T,i}$ calculated from $D'_{T,i}$ and diffusion matrix from Ref. [39]

		$D'_{T,i}$ [10^{-13} m ² /(sK)]	$S'_{T,i}$ [10^{-3} 1/K]
H2O	$i = 1$	4.36(.13)	1.33(.08)
ETH	$i = 2$	-3.30(.15)	-1.03(.09)
TEG	$i = 3$	-1.06(.13)	-0.30(.07)

the opportunity for an additional test of the picture developed so far. It is, besides sample 2, the only other DCMIX3 sample that has a positive separation ratio and can be measured by the thermogravitational column (TGC) technique with its superior contrast factor matrix. As shown in Fig. 5, sample 3 should be in the same zone IV as sample 2 with a positive Soret coefficient for H2O and negative Soret coefficients of ETH and TEG. In order to test this prediction, TGC measurements were performed following the identical protocol as employed for sample 2 in Ref. [38]. The results are listed in Table 7. The experiments yield directly the thermodiffusion coefficients $D'_{T,i}$. The Soret coefficients $S'_{T,i}$ are calculated as described in Ref. [38] using the diffusion matrix from Ref. [39]. As can be seen from Table 7, the signs of the three ternary Soret coefficients are in agreement with our model.

4 Summary and conclusion

We have presented Soret- and diffusion coefficients of the three binary subsystems of the ternary DCMIX3 system consisting of H2O, ETH, and TEG. All three binaries are strongly interacting hydrogen bonding mixtures with pronounced excess volumes of mixing [40]. We are not able to provide a fully quantitative model. There are, however, several remarkable properties that are common to all three mixtures but not necessarily found to the same extent in nonpolar organic liquids.

The most remarkable observation is a sign change of S_T as a function of concentration—in the case of TEG/ETH only below room temperature. In all binaries, the Soret coefficient is a decreasing function, which leads, together with the sign change, to a migration of the minority components to the cold side in the dilute limits. Correspondingly, the majority component has a negative Soret coefficient and goes to the hot side. As already observed for organic liquids, all three mixtures show a temperature invariant fixed point of S_T at a certain concentration, and S_T can be factorized into a concentration-dependent function $\alpha(c)$ with a temperature-dependent amplitude $\beta(T)$ plus the constant offset of the fixed point (Eq. (3)).

Although these observations can qualitatively be interpreted in terms of concepts discussed in the literature for organic mixtures, a fully quantitative description is still lacking for these hydrogen bonding systems. An example is the decrease in S_T with concentra-

tion, which is in agreement with predictions by Morozov [34, 35] for systems with negative excess volumes. Despite the nice qualitative agreement, we are not able to provide a quantitative model. Another example is the mentioned fixed point of the Soret coefficient and the parameterization of S_T according to Eq. (3). While these terms could be identified with the isotopic and the chemical contribution to the Soret coefficient in the case of organic mixtures, such an interpretation fails for the here considered strongly interacting polar mixtures.

Based on the knowledge of the signs of the Soret coefficients for the binaries and for the symmetric ternary mixture (DCMIX3-composition 2), it is possible to reconstruct the signs and sign changes also for the ternaries within the Gibbs triangle. Since the three Soret coefficients are not independent, two small Soret coefficients automatically imply that also the third one needs to be small. This, in combination with the low refractive index of water, leads to vanishing optical signals along the dashed line through the narrow overlap regions V and VI in Fig. 5, which are close to the loci where the Soret coefficients of TEG and H2O or ETH and H2O change their signs. Though its precise location has not been nailed down, these considerations necessarily imply the existence of a certain composition, point Z , where all three Soret coefficients vanish simultaneously and where no separation will occur in a temperature gradient.

On purpose, we have used as little experimental input as possible for the ternary mixtures inside the Gibbs triangle. The determination of the Soret coefficients for the ternaries requires two-color experiments, as employed for the DCMIX project, and the inversion of the optical contrast factor matrix. Due to the large condition numbers of the latter, the errors introduced by this procedure are unavoidably large. An exception is composition 2, which has been investigated in Ref. [38] both under microgravity and ground conditions. In particular, the employed thermogravitational column technique provides, for this particular system, superior contrast factor matrices. But since this method only works for positive separation ratios, it is limited to the DCMIX3-mixtures 2 and 3. These problems do not exist for the binaries and the reported data are generally of a high quality. Thus, it was our goal to investigate, how much information about the ternaries can be extracted for this particular system from the knowledge of the binaries alone. Even without DCMIX3 sample 2, the conclusions would be very similar and only the orange region with the negative Soret coefficient of ETH might

be drawn somewhat less toward the TEG corner. It should be remembered that the measurements shown in Fig. 6 to determine the dashed line were only made with a single color and did not involve the inversion of a contrast factor matrix.

Acknowledgements This work was developed in the framework of the cooperative project DCMIX (AO-2009-0858/1056) of the European Space Agency (ESA) and the Russian Space Agency (Roscosmos). The shadowgraphy measurements are supported by the ESA project GIANT FLUCTUATIONS and the ESA-MAP project TechNES (Grant 4000128933/19/NL/PG). M.S. and W.K. acknowledge the support by Deutsches Zentrum für Luft- und Raumfahrt (DLR) (Grants 50WM1544 and 50WM1850). A.M. acknowledges the support of the PRODEX program of the Belgian Federal Science Policy Office, ESA. H.B., F.C., and A.T.N. acknowledge support from the CNES and from the E2S UPPA Hub Newpores and the Industrial Chair CO2ES supported by the Investissements d’Avenir French programme managed by ANR (ANR-16-IDEX-0002) E.L, M.M.B., and V.S. acknowledge the support of the project micro4IoT (KK-2019/00101) from the Basque government and support from the Ministerio de Ciencia e Innovación, Spain (Grant PID2020-115086GB-C33).

Funding Open Access funding enabled and organized by Projekt DEAL.

Author contribution statement

MS, PM, CB, and WK performed and analyzed the OBD measurements. HB, FC, and ATN performed and analyzed the SG experiments. EL and MMB performed and analyzed the TGC experiments. AM and VS performed and analyzed the ODI and the. CFC experiments. WK wrote the manuscript. All authors analyzed and discussed the content of the paper.

Data availability Data are available upon reasonable request from the authors.

Open Access This article is licensed under a Creative Commons Attribution 4.0 International License, which permits use, sharing, adaptation, distribution and reproduction in any medium or format, as long as you give appropriate credit to the original author(s) and the source, provide a link to the Creative Commons licence, and indicate if changes were made. The images or other third party material in this article are included in the article’s Creative Commons licence, unless indicated otherwise in a credit line to the material. If material is not included in the article’s Creative Commons licence and your intended use is not permitted by statutory regulation or exceeds the permitted use, you will need to obtain permission directly from the copyright holder. To view a copy of this licence, visit <http://creativecommons.org/licenses/by/4.0/>.

References

1. W. Köhler, K.I. Morozov, J. Non-Equilib, Thermodyn. **41**, 151 (2016). <https://doi.org/10.1515/jnet-2016-0024>
2. M. Braibanti, P.A. Artola, P. Baaske, H. Bataller, J.P. Bazile, M. Bou-Ali, D. Cannell, M. Carpineti, R. Cerbino, F. Croccolo, J. Diaz, A. Donev, A. Errarte, J. Ezquerro, A. Frutos-Pastor, Q. Galand, G. Galliero, Y. Gaponenko, L. García Fernández, J. Gavaldà, F. Giavazzi, M. Giglio, C. Giraudet, H. Hoang, E. Kufner, W. Köhler, E. Lapeira, A. Laveron-Simavilla, J.C. Legros, I. Lizarraga, T. Lyubimova, S. Mazzoni, N. Melville, A. Mialdun, O. Minster, F. Montel, F. Molster, J. M. Ortiz de Zárate, J. Rodríguez, B. Rousseau, X. Ruiz, I. Ryzhkov, M. Schraml, V. Shevtsova, C. Takacs, T. Triller, S. VanVaerenbergh, A. Vailati, A. Verga, R. Vermorel, V. Vesovic, V. Yasnou, S. Xu, D. Zapf, K. Zhang, Eur. Phys. J. E **42**, 86 (2019). <https://doi.org/10.1140/epje/i2019-11849-0>
3. J.K. Platten, M.M. Bou-Ali, P. Costesèque, J.F. Dutrieux, W. Köhler, C. Leppla, S. Wiegand, G. Wittko, Philos. Mag. **83**, 1965 (2003). <https://doi.org/10.1080/0141861031000108204>
4. V. Shevtsova, C. Santos, V. Sechenyh, J.C. Legros, A. Mialdun, Microgravity Sci. Tec. **25**, 275 (2014). <https://doi.org/10.1007/s12217-013-9349-6>
5. A. Mialdun, M.M. Bou-Ali, M. Braibanti, F. Croccolo, A. Errarte, J.M. Ezquerro, J.J. Fernandez, L. García Fernández, Q. Galand, Y. Gaponenko, J. Gavaldà, W. Köhler, T. Lyubimova, J.M. Ortiz de Zárate, J. Rodríguez, X. Ruiz, I.I. Ryzhkov, V. Shevtsova, S. van Vaerenbergh, V. Yasnou, H. Bataller, Acta Astronaut. **176**, 204 (2020). <https://doi.org/10.1016/j.actaastro.2020.06.020>
6. T. Triller, H. Bataller, M.M. Bou-Ali, M. Braibanti, F. Croccolo, J.M. Ezquerro, Q. Galand, J. Gavaldà, E. Lapeira, A. Laverón-Simavilla, T. Lyubimova, A. Mialdun, J.M. Ortiz de Zárate, J. Rodríguez, X. Ruiz, I.I. Ryzhkov, V. Shevtsova, S.V. Vaerenbergh, W. Köhler, Microgravity Sci. Tec. **30**, 295 (2018). <https://doi.org/10.1007/s12217-018-9598-5>
7. P. Kolodner, H. Williams, C. Moe, J. Chem. Phys. **88**, 6512 (1988). <https://doi.org/10.1063/1.454436>
8. A. Königer, B. Meier, W. Köhler, Philos. Mag. **89**, 907 (2009). <https://doi.org/10.1080/14786430902814029>
9. O. Batiste, E. Knobloch, A. Alonso, I. Mercader, J. Fluid Mech. **560**, 149 (2006). <https://doi.org/10.1017/S0022112006000759>
10. P. Kolodner, A. Passner, C.M. Surko, R.W. Walden, Phys. Rev. Lett. **56**, 2621 (1986). <https://doi.org/10.1103/PhysRevLett.56.2621>
11. M. Giglio, A. Vendramini, Phys. Rev. Lett. **34**, 561 (1975). <https://doi.org/10.1103/PhysRevLett.34.561>
12. R. Piazza, A. Guarino, Phys. Rev. Lett. **88**, 208302 (2002). <https://doi.org/10.1103/PhysRevLett.88.208302>
13. A. Königer, H. Wunderlich, W. Köhler, J. Chem. Phys. **132**, 174506 (2010). <https://doi.org/10.1063/1.3421547>
14. G. Wittko, W. Köhler, Philos. Mag. **83**, 1973 (2003). <https://doi.org/10.1080/0141861031000108213>
15. A. Mialdun, V. Shevtsova, J. Chem. Phys. **134**, 044524 (2011). <https://doi.org/10.1063/1.3546036>

16. A. Mialdun, J.C. Legros, V. Yasnou, V. Sechenyh, V. Shevtsova, *Eur. Phys. J. E* **38**, 27 (2015). <https://doi.org/10.1140/epje/i2015-15027-2>
17. A. Mialdun, V. Yasnou, V. Shevtsova, *C.R. Méc.* **341**, 462 (2013). <https://doi.org/10.1016/j.crme.2013.02.001>
18. T. Janzen, S. Zhang, A. Mialdun, G. Guevara-Carrion, J. Vrabec, M. He, V. Shevtsova, *Phys. Chem. Chem. Phys.* **19**(47), 31856 (2017). <https://doi.org/10.1039/C7CP06515A>
19. A.T. Ndjaka, D.E. Bouyou Bouyou, A. Lassin, M. Azaroual, F. Croccolo, H. Bataller, *Eur. Phys. J. E* **submitted** (2021)
20. A. Vailati, M. Giglio, *Nature* **390**, 262 (1997). <https://doi.org/10.1038/36803>
21. A. Vailati, R. Cerbino, S. Mazzoni, C.J. Takacs, D.S. Cannell, M. Giglio, *Nature Commun.* **2**, 290 (2011). <https://doi.org/10.1038/ncomms1290>
22. F. Croccolo, J.M. Ortiz de Zárate, J.V. Sengers, *Eur. Phys. J. B* **39**, 125 (2016). <https://doi.org/10.1140/epje/i2016-16125-3>
23. P. Baaske, H. Bataller, M. Braibanti, M. Carpineti, R. Cerbino, F. Croccolo, A. Donev, W. Köhler, J.M. Ortiz de Zárate, A. Vailati, *Eur. Phys. J. E* **39**, 119 (2016). <https://doi.org/10.1140/epje/i2016-16119-1>
24. F. Scheffold, R. Cerbino, *Curr. Opin. Colloid Interface Sci.* **12**, 50 (2007). <https://doi.org/10.1016/j.cocis.2007.03.005>
25. F. Croccolo, H. Bataller, F. Scheffold, *J. Chem. Phys.* **137**, 234202 (2012). <https://doi.org/10.1063/1.4771872>
26. G. Cerchiari, F. Croccolo, F. Cardinaux, F. Scheffold, *Rev. Sci. Instrum.* **83**, 106101 (2012). <https://doi.org/10.1063/1.4755747>
27. M. Norouzisadeh, M. Chraga, G. Cerchiari, F. Croccolo, *Eur. Phys. J. E* **submitted** (2021)
28. M. Gebhardt, W. Köhler, *J. Chem. Phys.* **142**, 084506 (2015). <https://doi.org/10.1063/1.4908538>
29. S. Wiegand, H. Ning, H. Kriegs, *J. Phys. Chem. B* **111**, 14169 (2007). <https://doi.org/10.1021/jp076913y>
30. K.J. Zhang, M.E. Briggs, R.W. Gammon, J.V. Sengers, *J. Chem. Phys.* **104**, 6881 (1996)
31. K. Maeda, N. Shinyashiki, S. Yagihara, S. Wiegand, R. Kita, *J. Chem. Phys.* **143**, 124504 (2015). <https://doi.org/10.1063/1.4931115>
32. S. Iacopini, R. Rusconi, R. Piazza, *Eur. Phys. J. E* **19**, 59 (2006). <https://doi.org/10.1140/epje/e2006-00012-9>
33. G. Wittko, W. Köhler, *Europhys. Lett.* **78**, 46007 (2007). <https://doi.org/10.1209/0295-5075/78/46007>
34. S. Hartmann, G. Wittko, F. Schock, W. Groß, F. Lindner, W. Köhler, K.I. Morozov, *J. Chem. Phys.* **141**, 134503 (2014). <https://doi.org/10.1063/1.4896776>
35. K.I. Morozov, *Phys. Rev. E* **79**, 031204 (2009). <https://doi.org/10.1103/PhysRevE.79.031204>
36. M. Gebhardt, W. Köhler, *J. Chem. Phys.* **143**, 164511 (2015). <https://doi.org/10.1063/1.4934718>
37. J.M. Ortiz de Zárate, *Eur. Phys. J. E* **42**, 43 (2019). <https://doi.org/10.1140/epje/i2019-11803-2>
38. T. Triller, D. Sommermann, M. Schraml, F. Sommer, E. Lapeira, M.M. Bou-Ali, W. Köhler, *Eur. Phys. J. E* **42**, 27 (2019). <https://doi.org/10.1140/epje/i2019-11789-7>. <https://rdocu.be/bpGYk>
39. J.C. Legros, Y. Gaponenko, A. Mialdun, T. Triller, A. Hammon, C. Bauer, W. Köhler, V. Shevtsova, *Phys. Chem. Chem. Phys.* **17**, 27713 (2015). <https://doi.org/10.1039/C5CP04745E>
40. J. Zhang, P. Zhang, K. Ma, F. Han, G. Chen, X. Wei, *Sci. China Ser. B Chem.* **51**, 420 (2008). <https://doi.org/10.1007/s11426-008-0045-0>

Mass diffusion and Soret coefficient measurements of triethylene glycol/water binary mixtures by dynamic shadowgraphy

A.T. Ndjaka^{a,b}, L. García-Fernández^c, D. E. Bouyou Bouyou^a, A. Lassin^b, M. Azaroual^{b,d},
F.Croccolo^a, H. Bataller^{a*}

^a Université de Pau et des Pays de l'Adour, E2S UPPA, CNRS, TotalEnergies, LFCR
UMR5150, Anglet, France

^b BRGM, F-45060 Orléans, France

^c Department of Structure of Matter, Thermal Physics and Electronics, Faculty of Physics,
University Complutense of Madrid, Avda. Complutense s/n, 28040 Madrid, Spain

^d Univ. Orléans, CNRS, BRGM, ISTO, UMR 7327, F-45071, Orléans, France

* Corresponding author: henri.bataller@univ-pau.fr

Abstract

The investigation of the transport properties of binary fluid mixtures remains a topic of interest in relation to the more challenging studies of ternary mixtures. In fact, the study of the phase boundary limits of the Gibbs composition triangle can be the initial step for a more complete analysis of ternary mixtures. In this paper, we apply the dynamic shadowgraphy optical technique to study non-equilibrium fluctuations induced by the presence of a gradient of temperature and/or of concentration in the triethylene glycol (TEG)/water system. These thermodiffusion and free-diffusion experiments aim at measuring the transport properties of samples of the studied system at different experimental conditions. We scan both the average temperature and the TEG concentration, which allows us investigating both positive and negative thermodiffusive behaviours. The obtained values of mass diffusion coefficient are consistent with data available in the literature in the range of temperature investigated in this study. The mass diffusion coefficient of the sample prepared at 0.7 w/w TEG concentration are characterised by shadowgraphy following the two proposed methods, exhibiting consistent results. An increase of the mass diffusion coefficient as a function of the average temperature

is highlighted. On the other hand, the thermodiffusion coefficient appears to be independent of the average temperature of the sample at 0.3 w/w TEG concentration.

1. Introduction

The transport properties of complex fluids under non-equilibrium conditions are of interest from both scientific and technological points of view. Transport phenomena occurs in almost any multicomponent mixture present in nature and in industry and its comprehension is of great interest for many applications, such as the exploitation of crude oil wells and the storage of CO₂ in deep brine aquifers. [1], [2]. A suitable characterization of transport processes in complex mixtures requires a thorough understanding of simpler fluids. So far, binary mixtures have been extensively characterized [3], [4]. The extension of theories and experiments from binary to ternary mixtures requires further development due to the intrinsic and significant increase of difficulty with the number of components of the mixture and their mutual interactions. Currently, a great effort is devoted to investigate the transport phenomena in ternary mixtures. Thermodiffusion experiments in ternary mixtures are performed on ground, by using different optical techniques [3], [5]–[7], or in microgravity conditions in order to avoid both convection and sedimentation. The thermodynamic characterization of ternary mixtures is one of the objectives of different ESA projects, like: Diffusion Coefficient Measurements in ternary mIXtures (DCMIX) [7]–[11], Soret Coefficients in Crude Oil (SCCO) [12]–[15] and Giant Fluctuations [16], [17]. The knowledge of the behavior of the binaries associated to the ternaries remains an important step because they correspond to the binary phase boundary limits in the ternary Gibbs composition triangle, and interpolated values of the Soret coefficient can be obtained in some conditions [18].

Complex fluids subjected to non-equilibrium conditions exhibit non-equilibrium fluctuations (NEFs) of the thermodynamic variables [19]–[21]. These conditions can be induced, for

example, by applying a temperature gradient to a multicomponent fluid mixture, thus inducing a temperature gradient within the fluid as well as a composition gradient by means of thermodiffusion, also called the Soret effect [3], [22]. Superimposing two layers at different concentrations of a solution generates an initial gradient of concentration which evolves towards an equilibrium state by mass diffusion, in the absence of convective motions [23]. Both free-diffusion and thermodiffusion transport processes can be investigated by optical techniques and particularly by light scattering thanks to its ability to visualize NEFs without altering the intrinsic properties of the fluid. The transport properties of the fluid can be determined both at atmospheric [24] and at high pressure [25]. In this work, dynamic shadowgraphy has been adopted [23], [26], [27] to study the refractive index fluctuations as generated by the NEFs of the temperature and concentration in the case of thermodiffusion experiments, and of the concentration in the case of free-diffusion experiments. It is important to highlight the novelty of using this methodology to determine the transport properties of fluid mixtures in free-diffusion experiments. By shadowgraphy, a large range of fluctuation sizes λ or, conversely, of wave numbers $q = 2\pi/\lambda$, can be investigated at the same time, providing simultaneous reliable measurements of different transport properties, like mass diffusion coefficient or thermal diffusivity as well as Soret coefficient [5], [24], [28].

The aim of the present work is to investigate the diffusion and the thermodiffusion coefficients of the binary mixture of triethylene glycol (TEG) and water (H₂O), as one of the binary limits of the DCMIX3 ternary system, made of H₂O, ethanol and TEG [11]. These molecules are highly polar, and the prevailing hydrogen bonding leads to much more complex interactions than the dominating dispersion interactions in alkane mixtures for example. A consequence of these strong interactions are large negative excess volumes of mixing, leading to negative values of the Soret coefficient and to convective instabilities under terrestrial gravity conditions. In this study, it is worth noting the possibility of characterising mixtures with negative Soret

coefficients through the analysis of NEFs by using shadowgraph technique in both thermodiffusion and free-diffusion experiments.

The remainder of this paper is organized as follows: in section 2, the experimental procedure is described. In section 3, the theory of non-equilibrium fluctuations is summarized to provide the relevant working equations. The obtained results are presented in section 4, finally, conclusions are provided in section 5.

2. Experimental procedure

2.1. Solutions preparation and characterisation

Triethylene glycol (Sigma-Aldrich, T59455-1L, ReagentPlus®, purity 99%), used without further purification, and degassed de-ionized water (resistivity 18.5 MΩcm), retrieved from a Millipore Milli-Q filtration station, were used to prepare the studied samples at the required mixture compositions using an analytical balance (Sartorius TE313S, resolution 10^{-2} g/200 g). The thermophysical properties of the mixture, such as density, viscosity and both thermal and mass expansion coefficients are measured as follows.

The kinematic viscosity ν is measured at 20, 25 and 30 °C by capillary viscometer (Ubbelohde SCHOTT). The thermal and solutal expansion coefficients α and β , respectively, are defined as follows:

$$\alpha = -\frac{1}{\rho} \left(\frac{\partial \rho}{\partial T} \right)_{C,p} \quad (1)$$

$$\beta = \frac{1}{\rho} \left(\frac{\partial \rho}{\partial C} \right)_{T,p} \quad (2)$$

where ρ is the mixture density, T is the temperature and C is the TEG concentration in mass fraction.

The coefficients α and β are indirectly determined from measurements of the mixture density performed at different conditions through a Density Meter (ANTON PAAR, DMA 5000). First, in order to determine the thermal expansion coefficient, the density is measured at different temperatures (starting from 2 °C below the nominal temperature up to 2 °C above), while keeping the concentration constant. A linear relationship between the density and the temperature is observed in all cases. The parameter α is determined through Eq. (1), i.e. dividing the slope of the density vs. temperature by the density of the sample at the nominal temperature. Second, the mass expansion coefficient is obtained after measuring the density at different concentrations (starting from 2% w/w below the nominal concentration up to 2% w/w above), while keeping the temperature constant. A linear relationship between the density and the concentration is observed in all cases. The parameter β is determined through Eq. (2), i.e. dividing the slope of the density vs. concentration by the density of the sample at the nominal concentration. Measured values of ν , α and β are summarized in Table 1.

Table 1. Kinematic viscosity ν , thermal expansion coefficient α and solutal expansion coefficient β at different both mass fraction concentrations C of TEG and temperatures T .

T (°C)	ν (mm ² /s)	α ($\times 10^{-4}$ K ⁻¹)	β ($\times 10^{-1}$)
$C = 0.3$ w/w			
20	2.72 ± 0.03	4.22 ± 0.02	1.59 ± 0.08
25	2.32 ± 0.02	4.49 ± 0.02	1.55 ± 0.07
30	2.01 ± 0.02	4.77 ± 0.02	1.51 ± 0.07
$C = 0.5$ w/w			
20	6.25 ± 0.06	5.77 ± 0.01	0.145 ± 0.009
25	5.20 ± 0.05	5.87 ± 0.01	0.138 ± 0.005
30	4.34 ± 0.04	6.02 ± 0.01	0.134 ± 0.003
$C = 0.7$ w/w			

20	14.8 ± 0.1	6.633 ± 0.007	0.96 ± 0.02
25	11.9 ± 0.1	6.712 ± 0.004	0.949 ± 0.006
30	9.7 ± 0.1	6.799 ± 0.005	0.938 ± 0.008

The measurements of viscosity and density are repeated at least three times for each sample. The viscosities reported in Table 1 are calculated as the average of the three measurements and the corresponding uncertainties are the standard deviations. Considering the density uncertainties and the sensitivity of the method of least-square adjustment, the uncertainties on α and β are calculated by error propagation.

2.2. Free-diffusion and thermodiffusion cells

For the free-diffusion experiments, we used a diffusion cell specifically designed to put into contact two layers of two different liquid mixtures or two solutions of the same components at different concentrations, thus creating an initial step concentration gradient at uniform temperature while providing vertical optical access to a central area of the cell, similar to the flowing-junction cell already reported in literature [29]. The diffusion cell consists of a stainless steel annulus (see Fig. 1) with internal and external diameters of 30 mm and 80 mm, respectively, and a vertical thickness of $h = 10$ mm. The metallic annulus hosts four holes: two for fluids outlets at 180° in the horizontal plane and at mid-height of the cell in the vertical direction, and two for fluid inlet at 50° in the horizontal plane and at the same height in the vertical direction. In order to avoid the thermal contact between the liquid sample and the interior of the conductive metallic annulus, a polytetrafluoroethylene (Teflon®) ring with an internal and external diameter of 20 mm and 30 mm, respectively, is placed inside the stainless steel annulus (see Fig. 1a). This ring has also four thin holes in correspondence to those present in the metallic annulus to allow the circulation of the fluids. Moreover, the two holes for the

fluid inlets are inclined in the vertical direction so that one incoming fluid is steered to the top of the cell, while the other one is steered to the bottom of the cell.

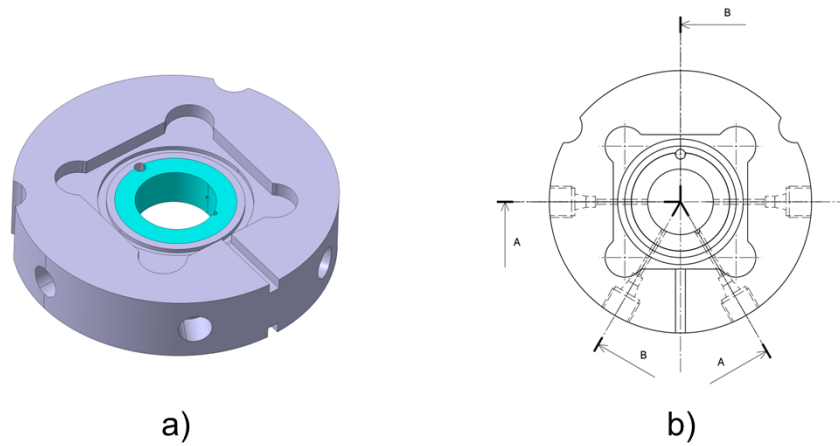


Figure 1: a) 3D-drawing of the stainless steel annulus with the Teflon ring in the inner part. b) 2D-drawing of the same, as observed from the top.

The stainless steel annulus is designed to accommodate two square sapphire windows ($8 \times 40 \times 40$ mm³), one on each vertical side with a groove for a Viton® O-ring for sealing. The two internal faces of the two sapphire windows are then separated by the metal annulus and kept apart by $h = 10$ mm, thus defining the vertical thickness of the fluid sample. The external surfaces of the two sapphire windows are in contact with two square aluminium plates with a central circular aperture with a diameter $d = 13$ mm. These plates are meant for hosting two temperature sensors so to measure the temperature as close as possible to the sapphires. The aluminium plates are also in contact with two square Peltier elements (Kryotherm, TB-109-1.4-1.5 CH) which can transport heat by means of a current flow and have the same central circular aperture. The Peltier elements provide/remove the heat necessary to maintain the set-point temperature as driven by two temperature controllers (Wavelength Electronics, LFI-3751) which use a proportional-integrating-derivative feedback system and maintain the temperature of the internal side of each Peltier device constant, with stability better than 1 mK RMS over 1 day. As shown in Fig. 2, all these elements are clamped by means of two aluminium blocks (with the same central circular

aperture) in which water coming from a thermostatic controlled bath (Huber, ministat 125), circulates in order to remove the Peltier elements excess heat.

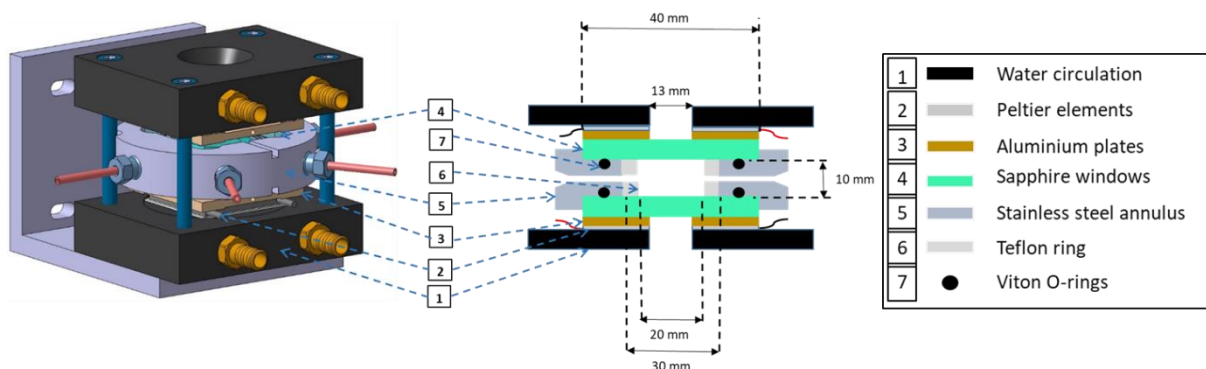


Figure 2: 3D drawing of the diffusion cell.

External to the stainless steel ring, metallic capillary tubes with external diameter of 1/8 inch and about 50 mm of length (the red stems visible in Fig. 2) are connected to each inlet/outlet. These capillary tubes end with a manual valve each (Swagelok, SS-41GS2), as shown in Fig. 3. The sample reservoirs are connected to the valves via flexible capillary tube (same external diameter as the metallic capillary tubes).

The cell filling is performed in two main steps. In the first step, the diffusion cell is completely filled with the less dense fluid. In order to do that, the fluid is slowly injected by gravity through the lower part, while air is let out of the outlet pointing to the top. By slightly tilting the cell, the residual air can be completely removed. Attention is paid to avoid any further air inlet while filling the other three capillary tubes. The second step consists of filling the bottom half of the cell with the denser fluid and create a sharp interface between the two fluids. This is achieved by filling the cell simultaneously with the two fluids from the bottom and the top inlets, while the remixed fluid is let out through the two outlets. Once half of the cell is filled with the denser fluid (the volume of fluid to be injected into the cell to fill it by half, taking into account the length and the internal diameter of capillary tubes and the dead volumes is calculated

beforehand), a relatively flat horizontal interface between the two fluids is formed. The four valves are simultaneously closed and the free-diffusion process starts.

For the thermodiffusion experiments the stainless steel annulus is replaced by a Viton O-ring with an internal diameter of $d = 25$ mm and thickness of $e = 3$ mm, the other components remain unchanged and capillaries are not necessary. The two sapphire windows are kept apart by four plastic spacers of $h = 2$ mm, thus defining the liquid layer thickness. The cell is filled by means of two syringe needles punctured through the Viton O-ring. During the filling procedure, the cell is inclined and the fluid is pushed through the bottom syringe while air is removed through the top one. After filling, the two needles are carefully removed and the holes in the O-ring close due to the pressure exercised on it by the sapphire windows. The cell is inserted into the shadowgraph setup once the filling is finished. For any given mean temperature, a temperature difference between the top and the bottom is applied by setting the corresponding temperatures to the Peltier elements. Once the stationary state is reached, i.e. after one diffusive time for the cell, the image recording is started.

2.3. Shadowgraph setup

The shadowgraph optical setup (Fig. 3) involves a super luminescent diode (Super Lumen, SLD MS-261-MP2-SM, $\lambda = 675 \pm 13$ nm), connected to a single-mode optical fiber. The divergent beam at the output of the fiber is collimated by an achromatic doublet lens (focal length $f = 150$ mm, and diameter $\phi = 50.8$ mm). The collimated beam passes through the free-diffusion cell, or the thermodiffusion cell, via two linear polarizers that allow adjusting the average transmitted light intensity, and is supposed to be perpendicular to the interface between the two solutions, in the case of free diffusion experiments, or parallel to the temperature gradient in the case of thermodiffusion experiments. A camera, whose detection plane is positioned at a distance of $z = (12.0 \pm 0.5)$ cm from the sample central plane, collects the sum of the light scattered by the

NEFs plus the transmitted one. As a camera sensor, we use a scientific-CMOS camera (Hamamatsu Digital Camera C13440, ORCA - Flash 4.0 V3) whose detector size is $s = 13.3$ mm. This camera sensor allows a fast image acquisition frequency, up to 100 Hz at full frame resolution of 2048×2048 square pixels with a pixel side of $l_{pix} = 6.5 \mu\text{m}$. Images are acquired in real time by the HCLive (x64) software program installed in a dedicated PC. In order to have both a good stability of acquisition frequency and a quick backup of the images, we use 4 Solid-State Drive (SSD) hard disks in RAID0 configuration.

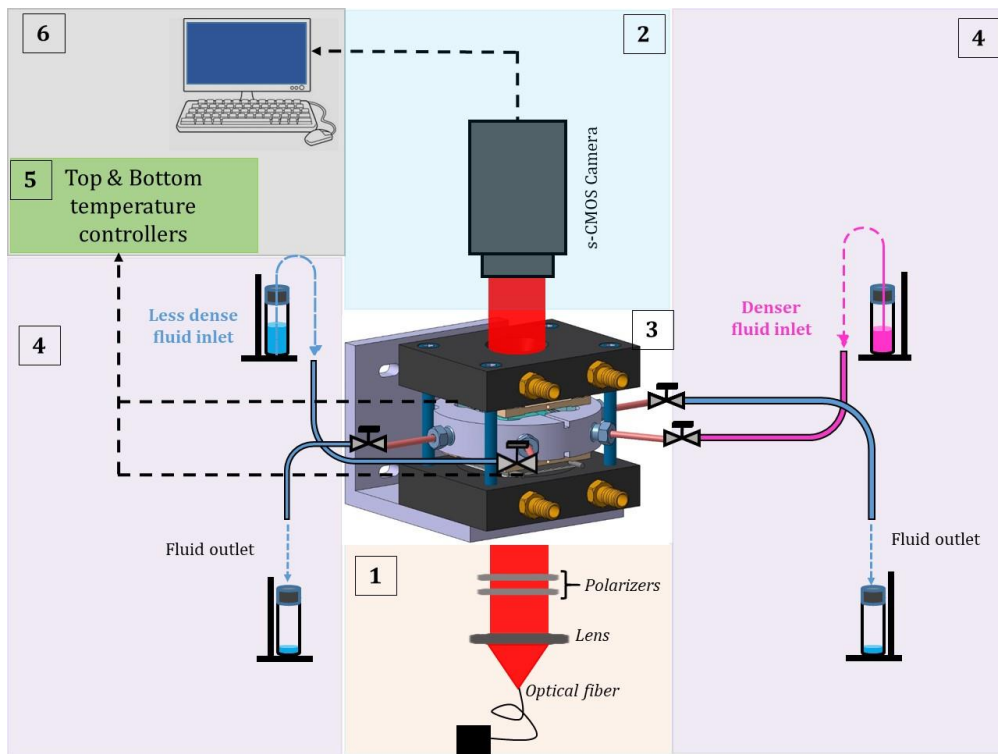


Figure 3: Shadowgraph optical set up summarized in six distinct blocks: 1) optical components; 2) s-CMOS Camera; 3) free-diffusion/thermodiffusion cell; 4) specific filling procedure; 5) temperature controllers; 6) computer equipment.

2.4. Dynamic Near field imaging

The images acquired in the near field consist of an intensity map $I(\vec{x}, t)$, generated by the interference on the s-CMOS plane between the portion of the incident beam that has passed undisturbed through the sample and the beams scattered by the refractive index fluctuations occurring within the sample. Here, \vec{x} and t stand for the position in the image plane and the time

lapsed during the acquisition, respectively. Thanks to the interference of different beams, the fluctuations in the fluid density, that are proportional to the fluctuations of the fluid refractive index, are transformed into fluctuations of the light intensity at the detector plane. Therefore, in order to study the dynamics of the density fluctuations in our samples, we calculate the Structure Function (SF) of the light intensity, i.e. of the acquired images, by means of an already proven Differential Dynamic Algorithm (DDA) [30]. The DDA algorithm consists of the following main steps: first, each recorded image $I(\vec{x}, t)$ is Fourier transformed in the 2D spatial space of the detector plane to obtain $I(\vec{q}, t) = \mathcal{F}(I(\vec{x}, t))$, then the Fourier transform (FT) is normalised by dividing it by the zero spatial frequency $i(\vec{q}, t) = I(\vec{q}, t)/I(\vec{0}, t)$ in order to remove the source intensity fluctuations. Then, the differences between normalized FTs at a given time difference Δt (called correlation time) $\Delta i(\vec{q}, t, \Delta t) = i(\vec{q}, t) - i(\vec{q}, t + \Delta t)$ are calculated. These Δt 's are, of course, multiples of the time delay dt_{\min} of the recording process, and cannot be larger than the acquisition duration. Finally, the 2D correlation functions are calculated by determining the - square moduli $|\Delta i(\vec{q}, t, \Delta t)|^2$ of the FT differences, and the individual spatial Fourier transforms of the image differences are averaged, first over all times t and second over the modulus of the wave number \vec{q} over the azimuthal angle. The result $\langle |\Delta i(q, \Delta t)|^2 \rangle_{q,t}$ is the SF of the recorded intensity fluctuations. In order to reduce the computational time to calculate the structure function out of the image series, we make use of a graphic card with the advantage of the massive parallelization on the Graphic Processing Unit (GPU) and an in-house developed software [30], [31]. This experimental quantity requires a physical model for its interpretation. The details of the theoretical model can be found elsewhere [19], [20]. In the present paper, we just recall the essential equations used to fit the SF.

2.5. Structure function analysis

The SF can be related to the power spectrum density fluctuation and the characteristics of the optical system as follows:

$$\langle |\Delta i(q, \Delta t)|^2 \rangle = 2\{T(q)S(q)[1 - ISF(q, \Delta t)] + B(q, \Delta t)\} \quad (3)$$

where $T(q)$ is the optical transfer function of the shadowgraph, $S(q)$ the static power spectrum of the fluctuations, the product $A(q) = T(q)S(q)$ is called the static structure factor (independent of the correlation time) and $B(q, \Delta t)$ is the signal background. It includes different contributions like electronic noise due to the camera and all the acquisition chain and can be modelled by $B(q, \Delta t) = C(q) + E(q) \cdot \Delta t + F(q) \cdot \Delta t^2$. The parabolic term $F(q) \cdot \Delta t^2$ becomes particularly important for the experiments performed in the free-diffusion configuration, where the system is never at the steady state, so that the background noise becomes time-dependent. The Intermediate Scattering Function $ISF(q, \Delta t)$ corresponds to the dynamic part of the SF, that can be described in many cases as the sum of exponential decays [32]–[34]: $ISF(q, \Delta t) = \sum_i a_i \exp(-\Delta t/\tau_i(q))$, where a_i are the amplitudes of the different modes with $\sum_i a_i = 1$ and $\tau_i(q)$ the wave-number-dependent relaxation times.

During a free-diffusion experiment, the density fluctuations recorded through the shadowgraph are mostly due to concentration-NEFs (c-NEFs) that are much more intense (orders of magnitude) than equilibrium temperature and/or concentration fluctuations present at the same time for the wave number range of our interest. Thus, the ISF is expected to be well described by a single exponential decay for all wave numbers. Thus, the SF is supposed to take the following form:

$$\langle |\Delta i(q, \Delta t)|^2 \rangle = 2 \left\{ A(q) \left[1 - \exp\left(-\frac{\Delta t}{\tau_c(q)}\right) \right] + C(q) + E(q) \cdot \Delta t + F(q) \cdot \Delta t^2 \right\} \quad (4)$$

where $\tau_c(q)$ is the decay time of the c-NEFs at wave number q .

When a stable temperature gradient parallel to the gravity field is applied to a homogenous binary fluid mixture, a concentration gradient is formed due to the Soret effect [3]. Hence, at the steady state of a thermodiffusion experiment a suitable expression for the *ISF* can be provided by the sum of two exponential decays given by the fluctuations of the concentration plus the fluctuations of the temperature (t-NEFs). The SF is supposed to take the following form:

$$\begin{aligned} \langle |\Delta i(q, \Delta t)|^2 \rangle = & 2 \left\{ A(q) \left[1 \right. \right. \\ & \left. \left. - \left\{ a \times \exp\left(-\frac{\Delta t}{\tau_T(q)}\right) + (1 - a) \times \exp\left(-\frac{\Delta t}{\tau_c(q)}\right) \right\} \right] \right. \\ & \left. + C(q) + E(q) \cdot \Delta t + F(q) \cdot \Delta t^2 \right\} \end{aligned} \quad (5)$$

where $\tau_T(q)$ is the decay time of the t-NEFs at wave number q .

$A(q)$, $\tau_i(q)$, $C(q)$, $E(q)$ and $F(q)$ are the fitting parameters at each wave number. In the case of a thermodiffusion experiment, if the steady state is fully reached, the term $F(q)$ is supposed to be negligible. However, we keep it in the fit in order to check the validity of our hypothesis and to be sure that the steady state has been reached. We use MatLab and an implemented Levenberg-Marquadt non-linear least-square fitting routine [35]. At the end of the fitting, we proceed to the analysis of the statics of the fluctuations through the static structure factor $A(q)$, as well as to the analysis of the dynamics of the fluctuations through the decay times $\tau_i(q)$. In the present paper, we will focus on the dynamics of the fluctuations.

3. Dynamics of the non-equilibrium fluctuations

The details of the theoretical description of the hydrodynamic behaviour of density fluctuations out-of-equilibrium can be found elsewhere [19], [20], so that here we just recall the main expressions useful for the experimental data analysis.

At intermediate and large wave numbers, in the absence of any convective movement, in the presence of the gravity force and in the bulk fluid, the decay time of the c-NEFs is given by:

$$\tau_c(q) = \frac{1}{Dq^2 \left[1 + \left(\frac{q_c}{q} \right)^4 \right]} \quad (6)$$

where D is the mass diffusion coefficient and q_c the cut-off wave number which defines the length scale below which the dynamics of the c-NEFs are no longer dominated by diffusion, but rather by buoyancy. The curve of the decay times as a function of wave numbers looks like a bell-shape (in log-log scale) and mirrors the presence of two distinct regimes as already reported in a number of previous publications [23], [24], [36]. The asymptotic behaviour of Eq. 6 for wave numbers larger than q_c is $\tau_c(q) = 1/Dq^2$ so that the diffusion coefficient D can be obtained from the fitting of the experimental data points in this region. In the case of a thermodiffusion experiment, the cut-off wave number is given by the expression [24], [25], [28], [37]:

$$q_c = \left(\frac{\beta g S_T C_0 (1 - C_0) \Delta T}{h \nu D} \right)^{1/4} \quad (7)$$

where β is the mass expansion coefficient of the binary mixture, g the gravitational acceleration, h is the vertical thickness of the sample, C_0 the equilibrium mass fraction of the denser component, S_T the Soret coefficient of the denser component, ΔT the difference of temperature between the top and the bottom of the thermodiffusion cell, and ν the kinematic viscosity of the binary mixture at the mean temperature of the experiment.

During a free-diffusion experiment, the concentration difference between the bottom and the top of the cell is assumed to remain constant until the diffusive process reaches the cell boundaries at the diffusive time $\tau_d = (h/2)^2/\pi D$. For times smaller than τ_d the cut-off wave number is given by the expression [23], [36], [38]:

$$q_c = \left(\frac{\beta g (C_1 - C_2)}{\nu D \sqrt{4\pi D t}} \right)^{1/4} \quad (8)$$

where C_1 and C_2 are the concentrations of the denser component, TEG, at the bottom and top layers in the diffusion cell, respectively. Unlike the thermodiffusion experiment, the cut-off wave number is time-dependent, following a power law with a $(-1/8 = -0.125)$ exponent.

Again, here we recall only the essential equations that are used to model the t-NEFs in the case of thermodiffusion experiments.

At intermediate and large wave numbers, in the absence of convection, in the presence of the gravity force and in the bulk fluid, the decay time of the t-NEFs is given by:

$$\tau_T(q) = \frac{1}{a_T q^2 \left[1 + \left(\frac{q_T}{q} \right)^4 \right]} \quad (9)$$

where a_T is the thermal diffusivity and q_T the thermal cut-off wave number which defines the length scale below which the dynamics of the t-NEFs is no longer dominated by thermal diffusion, but rather by buoyancy. The curve of the decay times as a function of wave numbers looks similar to the one described for c-NEFs, but, in general, decay times are shorter, due to the larger value of thermal diffusivity with respect to mass diffusion coefficient. The asymptotic behaviour of Eq. 9 for wave numbers larger than q_T is $\tau_T(q) = 1/(a_T q^2)$ so that the thermal diffusivity a_T can be obtained from the fitting of the experimental data points in this region.

4. Results and discussion

Mass diffusion and Soret coefficients for the mixture TEG/water at different concentrations are already known in the literature [39]. The present paper is intended to bring new measurements of the fluid transport properties at different temperatures. Some of the values reported here are anticipated in a joint paper about the system TEG/water/ethanol and the associated binary mixtures characterised by different measurement techniques [18]. Here we provide a full

detailed description of the experiments performed in our laboratory by means of dynamic shadowgraphy and the analysis of NEFs.

4.1. Thermodiffusion experiments

One remarkable property of the TEG/water mixture is that the sign of the Soret coefficient changes with respect to concentration. This implies that under thermal stress the denser component (TEG) migrates towards either the hot plate or the cold one. For $C=0.3$ w/w, the Soret coefficient is positive, so that the TEG migrates towards the cold plate, while for concentrations higher than $C=0.5$ w/w the Soret coefficient is negative in the temperature range between $15\text{ }^{\circ}\text{C}$ and $40\text{ }^{\circ}\text{C}$, so that the TEG accumulates at the hot plate. The presence of a negative Soret coefficient makes it difficult to perform thermodiffusion experiments in the presence of the gravitational field because, while heating the mixture from above, the density gradient generated by the concentration one (at the steady state of Soret separation) is unstable and can induce convection transport process in the system.

A first series of qualitative observations at the average temperature of $25\text{ }^{\circ}\text{C}$ have been performed for three different concentrations by applying to the samples either a stabilizing or a destabilizing temperature gradient. A stabilizing temperature gradient generates a density gradient parallel to the gravity acceleration. It is thus obtained by heating from above $\Delta T = +20\text{ K}$ and with a positive thermal expansion coefficient α . A destabilizing temperature gradient generates a density gradient anti-parallel to the gravity acceleration. It is thus obtained by heating from below $\Delta T = -20\text{ K}$.

C	$\Delta T = +20\text{ }^{\circ}\text{C}$	$\Delta T = -20\text{ }^{\circ}\text{C}$
-----	--	--

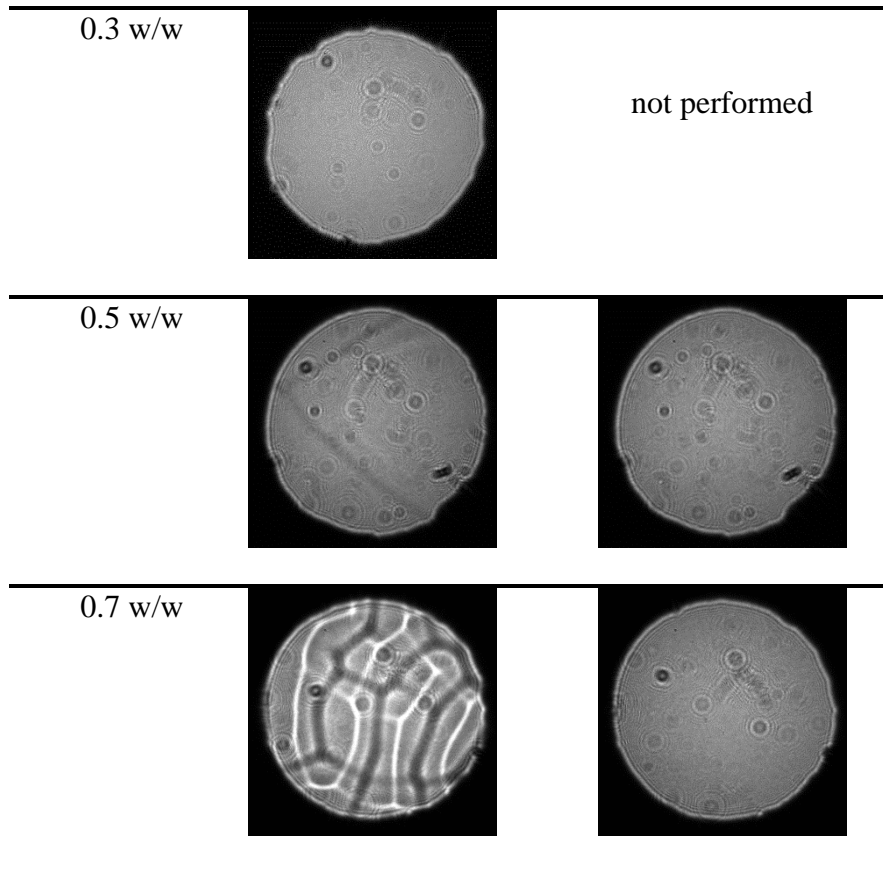


Figure 4: Shadowgraph patterns obtained at a mean temperature of 25 °C after applying different temperature gradients to samples of TEG concentration C (from top to bottom) 0.3, 0.5 and 0.7 w/w. The temperature difference over the cell thickness is of $\Delta T = +20$ °C for the left column, and $\Delta T = -20$ °C for the right one.

As visible in Fig. 4, samples for $C=0.3$, 0.5 and 0.7 w/w have been stressed by positive and negative temperature differences while shadowgraph images were recorded in order to evaluate the presence of convective patterns after reaching the steady state of the Soret separation. The patterns obtained by heating the samples for $C=0.3$ w/w from above (thermally stable), are featureless at the steady state, thus suggesting a stable configuration. In the patterns visible at $C=0.5$ w/w slight features appear, thus suggesting a moderate convective instability taking place within the fluid. This means that the density gradient originated by the concentration gradient is slightly larger in modulus than the density gradient generated by the temperature gradient. Finally, strong convective patterns appear in the case for $C=0.7$ w/w thus confirming

the negative sign of the Soret coefficient for the mixture TEG/water for concentration of TEG larger than 0.5 w/w.

For the cases when a stable configuration was reached at the steady state, series of images were recorded in order to analyse the NEFs and extract the transport properties of the mixture as described above. Series of 2500 images of 2048x2048 pix² were recorded at 100 Hz, 10 Hz and 1 Hz at different mean temperatures of 20, 25 and 30 ° C.

The SFs were calculated and concatenated according to a procedure already presented in our previous work [33], [34]. The resulting SFs obtained for the concentration of 0.3 w/w of TEG and the average temperature of 25 ° C is shown in Fig. 5.

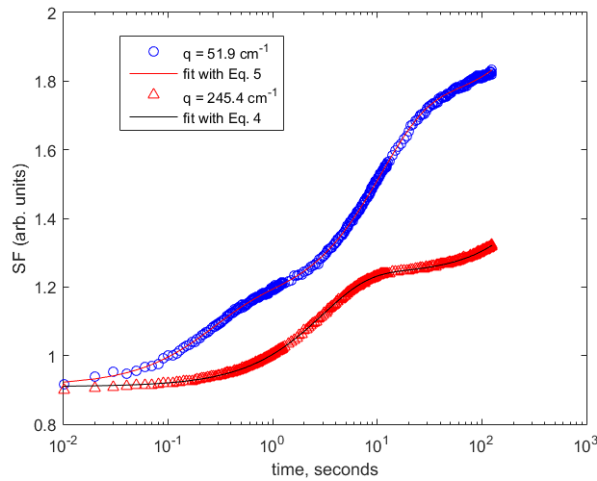


Figure 5: Concatenated structure functions for different wave numbers of the thermodiffusion experiment carried out at temperature difference of +20 °C, mean temperature of 25 °C and C=0.3 w/w.

The minimum accessible wave number is given by $q_{min} = 2\pi/L$, L being the side of the image in the real space. For the acquired images, $L = 1.33$ cm, so that $q_{min} = 4.72$ cm⁻¹. The theoretical maximum frequency is $q_{max} = (N_{pix}/2) \cdot q_{min} = 4833$ cm⁻¹, N_{pix} being the number of the pixels along one side of the images.

By the analysis of the concatenated SFs, like those shown in Fig. 5, we could determine that a double exponential decay is present for wave numbers $q < 200 \text{ cm}^{-1}$, while a simple exponential decay is present for wave numbers $q > 200 \text{ cm}^{-1}$. Following this observation, the SFs have been fitted by Eq. 5 for wave numbers smaller than 200 cm^{-1} and Eq. 4 for larger ones. As anticipated, the resulting values for the parameters $E(q)$ and $F(q)$ turned out to be negligible, as an indirect confirmation that the images have been acquired at the steady state of the thermodiffusion experiment. In this case, the quantity $A(q)/B(q)$ can be calculated and provides a useful indication of the signal-to-noise ratio of the measurement. In Fig. 6, the values of such ratio are reported for measurements performed at $C=0.3$ and 0.7 w/w and for different average temperatures.

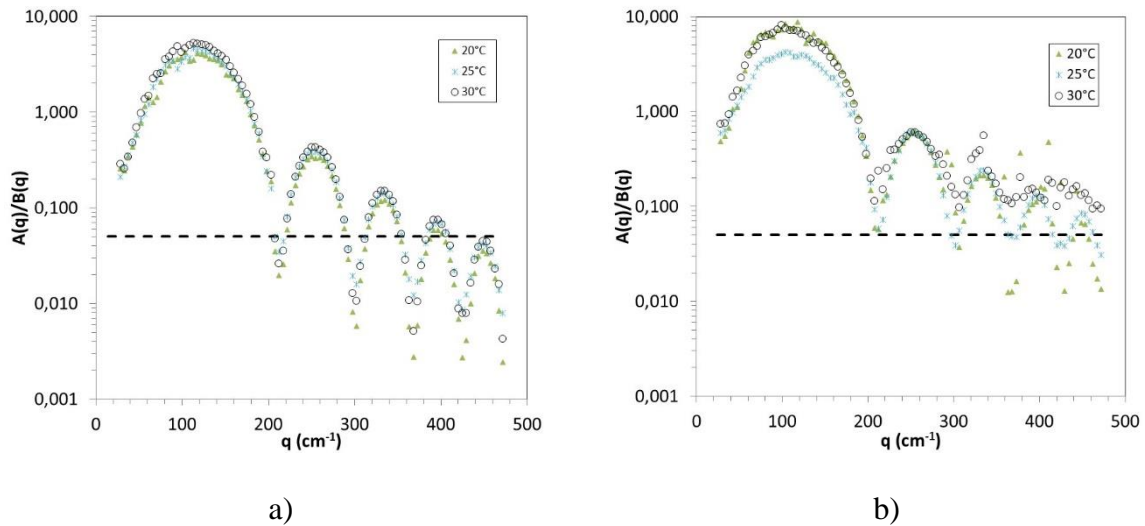


Figure 6: Ratio between the static structure factor and the signal background as a function of the wave number and the mean temperature for the thermodiffusion experiments carried out at temperature difference of a) $+20 \text{ }^\circ\text{C}$ for $C=0.3 \text{ w/w}$ and b) $-20 \text{ }^\circ\text{C}$ for $C=0.7 \text{ w/w}$.

The oscillations visible in the graphs are related to the shadowgraph transfer function $T(q)$ that vanishes at specific wave number. The horizontal line visible in Fig. 6 stands for the threshold value of 0.05 above which we consider that a shadowgraph measurement cannot provide reliable results [40], [41]. After such analysis, we decided to perform the fitting in the common

wave number range from 30 to 450 cm^{-1} for both mixtures, thus spanning more than one decade in wave numbers.

The decay times obtained by fitting data points with the model functions described above are reported in Fig. 7. In the latter, results are shown for the two concentrations of $C=0.3$ and 0.7 w/w at the three different temperatures.

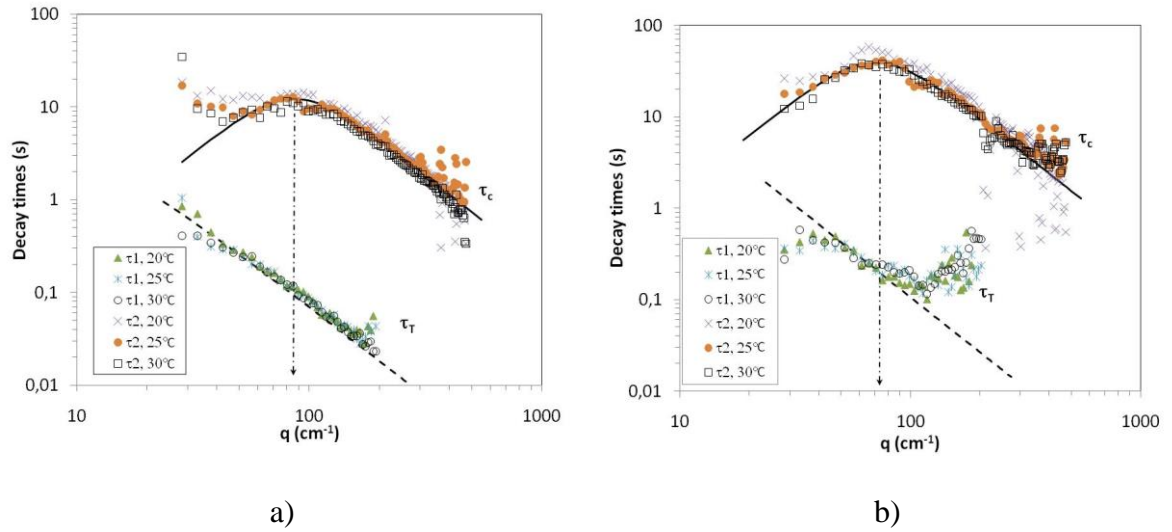


Figure 7: Decay times of the t-NEFs (τ_T) and the c-NEFs (τ_C) as a function of the wave number and for three different values of the mean temperature for the thermodiffusion experiments carried out at temperature difference of a) $+20^\circ\text{C}$ for $C=0.3$ w/w and b) -20°C for $C=0.7$ w/w. The continuous lines represent the fitting of the c-NEFs at 25°C with Eq. 6. The dashed lines represents the fitting of the t-NEFs at 25°C with the asymptotic behavior of Eq. 9.

In both cases, two time decays can be identified for most of the wave numbers. The fastest modes, corresponding to the smaller value of the time decay, are related to the decay of thermal fluctuations. Data points obtained for $C = 0.7$ w/w are more scattered than those obtained for $C = 0.3$ w/w. A possible explanation can be related to the negative Soret coefficient and the consequent coexistence of a stable density gradient stemming from concentration profile and an unstable one stemming from the temperature profile. Nevertheless, two diffusive regimes are clearly visible in both graphs, as indicated by the decay time behavior proportional to q^{-2} . On the contrary, the gravitational effect is almost not observable and no clear maximum can be

detected for the thermal modes. Nevertheless, fitting the thermal time decays with the asymptotic behaviour of Eq. 9 can provide a reliable estimation of the thermal diffusivity a_T . The slowest modes are then related to the decay of concentration fluctuations. For the two concentrations, a mass diffusive mode can be detected as well as the effect of gravity reducing the time decay of NEFs for wave numbers smaller than a characteristic value (q_c). Fitting the concentration time decays with Eq. 6, provides the mass diffusion coefficients D and the cut-off wave numbers q_c at different mean temperatures. At the smallest wavenumbers for $C = 0.3$ w/w, a deviation between the experimental points and the gravity behaviour predicted by Eq. 6 is noticeable. Such behaviour has already been observed on polymer-based systems (slowing-down of the larger fluctuations) [33], [34], and can be attributed to the coupling between different modes, and can also explain why the gravitational behaviour of the thermal fluctuations is not detectable. With the values of D , q_c , β and ν the Soret diffusion coefficients S_T are calculated through Eq. 7. The resulting values of the transport coefficients obtained by thermodiffusion experiments are reported in Table 2.

Table 2. Diffusion coefficients D , cut-off wave number q_c , thermal diffusivity a_T and Soret coefficient S_T obtained by thermodiffusion experiments of TEG/water mixtures at different mean temperatures T and TEG mass fraction concentration C .

T (°C)	D ($\times 10^{-6}$ cm ² /s)	q_c (cm ⁻¹)	a_T ($\times 10^{-4}$ cm ² /s)	S_T ($\times 10^{-3}$ K ⁻¹)
$C = 0.3$ w/w				
20	4.79 ± 0.12	86.7 ± 1.1	13.1 ± 0.4	2.3 ± 0.3
25	5.46 ± 0.15	86.8 ± 1.3	13.1 ± 0.2	2.3 ± 0.3
30	6.4 ± 0.3	84 ± 2	13.29 ± 0.13	2.0 ± 0.4
$C = 0.7$ w/w				
20	2.02 ± 0.08	70.7 ± 1.5	9.4 ± 0.2	-3.8 ± 0.6
25	2.6 ± 0.1	70.3 ± 1.4	9.4 ± 0.4	-3.9 ± 0.6
30	2.73 ± 0.06	70.5 ± 0.8	9.4 ± 0.4	-3.4 ± 0.3

Uncertainties for the mass diffusion coefficients, cut-off wave numbers and thermal diffusivities are those given by the fitting routine. Uncertainties for the Soret coefficients are calculated by error propagation. The values reported in Table 2 show that the diffusion coefficient increases with the temperature for the two TEG concentrations, which is a reasonable behaviour as fluid viscosity typically decreases with increasing temperature and the mass diffusion coefficient is inversely proportional to the fluid viscosity, following the Stokes-Einstein relation. Taking into account the uncertainties, the values of the Soret coefficient do not change over the investigated temperature range for $C=0.3$ w/w, and a clear trend is not observed for $C = 0.7$ w/w.

4.2. Free-diffusion experiments

For the concentration $C=0.5$ w/w it was not possible to obtain a reliable measurement of the mass diffusion coefficient from the thermodiffusion experiments, therefore free-diffusion experiments were performed at the different temperatures of 20, 25 and 30 °C. Further experiments were performed in free-diffusion for the concentration $C=0.7$ w/w in order to confirm the results obtained by thermodiffusion, given the fact that this is the first time that a shadowgraph investigation of NEFs is performed on a sample with negative Soret coefficients to extract its transport coefficients. In the case of a free-diffusion experiment, the diffusion cell is filled as described in section 2.2. Briefly, the diffusion cell is first filled with the less dense solution and subsequently, the less dense and the denser solution fills about half of the cell, the valves are closed and the free-diffusion process starts. In the case of the isothermal diffusion experiment, only one mode is expected to be measured corresponding to the relaxation of c-NEFs in the fluid mixture. The time decays are therefore expected to span a narrower range of time, so that only one series of images of 1024×1024 pix² is acquired at a frequency of 10 Hz. In this simpler case, the SFs are directly calculated by the DDA algorithm without further processing, as shown in Fig. 8 for the average concentration of $C=0.5$ w/w, a difference of

concentration of $\Delta C = C_1 - C_2 = 0.2$ w/w between the two superposed fluid layers, a homogeneous temperature of 25 °C, and 80 minutes after closing the valves.

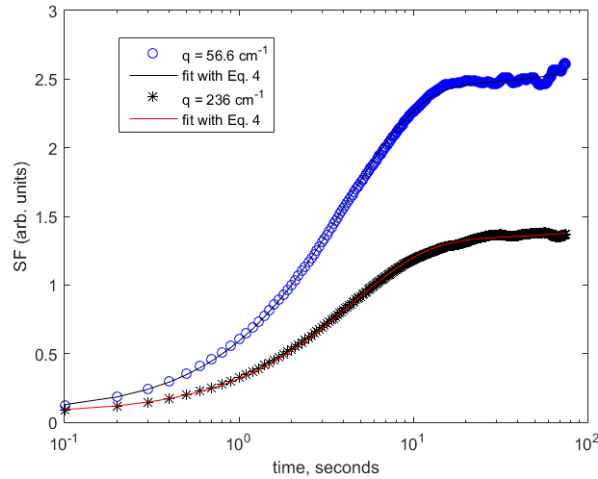


Figure 8: Structure function for different wave numbers of the free-diffusion experiment carried out at the mean concentration of $C=0.5$ w/w, difference of concentration $\Delta C = 0.2$ w/w between the bottom and top layer solutions, mean temperature of 25°C and 80 minutes after closing the valves.

In the case of free-diffusion experiments, the SFs show a single exponential decay, as expected, so that data points can be fitted through Eq. 4 for the entire range of wave numbers. In Fig. 9 the signal-to-noise ratio is shown for the sample with $C=0.5$ w/w and the homogeneous temperature $T=25$ °C for images taken 80 minutes after closing the inlet/outlet valves. The values are reported for three different values of the concentration difference $\Delta C = 0.1, 0.2$ and 0.4 w/w. By comparing Fig. 6 and 9, it is evident that the signal obtained in the case of free-diffusion experiments is much larger than the one obtained in the thermodiffusion experiments. That is due to the fact that the overall signal intensity is proportional to the square of the density gradient, that is much larger in the free-diffusion case due to the different shape of the concentration profile. The optical signal, however, is integrated over the entire fluid vertical thickness, which reduces the overall difference in signal intensity. As visible from Fig. 9, the signal also increases with increasing concentration difference and distance for ΔC between 0.1 and 0.2 w/w. However, it is approximately the same in a log-log graph whatever the distance

for ΔC between 0.2 and 0.4 w/w, which is coherent with a quadratic dependence of the signal to the concentration difference.

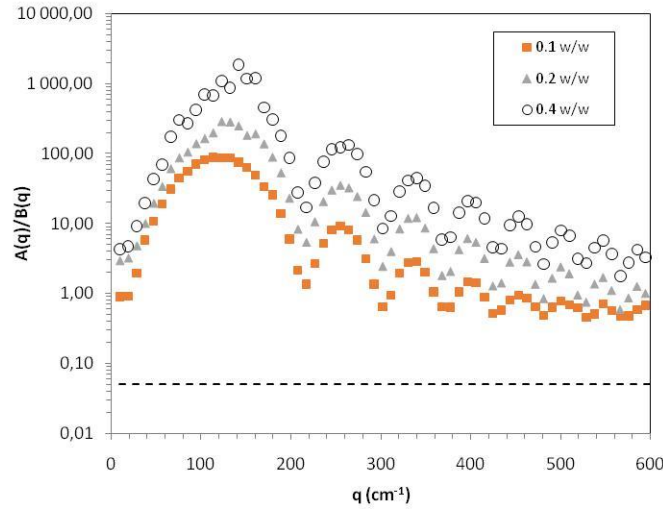


Figure 9: Ratio between the static structure factor and the signal background as a function of the wave number for the free-diffusion experiments carried out at mean concentration of $C=0.5$ w/w, and for different concentration differences between the bottom and the top layers, at 25°C and 80 minutes after closing the valves.

In the case of free-diffusion experiments, we decided to further analyse data points in the wave number range from 30 to 600 cm^{-1} , within which the signal-to-noise ratio indicator keeps above the threshold. In Fig. 10 we report the decay times obtained from fitting the SFs as a function of the wave number q and for different times after closing the inlet/outlet valves. The graph corresponds to a sample with $C=0.5$ w/w, $\Delta C = 0.2$ w/w and $T = 25^\circ\text{C}$. As stated before, only one mode can be detected corresponding to the decay of c-NEFs. By fitting the decay times through Eq. 6 we can obtain a measurement of the roll off wave number q_c and the mass diffusion coefficient D .

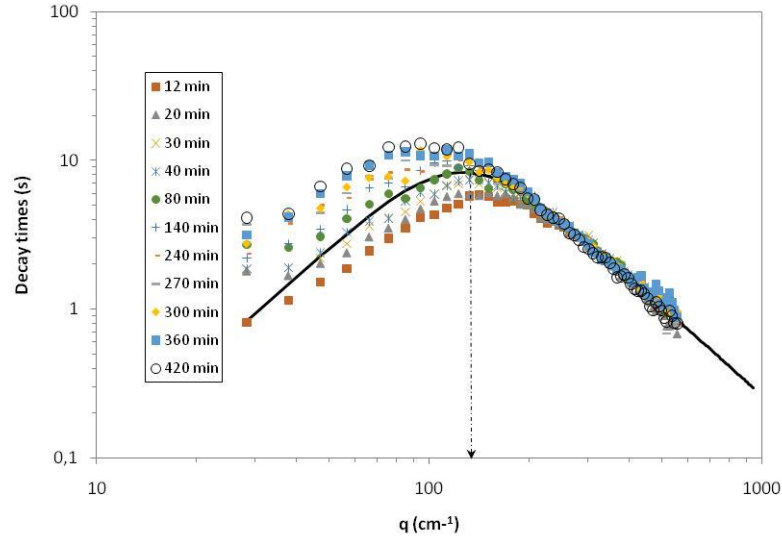


Figure 10 : Decay times of the c-NEFs as a function of the wave numbers for different times after closing the inlet/outlet valves for the free-diffusion experiment carried out at $C=0.5$ w/w, difference of concentration $\Delta C=0.2$ w/w and $T=25$ °C. The continuous black line corresponds to the curve got by fitting Eq. 6 to data points obtained 80 minutes after starting the free-diffusion experiment.

For all the times, the relaxation time curve has a bell-shape in the log-log plot of τ vs. q . As already reported in a number of publications, the right part of such curves for large wave numbers corresponds to the diffusive regime of c-NEFs. All curves collapse onto a single one for large wave numbers, because the mass diffusion coefficient remains constant during the free-diffusion process. This can be clearly observed also in Fig. 11-a, where the mass diffusion coefficients obtained after fitting time decays through Eq. 6 are shown as a function of the normalised time (i.e. t/τ_d , τ_d calculated using reference values of D). Moreover, the diffusion coefficient does not change with respect to the applied concentration difference ΔC . All data shown in Fig. 11 are relative to the average concentration $C=0.5$ w/w at $T=25$ °C. On the contrary, the position of the maximum of the decay time bell-shape, q_c , decreases with time, as shown Fig. 11-b.

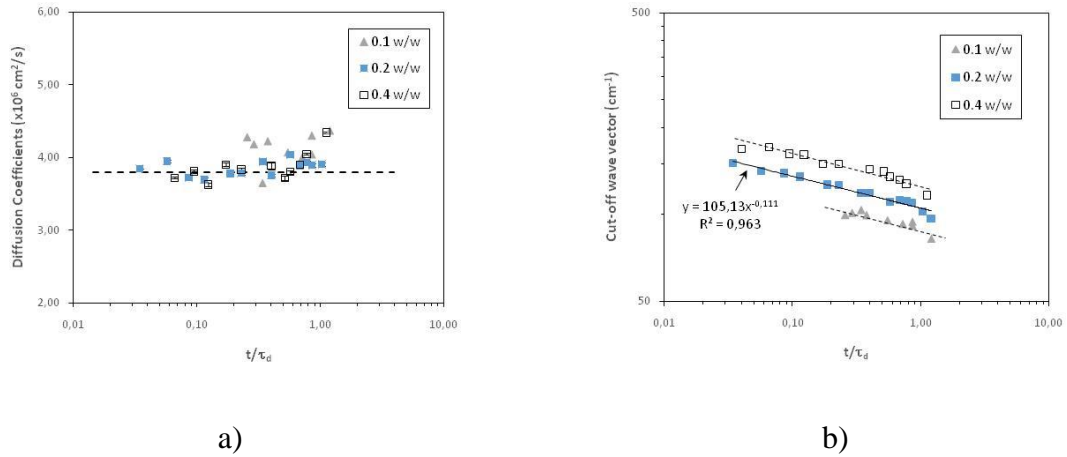


Figure 11: a) Mass diffusion coefficient D and b) cut-off wave number q_c as a function of the normalized time for different concentration differences for the free-diffusion experiments carried out at $C=0.5$ w/w and $T=25$ °C.

The values obtained for the mass diffusion coefficient D are nicely centred around the literature value obtained by Optical Beam Deflection (OBD) [18], that is represented by a horizontal dashed line in Fig. 11-a. The values obtained for $\Delta C=0.1$ w/w are somewhat more scattered, which mirrors the smaller signal-to-noise ratio, also visible in Fig.9. Moreover, the measurement error is increased for times close to the diffusive time of the cell, because, again, the signal-to-noise ratio decreases due to the decrease of the concentration gradient. The values obtained for the mass diffusion coefficient remain almost constant as a function of time and do not depend on the concentration difference imposed at the beginning of the experiment. Conversely, the cut-off wave number decreases with time and with the concentration difference according to Eq. 8. Fitting data point with a power law and free exponent provides a value of -0.11, rather close to the theoretical value of -0.125.

The experiments reported in Fig. 12 have been performed with average concentration $C=0.5$ w/w and concentration difference $\Delta C=0.2$ w/w. In Fig. 12-a we report the values of the mass diffusion coefficient and the cut-off wave number as a function of the normalised time and for

different values of the homogeneous temperature. In Fig. 12-b we report the values of the cut-off wave number as a function of the normalized time in the same conditions.

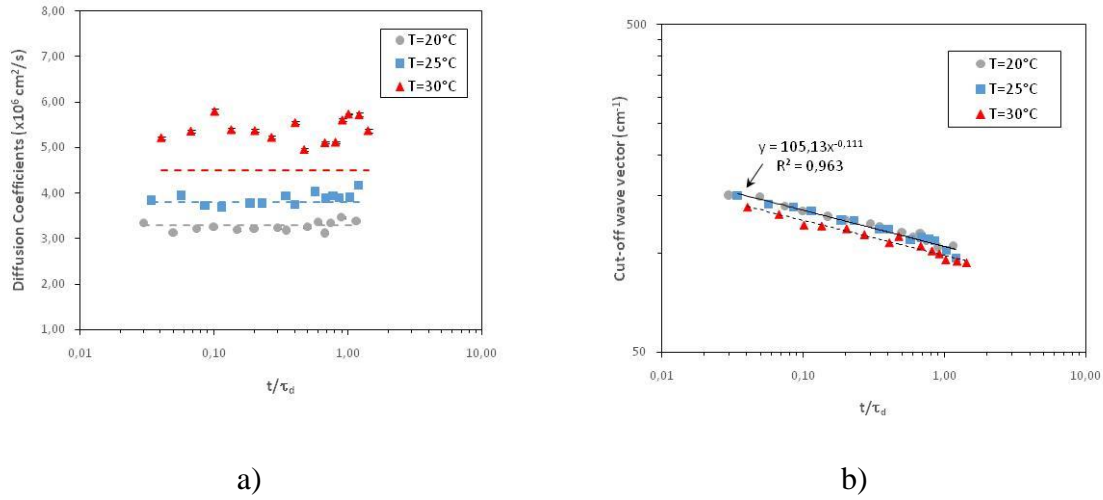


Figure 12 a) Mass diffusion coefficient and b) cut-off wave number as a function of the normalized time for different temperatures for the free-diffusion experiments with $C=0.5$ w/w and $\Delta C=0.2$ w/w.

In Fig. 12-a, the horizontal dashed lines provide a visual reference of the values of the mass diffusion coefficient obtained by OBD and reported in the literature [18]. The data points for $T=20$ and 25 °C are in very good agreement with the literature values, however those obtained at 30 °C show a 10% difference with respect to the literature one. In Fig. 12-b we can see that the wave numbers follow a power law dependence upon reduced time with an exponent close to the theoretical value of -0.125 for all the three investigated temperatures.

In Table 3 we provide the obtained values of the mass diffusion coefficients as obtained by the free-diffusion experiments performed at the two average concentrations of $C=0.5$ and 0.7 w/w, at the three different homogeneous temperatures of $T=20$, 25 and 30 °C. For the average concentration of $C=0.7$ w/w, the studied concentration difference between bottom and top solutions was $\Delta C=0.2$ w/w. The corresponding mass diffusion coefficients obtained at different temperatures are consistent or even compatible to those summarized in Table 2 for the same TEG concentration of 0.7 w/w.

Table 3. Mass diffusion coefficients D obtained by free-diffusion experiments at mean concentration C in mass fraction of TEG and homogeneous temperature T .

$D (\times 10^{-6} \text{ cm}^2/\text{s})$		
$T (\text{°C})$	$C = 0.5 \text{ w/w}$	$C = 0.7 \text{ w/w}$
20	3.27 ± 0.10	2.15 ± 0.16
25	3.86 ± 0.14	2.32 ± 0.06
30	5.4 ± 0.3	3.00 ± 0.13

The uncertainties reported in Table 3 correspond to the standard deviation with respect to the average value including the measurements obtained at different normalised times. In the case of the measurements performed at $C=0.5 \text{ w/w}$, we averaged data obtained for $\Delta C=0.2$ and 0.4 w/w .

5. Conclusion

In this paper, we have measured the mass diffusion and the thermodiffusion coefficients of triethylene glycol and water binary mixtures at different concentrations and average temperatures. Up to our best knowledge, this is the first time that the method combining dynamic shadowgraphy and the analysis of non-equilibrium fluctuations is used to measure the transport properties of a fluid mixture in a free-diffusion experiment. It is also the first time that the method is applied to measure the mass diffusion and the Soret coefficients in a thermodiffusion experiment for a sample of negative Soret coefficient as it is the case for the triethylene glycol/water mixture at $C= 0.7 \text{ w/w}$.

The obtained values of mass diffusion coefficient are consistent with data available in the literature for the range of temperature investigated in this study from 20 to 30°C. The mass diffusion coefficients of 0.7 w/w triethylene glycol/water mixture measured at different

temperatures through free-diffusion experiments are consistent with those determined by thermodiffusion experiments. An increase of the mass diffusion coefficient as a function of the average temperature is detected. On the other hand, the thermodiffusion coefficient appears to be independent of the average temperature of the sample at 0.3 w/w triethylene glycol concentration. Soret coefficients have been determined with a relative uncertainty of 10% without prior knowledge of optical contrast factors.

Acknowledgements

This work was developed in the framework of the cooperative project DCMIX (AO-2009-0858/1056) of the European Space Agency (ESA) and the Russian Space Agency (Roscosmos). The shadowgraphy measurements are supported by the ESA project GIANT FLUCTUATIONS and the ESA-MAP project TechNES (Grant 4000128933/19/NL/PG). We acknowledge financial support from the CNES and from the E2S UPPA Hub Newpores and the Industrial Chair CO2ES supported by the Investissements d’Avenir French programme managed by ANR (ANR-16-IDEX-0002), and BRGM and TotalEnergies. L. García-Fernández is thankful to Comunidad de Madrid for the financial support of the postdoctoral researcher contract “Atracción de Talento Investigador (2019-T2/AMB-15912)”.

References

- [1] F. Montel, J. Bickert, A. Lagisquet, and G. Galliéro, ‘Initial state of petroleum reservoirs: A comprehensive approach’, *Journal of Petroleum Science and Engineering*, vol. 58, no. 3, pp. 391–402, Sep. 2007, doi: 10.1016/j.petrol.2006.03.032.
- [2] H. Guo, Q. Zhou, Z. Wang, and Y. Huang, ‘Soret effect on the diffusion of CO₂ in aqueous solution under high-pressure’, *International Journal of Heat and Mass Transfer*, vol. 117, pp. 966–971, Feb. 2018, doi: 10.1016/j.ijheatmasstransfer.2017.10.058.

- [3] W. Köhler and K. I. Morozov, 'The Soret Effect in Liquid Mixtures – A Review', *Journal of Non-Equilibrium Thermodynamics*, vol. 41, no. 3, pp. 151–197, Jul. 2016, doi: 10.1515/jnet-2016-0024.
- [4] J. K. Platten *et al.*, 'Benchmark values for the Soret, thermal diffusion and diffusion coefficients of three binary organic liquid mixtures', *Philosophical Magazine*, vol. 83, no. 17–18, pp. 1965–1971, Jan. 2003, doi: 10.1080/0141861031000108204.
- [5] H. Bataller, T. Triller, B. Pur, W. Köhler, J. M. Ortiz de Zárate, and F. Croccolo, 'Dynamic analysis of the light scattered by the non-equilibrium fluctuations of a ternary mixture of polystyrene-toluene-n-hexane', *Eur. Phys. J. E*, vol. 40, no. 3, p. 35, Mar. 2017, doi: 10.1140/epje/i2017-11522-8.
- [6] H. Bataller, C. Giraudet, F. Croccolo, and J. M. Ortiz de Zárate, 'Analysis of Non-Equilibrium Fluctuations In A Ternary Liquid Mixture', *Microgravity Sci. Technol.*, vol. 28, no. 6, pp. 611–619, Dec. 2016, doi: 10.1007/s12217-016-9517-6.
- [7] M. M. Bou-Ali *et al.*, 'Benchmark values for the Soret, thermodiffusion and molecular diffusion coefficients of the ternary mixture tetralin+isobutylbenzene+n-dodecane with 0.8-0.1-0.1 mass fraction', *Eur. Phys. J. E*, vol. 38, no. 4, Art. no. 4, Apr. 2015, doi: 10.1140/epje/i2015-15030-7.
- [8] A. Ahadi, S. V. Varenbergh, and M. Z. Saghir, 'Measurement of the Soret coefficients for a ternary hydrocarbon mixture in low gravity environment', *J. Chem. Phys.*, vol. 138, no. 20, p. 204201, May 2013, doi: 10.1063/1.4802984.
- [9] A. Mialdun, I. Ryzhkov, O. Khlybov, T. Lyubimova, and V. Shevtsova, 'Measurement of Soret coefficients in a ternary mixture of toluene–methanol–cyclohexane in convection-free environment', *J. Chem. Phys.*, vol. 148, no. 4, p. 044506, Jan. 2018, doi: 10.1063/1.5017716.
- [10] A. Mialdun and V. Shevtsova, 'Temperature dependence of Soret and diffusion coefficients for toluene–cyclohexane mixture measured in convection-free environment', *J. Chem. Phys.*, vol. 143, no. 22, p. 224902, Dec. 2015, doi: 10.1063/1.4936778.
- [11] T. Triller *et al.*, 'Thermodiffusion in Ternary Mixtures of Water/Ethanol/Triethylene Glycol: First Report on the DCMIX3-Experiments Performed on the International Space Station', *Microgravity Sci. Technol.*, vol. 30, no. 3, pp. 295–308, May 2018, doi: 10.1007/s12217-018-9598-5.
- [12] M. Touzet, G. Galliero, V. Lazzeri, M. Z. Saghir, F. Montel, and J.-C. Legros, 'Thermodiffusion: From microgravity experiments to the initial state of petroleum reservoirs', *Comptes Rendus Mécanique*, vol. 339, no. 5, pp. 318–323, May 2011, doi: 10.1016/j.crme.2011.03.008.
- [13] G. Galliero *et al.*, 'Thermodiffusion in multicomponent n-alkane mixtures', *npj Microgravity*, vol. 3, no. 1, pp. 1–7, Aug. 2017, doi: 10.1038/s41526-017-0026-8.
- [14] S. VanVaerenbergh, S. Srinivasan, and M. Z. Saghir, 'Thermodiffusion in multicomponent hydrocarbon mixtures: experimental investigations and computational analysis', *J. Chem. Phys.*, vol. 131, no. 11, p. 114505, Sep. 2009, doi: 10.1063/1.3211303.
- [15] G. Galliero *et al.*, 'Impact of Thermodiffusion on the Initial Vertical Distribution of Species in Hydrocarbon Reservoirs', *Microgravity Sci. Technol.*, vol. 28, no. 2, pp. 79–86, May 2016, doi: 10.1007/s12217-015-9465-6.
- [16] P. Baaske *et al.*, 'The NEUF-DIX space project - Non-EquilibriUm Fluctuations during Diffusion in compleX liquids', *Eur. Phys. J. E*, vol. 39, no. 12, Art. no. 12, Dec. 2016, doi: 10.1140/epje/i2016-16119-1.
- [17] M. Braibanti *et al.*, 'European Space Agency experiments on thermodiffusion of fluid mixtures in space', *Eur. Phys. J. E*, vol. 42, no. 7, p. 86, Jul. 2019, doi: 10.1140/epje/i2019-11849-0.
- [18] M. Schraml *et al.*, 'The Soret coefficients of the ternary system water/ethanol/triethylene glycol and its corresponding binary mixtures', *Eur. Phys. J. E*, vol. 44, no. 10, p. 128, Oct. 2021, doi: 10.1140/epje/s10189-021-00134-6.
- [19] J. M. O. de Zárate and J. V. Sengers, 'Hydrodynamic Fluctuations in Fluids and Fluid Mixtures - 1st Edition'. <https://www.elsevier.com/books/hydrodynamic-fluctuations-in-fluids-and-fluid-mixtures/ortiz-de-zarate/978-0-444-51515-5> (accessed Sep. 30, 2021).
- [20] F. Croccolo, J. M. Ortiz de Zárate, and J. V. Sengers, 'Non-local fluctuation phenomena in liquids', *Eur. Phys. J. E*, vol. 39, no. 12, p. 125, Dec. 2016, doi: 10.1140/epje/i2016-16125-3.
- [21] A. Vailati and M. Giglio, 'Giant fluctuations in a free diffusion process', *Nature*, vol. 390, no. 6657, pp. 262–265, Nov. 1997, doi: 10.1038/36803.

- [22]E. Bouty, ‘CH. SORET. — Sur l’état d’équilibre que prend, au point de vue de sa concentration, une dissolution saline primitivement homogène, dont deux parties sont portées à des températures différentes; Archives de Genève, 3e periode, t. II, p. 48; 1879’, *J. Phys. Theor. Appl.*, vol. 9, no. 1, pp. 331–332, 1880, doi: 10.1051/jphystap:018800090033101.
- [23]F. Croccolo, D. Brogioli, A. Vailati, M. Giglio, and D. S. Cannell, ‘Nondiffusive decay of gradient-driven fluctuations in a free-diffusion process’, *Phys. Rev. E*, vol. 76, no. 4, p. 041112, Oct. 2007, doi: 10.1103/PhysRevE.76.041112.
- [24]F. Croccolo, H. Bataller, and F. Scheffold, ‘A light scattering study of non equilibrium fluctuations in liquid mixtures to measure the Soret and mass diffusion coefficient’, *J. Chem. Phys.*, vol. 137, no. 23, p. 234202, Dec. 2012, doi: 10.1063/1.4771872.
- [25]C. Giraudet, H. Bataller, and F. Croccolo, ‘High-pressure mass transport properties measured by dynamic near-field scattering of non-equilibrium fluctuations’, *Eur. Phys. J. E*, vol. 37, no. 11, p. 107, Nov. 2014, doi: 10.1140/epje/i2014-14107-1.
- [26]F. Croccolo and D. Brogioli, ‘Quantitative Fourier analysis of schlieren masks: the transition from shadowgraph to schlieren’, *Appl. Opt., AO*, vol. 50, no. 20, pp. 3419–3427, Jul. 2011, doi: 10.1364/AO.50.003419.
- [27]S. P. Trainoff and D. S. Cannell, ‘Physical optics treatment of the shadowgraph’, *Physics of Fluids*, vol. 14, no. 4, pp. 1340–1363, Apr. 2002, doi: 10.1063/1.1449892.
- [28]I. Lizarraga, C. Giraudet, F. Croccolo, M. M. Bou-Ali, and H. Bataller, ‘Mass Diffusion and Thermal Diffusivity of the Decane-pentane Mixture Under High Pressure as a Ground-based Study for SCCO Project’, *Microgravity Sci. Technol.*, vol. 28, no. 5, pp. 545–552, Oct. 2016, doi: 10.1007/s12217-016-9506-9.
- [29]F. Croccolo, D. Brogioli, and A. Vailati, ‘Cylindrical flowing-junction cell for the investigation of fluctuations and pattern-formation in miscible fluids’, *Review of Scientific Instruments*, vol. 90, no. 8, p. 085109, Aug. 2019, doi: 10.1063/1.5112778.
- [30]G. Cerchiarì, F. Croccolo, F. Cardinaux, and F. Scheffold, ‘Note: Quasi-real-time analysis of dynamic near field scattering data using a graphics processing unit’, *Review of Scientific Instruments*, vol. 83, no. 10, p. 106101, Oct. 2012, doi: 10.1063/1.4755747.
- [31]M. Norouziadeh, M. Chraga, G. Cerchiarì, and F. Croccolo, ‘The modern structurator: Increased performance for calculating the structure function.’, *submitted*.
- [32]J. M. O. de Zárate, C. Giraudet, H. Bataller, and F. Croccolo, ‘Non-equilibrium fluctuations induced by the Soret effect in a ternary mixture’, *Eur. Phys. J. E*, vol. 37, no. 8, Art. no. 8, Aug. 2014, doi: 10.1140/epje/i2014-14077-2.
- [33]F. Croccolo, L. García-Fernández, H. Bataller, A. Vailati, and J. M. Ortiz de Zárate, ‘Propagating modes in a binary liquid mixture under thermal stress’, *Phys. Rev. E*, vol. 99, no. 1, p. 012602, Jan. 2019, doi: 10.1103/PhysRevE.99.012602.
- [34]L. García-Fernández, P. Fruton, H. Bataller, J. M. O. de Zárate, and F. Croccolo, ‘Coupled non-equilibrium fluctuations in a polymeric ternary mixture’, *Eur. Phys. J. E*, vol. 42, no. 9, Art. no. 9, Sep. 2019, doi: 10.1140/epje/i2019-11889-4.
- [35]D. J. Higham and N. J. Higham, *MATLAB Guide, Third Edition*. SIAM, 2016.
- [36]F. Croccolo, D. Brogioli, A. Vailati, M. Giglio, and D. S. Cannell, ‘Use of dynamic schlieren interferometry to study fluctuations during free diffusion’, *Appl. Opt., AO*, vol. 45, no. 10, pp. 2166–2173, Apr. 2006, doi: 10.1364/AO.45.002166.
- [37]I. Lizarraga, F. Croccolo, H. Bataller, and M. M. Bou-Ali, ‘Soret coefficient of the n-dodecane-n-hexane binary mixture under high pressure’, *Eur. Phys. J. E*, vol. 40, no. 3, Art. no. 3, Mar. 2017, doi: 10.1140/epje/i2017-11520-x.
- [38]F. Croccolo, D. Brogioli, A. Vailati, M. Giglio, and D. S. Cannell, ‘Effect of Gravity on the Dynamics of Nonequilibrium Fluctuations in a Free-Diffusion Experiment’, *Annals of the New York Academy of Sciences*, vol. 1077, no. 1, pp. 365–379, 2006, doi: 10.1196/annals.1362.030.
- [39]J. C. Legros *et al.*, ‘Investigation of Fickian diffusion in the ternary mixtures of water–ethanol–triethylene glycol and its binary pairs’, *Phys. Chem. Chem. Phys.*, vol. 17, no. 41, pp. 27713–27725, Oct. 2015, doi: 10.1039/C5CP04745E.
- [40]K. He, M. Spannuth, J. C. Conrad, and R. Krishnamoorti, ‘Diffusive dynamics of nanoparticles in aqueous dispersions’, *Soft Matter*, vol. 8, no. 47, pp. 11933–11938, Nov. 2012, doi: 10.1039/C2SM26392K.

[41]M. S. Safari, M. A. Vorontsova, R. Poling-Skutvik, P. G. Vekilov, and J. C. Conrad, ‘Differential dynamic microscopy of weakly scattering and polydisperse protein-rich clusters’, *Phys. Rev. E*, vol. 92, no. 4, p. 042712, Oct. 2015, doi: 10.1103/PhysRevE.92.042712.